The CLARREO Mission - Earth's Climate Change Observations

Principal Investigator: Bruce A. Wielicki[1]

Project Scientist: Rosemary R. Baize[1]

Science Team:

D.F. Young[1], M.G. Mlynczak[1], K.J. Thome[2], S. Leroy[3], C.O. Ao[4], R. Bantges[5], F. Best[6], H. Brindley[5], J. Butler[2], R. Cageao[1], W. Collins[7], R. Cooke[14], J. Corliss[1], J.C. Currey[1], J.A. Dykema[3], D.R. Doelling[1], B. Dunn[1], D.R. Feldman[7], D. Goldin[10], H. Huang[8], R. Holz[6], Y. Huang[9], Z. Jin[10], D. Jennings[2], D.G. Johnson[1], S. Kato[1], R. Knuteson[6], G. Kopp[11], D.P. Kratz[1], X. Liu[1], C. Lukashin[1], A. Lyapustin[2], A. J. Mannucci[4], J. McCorkel[2], N. Phojanamongkolkij[1], P. Pilewskie[11], H. Revercomb[6], J. Rice[12], Y. Roberts[1], C.M. Roithmayr[1], F. Rose[10], W.L. Smith, Sr.[6], B. Soden[13], P.W. Speth[1], T.C. Stone[15], W. Sun[10], D. Tobin[6], X. Xiong[2]

Editor-in-Chief: Constantine Lukashin[1]

Affiliations

1. NASA Langley Research Center, Hampton, VA
2. NASA Goddard Space Flight Center, Greenbelt, MD
3. Harvard University, Cambridge, MA
4. Jet Propulsion Laboratory, Pasadena, CA
5. Imperial College, London, UK
6. University of Wisconsin, Madison, WI
7. Lawrence Berkeley National Laboratory, Berkeley, CA
8. University of Michigan, Ann Arbor, MI
9. McGill University, Montreal, Quebec, Canada
10. Science Systems and Applications, Inc., Hampton, VA
11. University of Colorado, Boulder, CO
12. National Institute of Standards and Technology, Gaithersburg, MD
13. University of Miami, Miami, FL
14. Resources for the Future, Washington, DC
15. US Geological Survey, Flagstaff, AZ

⋆ *In this document hyperlinks are shown in* *blue*; *Figures, Tables, and Equations are numbered by Section.*

Acknowledgments

Executive Summary

The Climate Absolute Radiance and Refractivity Observatory (CLARREO) is a high priority, NASA Decadal Survey mission recommended by the National Research Council in 2007. It fills the critical need for unambiguous climate change measurements with an unprecedented level of accuracy. The CLARREO mission will provide a metrology laboratory in orbit for the purpose of accurately quantifying and attributing climate change. The mission also provides the first orbiting radiometers with accuracy sufficient to serve as reference calibration standards for other space sensors, essentially serving as a "NIST in orbit." This will improve the accuracy, by a factor of 5 to 10, and relevance of a wide range of spaceborne instruments for observing Earth's changing climate.

Critical Observations of Climate Change: The climate change benchmarks established by CLARREO are critical for assessing changes in the Earth system as society works to meet the challenge of optimizing strategies for mitigating and adapting to climate change. The CLARREO data will be used to test and validate climate models. CLARREO benchmarks are obtained from direct measurements of the Earth's thermal infrared spectrum, the spectrum of solar radiation reflected by the Earth and its atmosphere, and radio occultation from which accurate temperature profiles are derived.

Near Term Science Impacts: CLARREO provides the first spectral observations of the far-infrared, which includes 50% of the Earth's energy emitted to space and contains most of the water vapor greenhouse effect. CLARREO's ability to establish a reference calibration standard for sensors in Earth's orbit will improve weather forecasting and data assimilation, and will improve the accuracy of a wide variety of climate-relevant observations including land processes, atmospheric state variables, aerosols and trace gases, and surface temperature.

CLARREO Societal Benefits: CLARREO provides the data necessary to accelerate decisions on public policy concerning climate change by 15 to 20 years. Earlier and better informed decisions provide a large economic benefit to the U.S. and the world, estimated to be approximately $12 Trillion over the next 40 to 60 years[1]. By reducing climate prediction uncertainties, CLARREO impacts: civil Government and military planning (i.e., Navy bases), disaster mitigation, response, and recovery (i.e., insurance industry), and U.S. international policy decisions.

CLARREO Technical Readiness: CLARREO successfully passed its NASA Mission Concept Review in November 2010, with recommendation to proceed to the next stage in development prior to a NASA budget decrease in 2011. The CLARREO instrumentation concepts are mature – TRL 6 and higher, and the level of technical risk is low.

CLARREO Mission Options: (a) *CLARREO Flying in 90° Inclination Polar Orbit*: A mission concept with a full suite of instruments: two of InfraRed and Reflected Solar spectrometers each , and two Radio Occultation instruments, flying on dedicated spacecrafts. (b) *CLARREO Flying on the International Space Station*: A mission concept to fly two instruments, InfraRed and Reflected Solar spectrometers, on the International Space Station and acquire the radio occultation data from the COSMIC. This option offers the best overall science value for the lowest cost. (c) *CLARREO-light option:* A mission concept to fly two reduced-mass spectrometers, InfraRed in sun-synchronous and Reflected Solar in polar orbits, on two small dedicated spacecrafts.

---

[1]Using the U.S. Interagency Memo of the Social Cost of Carbon (2010), CLARREO's value has been estimated at about $18 Trillion for a 2.5% discount rate, $12 Trillion for a 3% discount rate, or $3 Trillion for a 5% discount rate.

Contents

1   Introduction

The National Research Council Decadal Survey on Earth Science and Applications from Space concluded that one of the critical issues for many current climate change observations is the lack of absolute accuracy sufficient to confidently observe the small but critical climate change signals over decadal time scales [NRC, 2007; Trenberth et al., 2012; Trenberth and Fasullo, 2010; Ohring et al., 2005 and 2007]. Observing decadal climate change is critical to assessing the accuracy of climate model projections [IPCC, 2007a; Masson and Knutti, 2011; Stott and Kettleborough, 2002], as well as to attributing climate change to various sources [IPCC, 2007a]. Sound policymaking requires a high level of confidence in climate predictions verified against decadal change observations with rigorously known accuracy. Concerns about satellite data accuracy and the need for improvements have been expressed in U.S. interagency climate satellite calibration reports [Ohring et al., 2005, 2007], international climate observation system plans for the Global Earth Observing System of Systems [GEO, 2005], the Global Climate Observing System Implementation Plan [GCOS, 2011] and the Global Space Based Inter-calibration System [GSICS, 2006; Goldberg et al., 2011]. Common challenges with current satellite observations expressed in these documents include uncertain long term drifts of calibration, absolute accuracy lower than typical decadal change signals, and the inability to observe decadal climate change across gaps in observations [GEO, 2010].

The Climate Absolute Radiance and Refractivity Observatory (CLARREO) mission [Wielicki et al. 2013] addresses these concerns by providing a new level of absolute accuracy in global satellite observations that can be traced to international physical standards such as the SI standards for the second, the Kelvin, and the Watt. The CLARREO objectives of higher accuracy for decadal change observations lead to a very different set of observing strategies than have been employed in previous satellite missions, especially those designed for observing weather or climate processes. The required measurement accuracy levels are determined by the projected decadal changes in key climate parameters due to anthropogenic forcing as well as the background natural variability above which such changes must be detected. Because of this focus on longer time scales, CLARREO measurement requirements are determined not by instantaneous instrument noise levels, but instead by the long term absolute accuracy sufficient to detect climate decadal changes on large temporal and spatial scales (global, zonal, annual, and seasonal). The result is the creation of climate change benchmark measurements defined by three fundamental characteristics: (1) Traceability to fundamental SI standards at the accuracy level required to resolve decadal climate change signals, and to be robust to gaps in the observation record. (2) Sufficient temporal and spatial sampling to reduce aliasing error in global decadal change observations to levels well below predicted decadal climate change signals and below natural variability of the climate system. (3) Sufficient information content to determine change in key climate change variables.

The CLARREO benchmarks were defined in the NRC Decadal Survey as three different types of observations: (1) Spectrally resolved infrared (IR) radiance emitted from Earth to space measured with an accuracy of 0.07 K $(k = 2)$[2]. The infrared spectra are traced to the SI standard for the Kelvin. (2) Spectrally resolved nadir reflectance of reflected solar (RS)

---

[2]We use general coverage factor k to establish a more rigorous tie between the climate science and metrology research communities. In the case of a Gaussian distribution, $k = 2$ is the same 95% confidence level as for 2σ [BIPM, 2010; Datla et al. 2009].

radiation determined with an accuracy of 0.3% ($k = 2$). The percentage is relative to the mean spectral reflectance of the Earth of about 0.3. While spectral reflectance is a measurement relative to solar spectral irradiance, use of the spectral solar irradiance observations made by the Total Solar Irradiance Spectrometer (TSIS) enables traceability to the SI standard for the Watt. (3) Observations by Global Navigation Satellite Systems Radio Occultation systems (GNSS-RO, or simply RO). The GNSS-RO benchmark measurement is the phase delay rate of the transmitted GNSS signal occulted by the atmosphere from low Earth orbit (LEO) with an accuracy of 0.06% ($k = 2$) for a range of altitudes from 5 to 20 km in the atmosphere. The measurement is traced to the SI standard for the second.

The CLARREO IR, RS, and RO observations are designed to provide information on the most critical but least understood climate forcings, responses, and feedbacks associated with the vertical distribution of atmospheric temperature and water vapor (IR/RS/RO), broadband reflected (RS) and emitted (IR) radiative fluxes, cloud properties (IR/RS), and surface albedo (RS), temperature (IR), and emissivity (IR). The data will be used to achieve three independent CLARREO mission goals: (a) unambiguously documenting changes in the climate system, (b) testing and improving forecasts of future climate change, and (c) improving the accuracy of existing climate and weather sensors by providing reference spectrometers in orbit [NRC, 2007].

To achieve these goals, CLARREO will use two particular approaches: *climate benchmark spectral fingerprinting* and *reference inter-calibration*. Optimal detection methods [Leroy and Anderson, 2010] make use of spectral fingerprinting signals directly measured by the CLARREO instruments to determine climate response and climate system feedbacks [Leroy et al., 2008a; Huang et al, 2010a,b; Feldman et al, 2011a,b; Jin et al, 2011; Kato 2011]. The second approach is to use the CLARREO spectral measurement to calibrate operational satellite system instruments that do not reach decadal change absolute accuracy requirements. These include current and future instruments such as CrIS (Cross-track Infrared Sounder), IASI (Infrared Atmospheric Sounding Interferometer), CERES (Clouds and the Earth's Radiant Energy System), VIIRS (Visible Infrared Imager Radiometer Suite), Landsat, and all geostationary satellite radiometers. In this approach, CLARREO serves as a highly accurate, SI-traceable calibration standard in orbit, directly supporting international inter-calibration efforts such as GSICS [Goldberg, 2011]. Data from these other instruments, with calibration improved by CLARREO, are then used to more accurately retrieve changes in properties of the climate system on decade time scales. The use of CLARREO as a reference allows these instruments to bridge data gaps and to reduce their dependence on assumptions of stability and achieving continuity with overlap for climate data records.

The purpose of this report is to summarize 5 years of effort by a diverse CLARREO science team bringing the needed expertise from four different NASA centers, the National Institute of Science and Technology (NIST), four universities, as well as international collaboration from several university and agency organizations in the United Kingdom. The diversity of the team is a reflection of the wide range of climate science impacted by the CLARREO observations.

2   CLARREO Science Objectives

2.1   Challenges in Climate Prediction

The science value of the CLARREO mission has been formulated in terms of decadal change in climate forcing, response, and feedbacks relevant to the information content in the CLARREO RS and IR spectra and RO observations, as well as its ability to act as a reference radiometer in orbit to improve the accuracy of other reflected solar and infrared sensors [NRC, 2007; Leroy et al., 2008a; Huang et al., 2010a,b; Feldman et al., 2011b; Jin et al., 2011; Kato et al., 2011; Roberts et al., 2011]. Figure 2.1 shows a schematic summarizing the contributions of the CLARREO RS/IR/RO observations to climate change using a climate feedback schematic taken from Roe and Baker, 2007.
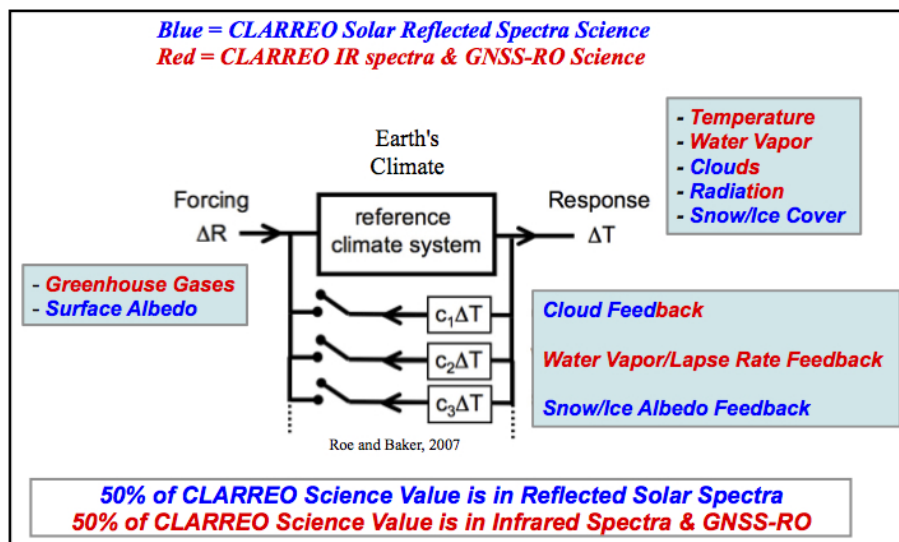
Figure 2.1: Science contribution from CLARREO RS, IR, and RO observations. Red and blue colors show contributions from IR/RO and RS observations, respectively. Climate forcing contributions (left), climate response (upper right), and climate feedbacks (lower right) are shown with text colored proportional to the relative impact of the CLARREO observation type on the science.

The published climate change literature has been used to derive the CLARREO requirements in terms of the mission's ability to measure decadal change for some of the most important elements of the climate system: temperature, water vapor, cloud properties, radiative fluxes, and surface properties including albedo. CLARREO decadal change observations are also key to reducing uncertainties in the climate feedbacks that drive uncertainty in climate sensitivity. Climate feedbacks in order of uncertainty in their magnitude are cloud feedback, temperature lapse rate/water vapor feedback, and snow/ice albedo feedback [IPCC, 2007a; Soden and Held, 2006; Bony et al., 2006; Roe and Baker, 2007]. In addition, CLARREO will help quantify radiative forcing from anthropogenic changes in land albedo, will confirm the effect of greenhouse gases on the infrared emissions to space, and will make some modest contributions to aerosol direct radiative forcing.

Figure 2.2 provides a diagram that illustrates the role of the CLARREO mission in relationship
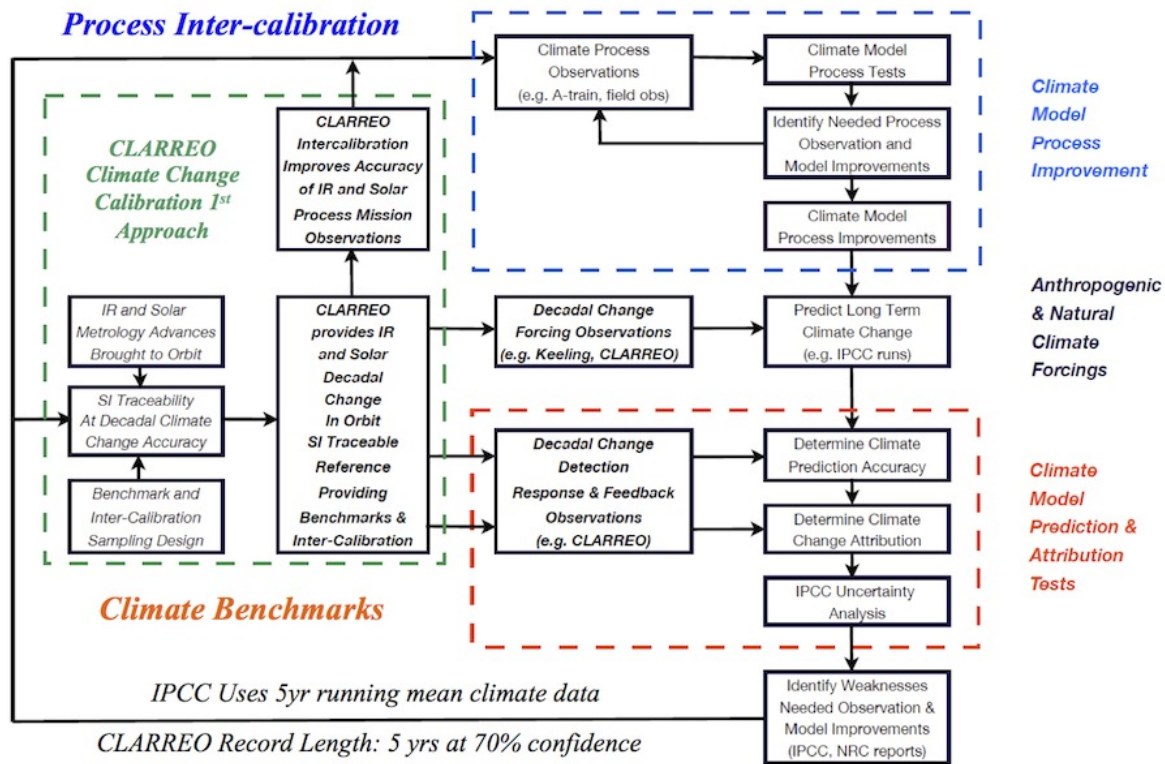
Figure 2.2: Climate science community approach to developing, testing, and improving climate predictions, climate change attribution to natural and anthropogenic sources, and prioritizing needed improvements. Most NASA climate missions are designed to improve climate processes such as clouds (blue box). CLARREO brings metrology advances (green box) from laboratories on Earth and launches them into orbit to provide a broad range of climate benchmarks (orange box) critical to observing climate change and to testing the accuracy of climate change predictions. CLARREO accomplishes this through a) spectral benchmarks fingerprinting, and b) providing in-orbit Reference Inter-calibration to other reflected solar and infrared instruments.

to other climate missions. Climate model process improvements (blue dashed box) typically require observations on short time and space scales. For example, NASA A-train satellite process data contain information on the instantaneous vertical profiles of clouds, aerosols, atmospheric state, and radiation, [e.g. Stephens et al., 2002; Winker et al., 2010]. These process observations drive improvements in cloud and aerosol processes that can be incorporated into improved representation in climate models. The new climate models are then used in assessments of climate change.

The models are driven by past and future natural and anthropogenic climate forcings to provide predictions of climate change over time frames from several years to decades to centuries. These climate predictions are then tested on decades of past climate observations, with the purpose of estimating the uncertainty of future climate projections (orange dashed box) based on anticipated human emissions of aerosols and greenhouse gases [IPCC, 2007a]. This same algorithm is used to evaluate the attribution of climate change to natural and anthropogenic causes. The resulting uncertainties in climate prediction and the attribution studies are then used to guide critical societal decisions on climate change mitigation and adaptation. They are

also used to determine future improvements needed in both climate observations and climate models.

Unfortunately, most of the global satellite data sets are not yet accurate enough to be used to test the small but critical signals of decadal change, since accuracy requirements are less strict for climate process studies. The CLARREO measurements are designed to fill this gap in the climate observing system by establishing for the first time satellite observations sufficiently accurate for decadal change. CLARREO relies on advances in metrology made over the past 10 years for much more accurate calibration of solar and infrared instruments, and on the advances in using radio occultation to probe the Earth's atmosphere (green box). CLARREO also detects for the first time over 95% of the entire spectrum of the Earth's thermal emitted radiation (200 – 2000 cm^{-1} or 5 to 50 μm wavelength) and its solar reflected radiation (350 – 2300 nm). This is the same spectrum of energy that drives the radiative forcing of climate change, the climate system response, and the resulting feedbacks that change climate sensitivity.

The full spectral coverage and accuracy of CLARREO impacts a wide range of essential climate variables. The highly resolved accurate spectra allow CLARREO to sense spectral fingerprints of decadal climate change. They also allow CLARREO to serve as a reference spectrometer in orbit to calibrate other infrared and reflected solar instruments [Goldberg et al., 2011]. In this sense, CLARREO is a metrology lab in orbit, and can anchor a substantial portion of the global satellite monitoring system because its spectral range spans many existing and planned instruments. An additional benefit of CLARREO as a metrology lab in orbit is the ability to improve and simplify use of process data satellite missions, enabling more accurate and consistent observations for a wide range of Earth science and application studies from space. An example is the ability to improve the consistency of observations from similar instruments on several spacecraft such as land resource sensors or weather sensors.

While most satellite missions strive for smaller spatial scales to resolve increasing details of Earth processes, a climate change metrology mission like CLARREO must focus on larger time and space scales. An example of the spatial scales of climate change can be seen clearly in the spatial patterns of critical climate feedbacks such as cloud, temperature, water vapor, and surface albedo feedbacks shown in Figure 2.3, taken from Soden et al. 2008. The results from a wide range of climate models show that these feedbacks occur on spatial scales of 2000 km or larger and are often very zonal in nature, as shown for the temperature, water vapor, and surface albedo feedbacks. We conclude that the observing time/space scale requirements for the CLARREO mission will focus not on high spatial resolution instantaneous measurements common to most process missions, but rather on the larger spatial and longer temporal scales that capture decadal changes in forcings, responses, and feedbacks.

The IPCC typically uses a 5-year running mean filter on all decadal time series [IPCC, 2007a] in order to reduce the level of natural variability from El-Nino – Southern Oscillation (ENSO) events, which typically have a 3 to 5 year period. As a result, the CLARREO observations focus primarily on the ability to observe annual and longer time scales, with an initial benchmark climate record of at least 5 years. A recent analysis confirms that 5 years provide a lower bound on the record length needed to accurately quantify feedbacks in coupled ocean atmosphere models [Chung et al., 2012]. Focusing on longer time scales also suggests that all measures of CLARREO accuracy will be determined using thousands of observations, never just a few as in weather or climate process missions. While low random noise from an in-
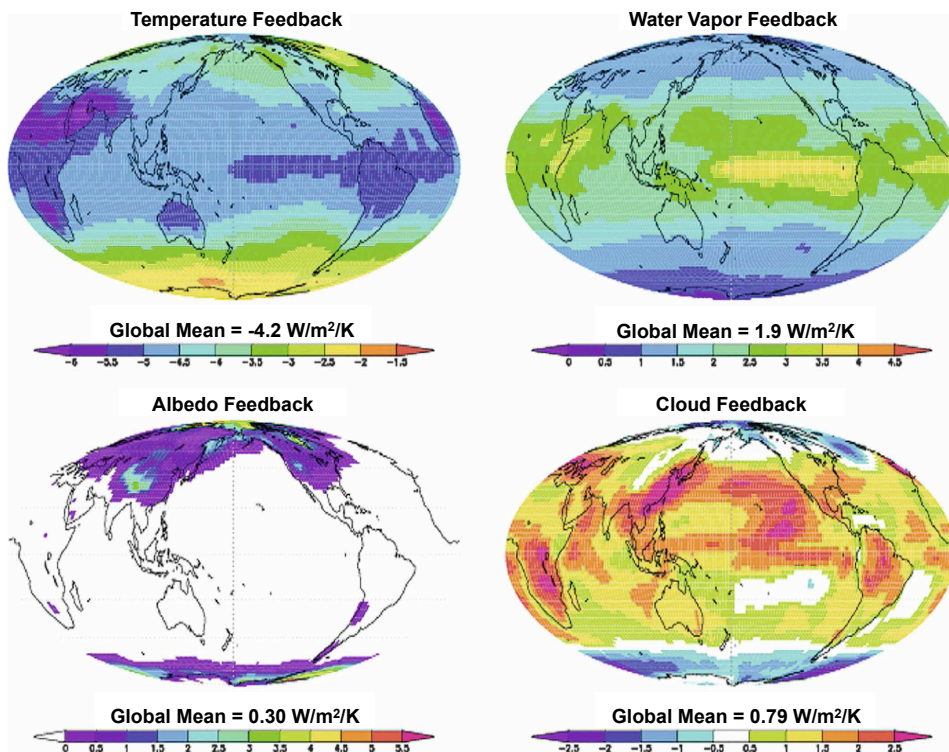
Figure 2.3: IPCC AR4 climate model ensemble-mean maps of the decadal temperature feedback, water vapor feedback, surface albedo feedback, and cloud feedback [Figure 8 from Soden et al., 2008]. The feedback maps show that only very large spatial scales of 2000 km and larger are driving sensitivity of the climate system to anthropogenic forcing. As a result the CLARREO mission focuses only on these very large spatial scales and long time scales.

strument is a high priority for process satellite missions, it will be a much lower priority for CLARREO. The CLARREO approach is therefore to average measured spectra over large time and space domains, which results in the reduction of uncertainty due to random noise as the Gaussian instrument random noise averages down to an insignificant level over time. On annual and longer timescales the main uncertainty in the measured CLARREO radiances becomes systematic uncertainty and not random noise. In the CLARREO temporally and spatially averaged data products (e.g., zonal annual means), the uncertainty is due to a combination of the radiometric uncertainty and the uncertainty in the time and space sampling of the Earth system.

The effective insensitivity of CLARREO mission objectives to higher random instrument noise levels in turn allows CLARREO to use smaller instruments with smaller optics and less cooling of detectors. This is especially important to enable CLARREO to measure the far-infrared portion of the spectrum. Existing pyroelectric detectors are sensitive in the far-infrared (wavelengths between 15 and 100 μm) and operate near room temperature. Both of these changes lead to much smaller, lighter, lower power, and lower cost instruments. Smaller instruments can use smaller spacecraft and launch vehicles, all of which drive down costs for the climate observing system. We conclude that the trade space and requirements for a mission focused on high absolute accuracy for decadal change, results in a very different design from those

for weather or climate processes. In fact, when working on the fundamental Level 1 mission requirements for CLARREO, NASA had no history or analog for accommodating such requirements. New requirements methods had to be developed based on much of the information discussed in this paper.

2.2   Climate Change Observations: Required Accuracy

Given the context above, the CLARREO mission science requirements have been stated in terms of the accuracy of decadal change observations. The focus on absolute accuracy for CLARREO means that these data will be relevant to decadal change observations not only 10 years, but 20, 30, and even 50 years from the start of CLARREO observations. As a result, unlike most missions, CLARREO must consider the impact of its science requirements on 10 to 50 year timescales. This suggests that requirement metrics be stated in terms of accuracy of decadal change and in terms of time to detect climate change. The former is more relevant to climate model testing, the later is more easily discussed in terms of relevance to the timing of societal decision making in a cost/value sense.

In general, the science community has struggled in making climate monitoring requirements more rigorous [Ohring et al., 2005]. But the science diversity of the CLARREO mission (reflected solar, thermal infrared, and radio occultation), along with recent budget challenges across all of science, demanded that a more rigorous approach be developed. What finally evolved from the CLARREO science team deliberations is explained in the remainder of this section, and should be applicable to a wide range of decadal climate change observations.

The critical insight to consider is that even a perfect observing system will have limitations in measuring long term forcing and response of the climate system [Leroy et al., 2008a]. A perfect observing system used to detect anthropogenic climate change is fundamentally limited by the noise of natural variability in the climate system. There are many examples of such variability on a range of time scales: ENSO (3 – 5 years), solar irradiance sunspot cycles (11 years), Arctic, North Atlantic, and Pacific decadal oscillations (10 to 30 years). But one of the dominant sources of such noise for large time/space scales is driven by ENSO. This importance is recognized by the IPCC in its use of 5-year running means for comparisons of decadal change data sets [IPCC, 2007a]. While noise from natural variability can be reduced in climate model predictions or hindcasts by running large ensembles of model simulations, there remains only one Earth, therefore all observed trends are subject to the confounding noise of natural variability. This realization means that there is a "floor" for required accuracy in climate trends: the observations need to have uncertainties smaller than natural variability. The key, therefore, is to understand how to quantify the relationship between natural variability and observing system accuracy.

In any analysis of climate trends, the changes are not simply linear over time. Even with this caveat, the use of statistical trend analysis provides a useful metric to compare the impact of different error sources in a robust framework. Fortunately, extensive literature exists on trend analysis [Leroy et al., 2008a,b; Weatherhead et al., 1998; Von Storch and Zwiers, 1999], and the CLARREO team has used this approach to quantify and compare different sources of uncertainty in setting requirements and in designing the mission. This does not mean that CLARREO data will only be used to determine trends, but instead that trend analysis provides

a critical insight into the mission science requirements and to the utility of the observations for decadal climate change science.

In our example for CLARREO, we define an uncertainty factor U_a for climate trend accuracy. This uncertainty factor is the ratio of trend uncertainty for a real climate observing system, to the trend uncertainty of a perfect observing system limited only by natural variability. The factor is unitless and can be applied generally to any climate variable: solar irradiance, reflected flux, surface temperature, spectral radiance, or sea-ice extent. A perfect observing system would have a U_a value of 1.0. Any real observing system will have uncertainties that increase the value of U_a above 1.0. Using the results of Leroy et al. [2008a] on the relationship between trend uncertainty for natural variability and uncertainty for the observing system, we can determine the accuracy uncertainty factor U_a as:

$$U_a = \left(1 + \frac{\sigma_{cal}^2 \tau_{cal} + \sigma_{inst.noise}^2 \tau_{inst.noise} + \sigma_{orbit}^2 \tau_{orbit}}{\sigma_{var}^2 \tau_{var}}\right)^{1/2} \tag{2.1}$$

where σ_{var}^2 is the variance of natural variability for the climate variable of interest, τ_{var} is the autocorrelation time scale for natural variability (which for global annual 500 hPa temperature variability was shown by Leroy et al. [2008a] to be ~1.5 years), σ_{cal}^2 is the variance of the uncertainty in absolute calibration of the orbiting climate instrument performing the observation, τ_{cal} is the absolute calibration time scale (typically instrument lifetime), and the remaining observing uncertainties are for instrument noise and orbit sampling. Instrument noise time scale is very short, while orbit-related sampling uncertainty tends to be determined by the climate record time sampling interval, typically monthly, seasonal, or annual. Note that additional error sources can be straightforwardly added to the numerator in Equation 2.1 as appropriate for each climate observation. Equation 2.1 is derived in Appendix A.

The expression for U_a provides a powerful tool for understanding the trade space of climate monitoring observing system design versus system cost. It enters almost all expressions for uncertainty in trend determination, whether it is the differennce between two missions broadly separated in time, the slope of a continuous time series of data, or even quadratic and higher order fitting to a long time series of data. The autocorrelation time scale τ for each uncertainty source essentially determines the number of independent samples n that will exist for any climate record of length Δt. If we consider the case of slow instrument calibration drifts in orbit that cannot be detected, or the case of changing absolute accuracy of instruments with time gaps between their deployments on orbit, the resulting relevant time scale for τ_{cal} is the instrument lifetime on orbit, typically about 5 years. Using Equation 2.1, we can see that when compared to orbit sampling time scales for annual mean time series, calibration drifts will in general have much more impact on uncertainty in climate trends, except if the orbit sampling uncertainty is caused by a slow systematic drift in the time of day of the observations, as seen in the NOAA polar orbit data in the 1980s and 1990s. Modern polar orbiters, however, are designed to maintain time of day and eliminate this long time scale. Examination of Equation 2.1 shows that the key metric for any individual error source is the ratio $(\sigma_i^2 \tau_i)/(\sigma_{var}^2 \tau_{var})$. As long as this ratio is significantly less than 1, then its impact on climate trends will be small. Equation 2.1 also allows the climate observing system to rigorously trade the value of decreasing one error such as calibration accuracy versus another such as orbit sampling. For the CLARREO mission, the requirement was set for all mission observations (reflected solar, thermal infrared, and radio occultation) to have a value of U_a less than 1.2. In other

words, CLARREO is designed to observe climate trends with an accuracy to within 20% of that afforded by a perfect observing system. This method of setting requirements allows a consistent treatment of climate monitoring requirements across diverse climate variables, each with their own estimates of natural variability. The method also avoids the costs of pursuing perfection that may not add much value to observing climate trends, and provides a quantitative "floor" for climate accuracy. In particular, Equation 2.1 shows that when error sources are a factor of 2 to 3 below the level of natural variability, we have reached the point of greatly diminished returns from any further increase in accuracy.

What about time to detect trends? Using Leroy et al. [2008a], we can define an analogous uncertainty factor U_t that is the ratio of the time to detect a trend using a real observing system, to the time to detect a trend using a perfect observing system. Note that such a ratio can be defined for any climate variable or statistical confidence bound desired. Again extending the results from [Leroy et al., 2008a] we can show that

$$U_t = \left(1 + \frac{\sigma_{cal}^2 \tau_{cal} + \sigma_{inst.noise}^2 \tau_{inst.noise} + \sigma_{orbit}^2 \tau_{orbit}}{\sigma_{var}^2 \tau_{var}} \right)^{1/3} \tag{2.2}$$

Comparing Equation 2.1 with 2.2, the only difference is that the square root on the right side of the equation becomes a cube root. Since the value of U_a and U_t are always greater than 1, and are usually near 1, Equations 2.1 and 2.2 can be used to show that

$$(U_t - 1) \approx \frac{2}{3}(U_a - 1) \tag{2.3}$$

Another way of interpreting the relationship shown in Equation 2.3 is that the degradation of trend accuracy for time to detect trends is only 2/3 of the degradation for accuracy in trends. For example, the CLARREO requirement that accuracy of trends be within 20% of a perfect observing system ($U_a = 1.2$), equivalently requires that the time to detect trends is within 13% of a perfect observing system ($U_t = 1.13$) using Equation 2.3. How do we interpret the meaning of $U_t = 1.13$? If a perfect observing system could detect a temperature trend with 95% confidence in 20 years, then the CLARREO observing system could detect the same trend with 95% confidence but with 13% more time required: 23 years instead of 20 years.

The combination of Equations 2.1 through 2.3 give a simple but powerful way to understand the value of observing system accuracy both for climate trend accuracy (e.g tests of climate predictions) as well as for time to detect trends (e.g. public policy decisions). They also provide a way to compare consistent metrics across a wide range of climate variables, as well as a wide range of sources of uncertainty in climate observations. We strongly encourage use of this approach to more rigorously understand and optimize climate observation requirements across the wide range of Essential Climate Variables (ECVs) [GCOS, 2011]. This is especially important given the limited resources available for global climate observations [Trenberth et al., 2012].

We now give an example of how to use climate trend uncertainty in the context of determining the absolute accuracy requirement of the CLARREO infrared and reflected solar spectrometers. This is one of the most critical requirements for this mission and will represent the greatest advance over current instruments in orbit.

We first consider the accuracy of temperature trends using the infrared spectrometer. The global average temperature trend uncertainty (95% confidence) is shown in Figure 2.4a as a
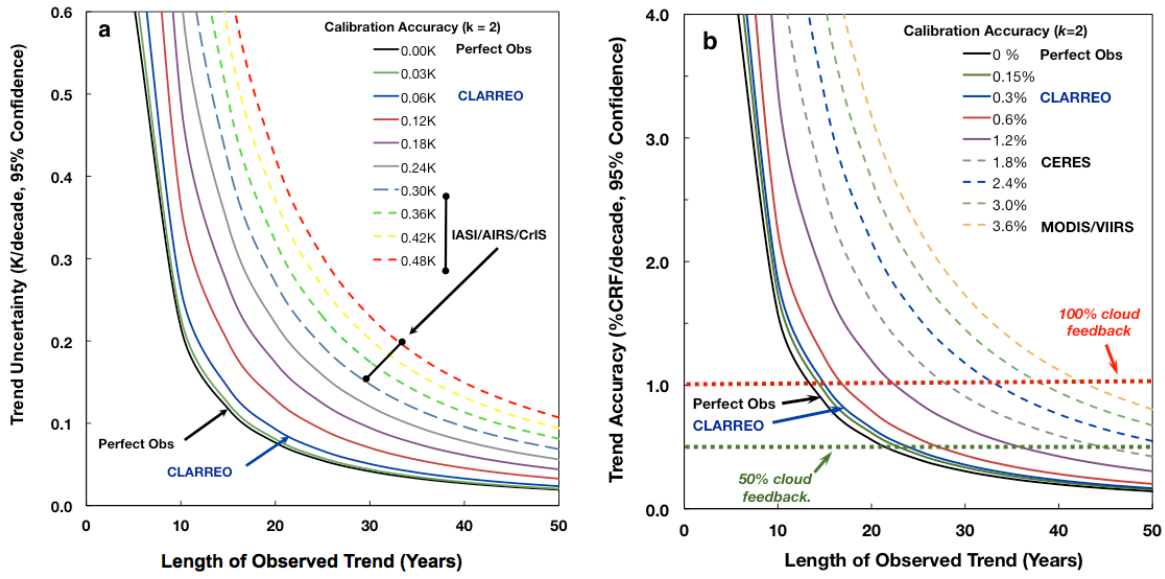
Figure 2.4: Figures (a) and (b) show the relationship between absolute calibration accuracy and the accuracy of decadal climate change trends. The results are shown for a perfect observing system as well as varying levels of instrument absolute calibration. The relationship between infrared (IR) spectra accuracy and temperature trends is shown in (a), while the relationship between reflected solar (RS) spectra accuracy and changes in cloud feedback is shown in (b). This illustrates the dramatic effect of measurement accuracy on both climate trend accuracy (vertical axis) as well as the time to detect trends. CLARREO's accuracy is a factor of 5 to 10 better than the absolute accuracy of current instruments in the RS, and a factor from 2 to 3 of existing IR instruments. Accuracy improvements beyond CLARREO have little difference when compared to a perfect observing system, which is shown by the black line in both figures.

function of the length of the observed trend Δt. Depending on the wavelengths chosen, the temperature trends could be examined for near surface temperatures, mid-troposphere, or stratosphere temperatures [Leroy et al., 2008a; Huang et al., 2010a,b]. The trend uncertainty shown in Figure 2.4a includes natural variability, absolute calibration uncertainty, instrument noise, and orbit sampling uncertainty as shown in Equation 2.1 for U_a, Equation 2.2 for U_t, and in the Appendix A Equation A.2 for the observed trend uncertainty δm. The values for these sources of trend uncertainty are shown in Table 2.1. Figure 2.4a shows the results for δm, and also serves to demonstrate the relationship to the key U_a and U_t metrics. The results for trend accuracy are shown as a function of the absolute accuracy of the infrared spectrometer, with the black line showing the result for a perfect observing system. As discussed earlier, even a perfect observing system is limited by natural variability.

In this example, natural variability is estimated using the infrared window observations from the CERES instrument on the SYN1deg-3Hour data product [Wielicki et al., 1996]. The CERES observations are inter-calibrated and merged with 3-hourly geostationary data to provide a consistent 10-year diurnally sampled record from 2000 to 2010 of highly accurate monthly averaged window brightness temperature as would be seen by an infrared spectrometer from surface and lower atmosphere thermal emission. The monthly values were used to determine de-seasonalized anomalies, and 12-month annual averages were used to reduce

short time scale noise. This provides a natural variability time scale similar to the 18 months found in Leroy et al. [2008a] using 4-D assimilation mid-tropospheric temperature fields. The analysis also uses one of the most accurate instruments in orbit in order to reduce confusion between instrument calibration drifts and natural variability. The CERES observations gave a natural variability estimate for global annual mean of 0.07 K ($k = 1$) for the 10 year record. A student-T distribution was used to account for the relatively short 10 year record, resulting in a final estimate of 0.08 K shown in Table 2.1. The resulting infrared variability correlates strongly with ENSO index as might be expected. The time scale used is 18 months, consistent Leroy et al. [2008a] and consistent with annual average anomalies being partially correlated. Note that the 10-year record used is sufficiently short that decadal change does not dominate the natural variability estimate. We also examined natural variability in surface temperature using preindustrial control runs of five coupled ocean atmosphere climate models and found values ranging from 0.06 to 0.12 with a mean value of 0.10 for the MPI, CanESM2, INMCM4, CCSM4, and GISS models [WMO Coupled Model Intercomparison Project (CMIP5)], Taylor et al. 2012].

	IR/RO Temperature Trends		RS CRF Trends	
Uncertainty Source	$\sigma(K)$	$\tau(years)$	$\sigma(CRF)(\%)$	$\tau(years)$
Natural Variability	0.085	2.3	0.60	0.8
Calibration Uncertainty	0.03	5	0.15	5
Orbit Sampling Uncertainty	0.018	1	0.21	1
Instrument Noise Uncertainty	0.005	1	<0.01	1

Table 2.1: Sources of climate trend uncertainty using global annual mean observations. Uncertainty sources for Figure 2.4a and 2.4b results using Equations 2.1, 2.2, and A.2 (Appendix A). Values for natural variability are derived using 10 years of CERES observations [Wielicki et al. 1996], calibration uncertainties are the absolute accuracy goals for CLARREO, orbit sampling uncertainties are derived using a single CLARREO 90° inclination polar orbit flown over 10 years of CERES SYN1deg-3Hour synoptic radiative fluxes and clouds observations interpolated to hourly and subsampled to nadir-only CLARREO orbit observations, and instrument noise values are the CLARREO mission specifications for averages at global annual scales. For natural variability, a Student's–T distribution is used to account for the relatively short 10-year record. CERES is chosen as one of the most stable instruments in orbit [Loeb et al. 2007]. The 10-year record is sufficient to capture the dominant ENSO variability but short enough to avoid being dominated by decadal climate change. Infrared values are from CERES $8 - 10 \ \mu$m window channel, and reflected solar cloud radiative forcing (CRF) from the broadband shortwave channel.

Natural variability cannot be known exactly. This uncertainty is partially due to the short observational records, partially because recent climate is not stationary, partly due to unresolved contributions of multi-decadal oscillations such as the Pacific Decadal and Arctic Oscillations, and partly because the magnitude of the ENSO variability has a decadal variation. A wide range of approaches to estimating natural variability in observations and climate models have been used [Swanson et al., 2009; DelSole et al., 2011; Huber and Knutti, 2011; Leroy et al., 2008a; Foster Rahmstorf, 2011]. What is clear from Equations 2.1 and 2.2, however, is that an exact knowledge of natural variability is not required in setting instrument accuracy requirements. Consider the CLARREO goal of $U_a = 1.2$. Further, assume that absolute calibration

dominates the observational uncertainty, which is true for global and zonal trends. To achieve $U_a = 1.2$, we can use Equation 2.1 to determine that we require:

$$\frac{\sigma_{cal}^2 \tau_{cal}}{\sigma_{var}^2 \tau_{var}} \leq 0.44 \tag{2.4}$$

In this case, even if σ_{var} is increased by 50%, U_a will only decrease from 1.2 to 1.1. Alternatively, we can see from Equation 2.4 that a 50% increase in σ_{var} will only cause a 20% change in the instrument absolute accuracy requirement σ_{cal}. Note that most of the uncertainties in σ_{var} mentioned above would tend to increase σ_{var}. We conclude that while knowledge of the magnitude of natural variability is critical to setting requirements for climate change observations, it is sufficient to know its value with 30 to 50% accuracy in σ_{var}.

Instrument noise used for the trend uncertainty shown in Figure 2.4a is 5K per instantaneous CLARREO observation, which represents a worst case in the far-infrared. This is a value 10 times larger than typical meteorological instruments, but sufficiently small that its uncertainty for global annual observations is much less than absolute calibration uncertainty. Finally, CLARREO orbit sampling errors are determined by flying simulated CLARREO 90° inclination polar orbits over the same CERES observations used to determine the natural variability. The CERES observations are gridded at 1° latitude/longitude, and the merged CERES/geostationary 3-hourly time sampling is interpolated to hourly time steps to allow realistic CLARREO satellite sub-sampling of Earth's weather and climate fields.

Given its focus on long time scale and large spatial scale climate change, the CLARREO spectrometers can simplify instrument design by limiting observations to nadir view beneath the spacecraft. For the infrared spectrometer, a single 25-km field of view is sampled every 200-km along the orbit track, which is within the spatial autocorrelation distance for infrared radiation. The orbit sampling error is determined from the monthly global difference between all hourly grid boxes and that for the sub-sampling of just the CLARREO single 90° inclined polar orbit with nadir sampling of a single field of view every 200-km. For global annual means, this sampling error is 1/7th the magnitude of σ_{var}, therefore its contribution to the trend uncertainty in Figure 2.4a is very small. A wide range of orbits were examined for CLARREO, but the 90° polar orbit gave the best combination of full diurnal sampling, exact annual repeat cycles, and full global sampling, thereby resulting in the smallest uncertainties for this error source.

The results in Figure 2.4a demonstrate several key points about climate observations. Trend accuracy increases with the length of the climate record, even for a perfect observing system. This result is driven by the need to average over noise in the climate system. Note that the IPCC predicted global surface air temperature and tropospheric air temperature increase for the next few decades is roughly 0.2 K/decade. At least 10 years of climate record is required to reach a trend uncertainty of 0.2 K/decade at a modest confidence bound of $k = 1$ (i.e. 1σ), *even for a perfect observing system.* This shows dramatically the importance of long climate records in understanding trends in climate change. If we desire a 4:1 signal to noise ratio on the expected 0.2 K/decade warming, then we desire a trend uncertainty level of 0.10 K/decade for 95% confidence. Figure 2.4a shows that this level of uncertainty requires a climate record of 17 years.

The colored lines in Figure 2.4a show the impact of absolute calibration accuracy on climate trends. The CLARREO requirement is shown as the solid blue line at 0.06 K ($k = 2$) or

12

equivalently 0.1 K ($k = 3$). For this level of absolute accuracy, even short gaps in the climate record do not significantly affect its accuracy [Leroy et al., 2008a]. In fact, the trend accuracy is very close to that of a perfect observing system. Improving the CLARREO accuracy by a factor of 2 to 0.03 K ($k = 2$) is shown in the solid green line and is almost on top of the perfect observing system. However, the overall improvement in trend accuracy (vertical separation of the lines), or time to detect trends at a given confidence level (horizontal separation of the lines) is very small. Clearly this has reached the point of diminishing returns. Reducing the CLARREO accuracy by a factor of 2 to a value of 0.12 K ($k = 2$) has a very significant effect. Trend accuracy degrades by more than 20% and the time to detect a trend at 0.1 K 95% confidence increases from 19 years to 23 years. In fact, Figure 2.4a shows that every further degradation of calibration absolute accuracy by an additional 0.06 K acts to further delay the time to detect such a trend by an additional 5 years.

The absolute accuracy of current and planned future weather spectrometers in orbit are shown in the dashed lines with accuracy between 0.3 to 0.5 K ($k = 2$). For these instruments we must rely on much weaker constraints for climate trends: we have to have overlap of the instruments, typically for a year or more [Loeb et al., 2009], and we must rely on assumptions of instrument calibration stability over a period of years [Ohring et al., 2005, 2007]. The results in Figure 2.4a assume that either short gaps and/or instrument calibration drifts occur at the level of the absolute accuracy uncertainty defined for each instrument. This is a worst case assumption, but for a result as critical as climate change, it is an essential assumption. We conclude that absolute accuracy and long climate record lengths are the keys to highly robust and highly accurate climate trend observations.

Since the results shown in Figure 2.4a are for global temperature trends, the question immediately arises as to how well such concepts apply to other spatial scale trends such as zonal or regional. This question is especially relevant to observing and understanding the difference between tropical and polar trends, or land versus ocean trends. We examined the same 10 years of CERES observations and found that, as expected, the natural variability increases as spatial scale decreases. For 10-degree zonal means, the natural variability more than tripled to 0.2 K (1σ) from the global average value of 0.07 K. For 10-degree latitude by 30-degree longitude regions, the natural variability increased further to 0.5 K (1σ). As a result, regional trends must be much larger than global trends in order to detect them above natural variability. For a mission like CLARREO with only nadir views, orbit sampling and instrument noise uncertainties increase at these smaller scales, but relative to natural variability, they still increase slowly enough to ensure the same $U_a < 1.2$ found for global average. The relative balance of the different sources of instrument uncertainty in Equation 2.1 varies with time/space scale, but the overall uncertainty is similar. We conclude that for the large time/space scales typical of global climate change [Soden et al., 2008], a single metric of climate change accuracy was sufficient to design a consistent set of mission and instrument requirements. Note that at much smaller spatial scales such as 100 to 1000 km, orbit sampling will play an increasingly large role, and a simple nadir viewing instrument like CLARREO cannot meet the sampling requirements at these scales. In this case, the more traditional weather and climate instruments such as MODIS, VIIRS, CrIS, IASI, and CERES can meet these requirements when they are inter-calibrated against the CLARREO infrared and reflected solar spectrometers. We will return to this topic later in the report.

Figure 2.4b shows the analogous result for the reflected solar spectrometer accuracy. The

estimates for natural variability were again taken from the CERES instrument data, although this time using broadband solar reflected flux, instrument noise was set to the CLARREO signal to noise requirement of 30:1 for a solar zenith angle of 75° and a global average albedo of 0.3. Again, absolute calibration uncertainty dominates the accuracy of global average trends. Since temperature trends are not relevant for reflected solar radiation, we instead select one of the metrics most critical for determining climate sensitivity. Uncertainty in climate sensitivity is driven primarily by uncertainty in cloud feedback, while uncertainty in cloud feedback is driven primarily by low clouds and their effect on planetary albedo [IPCC, 2007a; Bony et al., 2006; Soden et al., 2008]. We can derive a simple metric of cloud feedback for reflected solar by considering the change per decade in global mean shortwave cloud radiative forcing or SW CRF [Soden et al., 2008; Loeb et al., 2007]. Global mean SW cloud radiative forcing is simply the difference in all-sky reflected flux minus clear-sky reflected flux. Since instrument calibration uncertainty for reflected solar radiometers is usually quoted in percent, we consider the accuracy of trends in SW CRF in percent per decade in Figure 2.4b. Examination of natural variability for SW CRF in the same five Coupled Model Intercomparison Project phase 3 (CMIP3) climate models used for temperature again gave an average value similar to the CERES observations used here.

The results shown for reflected SW in Figure 2.4b are very similar to those for temperature trends in Figure 2.4a. The perfect observing system is again shown as a solid black line and again shows the need for long climate records. As in Figure 2.4a, results in this figure are shown for a 95% confidence level. A dashed red line is shown at the level of 1.0% CRF/decade change that would be roughly equivalent to a 100% cloud feedback amplification of anthropogenic radiative forcing. To see this, consider that the IPCC estimated anthropogenic radiative forcing for the next few decades is expected to be approximately 0.5 Wm^{-2} per decade [IPCC, 2007a]. The global average SW CRF is ~50 Wm^{-2} [Ramanathan et al., 1989] so that a change equal to the radiative forcing of climate would have a magnitude of $0.5/50 = 1.0\%$ per decade in SW CRF. This is the value shown as the red line. A 50% amplifying cloud feedback would be half as large, or roughly 0.5%/decade. Note that for low clouds as considered here, there is very little compensating thermal infrared change in CRF, and that small amount is ignored in this calculation. We see that observing a 50% amplifying cloud feedback in SW CRF would require 22 years of observations at 95% confidence, and observing a 25% feedback would require about 30 years.

As for the infrared example, the CLARREO accuracy requirement for the reflected solar spectrometer of 0.3%($k = 2$) provides an observing system very close in accuracy to a perfect observing system. However, as the accuracy is degraded from the CLARREO requirement, the accuracy of trends and the time to detect trends decays rapidly. Current instruments in orbit are shown again as dashed lines and include CERES (2%) and MODIS (4%) for $k = 2$ absolute accuracy. Both of these current instruments must rely on extensive overlap and assumptions about stability on orbit [Loeb et al., 2007]. Any gaps in these climate records in essence act to restart the climate record from zero because of their reduced absolute accuracy [Loeb et al., 2009].

2.3 CLARREO Climate Benchmarks Sampling

2.3.1 Sampling for RS and IR Observations

The goals of the CLARREO mission is to monitor the climate with well calibrated and traceable benchmark hyper-spectral radiances. The reflected shortwave and longwave hyper-spectral measurements will provide climate signal snapshots or benchmark spectral finger-prints, which can be used to determine climate response and feedbacks by comparing the spectra between two observation periods. The CLARREO observations include errors due to instrument design and calibration and the measurements are limited both spatially and temporally due to the satellite orbit. This study focuses on the sampling errors, which can be mitigated through the careful selection of satellite orbits. The given satellite configuration must properly sample both the natural variability and the predicted climate change signal. In order to ensure that orbital characteristics do not introduce sampling biases into the observed record, the CLARREO constellation must accurately sample the diurnal, seasonal and inter-annual, and other natural cycles, such as surface diurnal temperature variations, seasonal arctic sea ice melting, and ESNO events.

The original mission recommended by the NRC 2007 involved three 90° inclined polar orbits, which pass over both poles and where the local equator crossing times cycle through 24 hours annually, to capture the inter-annual diurnal variability from regional to global spatial scales. The 90° polar orbits greatly reduced the error due to imperfect sampling of the diurnal cycle and were based on a 5-year geostationary IR imager dataset [Anderson et al., 2004; Kirk-Davidoff et al., 2005]. The current study and results incorporate a longer 10-year CERES flux dataset, based on well-calibrated CERES instrument broadband shortwave, broadband longwave, and IR window fluxes from both Terra and Aqua satellites and include 3-hourly geostationary derived fluxes, which have been carefully normalized to the CERES fluxes [Doelling et al., 2013] to evaluate the sampling errors from the proposed CLARREO satellite configurations. The CERES instrument calibration stability is 0.2% per year and the CERES SW and LW flux anomalies correlate very well to the Sea-Viewing Wide-Field-of-View Sensor (SeaWIFS) Photosynthetically Active Radiation (PAR) and the Atmospheric Infrared Sounder (AIRS) fluxes, respectively [Loeb et al. 2007 and Loeb et al. 2012]. The multivariate ENSO index (MEI) correlates well to the CERES LW flux anomaly [Loeb et al., 2012], indicating that the CERES flux product captures the natural oscillations of the current climatic state.

The natural variability observed by the CERES record is dominated by the inter-annual and seasonal oscillations, such as ENSO, which drives the regional migration of cloud fields. Similar to the findings of Taylor and Loeb 2012, the diurnal variability is a rather small component of the overall natural variability. It is also apparent from the large amplitudes in the seasonal and diurnal cycles that any aberrations in the satellite orbit have the potential of introducing spurious signals into the satellite sampled data record. The 10-year CERES dataset encompasses a time period of small MEI standard departures and implies that the 2001 to 2010 CERES flux record may underestimate the long-term ENSO natural variability.

The on-orbit sensor sampling error can be determined by simulating the CLARREO instrument footprint frequency along the satellite ground track. The CLARREO instrument will not scan, but only observe footprints along the ground track in order to improve the calibration

reliability of the hyper-spectral instrument. The footprint location and time determines the appropriate sampled flux from the hourly and regionally gridded CERES 10-year dataset. The sparsely sampled satellite observed fluxes are then time and spatially averaged and compared with the complete or 100% sampled CERES dataset to estimate the sampling error.

Two types of low earth orbits (LEO) are considered in this study: sun-synchronous (SS), where the local Equator Crossing Time (LECT) is fixed, and precessionary orbits, where the LECT changes incrementally in time. The precessionary inclinations of 90°, 83°, and 74°, which are referred to as P90, P83, and P74, cycle through the 24 local hours exactly once, twice ,and three times per year, respectively. By definition, the 90° inclined orbit does not precess, but for the purpose of this study, the orbit has been grouped with the precessionary satellites, since it cycles through all hours. The inclination angle also determines the maximum latitude extent of satellite orbit. P90, P83, and P74 provide approximately 100%, 98.5%, and 92.5% global coverage, respectively. The SS orbits have an inclination of 98° and the retrograde orbits have a maximum latitude extent of ±83°. Since all LEO orbits revolve around the Earth ∼14 times per day, each zone is traversed ∼28 times per day. Because the equatorial zone has the greatest circumference, it also has the sparsest daily spatial sampling.
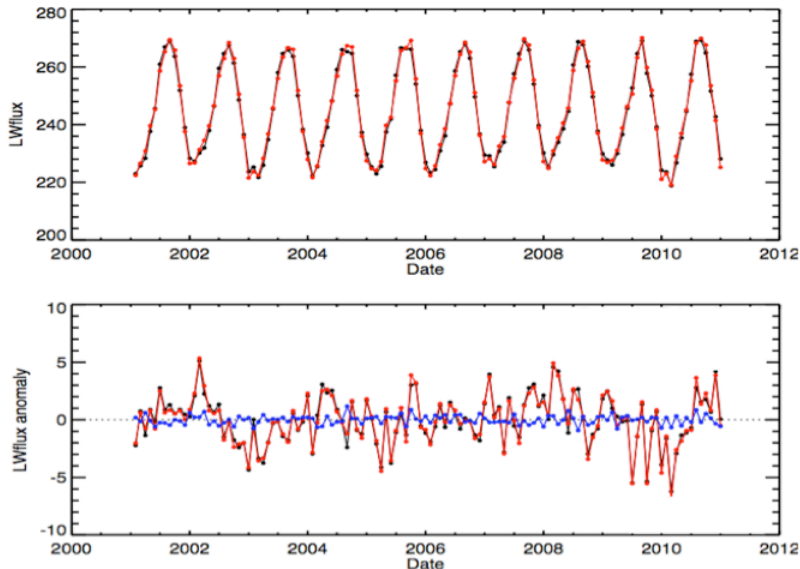
Figure 2.5: Top: The monthly 2001 to 2011 30° to 40° zonal mean CERES (black line) and P90 sampled (red line) LW flux (Wm^{-2}). Bottom: The associated CERES (black line), P90 (red line), and sampling error (blue line) LW flux anomaly (Wm^{-2}) after de-seasonalization.

There are four factors that determine the length of time needed to detect trends with sufficient confidence [Weatherhead et al., 1998; Leroy et al., 2008a]. The first is the natural variability in which the given trend is embedded. Increasing the magnitude or periodicity of the natural variability will increase the detection time. Second is the magnitude of the trend to be detected. Third is the magnitude of the observing system errors. Fourth is the measurement and natural variability auto-correlation time period. Even for a perfect observing system, the time to detect a trend is based on the natural variability and the magnitude of the trend. The satellite sampling cannot reduce the underlying detection time. The calibration and satellite sampling errors will add noise to the natural variability and increase the time to detect the trend. The observing system sampling error is then stated as the ratio of the time to detect

16

the trend with the sampling error, divided by the time without the sampling error included, and is defined as the time degradation ratio (F_t).

The CLARREO objectives are to measure the SW radiative effect trends, which are highly correlated with the CERES SW measurements, and the IR temperature trends, which can be measured by both the CERES window (WN) and the broadband longwave (LW) measurements. The 30° to 40° latitude band monthly LW fluxes for the P90 single satellite are shown in Figure 2.5. In this case, the satellite sampling error is 18.2% of the de-seasonalized natural variability for this zone.

Since the P90 orbit precesses only once a year, the initial Orbit Injection Time (OIT), or the LECT of the first day of orbit, may have an impact on the F_t. In particular, the time period during the year when the P90 orbit is situated in a terminator orbit may impact the SW sampling errors. To evaluate this impact, 48 OIT P90, P83, and P74 ground track files were generated, where the OIT is a half hour apart or 7.5° of longitude at the equator. For this study, 22 OIT SS ground track files were generated, with LECT between 9:30 AM and 14:30 PM for either the ascending or descending nodes. For multiple satellite constellations, the precessionary OIT are placed 6-hours apart for two satellites, for a possible 24 half-hour spaced OIT combinations, and placed 4-hours apart for three satellites, for a possible 16 half-hour spaced OIT combinations. In this way, the measurements are equally spaced in time. 10 half-hour spaced OIT for two satellite SS orbits were configured symmetrically about noon (e.g Terra (10:30AM) and Aqua (1:30PM) configuration). Another 8 half-hour spaced SS OIT was placed 5 hours apart between 8:30 AM and 3:30 PM LECT. No 3-satellite SS configurations were considered for this study.
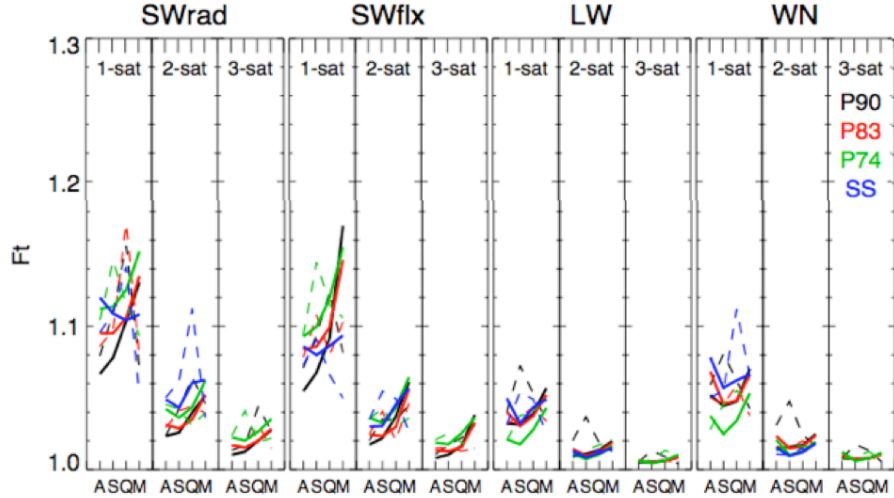
Figure 2.6: THE GLOBAL TIME DEGRADATION RATIOS F_t [WEATHERHEAD, 1998] (SOLID LINE) AND F_t [LEROY, 2008A] (DASHED LINE) FOR THE P90 (BLACK LINE), P83 (RED LINE), P74 (GREEN LINE), AND SS (BLUE LINE). EACH PANEL IS SUBDIVIDED INTO 4 COLUMNS AND REPRESENT, FROM LEFT TO RIGHT, THE SW RADIANCE (SWRAD), SW FLUX (SWFLX), LW, AND WN FLUX RESULTS. EACH COLUMN IS FURTHER DIVIDED INTO 3 SUB-COLUMNS, STRATIFYING THE RESULTS BY NUMBER OF SATELLITES EMPLOYED. THE SUB-COLUMN X-AXIS TICK MARKS DEMARCATE THE ANNUAL (A), SEMI-ANNUAL (S), QUARTERLY (Q), AND MONTHLY (M) RESULTS. THE AVERAGE (SOLID LINE) AND STANDARD DEVIATION (DASHED LINE) WAS BASED ON ALL OIT.

17

In order to capture most of the potential orbit configurations, the F_t upper limit is computed from the mean plus one standard deviation F_t of all of the individual OIT. The Figure 2.6 F_t represents the upper limit based on 84.1% of the individual OIT global F_t. Figure 2.6 does not contain the instrument calibration error. Both the F_t [Weatherhead, 1998] and F_t [Leroy, 2008a] methods, based on two independent autocorrelation estimations, are similar, which greatly increases the confidence that the autocorrelations were properly computed. The F_t of the SW radiance is slightly greater than the SW flux. The WN flux is also slightly greater than the LW flux, and the SW flux F_t is twice the magnitude of the LW flux. With each introduction of another satellite, the F_t [Weatherhead, 1998] is decreased by a factor of ∼2.5. All of the LW and WN flux F_t are less than 1.07, thereby meeting the CLARREO trend accuracy goal of 1.2 if half of the observing errors are attributed to the sampling error. The SW F_t is 1.13, which is at the cusp of the CLARREO trend accuracy goal [Wielicki et al., 2013]. However, the CLARREO SW F_t expectation is met using any dual satellite combination. The long-term, greater than a decade, F_t maybe overestimated since the CERES record occurred during a decade with low natural variability. No major ENSO and volcanic events were observed during the CERES record.

Satellite sampling errors are directly correlated to the frequency of observations available for a given domain. The sampling error is twice for the SW than it is for the LW, since only one-satellite node views the sunlit disc of the globe. There are many orbit characteristics that are similar among LEO satellites. All LEO satellites orbit the globe ∼14 times a day, across all latitude bands. Therefor the tropics have the least spatial sampling frequency and the greatest sampling error, which happens to be the domain with the greatest number of climate regimes.

Only the OIT, precessionary frequency, and altitude can be adjusted in a LEO. The OIT and precessionary frequency had little effect on the domain sampling error, except at the orbit inclination latitude where the ascending and descending nodes converge, which reduces the sampling to one node per orbit. Increasing precessionary cycles decreases the satellite inclination angle and reduces the global coverage. The LEO altitude determines the orbit repeat cycle and slightly affects the precessionary inclination. Increasing the orbit repeat cycle allows greater spatial sampling with nadir measurements.

The P90 orbit is preferred, since it has global coverage, samples the diurnal cycle uniformly over all latitudes, and can inter-calibrate all operational SS sensors. No other proposed orbit has all of these characteristics. The preference is not based on superior sampling error results, since all of the proposed orbit predicted sampling errors were similar. For the LW and WN, any single satellite orbit is sufficient to meet CLARREO goals. Since the SW radiance results are similar to the SW flux statistics, this indicates that the scene angular dependencies are not aliased into the SW radiance nadir measurement record. For a single satellite mission, the SS orbit has a slight sampling advantage in the SW, since it does not cycle through terminator conditions. This study used annually replicated orbits for consistent solar angle sampling. However, the sampling error on non-maintained orbits is uncertain, where the large seasonal and diurnal amplitudes could alias into the natural variability.

2.3.2 Sampling for GNSS Radio Occultation Observations

Individual radio occultation events occur when a satellite of one of the Global Navigation Satellite Systems (GNSS) is occulted or emerges from occultation by the Earth's atmosphere from the vantage point of a CLARREO satellite in LEO. The GNSS are comprised of a variety of constellations of satellites transmitting signals intended for high precision positioning. The best known is the Global Positioning System (GPS) of the U.S. Air Force. Others include the Russian Global Navigation Satellite System (GLONASS), the European Galileo navigation system, and the Chinese COMPASS (global navigation system). GLONASS is a fully deployed system. Full deployment of the Galileo navigation system is expected by 2019. COMPASS is planned for global use by 2020. The TriG receiver developed by the Jet Propulsion Laboratory can be configured to track any of these GNSS and should be able to obtain radio occultation soundings from any of their satellite transmitters. The CLARREO GNSS Radio Occultation instrumentation is described in Section 4.4.

The GNSS orbits were designed for maximum availability for positioning on the Earth's surface. The GNSS orbits all have inclinations of approximately 55° for this reason. Unlike positioning on the Earth's surface, simple availability of transmitting satellites is not as consequential as the distribution of occultation events in longitude, latitude, and time, which is a function of the CLARREO LEO orbits as well as the GNSS orbits. A GNSS transmitting satellite is available for tracking by a receiver on a CLARREO LEO as long as the Earth is not occulting (i.e., blocking the signal of) the transmitter. Given the relative motions of GNSS transmitting satellites and CLARREO LEO satellites, GNSS transmitters emerge from occultation by the Earth and its signals pass through the atmosphere on their path to a CLARREO LEO, yielding a "rising" occultation event. Also, GNSS transmitters that are available for tracking will pass into Earth occultation due to relative motion. Their signals pass through the Earth's atmosphere in the transition from availability to occultation by the Earth, yielding a "setting" occultation. When either transition occurs, an "occultation event" occurs, wherein occultation refers specifically to occultation by the Earth's atmosphere.

The number and distribution of occultation events depends on several elements of experimental configurations in addition to the orbits of the CLARREO LEO satellites. First, the receiver on the CLARREO satellites can be enabled or disabled from tracking various GNSS satellites. By default, they will track the GPS satellites. Tracking additional GNSS, though, in general, requires more computational capability and increased bandwidth and power. Second, the receiver can be configured to track either rising or setting occultation events or both. Obtaining rising occultation events requires mounting an array antenna on the CLARREO satellite that views the Earth's limb in the satellite's forward velocity direction. Likewise, obtaining setting occultation events requires mounting a separate array antenna that views the Earth's limb in the satellite's anti-velocity direction. Each antenna is expected to contribute the same number of occultation events in a specified amount of time, and the longitude-latitude distribution is expected to be nearly the same.

The number of occultation events that occurs daily is easily estimated. The GNSS satellites orbit the Earth twice daily and the CLARREO satellites 14.7 times daily. From the vantage of a single CLARREO satellite, each GNSS satellite appears to rise out of Earth occultation once per orbit and set into Earth occultation once per orbit. Not all occultation events are recorded, however, because only those whose apparent sounding profile is nearly vertical are readily

analyzed. Practically, only those events occuring within a certain angle in the occultation antenna's orientation are recorded, thus assuring nearly vertical cuts of atmospheric sounding. Here we have assumed that only those occultation events that occur within 60° azimuth of the antenna's center are accepted. Approximately $|sin(60°)|$ of all occultation events are accepted. Hence, approximately 313 occultation events per day per receiver occultation antenna are obtained given a 24-satellite GPS transmitting constellation only .Figure 2.7 shows a simulated distribution of occultation events.
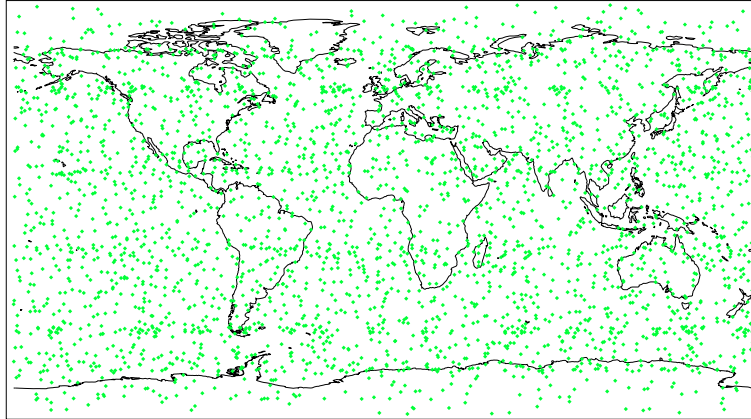
Figure 2.7: DISTRIBUTION OF SIMULATED RADIO OCCULTATION EVENTS BY ONE CLARREO SATELLITE WITH BOTH FORE-VIEWING AND AFT-VIEWING OCCULTATION ANTENNAS TRACKING 24 GPS SATELLITES FOR 5 DAYS. ONLY EVENTS WITHIN 60° BORESIGHT AZIMUTH OF THE OCCULTATION ANTENNA ARE RETAINED, YIELDING 3094 TOTAL ACCULTATION EVENTS.

We pursued sampling error for refractivity at 18 km height following the prescription for accuracy requirements for the GNSS radio occultation instrument. Toward that end, we have simulated distributions of radio occultation events for four different configurations: (1) for one CLARREO satellite tracking GPS only, (2) for one CLARREO satellite tracking GPS and Galileo signals, (3) for two CLARREO satellites separated by 90° in ascending node tracking GPS and Galileo signals, and (4) for one CLARREO satellite tracking GPS and Galileo signals and experiencing periodic resets of the receiver due to charge particle interactions. All CLARREO satellites are considered purely polar orbiters, with inclination of 90°. The GPS constellation consists of 24 satellites, 4 of which are approximately equally spaced in true anomaly in each of 6 orbit planes equally distributed in ascending node, having an inclination of 55° and an orbital radius 26610.223 km. The Galileo constellation consists of 27 satellites, 9 of which are equally spaced in true anomaly in each of 3 orbit planes equally distributed in ascending node and inclined at 56° and with an orbital radius of 29600.0 km. All satellites undergo nodal regression using $J_2 = 1.08 \times 10^{-3}$ for the Earth, and all orbits are circular. The Earth itself is considered an oblate spheroid with an equatorial radius of 6378.245 km and flattening of 1298.3. The resets of the occultation receiver are a common feature of previous GNSS radio occultation missions. They are caused by bombardment by ionospheric electrons, particularly over the South Atlantic Anomaly, the result being a rebooting of the receivers computer. In simulation (d) above, the probability per unit time of a singular event upset (SEU) is 0.02 s^{-1} if the receiver is over the South Atlantic Anomaly. No occultations are recorded until the receiver resets after 6 minutes. The logarithm of refractivity at 18

km height is interpolated from the ERA-Interim reanalysis[3] at the positions and times of all occultation events.
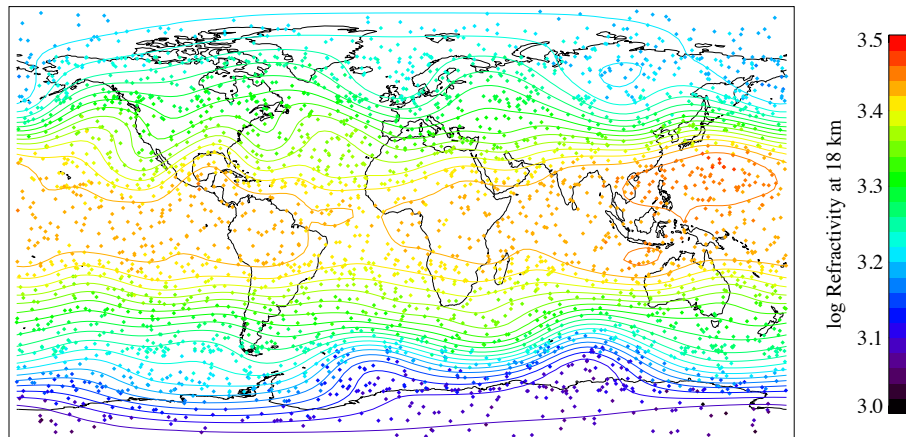
Figure 2.8: Mapping of radio occultation events by Bayesian interpolation. After interpolating the logarithm of refractivity at 18 km geopotential height from ERA Interim for the period 15 November 2000 (solid diamonds), the field was mapped by Bayesian interpolation (colored contours).

Building climatologies of the simulated log-refractivity data calls for special handling because of the non-homogeneous distribution in space and time of the occultation events. The occultation events are globally distributed, but the density of soundings is highly irregular and varies due to mutual precession of the satellites' orbits. Of primary concern are local singularities in the density of soundings at specific latitudes. The singularities lie at 21.07° and 48.75° north and south for GPS and at 21.50° and 46.33° north and south for Galileo transmitters. The existence of these singularities means that any climatology based on binning and averaging will yield climatologies with systematic errors. To circumvent this problem, a specialized mapping algorithm was developed that accounts for irregularities in the density of radio occultation soundings [Leroy et al. 2012]. This method was applied in the computation of sampling error for the satellite configurations given above. Figure 2.8 shows an example of the performance of the mapping technique.

The calculation of sampling error was executed for 10 years, interpolating ERA-Interim from 2000 through 2009. To process climatologies, data were binned into pentads within each month. For months without a perfect multiple of 30 days, some pentads were expanded to 6 days or shortened to 4 days. For each pentad, the data were mapped according to Leroy et al. (2012) using a 15-th order spherical harmonic expansion as the basis. The pentad maps were then averaged together, weighted by the actual number of days within each pentad, to form monthly maps. Finally, the monthly maps were averaged together to form annual average maps. The statistics for sampling error are then computed from the differences of the zonal average, annual averages of the mapped "data", and the gridded ERA-Interim fields, which are taken as "truth." The statistics of sampling error contain a large systematic component and a lesser random component, both shown in Figure 2.9. The systematic sampling error was unforeseen in the specifications of the Level 1 requirement for GNSS radio occultation sampling

---

[3]ERA-Interim is a global atmospheric reanalysis from 1979, continuously updated in real time.

(see Section 4.1), and so it is considered here only as a component of what was designated the "random sampling error" in the Level 1 requirements. The systematic sampling error is a direct consequence of under resolution of the background atmospheric structure by the 15-th order spherical harmonic expansion. It is expected that higher order expansions should reduce the systematic sampling error.
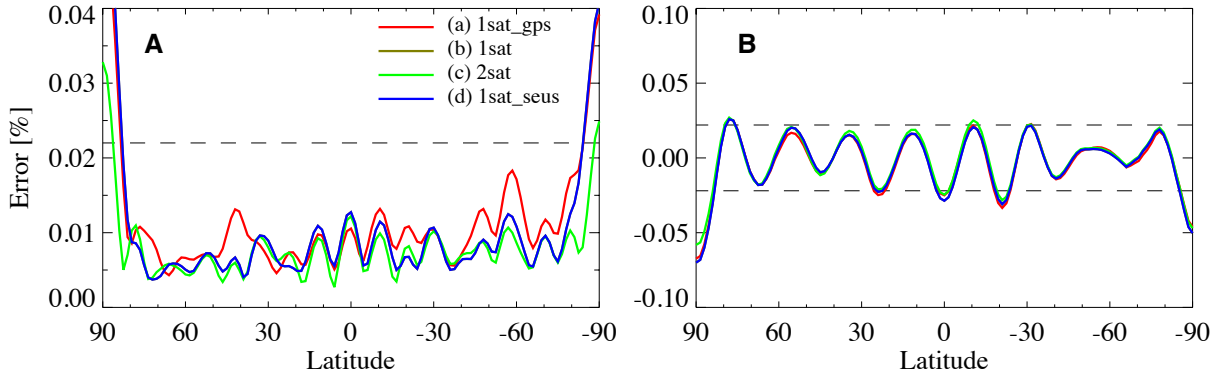
Figure 2.9: Summary of statistics of radio occultation sampling error. For each of the four configurations listed in the text – (a) one CLARREO satellite receiving GPS signals only, (b) one CLARREO satellite receiving GPS and Galileo signals, (c) two CLARREO satellites receiving GPS and Galileo signals, and (d) one CLARREO satellite tracking GPS and Galileo but subject to singular event upsets – both the random error (A) and systematic error (B) are shown. All statistics are for zonal average, with an annual average microwave refractivity at 18 km geopotential height. The dashed lines are the level 1 requirements on random sampling error for refractivity at 18 km, which is 0.022%.

Random sampling error, for any of the four configurations considered, does not contribute significantly to sampling error. Even the most meager of the configurations adequately samples the climate system.

2.3.3 Short-term Variability and Long-term Change in IR Observations

The work described in this section addresses the challenge of understanding the exact nature and level of background variability seen in observed all-sky spectra by exploiting the emerging radiance record available from the Infrared Atmospheric Sounding Interferometer (IASI) currently flying on the European MetOp-A satellite [Simeoni et al., 2004]. A second strand of inquiry being pursued relates to the identification of signals of multi-decadal change that might be anticipated to be present when comparing IASI observations with measurements from the InfraRed Interferometer Spectrometer (IRIS), which flew on the Nimbus-IV satellite, providing data from April 1970 to January 1971 [Hanel et al., 1972]. The operational period of IRIS means that in isolation it can, at best, only represent a relatively short snapshot of conditions at the time. However, if differences between the two datasets are seen that both emerge from commensurate observational estimates of short-term variability from IASI, and are outside the range of instrumental calibration uncertainty, this would, in principle, constitute a robust change detection. The key aspect of this work lies in the assessment of the reliability of, in particular, the IRIS dataset.

A. Inter-annual variability from IASI

Details concerning IASI instrument characteristics and performance can be found in Hilton et al., 2012. Given the ultimate goal of comparisons between IASI and IRIS, here IASI spectra are degraded from their nominal spectral and spatial resolution of 0.5 cm^{-1} (apodised) and 12 km respectively to match, as closely as possible, the 2.8 cm^{-1} (apodised) and 100 km resolution of IRIS. In addition, since IRIS was nadir viewing, only 'near-nadir' (in practice within 5° of nadir) IASI spectra are used when performing the degradation. Over the five years that have been considered (January 2008 – December 2012), this results in approximately 160 million spectra being used as input to this study. For clarity, the degraded IASI spectra are referred to in the following as IASI Reduced Resolution (IRR).

Once created, the IRR data are binned according to location and month in order to create well-sampled average spectra. Here we focus on the results obtained using annual averages, but the analysis is currently being extended to seasonal and monthly timescales. Given the anticipated mission design of CLARREO, the variability seen in all-sky spectra at relatively large spatial scales is considered, ranging from 10° latitude band averages to the global mean.
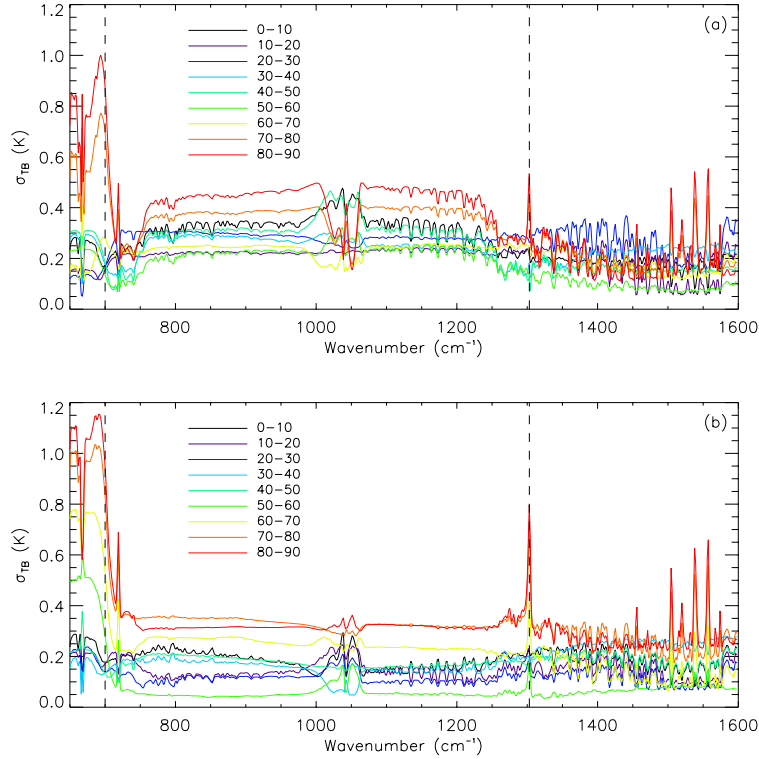
Figure 2.10: Standard deviation in 10° zonal, annual mean all-sky IRR brightness temperature spectra for the northern (a) and southern hemisphere (b). Vertical dashed lines are provided at 700 and 1303 cm^{-1}.

Figure 2.10 shows the inter-annual spectral variability (expressed as the standard deviation in annual mean brightness temperature, σ_{T_B}) at the 10° zonal mean scale for the northern (a) and southern (b) hemisphere. Maximum σ_{T_B} occurs across the 15 μm CO$_2$ band center (from $\nu \sim 645 – 700$ cm^{-1}) at northern and southern high latitudes, peaking at ~ 690 cm^{-1} in these zones. Emission to space at the very center of the band at 667 cm^{-1} originates from

the mid-upper stratosphere. Moving away from the central peak, emission to space occurs from systematically lower levels in the stratosphere, until by ~ 680 cm^{-1} one is effectively sounding the tropopause. As wavenumber increases over the CO_2 band wing ($\sim 700 - 760$ cm^{-1}), emission from successively lower levels in the troposphere is observed. Distinct peaks in σ_{T_B} are also seen in the center of the 1303 cm^{-1} CH$_4$ band and strong water vapor lines at wavenumbers > 1500 cm^{-1}. These are largest within the $80 - 90°$ zones but are still clearly apparent at lower latitudes, particularly in the southern hemisphere. Within the northern hemisphere, variability within the atmospheric window region ($\sim 800 - 1250$ cm^{-1}) is typically higher than that seen within the CO_2 band wing (from $720 - 760$ cm^{-1}) and across the 6.3 μm water vapor vibration-rotation band ($\nu > 1250$ cm^{-1}). No consistent pattern with latitude is seen within the 9.6 μm O$_3$ band ($\nu \sim 1000 - 1070$ cm^{-1}), although for the majority of zones the variability here is higher than across the atmospheric window as a whole.
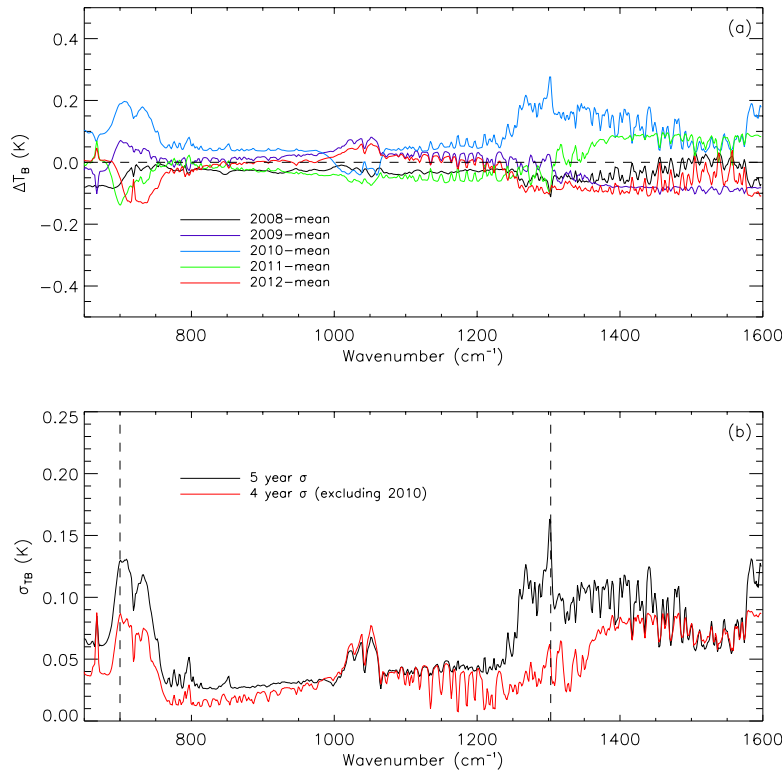
Figure 2.11: (a) Deviation in annual global mean brightness temperature from the five year average global annual mean spectrum from $2008 - 2012$; (b) Standard deviation in global annual mean IRR brightness temperatures for all 5 years (black) and excluding 2010 (red). Dashed vertical lines are as in Figure 2.10.

Figure 2.11b shows identical information for the global mean case. As might be anticipated, compared to the 10° results the level of variability is typically reduced across the spectrum. However, of potentially greater interest is the fact that the spectral shape of the variability alters. The smallest values of σ_{T_B} are contained within the window, while enhanced variation is seen within the CO_2 band wing, the center of the CH$_4$ band, and, to a lesser extent, toward the center of the H$_2$O vibration-rotation band. This result may be interpreted as being indicative of the increasing importance of upper tropospheric temperature and humidity in

driving variability as spatial scale increases relative to the role of surface temperature and cloud. The results are important to note for the CLARREO IR instrument design as they indicate that if the goal is to measure to within a certain percentage of natural (interpreted here as short-term) variability, different target accuracies can be set as a function of wavelength. However, it is clear that these target accuracies will change spectrally as a function of the spatial scale being considered. Moreover, it might also be anticipated that similar dependencies will emerge as a function of averaging time. Further work is required to assess the level of temporal auto-correlation present within the spectra, both at individual wavelengths and between different spectral regimes.

In Figure 2.11b the equivalent σ_{T_B} obtained when one year (2010) is removed from the analysis is also shown. As seen in Figure 2.11a, in terms of global annual mean behavior over the period 2008 – 2012, 2010 is rather anomalous. This is likely related to the phase and strength of the El Nino Southern Oscillation over the period [e.g. Loeb et al., 2012; Susskind et al., 2012]. Observations from the CERES broadband instrument [Wielicki et al., 1996] over this period also show a peak in global annual mean outgoing longwave radiation during 2010. Not surprisingly, removing this year from the analysis reduces the overall inter-annual variability. In addition, the contrast between the window and spectral regions sensitive to, in particular, upper tropospheric and stratospheric temperature is slightly suppressed. Again, this has implications for the length of any CLARREO mission in terms of its ability to truly sample the magnitude and spectral behavior associated with natural climate variability.

It is worth recognizing that in all of the above discussion the implicit assumption has been made that the IRR measurements are themselves capturing the full range of inter-annual variability. Given the sun-synchronous orbit of MetOp A, analysis performed by members of the CLARREO team indicates that this is unlikely to be completely true. However, previous studies [Kirk-Davidoff et al., 2005] suggest that the timing of the IASI orbit should minimize errors caused by inadequate diurnal sampling, and that any errors are likely to be highly correlated from year to year. In addition, cross comparisons with the inter-annual variability seen in CERES observations from both Terra (morning orbit) and Aqua (afternoon orbit) corroborate the findings concerning the latitudinal distribution of variability and its reduction with scale. They also show a more rapid reduction in window compared to non-window and broadband variability as spatial scale increases.

B. Longer Term Signals of Change

Figure 2.12a shows the global mean difference radiance spectrum averaged over a three month period from June to August, between IRIS in 1970 and IRR for five consecutive years (2008 to 2012), presented in the sense IRR minus IRIS. The equivalent brightness temperature differences are shown in Figure 2.12b. As might be anticipated from the results of the previous section, the spectral shape and magnitude of the differences are extremely consistent from year to year, reflecting the low level of inter-annual variability in the IRR spectra.

Taken at face value, these differences provide an insight in to how the Earth's OLR has changed over a period of four decades. Maximum positive differences are seen within the atmospheric window between 800 – 1000 cm^{-1}, reaching values of up to 3 mW m^{-2} sr^{-1} (cm^{-1})$^{-1}$ or equivalently 2 K in brightness temperature. The largest negative differences, of magnitude 6 K, are located in the Q-branch of CH$_4$, centeredat 1303 cm^{-1}. Despite considering all-sky as opposed to nominally clear-sky conditions, both the spectral shape and magnitude of the
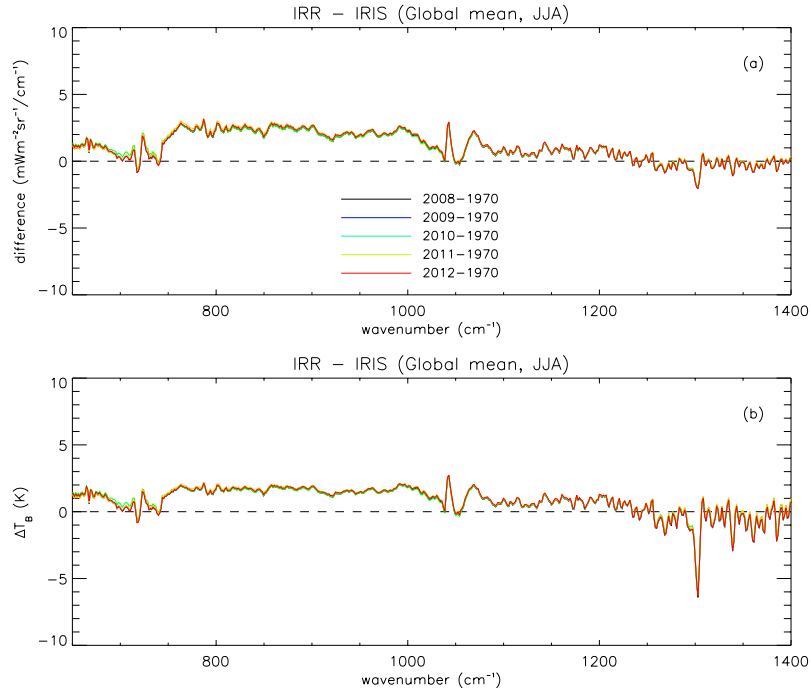
Figure 2.12: DIFFERENCE BETWEEN IRR AND IRIS THREE MONTH MEAN AVERAGE, GLOBAL ALL-SKY SPECTRA. DIFFERENCES EXPRESSED AS (A) RADIANCE AND (B) EQUIVALENT BRIGHTNESS TEMPERATURE.

differences are similar to those reported in Harries et al. (2001) between observations made by the Interferometric Monitor for Greenhouse Gases (IMG) instrument [Kobayashi, 1999] in 1997 and IRIS.

Estimates of noise equivalent radiance for IRIS are of the order 0.5 mW m^{-2} sr^{-1} (cm^{-1})$^{-1}$ over most of the spectral range shown in Figure 2.12, rising to around 1.0 mW m^{-2} sr^{-1} (cm^{-1})$^{-1}$ at wavenumbers greater than 1350 cm^{-1} [Hanel et al., 1972]. Similarly, Hilton et al. (2012) indicates that for the spectral range considered here, the noise equivalent brightness temperature for IASI at a reference temperature of 280 K is always below 0.4 K except at wavenumbers below 680 cm^{-1}. This value would translate to a radiance uncertainty of between 0.15 and 0.6 mW m^{-2} sr^{-1} (cm^{-1})$^{-1}$ depending on wavenumber. In the worst case scenario, assuming all noise on both instruments to be systematic, this would imply that the differences seen across the majority of the window and at the center of the CH_4 band in Figure 2.12 are outside the range of calibration error. In practice, one might expect that at least part of the noise reported for each instrument was random in nature and would reduce with averaging. Agreement seen between IASI, AIRS, and aircraft instrumentation also suggests that uncertainties are smaller than 0.4 K [Wang et al. 2011, Larar et al., 2010].

Nevertheless, the differences across the window seen in Figure 2.12 appear rather large in the context of known decadal trends in global mean surface temperature, which are of the order 0.15 K/decade [Hansen et al., 2010]. Even assuming the maximum errors quoted above, the minimum 800 – 1000 cm^{-1} window difference would be of the order 1 – 1.5 mW m^{-2} sr^{-1} (cm^{-1})$^{-1}$, or 1 – 1.5 K, implying a significant change in cloud amount, height, or properties has occurred over the last 40 years. Observationally based estimates of changes to cloud fields over these time scales are subject to high uncertainty with different records showing

26

substantially different geographical patterns and trends [e.g. Wylie et al., 2005]. More recently, measurements of backscattered UV radiation have been used to show that the Earth's reflectivity at the global scale has a negative trend over the past 30 years [Herman et al., 2013]. While this might be associated with a reduction in cloud cover, the metric combines the effects of changes in both cloud and aerosol fields, the latter of which have seen significant changes at the regional scale.

As an attempt to further evaluate the quality of the IRIS data, best efforts were made to simulate individual spectra. Radiosonde profiles near Guam during the IRIS period of operation were made available [M. Iacono, pers. comm., 2013] and cases where near coincident, nominally clear-sky IRIS observations were identified based on the cloud detection schemes described in Iacono and Clough (1996) and Harries et al. (2001). The radiosonde profiles were combined with a standard tropical profile from Anderson et al. (1986) to simulate IRIS spectra using the Line-By-Line Radiative Transfer Model (LBLRTM) v12.2 [Clough et al., 2005]. The sea surface temperature (SST) used was a monthly mean value obtained from the Extended Reynolds Sea Surface Temperature (ERSST) version 3b [Smith et al. 2008].
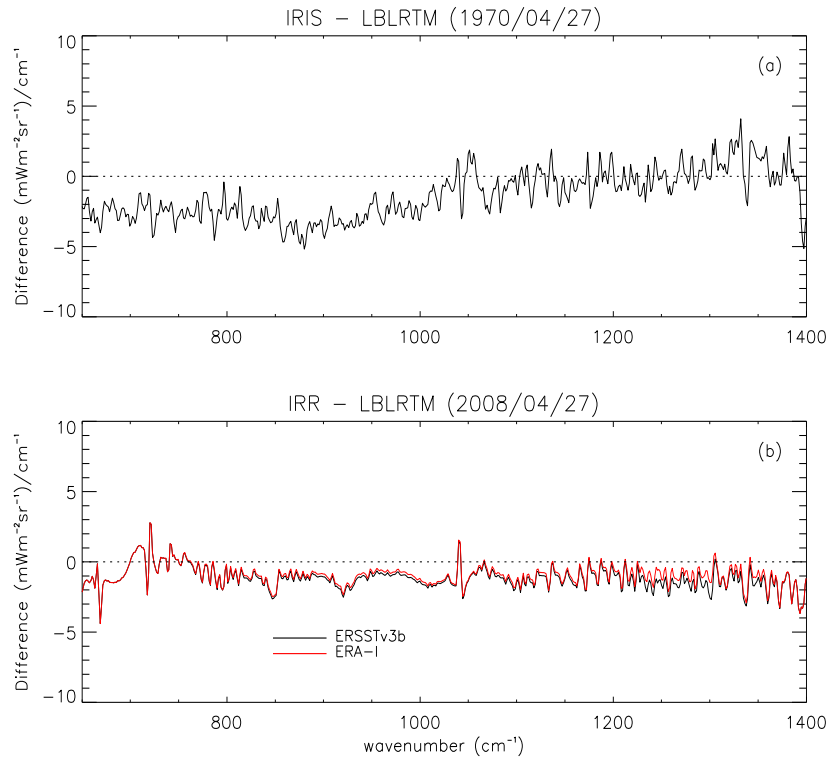
Figure 2.13: (A) IRIS – LBLRTM DIFFERENCE SPECTRUM FOR AN OBSERVATION TAKEN NEAR GUAM FOR APRIL 27TH, 1970; (B) AS (A) BUT FOR IRR – LBLRTM ON APRIL 27TH, 2008. IN THIS CASE, THE IMPACT OF USING SURFACE TEMPERATURES TAKEN FROM RECORDS WITH A DIFFERENT TEMPORAL RESOLUTION IS ALSO SHOWN.

Figure 2.13a shows an example of a difference spectrum between IRIS and the corresponding LBLRTM simulation from April 1970. Similar to the differences seen in Figure 2.12a, other cases not shown here, and previous simulation attempts [Iacono and Clough, 1996], across the window there is a significant jump in the level of the difference observed on either side of the 9.6 μm O_3 band. A similar differential window signal was also observed by Harries et

al. (2001). In that work, it was suggested that this was likely the result of residual cirrus cloud contamination in the IRIS data owing to its larger field of view relative to IMG, since no attempt was made to match the spatial resolution of the two instruments. While it is possible that cirrus contamination is also present in the observations used in Figure 2.13a, given the effort made to match the IRIS spatial resolution in the IRR data it seems less likely that this is the cause of the differences seen in Figure 2.12. To determine whether a similar difference between the observations and simulations was present for IASI, a similar method was employed to simulate IRR spectra. Again, radiosonde profiles from Guam were used as input to LBLRTM, matched in time and space to nominally clear IRR spectra. To assess the uncertainty introduced by using a monthly mean SST in the simulation, two simulations for each case were performed; one using ERSST v3b, and a second using the European Centre for Medium-Range Weather Forecasts (ECMWF) Reanalyses interim (ERA-I) 6-hourly resolution SST. Figure 2.13b shows example difference spectra from April 2008. Small differences between the data and the simulation do remain, but there is an absence of any noticeable offset across the 9.6 μm O_3 band. It is also clear that the use of a higher temporal resolution estimate of SST does not have a major impact in this case.

While it is true that the quality of the atmospheric and surface data used as input to LBLRTM in 1970 is likely to be reduced relative to the IASI period, sensitivity studies perturbing SST, surface emissivity, and lower tropospheric water vapor by realistic amounts were unable to produce the differential window signal seen in the differences with IRIS observations (not shown). Hanel et al. (1972) indicate that as part of the calibration of the IRIS spectra, several corrections were applied to the data. One such correction was to the calculated emissivity of the blackbody calibration source. It is possible that the variation in shape and amplitude of the correction could explain some of the observed differences found between the IRIS observations and both the IRR spectra and the simulations. If a systematic calibration issue is inherent to the IRIS data, such as an error in the emissivity of the calibration source, this would result in an error in the spectral response of the instrument. We would expect to observe this as a scene dependent variation in comparisons with other, better calibrated instruments.

To investigate this possibility, probability density functions (PDFs) of brightness temperature differences (ΔT_B) between two wavenumbers either side of the 9.6 μm O_3 band have been constructed for a range of different conditions. For the purposes of this comparison, observations from June 1970 (IRIS) and 2008 – 2012 (IRR) covering 60° North to 60° South were used. The two wavenumbers (909 cm^{-1} ($\sim$11 μm) and 1250 cm^{-1} ($\sim$8 μm)) were selected based on work by Ackerman et al. (1990) to identify cirrus and are consistent with those used by Harries et al. (2001).

Normalized PDFs of ΔT_B for IRR observations indicate remarkable similarity between each year when the data are subdivided according to day, night, ocean, and land (not shown). While the widths of the equivalent IRIS distributions are similar, their peaks are always shifted to lower ΔT_B values by between 3 – 4 K. This is consistent with the differences seen in Figure 2.12. Further subdivision into daytime and nighttime land and ocean scenes, respectively, show that a shift of about 2 K is seen for ocean scenes during both night and day. This day/night similarity appears contrary to results reported by Aumann et al. 2011, who use comparisons between IRIS and AIRS to infer a marked cold bias in the IRIS data over the tropical oceans at night, which is not seen during the day. For land scenes our results show a much more pronounced diurnal difference in the magnitude of the shift, with a maximum difference of

~ 4 K seen during the night. During the day the distributions look almost identical. This change in behavior is likely to be related, at least in part, to the different sampling times of the two instruments coupled with the diurnal cycle in land surface temperature.
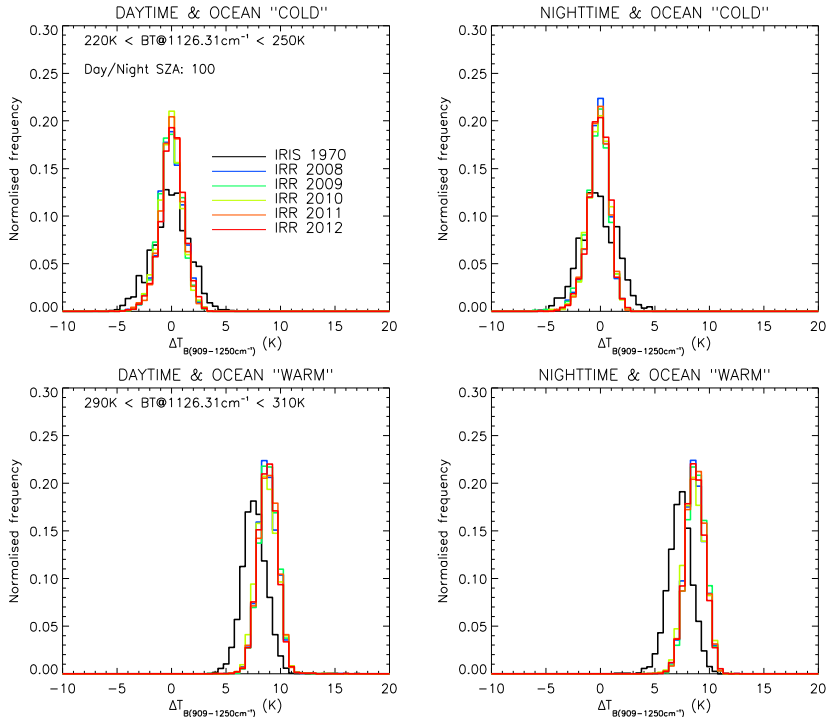
Figure 2.14: NORMALIZED PDFs OF $11 - 8$ μM BRIGHTNESS TEMPERATURE DIFFERENCES (ΔT_B) FOR JUNE IRIS AND IRR DATA OVER OCEAN BETWEEN $60°$N AND $60°$S STRATIFIED ACCORDING TO 1126 CM^{-1} BRIGHTNESS TEMPERATURE (T_{B1126}) AND DAY OR NIGHT OVERPASS TIME. WARM SCENES ARE CLASSIFIED AS 290 K $< T_{B1126} <$ 310 K; COLD SCENES AS 220 K $< T_{B1126} <$ 250 K.

While the results above provide an overall assessment of the similarity of the two datasets, more insight can be gained by classifying the data according to the observed brightness temperature at a reference wavenumber, in this case, 1126 cm^{-1}. Figure 2.14 shows ΔT_B PDFs derived for cold and warm scenes, further sub-divided according to night and day. Given the potentially confounding effect of diurnal sampling noted above, these data are restricted to ocean scenes. In all cases, the IRR distributions are narrower than IRIS. There is also a clear offset between the IRR and IRIS PDFs for the warm scenes that is not present for the cold cases. Preliminary comparisons indicate that the shift in peak ΔT_B towards higher values for warmer scenes in the IRR data is consistent with that seen in simulated spectra matched to the IRR overpass times [X. Huang, pers comm., 2014]. Theoretical calculations of the equivalent Planck radiance for a blackbody at 220 K and 310 K indicate that subtle changes to the spectral emissivity of the IRIS instrument in the window regions either side of the 9.6 μm ozone band could potentially "correct" these differences. However, the mixture of scene types and, more crucially, the absence of the raw IRIS interferograms and associated calibration parameters, would make this a highly empirical approach. More analysis is needed to definitively isolate sampling and calibration effects, but the difficulties that we have encountered in this work clearly re-emphasize the need for careful quantification of both in future mission design if the full potential of spectrally resolved measurements for climate monitoring is to be unlocked.

29
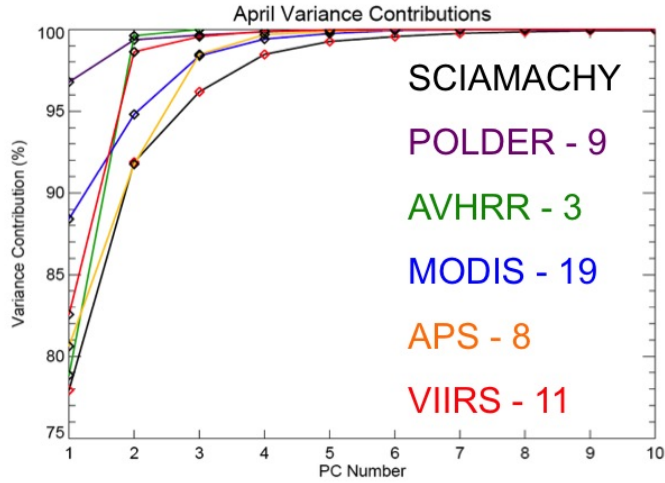
Figure 2.15: THE PC CUMULATIVE VARIANCE CONTRIBUTION FOR REFLECTED RADIANCE DATA SETS RE-SAMPLED TO THE SPECTRAL RESOLUTIONS FOR SEVERAL REFLECTED SOLAR INSTRUMENTS. THE NUMBERS NEXT TO THE NAMES OF THE SENSORS INDICATE THE NUMBER OF BANDS EACH INSTRUMENT HAS WITHIN THE SPECTRAL RANGE (300 – 1750 NM). IN CONTRAST TO THE DISCRETE-BAND SENSORS, THE SCIA-MACHY DATA SET HAS A SPECTRAL RESOLUTION OF 10 NM AND A CONTINUOUS 3 NM SAMPLING ACROSS THE SPECTRAL RANGE, RESULTING IN 484 SPECTRAL BANDS. THE DISCRETE-BAND DATA SETS CONTAIN LESS INFORMATION THAN THEIR HYPERSPECTRAL COUNTERPART.

2.4 Information Content in Reflected Solar Observations

Spectrally resolved reflected solar radiation at the top of the atmosphere (TOA) contains information about Earth's surface features such as vegetation, snow, and sea ice coverage, and atmospheric variables, such as clouds, aerosol particles, and greenhouse gases. Our work has demonstrated how the information in the spectral variability of directly measured shortwave (solar) radiation reflected by the Earth system can be used to monitor changes in climate. Different surface materials, such as minerals and vegetation, have unique spectral signatures that are caused by the interaction of the specific atoms that comprise the surface materials with electromagnetic radiation at different energy levels [Hunt, 1977]. Through radiative transfer theory, it is known that molecules, cloud particles, and aerosol particles in the atmosphere interact with solar radiation through wavelength-dependent scattering and absorption processes.

There are several methods that can be used to extract and quantify the multitude of information in *hyperspectral* reflectance (i.e. spectrally resolved measurements with overlapping, contiguous spectral bands [Goetz, 2009]). The CLARREO Science Definition Team's efforts have focused on using multivariate analysis techniques to extract information about the climate system exclusively from the measured data, without using external, model-based or retrieval techniques, or assumptions. Particularly, principal component analysis (PCA) and its time series equivalent, singular spectrum analysis (SSA) were applied to measured and simulated hyperspectral radiance and reflectance. PCA quantifies dominant modes of variability exclusively in terms of the information contained in the data.

Using PCA, we demonstrated the importance of the distinguishing attribute of hyperspectral measurements from broadband and discrete-band measurements: spectral contiguity. Figure
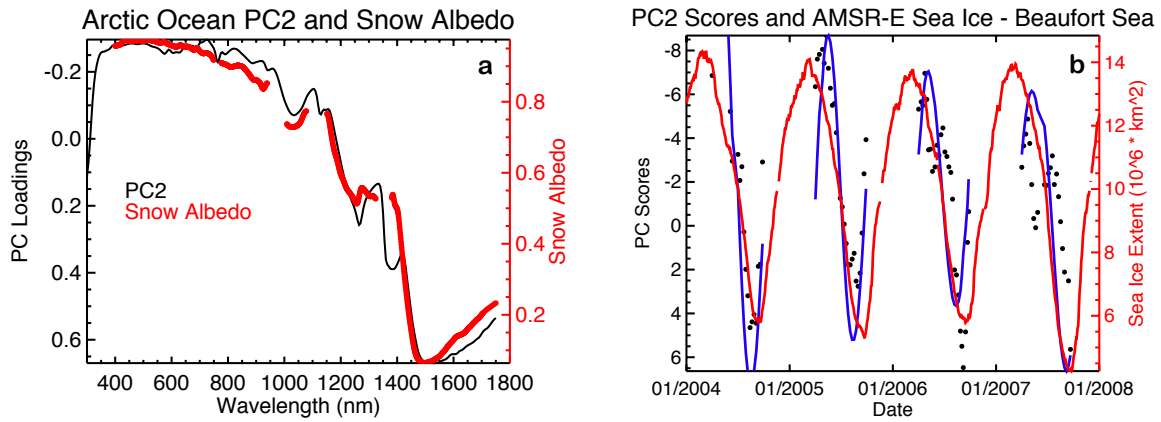
Figure 2.16: a) THE SPECTRAL SHAPE OF THE SECOND PRINCIPAL COMPONENT CALCULATED FROM REFLECTED RADIANCE MEASURED EXCLUSIVELY OVER THE ARCTIC OCEAN SHOWED A CLOSE COMPARISON TO A SNOW ALBEDO SPECTRUM [SCHMIDT ET AL., 2009]. b) A COMPARISON OF THE PC2 SCORES (BLACK) AND THE SSA RECONSTRUCTION OF THESE SCORES (BLUE) TO THE ARCTIC OCEAN SEA ICE EXTENT FROM AMSR-E (RED) REVEALS A CLOSE SIMILARITY BETWEEN THE PC2 AND ARCTIC SEA ICE EXTENT TEMPORAL VARIABILITY.

2.15 compares the cumulative variance contributions calculated from PCA for a hyperspectral reflected radiance data set (SCIAMACHY) to the cumulative variance calculated from hyperspectral data resampled to the spectral resolutions and samplings of several discrete-band instruments. This comparison demonstrates that as the spectral resolution and sampling degrades, the amount of information contained in the data set also decreases. Although the SCIAMACHY cumulative distribution shows that only six principal component dimensions are needed to explain 99.5% of the total data variance, linear combinations of all the 484 spectral bands are needed to create those six variance-driving PC variables.

PCA was also used to demonstrate that climate-relevant variables could be identified from the quantified data variability of hyperspectral radiance measurements [Roberts et al., 2011]. For example, applying PCA to spectral radiance measured exclusively over the Arctic Ocean illustrated that the information in the spectral range between 300 and 1750 nm could be used to discriminate between clear and cloudy scenes in the cryosphere, a notoriously difficult problem in the reflected solar. The first PC in this case resembled a cloud reflectance spectrum, and the second PC resembled a snow albedo spectrum (Figure 2.16a). Because only ocean pixels were included, it can be assumed that any snow or ice signal detected was associated with sea ice cover. Additionally, the temporal variability of the second PC predominantly represents the temporal variability of Arctic sea ice cover (Figure 2.16b). In addition to demonstrating physical attribution using the spectral principal components and their time series, [Roberts et al., 2011] also illustrated using the spatial variability of PCs to attribute physical variables dominating the spectral variability of hyperspectral radiance.

Roberts et al. 2014 (in review) presented the first results quantifying the eight-year (2002 – 2010) of observed hyperspectral reflectance. Using 30° zonal bands, the variance-dominating spectral variables from this analysis demonstrated the temporal variability of physical variables, such as the seasonal movement of the Intertropical Convergence Zone and the annual cycle of the cryosphere.
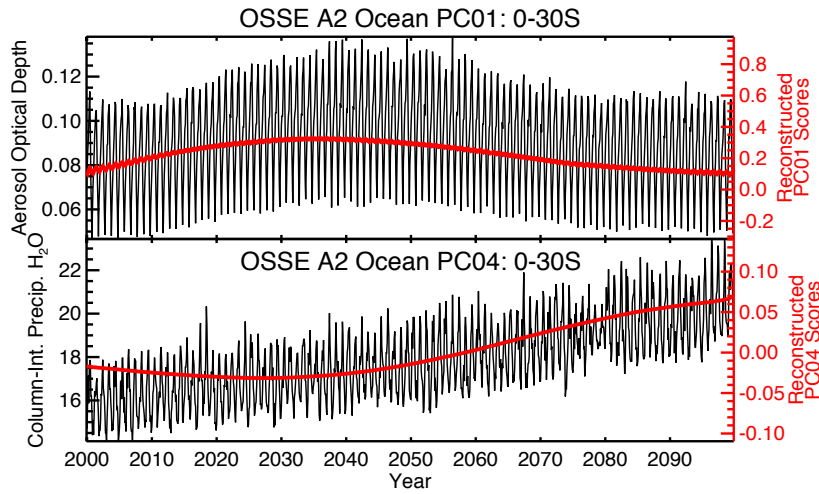
Figure 2.17: THE SSA-RECONSTRUCTED SECULAR PARTS OF THE OSSE A2 EMISSION PC1 AND PC4 OCEAN TIME SERIES (RED) OVERLAID ON THE CENTENNIAL VARIABILITY OF THE CCSM3 AEROSOL OPTICAL DEPTH AND COLUMN-INTEGRATED PRECIPITABLE WATER $(kg\,m^{-2})$ (BLACK).

Using the climate Observing System Simulation Experiement (OSSE) (see Section 2.6) output generated between 2000 to 2099, the spectral, spatial, and centennial variability of IPCC AR4 forced (A2) and unforced (constant CO_2 concentration) climate scenarios was quantified to illustrate how the variability of Earth's climate can be characterized by the application of multivariate tools to shortwave hyperspectral reflectance. The time series corresponding to the PCs calculated from the unforced OSSE case exhibited annual and seasonal patterns, but no secular trends. However, the time series corresponding to the PCs calculated from the forced OSSE scenario exhibited secular trends such as changes in aerosol amount and total column water vapor during the simulation period (Figure 2.17). The PCA results quantifying the OSSE centennial variability demonstrate how hyperspectral reflectance could be used to detect and attribute temporal changes in Earth's climate. These results imply that with CLARREO-like measurements that had high accuracy and information content and that were taken over a sufficiently long time, we would be able to detect climate signals in the Earth's climate system and attribute those climate changes to geophysical variables.

This area of research is rich with possibilities for continuation of the work that the CLARREO Science Definition Team already completed. Our work has illustrated the value of the high information content in direct measurements of hyperspectral reflected solar data for studying Earth's climate variability. There are several other applications of the information content of reflected solar hyperspectral reflectance and radiance. This work has supported the value of spectral fingerprinting (see Section 2.5.2) by illustrating that even without isolating specific processes or applying any model-based techniques, geophysical variables are identifiable in the variance-driving spectral variables in hyperspectral reflected radiance and reflectance measurements. In addition to climate change attribution with spectral fingerprinting, our work can be used for additional attribution techniques to be developed. Using exploratory methods to extract information from directly measured radiance, rather than retrieved parameters, prevents the uncertainty and error introduced to climate change analysis during the retrieval process. If independent attribution techniques provide similar results, this strengthens the validity of each of the techniques.

Information Theory provides powerful tools that have been widely applied to a diverse set of fields and has been critical to the success of endeavors such as the Voyager missions to deep space. The amount of self-information in a data set depends upon the probability of occurrence of the random variables within that data set: the smaller the probability of observing the random variables, the larger the self-information and, therefore, the information content. The climate system has natural randomness, or natural variability, over a range of spatial and temporal scales.

Members of the CLARREO science team are developing a framework that will employ self-information to objectively quantify the information content contained within shortwave reflectance measurements made with a variety of measurement requirements. Although there are many measurement requirements that affect the information content of reflected solar measurements, our initial development of this information content framework (ICF) will focus on a subset: radiometric accuracy; spectral resolution, sampling, and range; and temporal and spatial coverage, sampling, and resolution. Output from the ICF will provide the rationale for how to maximize the information content of different measurements for studies of the climate system designed to answer specific science questions.

2.5   Climate Fingerprinting and Attributions

Atmospheric temperature, water vapor amount, and cloud property (fraction, height, optical thickness, phase, particle size), and change as a response to increasing the carbon dioxide concentration are difficult to observe because the magnitude of natural variability is larger than the change of these properties occurring over a time scale equivalent to the lifetime of satellite instruments. Even though these properties are currently observed from satellite-based instruments, the uncertainty in the calibration of instruments usually makes it difficult to detect such changes within the lifetime of the instruments or even the duration of the missions. Subtle spectral radiance changes appear when observed radiances are averaged spatially and temporally. A possibility of detecting such subtle atmospheric and cloud changes by observing spectral radiances is discussed, for example, by Goody et al. (1998), Leroy (1998a), and Anderson et al. (2004).

Once observed radiances are averaged, both instrument noise and natural variability are reduced, with the larger the time and space averaging, the larger the reduction. Unlike retrievals from instantaneous observations, detecting the trend of atmospheric and cloud properties from the highly averaged spectral radiance requires separating cloud and atmospheric changes contributing to the spectral radiance change. Hereinafter, the process separating contributions from highly averaged spectral radiance change is called "retrieval" by the average-then-retrieve approach. A possibility of such retrieval is investigated in detail by the CLARREO Science Definition Team (SDT) members using longwave spectral radiances by Leroy et al. [2008a], Huang et al. [2010a], Kato et al. [2011], and shortwave spectral radiances by Feldman et al. [2011], Jin et al. [2011], Roberts et al. [2011], and longwave spectral radiances combined with radio occultation data by Huang et al. [2010b].

2.5.1 Climate Fingerprinting in InfraRed

Results using longwave spectral radiances show that clear-sky atmospheric property changes, such as temperature and water vapor amount, can be retrieved from highly averaged spectral radiance change [Leroy et al. 2008a]. However, a larger error occurs in retrieving cloud property (e.g. fraction, height, optical thickness, particle size) changes [Kato et al. 2011]. Because it uses a linear regression to separate contributions, necessary conditions for the average-then-retrieve approach to work are: (1) TOA spectral radiance change can be expressed as a linear combination of spectral radiance changes caused by cloud and atmospheric properties, (2) the magnitude of spectral radiance changes linearly corresponding to a small perturbation of cloud or atmospheric property, at least in the relevant parts of the spectrum, and (3) changes of cloud and atmospheric properties provide unique spectral radiances that can be separated by a linear regression. These assumptions are tested in an earlier study [Kato et al. 2011] and proved to be valid assumptions at least for annual and monthly and 10° zonal scales. In addition, conditions (1) and (3) are shown to be valid at an annual scale shown by Leroy et al. [2008a] for clear-sky and by Huang et al. [2010a] for all-sky. Their results also imply that condition (2) is valid.

All earlier studies investigate the possibility of separating contributions using two time periods and deriving changes of cloud and atmospheric properties contributing to the difference of the spectral radiance averaged over two time periods. Even if the error in separating the change of cloud properties contribution is large, when property changes are retrieved a sufficient number of times, the trend of property changes can be correctly inferred from retrieved properties [Kato et al. 2014]. Studies by Weatherhead et al. (1998), Leroy et al. (2008b), and Wielicki et al. (2013) indicate that requirements for retrieving a trend are: (1) any retrieval bias error must be stable at a level much smaller than that of the trend of interest and (2) any random error must be sufficiently small with sufficient independent samples to allow accurate detection of the trend.
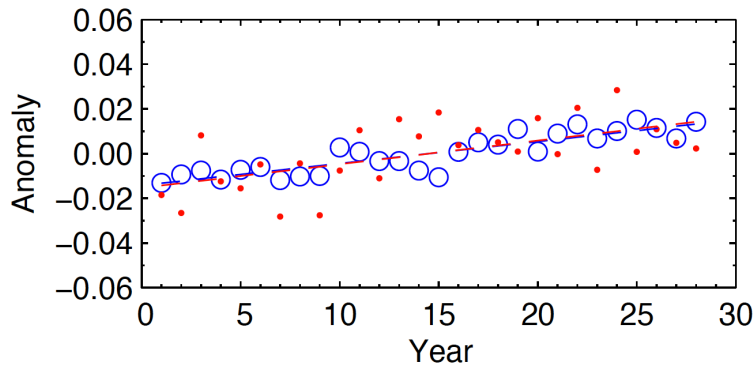
Figure 2.18: Low-level cloud fraction annual anomalies retrieved by the average-then-retrieve approach (closed red circles) plotted with true anomalies from the Modern Era Retrospective-Analysis for Research and Applications (MERRA) (blue open circles) for the latitude between 30°S and 40°. Red and blue dashed lines are linear regression lines computed with, respectively, retrieved and true anomalies. The slope of the linear regression line of retrieved values is very close (0.0011 per year) to the regression line computed from the true values (0.0010 per year). Low-level clouds are defined as clouds with a cloud top pressure greater than 700 hPa.

A study by Kato et al. (2014) demonstrates that when cloud and atmospheric contributions to the spectral radiance annual 10° zonal anomalies are retrieved, the error in their trends is small. Figure 2.18 shows an example of a small error in estimating a trend. The retrieval errors have both a positive and a negative sign occurring somewhat randomly so that the root mean square (RMS) difference is 0.013 and the correlation coefficient between the retrieved and true cloud fraction is 0.52. When the trend is estimated by the linear regression, however, the slope of the linear regression line of retrieved values is very close (0.0011 per year) to the regression line computed from the true values (0.0010 per year). When cloud and atmospheric properties are retrieved for all 18 latitudinal zones, approximately 30% of 10° zones meet conditions that the true temperature and water vapor amount trends are within a 95% confidence interval of retrieved trends, and that the standard deviation of retrieved anomalies, σ_{ret}, are within 20% of the standard deviation of true anomalies, σ_n. In addition, if (σ_{ret}/σ_n - 1) is within ± 0.2, 91% of the true trends fall within the 95% confidence interval of the corresponding retrieved trend. Furthermore, the authors demonstrate that the retrieval error of cloud property anomalies does not affect the temperature and water vapor anomaly retrieval. As a consequence, the error in the temperature and water vapor amount anomalies retrieved from all-sky spectral radiance anomalies is equivalent to the retrieval error derived from the clear-sky spectral radiance anomalies. The result does not rule out the possibility of reducing the retrieval error by separating clear-sky from cloud-sky when a more sophisticated algorithm is used, especially for retrieving cloud property anomalies. If the clear-sky retrieval is separated from all-sky retrievals, however, one needs to contemplate at least the following two points:

(1) The clear-sky needs to be well defined because the sensitivity of cloud detection varies with instrument type and the resolution. When the clear-sky scene is defined, the effect of the scene identification error on the retrieval needs to be small.

(2) Even if clear-sky retrieval is separated from all-sky with a minimum error, temperature and humidity anomalies need to be retrieved from cloudy or overcast spectral radiances because those under all-sky or overcast conditions might be different from those under clear-sky conditions. The separation of clear-sky from cloudy-sky has to bring additional constraints to compensate the error introduced in identifying clear-sky scenes.

Possibilities to reduce attribution error

(1) For the average-then-retrieve approach to work, the spectral radiance must change linearly with the perturbation of atmospheric and cloud properties. This means that variability of these properties needs to be small. Because the variability increases with decreasing spatial and temporal scales, this sets the lower bound of temporal and spatial scale for the spectral radiance to be averaged, although the exact limit of the scale needs to be determined. While natural variability decreases with the temporal and spatial scale of averaging, the signal (trend) increases with temporal averaging scale. Therefore, a longer temporal average and a larger spatial average make the retrieval error smaller, but lose the resolution in which retrieved values can be used for analyses. There must be optimum temporal and spatial scales.

(2) The study by Kato et al. [2014] indicates that the vertical resolution to retrieve temperature, humidity, and cloud top height change needs to be investigated especially near the tropopause and the top of the boundary layer. A requirement is that the property (e.g. temperature) change within the layer needs to be nearly uniform. The lower limit of layer thickness is determined by the natural variability of properties within the layer. The optimum

vertical resolution, which might be regional dependent, needs to be determined.

(3) The sensitivity of the nadir-view spectral radiative kernel to the perturbation of surface, atmospheric, and cloud properties depends on the transmissivity of the atmosphere. This means that it depends on mean atmospheric states and cloud fields. Although the effect of the mean state to the broad band radiative kernel might be of the order of 10% [Soden et al. 2008], the sensitivity of spectral radiative kernel, especially to cloud fields, needs to be investigated.

(4) Optimizing the linear regression. Although optimized linear regression is used in Leroy et al. (2008), Huang et al. (2010a), and Huang et al. (2010b), one of the issues for the optimization is to form a covariance matrix properly. Earlier studies used spatial correlations to form the covariance matrix, while temporal correlations might be needed. The way to form a proper covariance matrix needs to be investigated. In addition, Kato et al. (2014) shows that the product of the eigenvalue and the diagonal term of a smoothing matrix can be determined by comparing the standard deviation of retrieved value and natural variability. Selecting regional dependent of the product also reduces the retrieval error. Finding the proper value of the product needs to be investigated.

(5) Combining reflected solar with infrared spectra. Some cloud properties, such as optical thickness and cloud fraction, can be retrieved from reflected radiance better than those derived from the infrared radiance. An investigation of whether or not such combination can improve the retrieval is needed.

Contribution to detecting feedback and constraining GCM's

The average-then-retrieve approach developed by the CLARREO SDT summarized above can retrieve the trend of temperature, water vapor amount, and cloud properties. Because the average-then-retrieve approach separates the observed spectral radiance change by CLARREO instruments into contributions by surface, atmospheric and cloud properties, the sum of the contributions is equal to the radiance change observed by the CLARREO instruments. The retrieved trends can be converted to the top-of-atmosphere (TOA) irradiance change using, for example, radiative transfer models. Because CERES instruments are calibrated against CLARREO instruments, the sum of TOA irradiance change computed from retrieved values agrees with the irradiance change derived from CERES instruments to within the calibration uncertainty. Once the TOA irradiance changes are combined with the surface temperature change as a response to increasing the carbon dioxide concentration, we should be able to estimate feedbacks observationally. These observationally derived feedbacks can be used to evaluate feedbacks computed by climate models. For example, we should be able to include observational data points in Figure 9.43 in IPCC WG1 AR5 chapter 9 [Flato et al. 2013].

2.5.2 Climate Fingerprinting in Reflected Solar

The Earth's reflected solar spectrum contains ample information about several variables relevant to changes in Earth's climate, including cloud properties, aerosols, atmospheric trace gases, and surface conditions. Changes in these variables lead to unique changes in the outgoing spectrum at the top-of-atmosphere, and therefore, leave unique fingerprints of individual feedbacks or climate responses in the outgoing spectra. Because of the existence of these

unique spectral fingerprints for individual variables, long term data record in the large domain-averaged spectrum (i.e., average over large space and time scales) could reveal the trends of those important climate variables, and therefore, be used to detect climate changes. Climate responses to changes in these variables in the shortwave spectrum are very different from those in the InfraRed (IR) spectrum. Therefore, the reflected solar spectrum provide unique and complementary information on climate change in addition to the IR spectra. Research results in Jin et al. [2012] showed that the interannual variations in the solar spectral reflectance averaged over large spatiotemporal scales are well correlated with the interannual variations of the averaged atmospheric and surface properties. This correlation between spectral variation and climate parameter changes provides the physical foundation for attributing the radiative signals of climate change to different parameters of the Earth's climate system through the reflected solar spectrum.
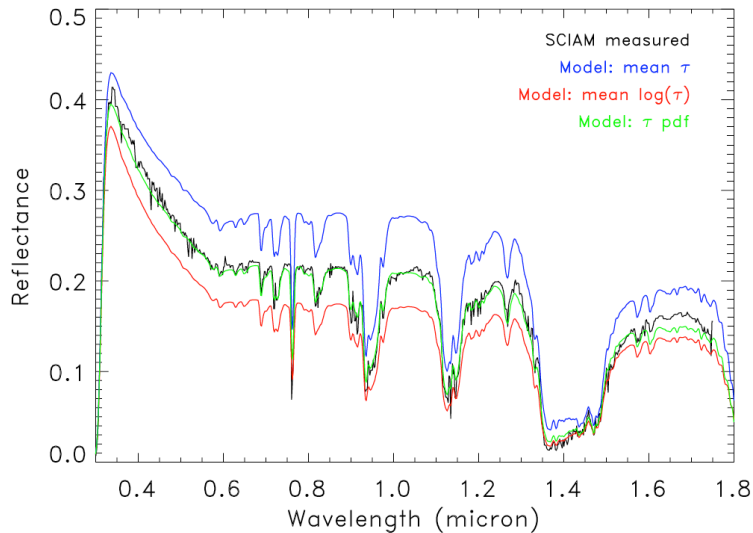
Figure 2.19: Monthly mean spectral reflectance: Comparison between SCIAMACHY measurements (black dashed line) and the model calculations with different inputs for cloud τ (the three colored solid lines). This example is for one zone, from 30°S to 35°S, over the ocean in January 2006.

As demonstrated by the observational data, the interannual variability in the large domain-averaged solar reflectance spectrum decreases as the time and space scales used for averaging increase [Jin et al., 2014]. When averaged over large spatiotemporal scales, the interannual difference of the solar spectral reflectance is small compared to the mean reflectance (typically a few percent for monthly and global means) and thus, can be considered as a perturbation from the mean state. Therefore, attributing the small spectral reflectance change to different physical causes can be formulated as a multivariate linear regression problem as

$$\Delta R = K\Delta X + e \tag{2.5}$$

where ΔR is the spectral change vector with a dimension of $[n_w]$ (n_w is the number of spectral bands), the spectral kernel matrix $K[n_w, n_x]$ represents the spectral fingerprints of n_x variables related to the spectral change, the column vector $\Delta X[n_x]$ is the variable change we seek, and $e[n_w]$ is the error vector. A kernel describes the differential response of radiation to a change in a feedback variable between two climate states, a kernel depends only on the radiative

transfer algorithm and the unperturbed climate state. The more linear the kernel, the smaller the error. Different techniques could be used to take into account the uncertainty of e. A common approach used in climate fingerprinting is optimal detection. The optimal detection solution of Equation 2.5 is

$$\Delta X = \left(K^T E^{-1} K\right)^{-1} K^T E^{-1} \Delta R \tag{2.6}$$

where E is the covariance matrix of e.

The formulation for the fingerprinting retrieval described above is no different from the conventional retrieval using the instantaneous satellite data. However, the fingerprinting is different from the conventional remote sensing retrieval in the following:

(1) It is for the averaged quantities over large spatiotemporal scales instead of the local or instantaneous values.
(2) It for the relative changes between two climate states instead of the absolute values.

Because the radiative response to changes in variables are inherently nonlinear, the ΔR and ΔX have to be small compared to the mean state values. This is indeed the case for the climate change signals and for the interannual changes in variables averaged in large climate domains. For example, when averaged to large latitude zones, probability distribution function (PDF) of the mean cloud optical depth, τ, changes little from year to year and the anomaly in the averaged monthly and globally spectral reflectance is generally within 5% of the mean value [Jin et al., 2012 and 2014]. This result suggests that it is a viable approach to use the averaged reflectance spectra in large climate domains for the attribution or fingerprinting of climate changes.

As shown in Equations 2.5 and 2.6, the spectral kernel K and the domain-averaged spectrum R are the two important variables required to obtain the fingerprinting solution ΔX. While K cannot be measured directly, the spectrum R can be obtained either from observation or from model simulation. Spaceborne sensors have measured the atmospheric and surface properties over the globe for decades and have accumulated a large volume of data. This makes it possible for us to use the real observational data as model inputs to simulate spectral radiation over large time and space scales. However, because of the expense of computation time, it is a formidable task to simulate the mean spectral reflectance over large climate domains using explicit RT computations at satellite footprint scales. To circumvent this problem, we recently developed the cloud PDF approach [Jin et al., 2013]. This PDF approach statistically accounts for the wide variation of cloud properties in different satellite footprints in the domain considered. This novel method essentially organizes the large number of satellite instantaneous measurements according to the cloud optical depth (τ) distribution, so that those footprints with similar τ and other atmospheric/surface properties are treated once, rather than footprint by footprint repetitively, in the RT modeling. Therefore, the computation time is reduced significantly compared to computing footprint by footprint. The method is particularly suitable for simulating the mean spectral radiance or reflectance in large climate domains with a large volume of instantaneous satellite data. Figure 2.19 is an example that compares zonal mean reflectance using the PDF method (the green line) with the SCIAMACHY measurement and with those simulated by other methods. The input data used for the model computation were all from observations, including the instantaneous MODIS clouds and aerosols nested in the CERES SSF product. Compared to all of the SCIAMACHY measurements from 2004 to

2009, the PDF simulations showed an RMS error of about 3% for the monthly global mean reflectance. This error is smaller in the Tropic regions but larger in the polar regions.
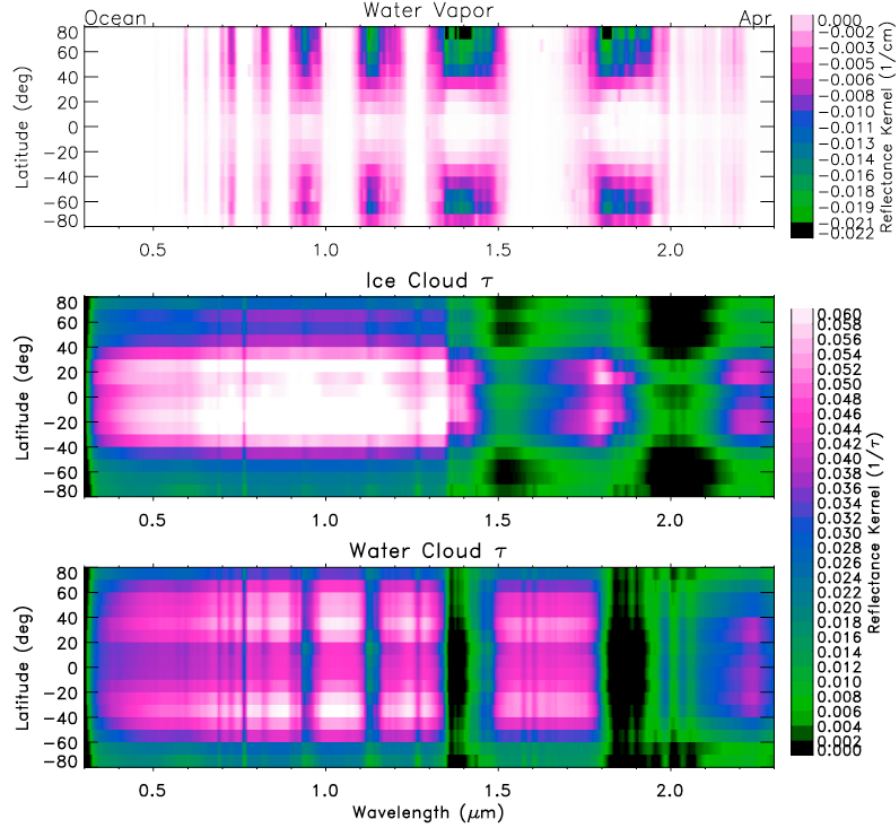
Figure 2.20: THE SOLAR SPECTRAL REFLECTANCE KERNELS FOR THREE PARAMETERS. THIS EXAMPLE IS FOR THE MONTHLY MEAN REFLECTANCE OVER THE OCEAN IN APRIL. IN EACH PANEL, THE X AXIS IS FOR WAVELENGTH AND THE Y AXIS IS FOR LATITUDE.

The kernel matrix K includes the spectral fingerprints for individual variables. The fingerprints can be calculated by the partial radiative perturbation (PRP) method [Wetherald and Manabe, 1988], as used in IR fingerprinting [Huang et al., 2010]. We used a modified PRP method to calculate the kernels specifically for the shortwave spectrum:

$$K_i = \frac{1}{2} \left[\frac{r(\bar{x}, \bar{x}_i + \delta \bar{x}_i) - r(\bar{x})}{\delta \bar{x}_i} + \frac{r(\bar{x}) - r(\bar{x}, \bar{x}_i - \delta \bar{x}_i)}{\delta \bar{x}_i} \right] = \frac{r(\bar{x}, \bar{x}_i + \delta \bar{x}_i) - r(\bar{x}, \bar{x}_i - \delta \bar{x}_i)}{2\delta \bar{x}_i} \quad (2.7)$$

where K_i is the kernel for the i-th parameter x_i, and r is the spectral reflectance. The $\bar{x} = (x_1, ...x_i, ...x_n)$ represents an ensemble of n climate variables at mean state, δx_i, is the perturbation of x_i from its mean state. Reflectance instead of radiance is used because the reflectance has much less (or flatter) spectral variation than the radiance. More importantly, the reflectance response is directly related to the variations of the underlying terrestrial climate parameters. Radiance is less favored because of its sensitivity to changes in incoming solar radiation; these changes are due to both the seasonal variation of Earth – Sun distance and more sporadic, spectral shifts associated with the activity of the Sun itself. However, a reflectance kernel can be conveniently converted to a radiance kernel through the solar irradiance if desired. Using the $1° \times 1°$ gridded monthly mean data of atmospheric and surface

properties, we created a set of solar spectral kernels for thirteen variables for the first time [Jin et al., 2011]. The kernel linearity was tested and the results showed that the kernels non-linearity error varies strongly depending on climate variable, wavelength, surface, and solar elevation. It is large in some absorption bands for some parameters (e.g. cloud height).

Figure 2.20 is an example of the 10° zonal mean solar spectral kernel for three variables over the entire global ocean. The upper panel is for the precipitable water (PW) and represents the nadir reflectance change expressed per 1cm of PW change. The middle and bottom panels show the reflectance kernels of cloud optical depth (τ) for liquid water and ice clouds, respectively, and they represent the nadir reflectance change expressed per unit of τ change. The absolute value of the PW kernel (the reflectance change expressed per 1cm of change in water vapor) becomes more negative from equator to pole because of lower mean PW and higher solar zenith angle (longer optical path for absorption) in higher latitudes. On the contrary, the kernel of cloud τ becomes less positive toward the poles due to the increasing solar zenith angle, but the latitude variation of the mean cloud τ is also a factor here. The ice cloud kernel (middle panel) shows quite different spectral characteristics than the liquid water cloud kernel (bottom panel). Many of the differences correspond to the water vapor absorption bands shown in the top panel. The kernel is much more sensitive to ice cloud properties than to water cloud in the absorption bands. The kernels for all other variables (not shown) also show different spectral characteristics, demonstrating the different fingerprints for different climate variables.
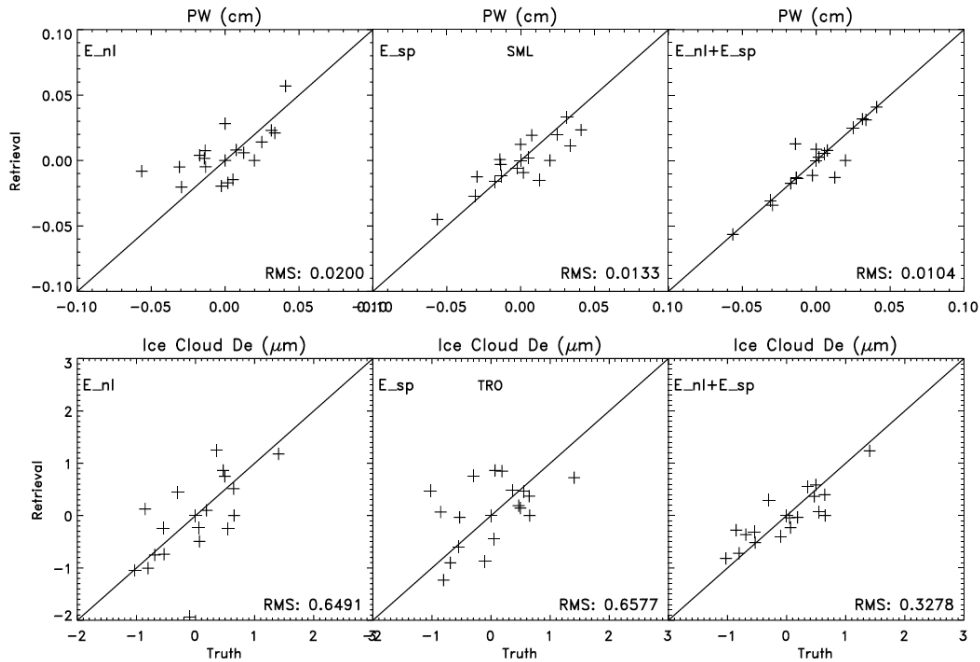
Figure 2.21: COMPARISON OF THE FINGERPRINTING RETRIEVAL AND THE TRUTH IN THREE DIFFERENT REGIONAL EXTENTS (THE THREE COLUMNS). SHOWN ARE THE ANOMALIES FOR THE MONTHLY MEAN CLOUD τ (THE UPPER PANELS) AND THE CLOUD AMOUNT (THE LOWER PANELS).

We calculated the kernels for four months: January, April, August, and October, for various latitude regions, separately for land and ocean. These kernels were applied to the reflectance anomaly spectra simulated over five years, from 2001 to 2005, to test the reflected solar fingerprinting approach to retrieve the corresponding changes in the 13 variables over land and

40

the 11 variables over ocean. Figure 2.21 is an example to compare the fingerprinting retrieved changes (anomalies) of the cloud optical depth (the upper panels) and cloud coverage (the lower panels) with the truth. The truth parameter changes were derived from the instantaneous MODIS data used in the RT model simulation. The three columns represent the three regions with size increasing from the left to right. The results show that as the spatial size increases the retrieval accuracy decreases. This is because the nonlinearity and the spectral shape uncertainty in mean spectral kernels increases as the spatial extent used for averaging increases. Results for other parameters show similar phenomena as shown in Figure 2.21.

Due to the inherently non-linear radiative response to individual variable changes and the radiative interactions among different variables, there are nonlinearity errors in the model calculated kernels. Due to the radiative interactions, the simple sum of the responses to individual variable changes differs from the total response that is obtained with all variables changed simultaneously (i.e. $\delta R \neq \sum R_i$). The spectral shape uncertainty results from the spatial variability of the local fingerprints, and is dependent on the location and extent of the region used to define the mean fingerprints. We have quantified the effect of these errors on the fingerprinting retrieval. Figure 2.22 is an example to show these error effects on the retrieval of PW (upper panels) and the effective cloud particle size (the lower panels). The results show that these significantly affect the retrieval accuracy, but the effects are different for different variables.
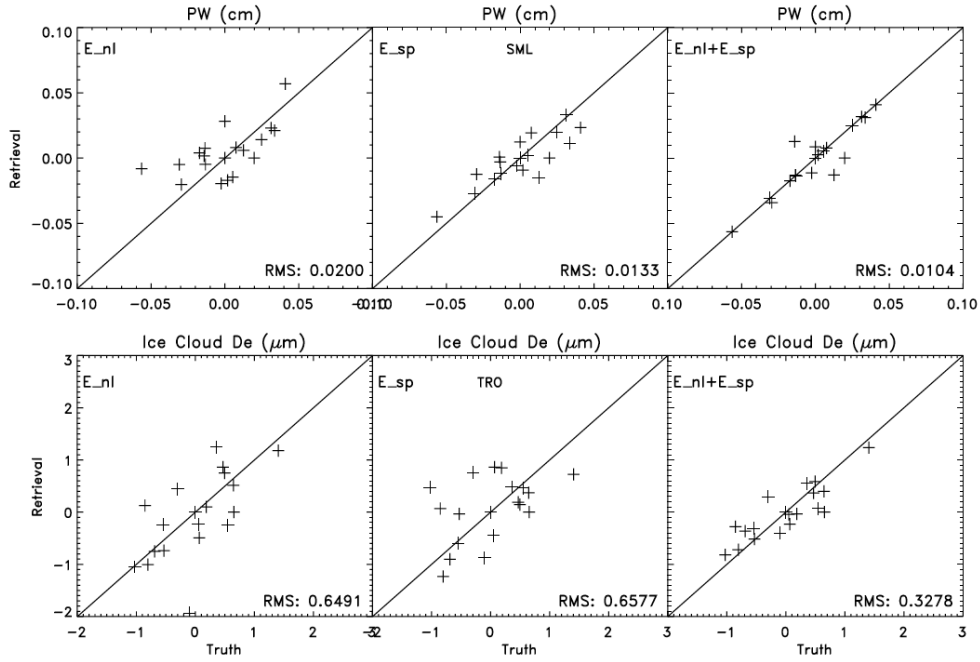
Figure 2.22: An example to show the effects of errors in kernels on the fingerpring retrieval. The nonlinearity error, E_nl, is accounted for in the left column, the shape uncertainty, E_sp, is considered in the middle, and both are considered in the right.

The initial fingerprinting results using the simulated solar reflectance are encouraging, but many issues need to be resolved, especially when the real observational reflectance spectra are used. It is critical to evaluate the ability of using CLARREO RS benchmark spectrum to detect the feedbacks important to climate change.

2.6 Climate Change OSSE's

The perspective presented in Section 2.2 is very effective in deriving a simple yet powerful understanding of climate change observing system requirements. While the examples were given for the CLARREO mission, they are generally applicable to any climate observation. There will be times, however, that this simple view will not capture all the aspects of a key climate observation. An example for CLARREO is climate change spectral fingerprinting [Goody et al., 1998; Huang et al., 2010a,b; Feldman, 2011; Jin et al. 2011; Kato et al., 2011].

Spectral fingerprints use the decadal change in Earth's emitted infrared spectra and reflected solar spectra to "fingerprint" signals of climate change ranging from surface temperature to tropospheric or stratospheric temperature, lower or upper atmosphere water vapor, cloud properties, surface vegetation, snow/ice cover, or the effects of greenhouse gases on thermal emission. The effects are broad because they include the entire spectrum of Earth's reflected and emitted radiation. Since climate change is primarily driven by changes in planetary radiation, different portions of the Earth's spectrum respond in climate change scenarios. Figure 2.23 [Feldman et al., 2014a] shows modeled globally-averaged infrared spectral radiance and solar reflectance and estimated trends from the A2 Emission Scenario indicating numerous factors that contribute to the spectra.
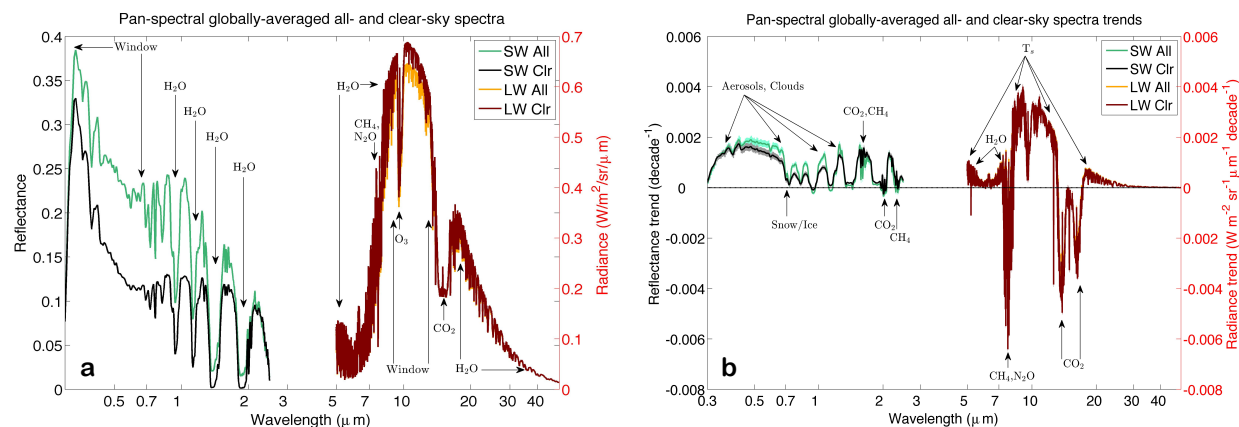
Figure 2.23: (A) PAN-SPECTRAL COMPOSITE OF THE GLOBALLY-AVERAGED ALL- AND CLEAR-SKY RE-FLECTANCE AND LONGWAVE RADIANCE FROM JANUARY 2000 FOR THE A2 SIMULATION. (B) SAME AS (A) BUT SHOWING THE TRENDS IN SW REFLECTANCE (IN REFLECTANCE UNITS) AND LW RADIANCE (IN $W/M^2/SR/\mu M$). SHADING INDICATES 95% CONFIDENCE INTERVAL OF UNCERTAINTY IN TRENDS.

Spectra have typically been used for instantaneous satellite retrievals of geophysical properties as well as radiance constraints for weather assimilation and reanalyses [Kalnay et al., 1996; Derber and Wu,1998; McNally et al., 2006]. For the former application, the formulation of the retrieval algorithm and the assimilation generally operates by achieving global rather than local minima [Migliorini et al, 2008, Aghedo et al, 2011a, Inness et al, 2013] and the propagation of errors in retrieval parameters leads to Gaussian uncertainties [Kulawik et al, 2008, Migliorini et al, 2008]. Aghedo et al, [2011b], for example, showed that non-linearities in water vapor retrievals could lead to biases in zonal mean fields. It has been noted that there is significant potential for retrievals to be problematic when subjected to biased *a priori* information [Kulawik et al, 2008; Thies and Bendix, 2011]. For the latter application, while

re-analyses are useful for many scientific applications, they continue to struggle to achieve highly accurate climate trend observations [Dee 2005; Saha et al. 2010; Thorne and Vose 2010; Rienecker et al. 2011].

To avoid these pitfalls, spectra are averaged over space and time to provide climate change spectral anomalies. These spectral anomalies are then used to understand the climate change that has occurred. The advantage of this new approach is to eliminate the instantaneous nonlinear retrieval step of the process and to explicitly account for how *a priori* information contributes to the analyzed climate change signal in retrievals and assimilation systems.

In order to use time-space averaged spectra to fingerprint climate change, we require that the spectra changes are essentially linear with changes in geophysical variables, so that space/time averaging does not corrupt the climate change signals. Since the instantaneous retrievals from spectra are nonlinear, this might appear to be a poor assumption. At the small time and space scales associated with weather, there are large changes in temperature, humidity, and clouds, so that linearity can be a poor assumption. Climate change, however, consists of very small changes in distributions of geophysical variables, much like the small change approximations used for Taylor expansions of nonlinear mathematical equations. Typical decadal time scale changes are much less than 1% in magnitude and clearly qualify as small perturbations and therefore require a verification of the degree of linearity that can be achieved. Our simple Equation 2.1 does not answer this more sophisticated question, but a climate OSSE can. We first define what a climate OSSE is, and then show some key examples of how such experiments can be a powerful additional understanding of climate observation requirements.

A climate OSSE is based entirely on a climate model and its simulations of the global climate system. While a climate model is not exactly the Earth, the model has many advantages for testing concepts of improved observing systems: the model climate change is known exactly, the model anthropogenic forcings (if included) are known exactly, the model output "data" is known exactly, and has no data gaps, sampling uncertainties, or drifting instrument calibration issues, and the model represents a possible realization of the Earth's response to the known forcings. Thus, a climate model is in essence an ideal test-bed. A climate OSSE uses simulations of anthropogenically-forced climate change over decades to test the value of a particular observing system that could be produced to understand similar components of the Earth's climate system. An example is climate sensitivity. A climate OSSE can very accurately determine the sensitivity of the model climate, and can evaluate the utility of varying observations to separately understand individual climate feedbacks that drive climate sensitivity such as feedbacks from cloud, water vapor, temperature lapse rate, and surface snow and ice [Soden et al., 2008]. Figure 2.3 [from Soden et al., 2008] shows one type of climate OSSE, using the spatial patterns of climate feedbacks to understand the required spatial resolution of decadal climate change observations. The figure shows that climate feedbacks occur on the scale of 1000s of km and are often zonal in spatial structure.

While understanding spatial sampling requirements is a good first step, CLARREO needed a different approach to understand the ability of spectral fingerprinting to observe climate change and to rigorously test climate model predictions. The climate OSSE approach uses climate model output histories to drive high spectral resolution radiative transfer models that could simulate the CLARREO infrared and reflected solar spectra on regional spatial scales as well as monthly, decadal, and even century time scales. This effort began with pioneering efforts in the infrared spectra [Leroy et al., 2008a; Huang and Ramaswamy, 2009; Huang et al.,

(a) InfraRed Fingerprints.

(b) Linearity of InfraRed Fingerprints.
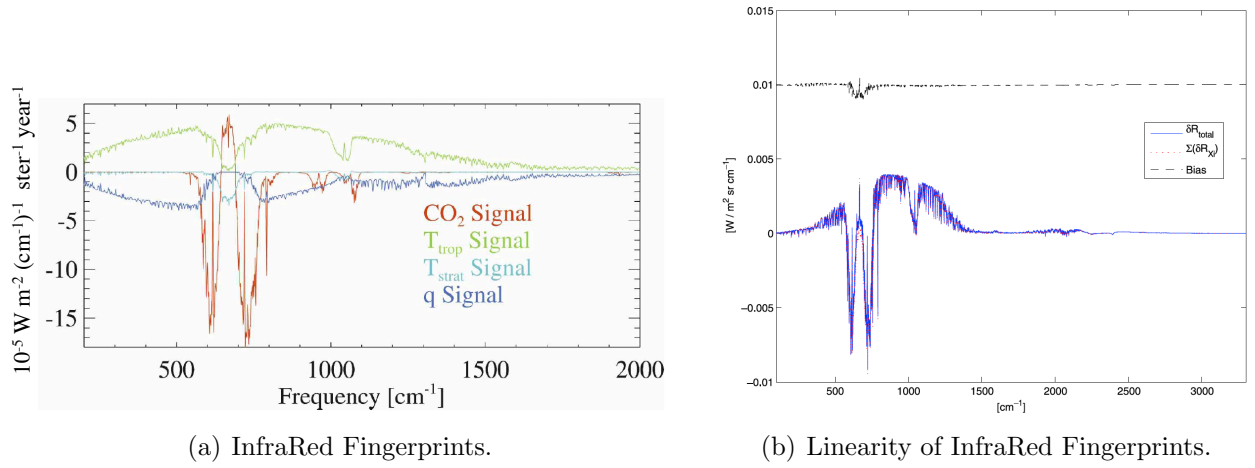
Figure 2.24: (A) Global average spectral infrared fingerprints of climate change trends based on the first 50 years of an IPCC SRES A1B climate change scenario (From Figure 1 of Leroy et al., 2008a). The legend shows each climate variable changed individually while holding all other variables fixed: CO_2 shows the effect of increased carbon dioxide, T_{trop} the effect of tropospheric temperature, T_{strat} is stratospheric temperature, while q is tropospheric water. (B) Shows the high degree of linearity of the global spectral fingerprints, with "all" showing the result for all climate changes together (temperature, water vapor, CO_2, and clouds), while the red line gives the result of simple addition of the fingerprint changes of each individual climate variable. The difference between the two is offset and shows significant nonlinearity at the 10% level in the most absorbing CO_2 wavelengths (from Figure 3 in Huang et al. 2010a).

2010a,b; Huang et al., 2011]. Figure 2.24a shows an example of the thermal infrared climate change spectral fingerprints for a range of climate variables for tropical clear-sky conditions: atmospheric carbon dioxide concentration, tropospheric and stratospheric air temperatures, and tropospheric water vapor [Leroy et al., 2008a]. The examples are developed from the first 50 years of a climate model simulation using the IPCC A1B emissions scenario. Most of the climate change spectral fingerprint signals occur in the spectrum between 200 and 2000 cm^{-1}, a spectral region that includes over 95% of the infrared energy that the Earth emits to space. The spectral fingerprints demonstrate the diversity of climate change signals and do not require satellite nonlinear retrievals to observe. Future climate models could directly predict the amplitude and shape of such fingerprints, both for natural and anthropogenic climate change, and then use these as a test against climate observations [Leroy et al., 2008b; Kato et al., 2011].

Climate model OSSE results were also used to test the linearity of the infrared spectral fingerprints and this is shown in Figure 2.24b. The linearity is tested by determining the infrared spectra changes to the simple sum of 9 individual climate change variables (those used in Figure 2.24a and additional cloud property changes), versus the full climate system with all 9 variables changing at the same time. The difference from exact linearity is typically a few percent at each wavelength, with only a few wavelengths reaching 5% in the deepest bands of the CO_2 absorption lines near 650 cm^{-1}. The difference is so small that the two lines essentially overlap. The small difference is shown in the dotted offset line for clarity.

The linearity of spectral signals has also been demonstrated from instantaneous observations averaged to larger time and space scales [Kato et al., 2011]. Finally, the climate OSSEs also provide methods to determine the ability of spectral fingerprints to determine cloud feedbacks, which have been shown to be more effective for high clouds than for low clouds [Huang et al., 2010a,b; Kato et al., 2011].

(a) OSSE climate change signals.

(b) OSSE estimates time to detect trend.
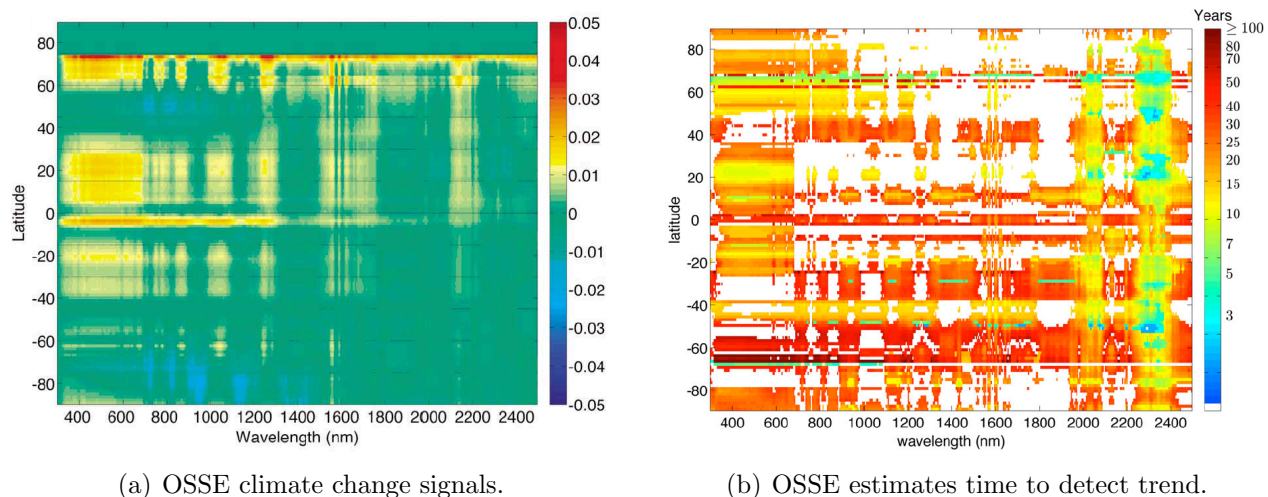
Figure 2.25: A climate model simulation of the CLARREO zonal mean spectral nadir reflectance changes predicted using the IPCC AR4 climate model output for the A2 anthropogenic forcing scenario [Feldman et al., 2011]. Figure (a) shows the latitudinal dependence of spectral climate change signals from the ultraviolet (350nm) to the near infrared (2500nm), and show climate change anomalies for the 2050's decade versus the 2000's decade. Figure (b) uses the estimates of natural variability in combination with the climate change signals in (a) in order to quantify time to detect climate trend. Clear regions are those where time to detect spectral trends are similar to those for broadband reflected solar radiation, while colored regions have shorter time to detect trends. All results are for the NCAR CCSM 3.0 climate model.

CLARREO climate OSSEs have also been carried out for the reflected solar spectra and are shown in Figure 2.25 [Feldman et al., 2011a,b]. Figure 2.25a shows the zonal mean spectral climate change fingerprints from 350 nm through 2500 nm, where over 96% of the solar energy that the Earth reflects back to space. The example shown uses the NCAR CCSM 3.0 climate model output for a 100 year IPCC AR4 A2 anthropogenic climate change scenario, and adds much more sophisticated surface, cloud, and atmosphere solar scattering, including the 4 nm CLARREO spectral resolution used to resolve climate change signals. The spectral fingerprints shown in Figure 2.25a are for all-sky reflectance and show the signals of high northern latitude snow and ice changes, water vapor changes, and cloud changes. Different clear-sky and cloudiness changes can be separated by considering all-sky and clear-sky only spectral fingerprints [Feldman et al., 2011a,b]. Given the critical importance of determining the time needed to detect climate change above natural variability, climate OSSEs can also use unforced "nature" runs to determine the climate model natural variability level, and then use this when determining the time to detect trends. Figure 2.25b provides an example of this for the CLARREO spectra and show that the time to detect trends (color) is a strong function of latitude and wavelength. White portions of the figure indicate no improvement

over detection based on broadband energetic constraints from instruments such as CERES. Water vapor trends can be detected near 2300 nm in as little as 5 to 7 years, while cloud and surface trends vary from 10 to 30 years. A study of the linearity of reflected solar spectral fingerprints [Jin et al., 2011] has shown a very high degree of linearity for climate change signals, similar to the results for the thermal infrared spectra shown in Figure 2.24b.
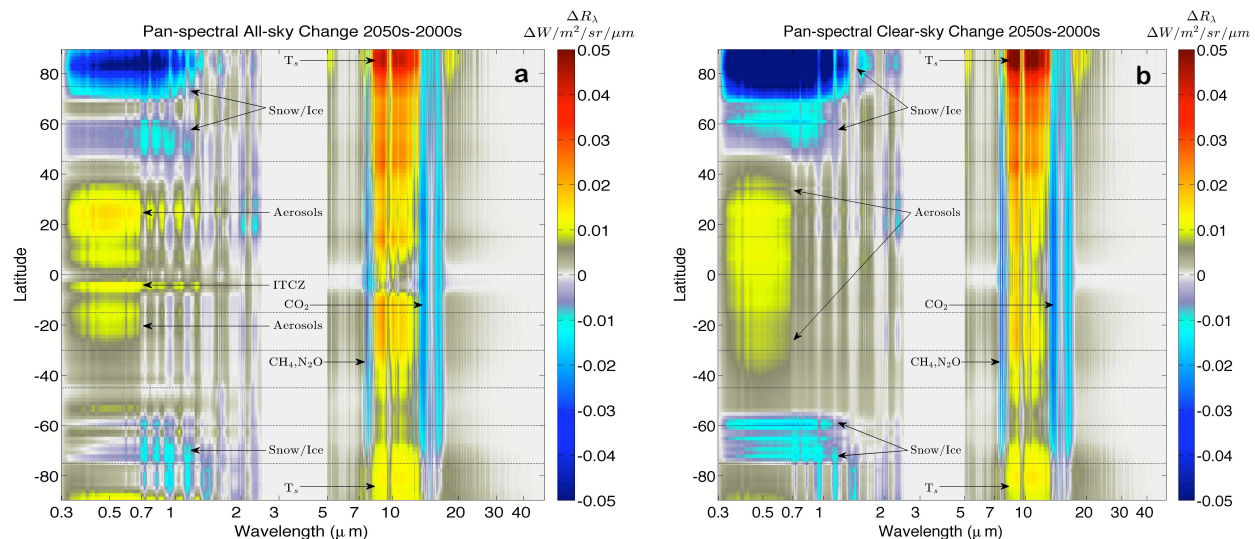
Figure 2.26: (a) DIFFERENCES IN ZONALLY- AND DECADALLY-AVERAGED PAN-SPECTRAL CLEAR-SKY COMPOSITE FOR 2050 – 2059 AND 2000 – 2009 FOR THE A2 SIMULATION. (B) SAME AS (A) BUT PLOTTING DIFFERENCES IN ALL-SKY CONDITIONS BETWEEN THE 2050'S AND THE 2000'S.

The CLARREO climate OSSEs have proven extremely useful in these early results. Next steps are already underway including configuring OSSE's based on different satellite orbits, and combining shortwave reflectance, longwave radiance, and radio occultation simulations, which, as shown in Figure 2.26 [Feldman et al., 2014a], can reveal the spatial and spectral patterns of climate change in the solar and infrared. Another major next step is to evaluate whether there are significant spectral differences between climate models that exhibit low and high sensitivities in the CMIP archives. This will be critical for three reasons: (1) It will establish how long-duration spectral observations can be used to constrain climate model sensitivities, (2) It will help engage with the modeling centers regarding the value of spectra for ultimately reducing uncertainty in climate sensitivity, and (3) It will provide estimates of the scientific value of the decadal length records from existing hyperspectral sounders and of their ongoing operation.

Climate OSSEs combining IR/RO have already shown that the combination of these two observations significantly improves the discrimination of the climate change fingerprints [Huang et al., 2010b; Ringer and Healy 2008; Leroy et al., 2006]. Many more climate observation systems would greatly benefit from climate OSSE's to improve their understanding of the observation requirements, as well as the trade space for prioritization of different observational approaches. Given the severely cost-constrained environment for new climate observations, climate OSSEs represent a critical tool for more effective and more efficient planning of climate observing systems.

2.7 Climate Models Testing and Validation

It is generally understood that, for the purposes of climate prediction, climate models must be able to replicate the past in some ways. The climate system, though, is subject to many influences, ranging from large-scale motion, thermodynamics, and radiation to micro-scale interactions with aerosols, water in its various phases, the biosphere, etc. It is unreasonable to expect that all important processes can be captured prognostically in a climate model. It is also unreasonable for a climate model to replicate all aspects of the past. Nevertheless, it is still necessary to condition models on data so that they can be made more credible for predicting climate change, a capability that is demanded by public and private society. A major driver of CLARREO is that climate models must be able to replicate long-term trends in the climate system should they be made more credible for climate prediction. While this seems to be true on the surface, it has yet to be verified rigorously. Moreover, it is neither clear what might be considered a satisfactory correspondence between model and data nor obvious what types of data should be given priority in the testing of a climate model.

The method for prioritizing data types for testing climate models is a straightforward application of Bayesian theorem: the probability density function of a predictable quantity given specific data (the *posterior*) is directly proportional to the probability density function of the predictable quantity without knowledge of the data (the *prior*) multiplied by the probability that the data that was obtained would have been obtained if the prior prediction were true (the *likelihood* of the data). Practically, an ensemble of climate models is used to form a joint hindcast and prediction probability density function. The marginal probability of the prediction – the probability distribution if you ignore the hindcast – is the prior, and the cut through the joint distribution where the hindcast equals the data, is the posterior. It is only necessary to form the joint hindcast – prediction distribution using an ensemble of climate models that adequately spans all uncertainties in climate. This approach to modifying ensemble prediction using data has been undertaken using existing data many times [Forest et al., 2002; Rowlands et al., 2012; Sexton et al., 2012; Sexton and Murphy 2012]. The priority of a data type is ratio of the widths of the prior (the climate prediction before modification by data) and the posterior (the climate prediction after modification by data). The test of a climate model that is given highest priority is the one that most constrains uncertainty in climate prediction.

Before performing a prioritization, it is first necessary to choose a quantity to predict. A focus of the climate community has been climate sensitivity. Reducing uncertainty in climate sensitivity using existing data, primarily long-term averages of surface air temperature and top-of-atmosphere radiation, has proven extremely difficult, and yet the need to reduce uncertainty in climate prediction persists. Hence, the CLARREO project continues to pursue an understanding of how long-term averages and trends in its prospective data types can be manipulated to improve climate prediction and what the relative priority of those data types might be.

In one study, long-term trends in a variety of data types, both in situ and remotely sensed, were simulated from the output of CMIP3 ensemble of climate models with the intention of modifying the prediction of a 50-yr global average trend in surface air temperature [Huang et al., 2011]. Unsurprisingly, the longer the trend in the simulated data types, the better they were able to reduce uncertainty in predicting the 50-yr temperature trend. Overall,

the remotely-sensed data types (spectral longwave, radio occultation, reflected shortwave) outperformed in situ data types (temperature and height fields). The number of models used to estimate correlations between hindcast and prediction was extremely limited, and no account was taken of the spatial patterns of emerging trends in data. In a follow-up study, the CMIP5 ensemble of climate models was used to simulate CLARREO data types (radio occultation, outgoing longwave, reflected shortwave) over a 35-yr period to predict global average change in surface air temperature over a 90-yr period [Leroy et al., 2014]. While differences in model hindcasts of climate are clearly due to changes in cloud structure, mainly in the tropics, very little correlation was found with 90-yr temperature change even when spatial patterns are considered. Both of these studies are based in a general application of Bayes theorem.

Previous studies in the CLARREO project have focused on the detection of emerging trends in CLARREO data types. Optimal fingerprinting techniques applied to such emerging trends are linked to general Bayesian approaches [Leroy and Anderson 2010]. It is from these studies that stronger links between hindcast and climate prediction will be found in CLARREO data types than have been found in prior studies. The radiance data types of CLARREO have been shown to contain fingerprints of climate's radiative feedbacks, and radio occultation can be used to disentangle ambiguities between longwave temperature and cloud responses. These studies are described in Section 2.7.1. In the future, the CLARREO project will pursue studies in improving climate prediction based on the possibility that its data types can be used to separate the radiative forcing of climate from the radiative response of climate.

2.7.1 Spectral InfraRed and Radio Occultation

The thermal infrared spectrum and radio occultation, both of which are capable of observing atmospheric change with demonstrable accuracy suited to true climate benchmarking [Dykema 2006; Leroy et al., 2006b], offer complementary information that is useful for testing climate models. The thermal infrared spectrum ($200 - 3000$ cm^{-1}), when spectrally resolved at ~ 1 cm^{-1}, is sensitive to temperature from the surface to the stratopause, to water vapor from the surface to the tropopause, to stratospheric ozone, to the well-mixed greenhouse gases carbon dioxide, nitrous oxide and various halocarbons, and to clouds and aerosol everywhere. Radio occultation, which measures the atmosphere's refractive properties at 1575.42 MHz in the microwave, is sensitive to temperature and pressure from the surface to the mid-stratosphere, to water vapor from the surface through the mid-troposphere, and to free electrons wherever they exist. Unlike the thermal infrared, radio occultation can be considered insensitive to clouds and aerosol. Sensitivity, however, does not imply diagnostic – two potential causes of a fluctuation in an observed quantity may not be distinguishable from the data alone. Both the infrared spectrum and microwave refractivity, despite their sensitivities, contain ambiguities that confound simple attribution to specific causes. When considered together, however, many of the ambiguities can be resolved. In the lead-up to the prescription of the CLARREO mission, and since the establishment of its Science Definition Team, detecting climate signals in radio occultation and in the thermal infrared spectrum has been explored, as has attributing emerging signals in each to specific causes. In addition, the utility of each to inform multi-decadal climate prediction has been investigated. These activities are detailed below.

A. Radio Occultation

Radio occultation is a technique of atmospheric measurement wherein the bending of microwave signals is measured from shifts of the frequency of the carrier signal induced by the bending. The satellites of the Global Navigation Satellite Systems (GNSSs) serve as transmitters of opportunity, the best known of which is the Global Positioning System (GPS). Details of the technique are provided elsewhere [Kursinski et al., 1997, 2000; Hajj et al., 2002]. In short, gradients in the microwave index of refraction bend rays as they transect the atmosphere in limb-sounding geometry, the microwave index of refraction n is related to microwave refractivity N through $N = (n - 1) \times 10^6$, and the refractivity is related to the atmosphere through

$$N \cong c_1 \frac{p}{T} + c_2 \frac{p_w}{T^2} - c_3 \frac{n_e}{\nu^2} \,. \tag{2.8}$$

The variables p, T, p_w, n_e, and ν are atmospheric pressure, temperature, water vapor partial pressure, electron number density, and frequency of the microwave carrier signal; the constants c_1, c_2, and c_3 are 77.6 K hPa^{-1}, 3.73×10^5 K^2 hPa^{-1}, and 4.03×10^7 m^3 Hz^2. The third term, due to electron number density primarily in the ionosphere, is removed in ionospheric calibration using a second carrier signal of GPS at 1227.60 MHz. Thus, the ionospheric-calibrated refractivity can be considered sensitive solely to atmospheric thermodynamic variables and water vapor density. In radio occultation, Doppler shifts and bending angles are measured and a function of time, and retrieval generates microwave refractivity as a function of geopotential height, the natural independent coordinate of radio occultation inversion [Leroy 1997].

A climate observational system simulation experiment for radio occultation revealed that the earliest detectable signal in radio occultation corresponds with poleward migration of the baroclinic zones of the atmosphere, including the subtropical and mid-latitude jets [Leroy et al. 2006a]. In this study, the radio occultation quantity "dry pressure" was simulated from output temperature and humidity of CMIP3 models. Dry pressure p_N is the integral of refractivity in geopotential height h multiplied by a constant:

$$p_N(h) = (0.440 \, hPa \, km^{-1}) \int_h^\infty N(h')dh' \,. \tag{2.9}$$

When there is no water vapor in the atmosphere it is the same as kinetic pressure; otherwise it can be thought of as kinetic pressure with column water vapor above height h added. Future trends in zonal-average, and annual average log-dry pressure were simulated from a CMIP3 future scenario run, and natural variability in the same quantity was simulated from several present day control runs (Figure 2.27). Optimal detection revealed that the most detectable signal should be log-pressure/geopotential height in northern and southern mid-latitudes. The result is model independent. While optimal detection studies such as this are useful for pointing toward where to look for the first emergence of a global warming signal, they do not offer any direct information on how a detected climate signal can improve climate prediction. Succeeding work has shown that a climate signal has emerged in available radio occultation data [Steiner et al., 2009].

B. Spectral Thermal InfraRed

Trends in outgoing longwave radiation are expected from radiative forcing by well-mixed greenhouse gases and from the climates response to that forcing. For this reason, manipulation
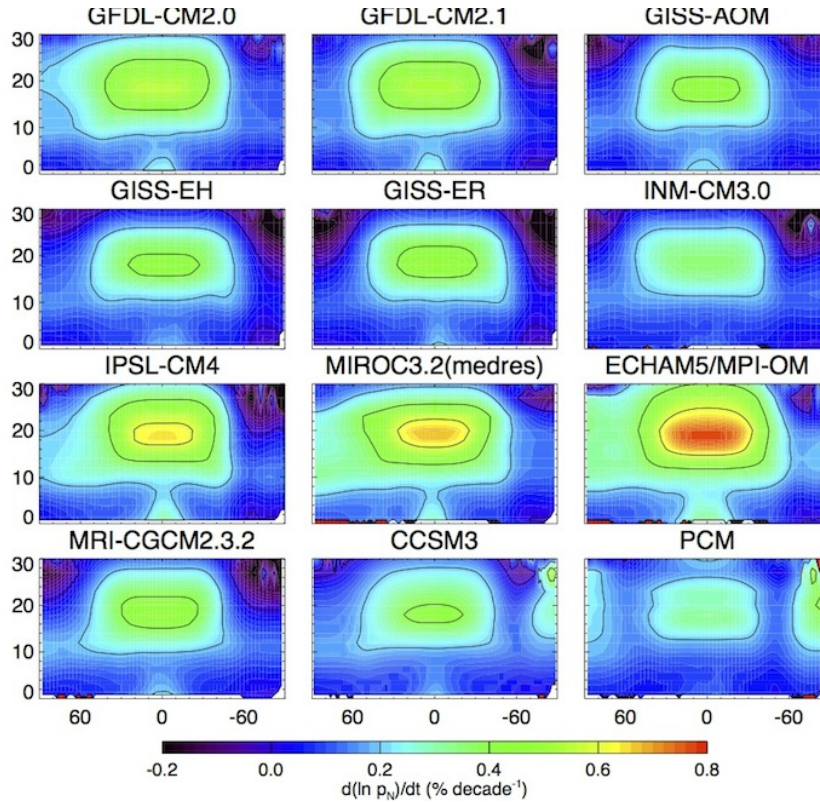
Figure 2.27: FINGERPRINTS OF GLOBAL WARMING IN ZONAL AVERAGE LOG-DRY PRESSURE FOR TWELVE CMIP3 MODELS SUBJECT TO SRESA1B FUTURE FORCING. THE ORDINATE IS GEOPOTENTIAL HEIGHT IN KM, AND THE ABSCISSA IS LATITUDE FROM NORTH TO SOUTH. TAKEN FROM [LEROY ET AL., 2006B].

of the thermal infrared spectrum can be expected to yield great dividends in informing climate prediction through partial constraint on climate sensitivity. In a series of papers on the topic, the CLARREO SDT has shown how trends in the thermal infrared spectrum can be interpreted according to climate's radiative forcings and feedbacks.

In the absence of clouds and aerosols, the radiative forcing by carbon dioxide, the radiative response of the stratosphere, and the lapse rate and longwave feedbacks have been shown to have distinctive spectral signatures in the tropics, where the upper air radiative feedbacks are most important [Leroy et al. 2008b]. The calculation of the spectral fingerprints was accomplished by partial radiative perturbation (PRP) based on monthly average atmospheric variables by the climate models. Already apparent are similarities in the spectral fingerprints of tropospheric temperature and tropospheric humidity. Both are expected to show substantial inter-annual variability; however, the stratospheric temperature response and the radiative forcing by carbon dioxide and other well-mixed greenhouse gases by extension should be easily detected with a decade of data.

Follow-up work included clouds in the calculation. The climate model intercomparison projects have not systematically generated cloud variables necessary to the simulation of outgoing infrared spectra, and so initial studies turned to the Cloud Feedback Model Inter-comparison Project for model output instead [Huang et al. 2010a]. Spectral fingerprints for all of the longwave radiative feedbacks and other signatures were produced at all locations on the globe. The method again was partial radiative perturbation; however, the spectral fingerprints were pro-

duced from a scenario in which carbon dioxide concentrations were abruptly doubled. When clouds are included in the calculation, ambiguities in the spectral fingerprints become significantly more pronounced. Of particular concern are ambiguities between lower tropospheric clouds (stratocumulus) and surface temperature; between upper tropospheric clouds, temperature and humidity. The latter ambiguity is pronounced about the inter-tropical convergence zone (ITCZ) because of the generation and presence of cirrus.
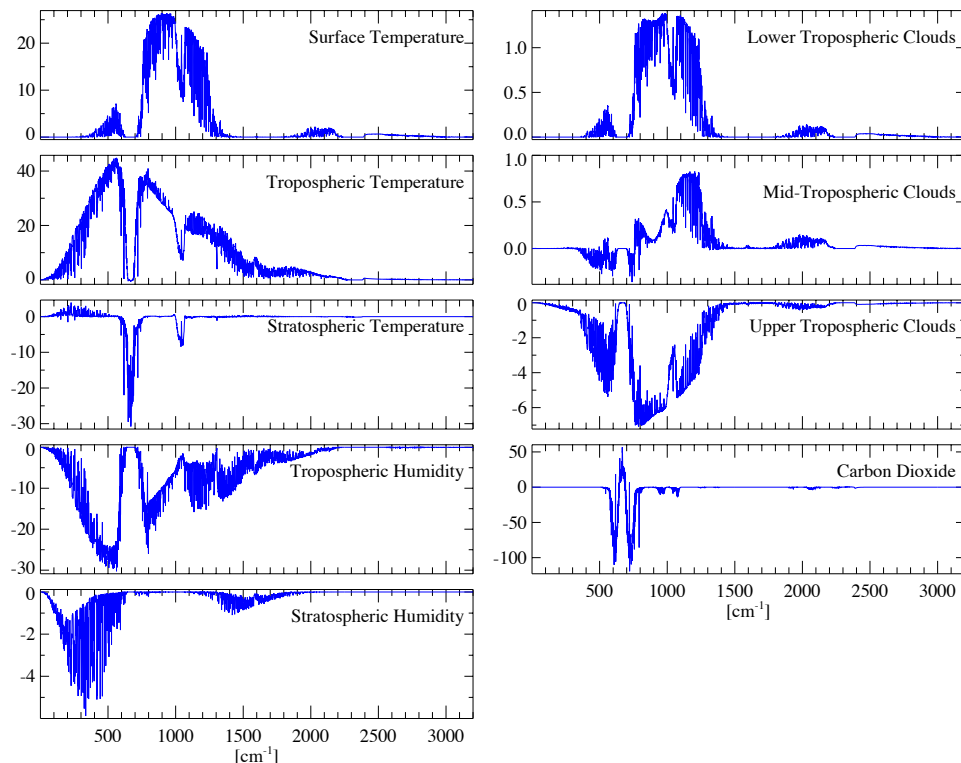
Figure 2.28: THERMAL INFRARED FINGERPRINTS FOR COMMON RADIATIVE FORCINGS, FEEDBACKS, AND RESPONSES. EACH IS THE PREDICTED GLOBAL AVERAGE, STEADY-STATE RESPONSE IN RADIANCE (10^{-8} W CM^{-2} (CM^{-1}) SR^{-1}) AFTER A DOUBLING OF CARBON DIOXIDE OF THE CCMA AGCM 4.0 CLIMATE MODEL. TAKEN FROM COMPUTATIONS PERFORMED IN [HUANG ET AL., 2010B].

Disambiguation of the spectral signals is possible with radio occultation, because radio occultation is insensitive to clouds, which are generally responsible for the spectral response ambiguities in thermal infrared spectra alone. Another study examined the attribution of spectral signals to specific causes when spectral infrared data is considered conjointly with radio occultation data [Huang et al. 2010b]. In addition to spectral fingerprints computed by partial radiative perturbation as taken from Huang et al. 2010a, the same perturbation was applied to profiles of log-dry pressure in geopotential height from 2 through 27 km. Because radio occultation is insensitive to clouds, surface temperature, and carbon dioxide, no radio occultation fingerprints exist for the radiative forcing by well-mixed greenhouse gases, surface temperature response, and cloud feedback. The radio occultation fingerprints that do exist, however, are distinctive and can be used to unambiguously determine long-term tropospheric temperature change (lapse rate feedback), lower tropospheric humidity change (lower tropospheric water vapor feedback), and stratospheric temperature response. In concept, with those responses determined from radio occultation data alone, their signals can be removed

from spectral infrared trends and the upper air cloud feedbacks determined. The ambiguity between surface temperature response and stratocumulus response, though, remains.
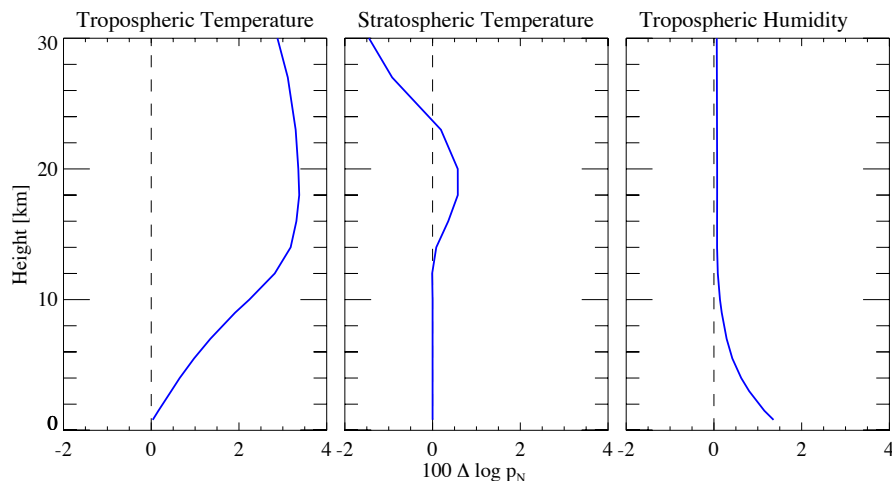
Figure 2.29: THE FINGERPRINTS OF FEEDBACKS IN RADIO OCCULTATION LOG-DRY PRESSURE. SAME AS IN FIGURE 2.28 BUT FOR THE RADIO OCCULTATION QUANTITY LOG-DRY PRESSURE MULTIPLIED BY 100. THE INDEPENDENT COORDINATE IS GEOPOTENTIAL HEIGHT ON THE ORDINATE. ONLY TROPOSPHERIC TEMPERATURE, STRATOSPHERIC TEMPERATURE, AND TROPOSPHERIC HUMIDITY HAVE NON-ZERO FINGERPRINTS IN RADIO OCCULTATION DATA, WHICH ARE INSENSITIVE TO CLOUDS. TAKEN FROM [HUANG ET AL., 2010B].

Figure 2.28 shows the spectral fingerprints of nine signals expected to emerge with global warming. For the sake of presentation, they show only the global average fingerprints. Figure 2.29 shows the fingerprints in radio occultation log-dry pressure for the tropospheric temperature signal, which corresponds to the lapse rate feedback, the stratospheric temperature signal, and the tropospheric humidity signal, which corresponds strongly to the lower tropospheric humidity-longwave feedback. In the radio occultation data it should be simple to distinguish the fingerprints inasmuch as they are unambiguous in vertical pattern.

2.7.2 Hyperspectral Reflectance

The CLARREO Science Definition Team has demonstrated the immense value of the multitude of information in direct measurements of hyperspectral reflected solar radiance and reflectance for characterizing the variability of the Earth's climate system (see Section 2.4). The high information content in these measurements can serve another valuable purpose: rigorous validation of climate model output. Climate model process parameterizations are validated and improved with process-specific studies and field campaigns. However, climate models are designed to predict changes in Earth's climate on decadal scales and therefore need to be evaluated on those scales. CLARREO-like systems that have high accuracy and the ability to monitor that accuracy on-orbit are ideal for validating climate models on these scales. The SDT has therefore been developing techniques for using direct measurements of hyperspectral reflectance to evaluate climate model performance.

One direct method for comparing the information in two data sets is to use the annual, multi-year, or decadal averages of spectral reflectance. If there is a sufficiently long data record, the spectral trends could also be used to understand the differences between two data sets.
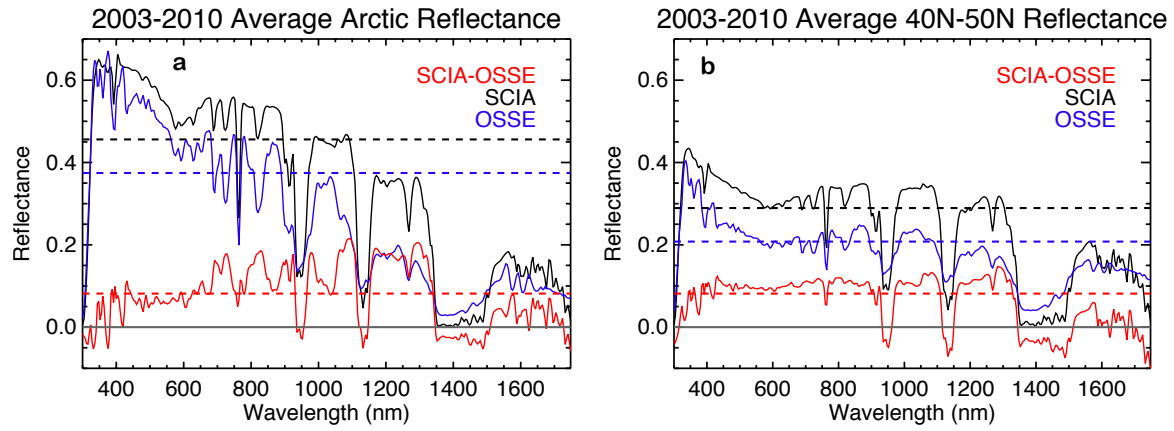
Figure 2.30: EIGHT-YEAR SCIAMACHY (BLACK) AND OSSE (BLUE) AVERAGES FOR THE ARCTIC OCEAN (A) AND THE MIDLATITUDES (B). HYPERSPECTRAL AVERAGES (SOLID) AND BROADBAND AVERAGES (DOTTED) SHOW THE COMPLEXITY IN THE HYPERSPECTRAL DATA. THE BROADBAND DIFFERENCES BETWEEN THE SCIAMACHY AND OSSE DATA (RED) ARE NEARLY THE SAME FOR THE TWO LOCATIONS, BUT THE HYPERSPECTRAL DIFFERENCES SHOW THAT THE PHYSICAL PROCESSES CONTRIBUTING TO THOSE DIFFERENCES ARE NOT THE SAME BETWEEN THE TWO LOCATIONS.

Because we currently have access to only eight years of data, we compared the eight-year averages of SCIAMACHY-measured and OSSE-simulated hyperspectral reflectance (Figures 2.30a and 2.30b).

To illustrate the value of using hyperspectral reflectance rather than broadband reflectance for climate model evaluation and attribution of the differences between two data sets, this comparison includes the broadband and hyperspectral differences between the data sets for two regions: the Arctic Ocean and the midlatitudes between 40°N and 50°N. The broadband difference between the SCIAMACHY and OSSE data in the Arctic is 0.082, and the broadband difference in the midlatitude case is 0.081. Although the broadband differences are nearly identical, the hyperspectral averages and differences illuminate some physical differences between the observed and simulated data sets that are different between the two regions. For example, the high visible reflectance in the visible is indicative of the highly reflective sea ice that is present over the Arctic Ocean region in the winter and spring; however, there is not such high visible reflectance in the midlatitude eight-year averages.

Multivariate analysis can also be used to quantify the differences between two hyperspectral data sets. The principal components explaining the majority of the variance in a data set characterizes the variability of multivariate data, which can be used as an objective and quantitative measure of the similarity between two data sets (e.g. observed and simulated hyperspectral reflectance). The intersection between the two subspaces formed by a subset of principal components can be used to estimate how many dimensions two data sets share and can be used as a transformation between them. The spectral decomposition of the intersection between two subspaces can be used to quantify their similarity [Crone and Crosby, 1995; Krzanowski, 1979; Roberts et al., 2013]. *Subspace distance*, the metric used as a measure of similarity, has been employed in other fields, such as face recognition science, but prior to the studies conducted in [Roberts et al., 2013] by the CLARREO science team, it had not been used to quantify the similarity between two multivariate remote sensing data sets.
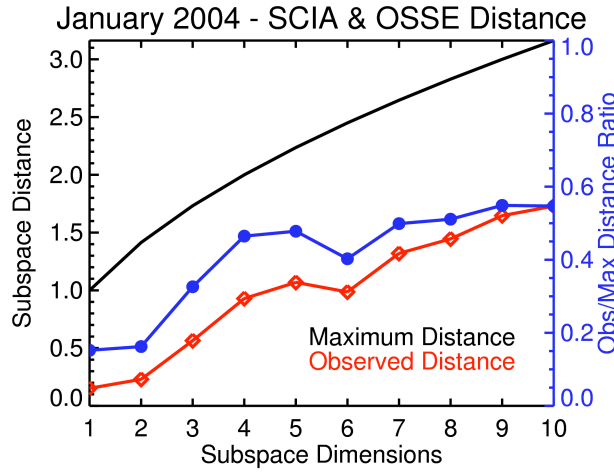
Figure 2.31: The subspace distances between the SCIAMACHY and OSSE reflectance subspaces for ten subspaces (red) compared to the maximum possible distance between the two subspaces (black). The blue line shows the observed subspace distances relative to the maximum possible distance for each number of subspace dimensions, that is, the ratio of the values on the red line to the values on the black line.

Our team employed a statistical significance test based on [Crone and Crosby, 1995] to quantify how well simulated CLARREO reflectance spectra [Feldman et al., 2011] reproduced the variability in SCIAMACHY-observed spectra at the beginning of the 21st century at the 95% confidence level [Roberts et al., 2013] (e.g. Figure 2.31). These quantitative, objective comparisons concluded that in four months during 2004 the SCIAMACHY and OSSE data sets agreed over seven or eight transformed Principal Component (PC) dimensions, which together explained over 99% of the variance in each data set. This was the first time the subspace intersection and distance has been applied to evaluate model output relative to observations. This technique can also be applied to compare other types of multivariate data in the atmospheric sciences and other fields. This work contributed to the CLARREO project by quantifying the comparison of spectral variability in the CLARREO-simulated (OSSE) reflectance spectra to SCIAMACHY reflectance measurements.

The intersection was also used to compare the temporal variability of the OSSE reflectance to that observed by SCIAMACHY during the first decade of the 21st century. The intersection method presented in [Roberts et al., 2013] was used to directly compare the temporal variability within SCIAMACHY measurements and OSSE simulations during the same time period. To evaluate how well the OSSE-simulated reflectance spectra reproduced the temporal variability in the observed spectra, [Roberts et al., 2014] calculated the intersection between the two data sets in the 0° – 30°S (SH Tropical) zonal band. The first two transformed PCs (TPCs) had correlations above 0.99. For these two transformed dimensions, the OSSE and SCIAMACHY land time series overlap (Figure 2.32a), but the OSSE ocean time series exhibits phase differences relative to the SCIAMACHY ocean time series (Figure 2.32b). Further investigation is needed to determine what is causing the differences between these time series, but it demonstrates that the OSSE may not be simulating the ocean-atmosphere temporal variability accurately in the SH Tropics. The variables dominating the top-of-atmosphere spectral variability over ocean are primarily clouds. Clouds likely have a smaller dominating

impact over land, where, in many locations, the surface is much brighter than the ocean, at least in parts of the spectrum (e.g. vegetation has high reflectance in the near infrared, but low reflectance comparable to ocean reflectance in the visible). It is challenging for climate models to accurately simulate clouds, and a dominant reason for the spread in climate sensitivity calculated by climate models is the spread in cloud feedback [IPCC, 2007b].
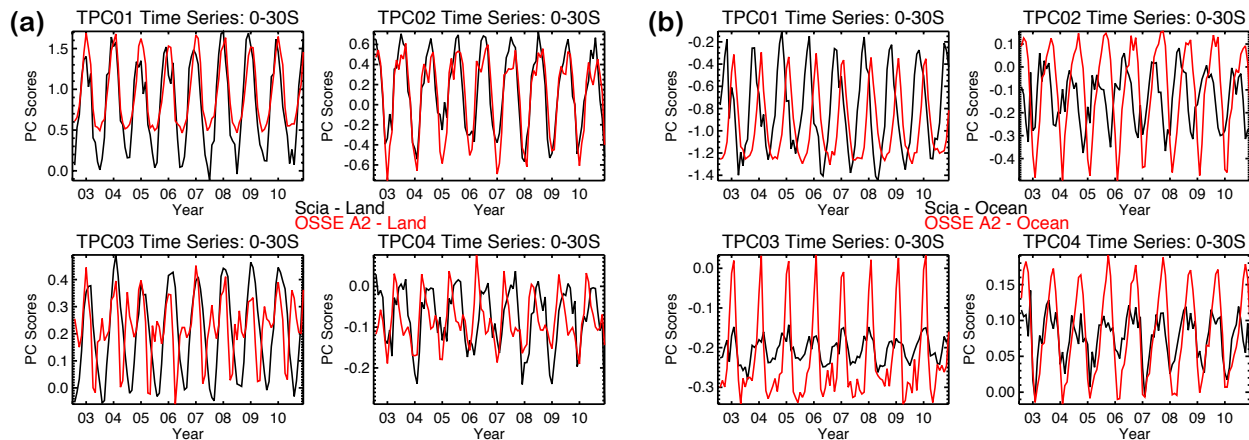
Figure 2.32: The transformed principal components (TPCs) land (a) and ocean (b) scores time series corresponding to the $0° - 30°$S SCIAMACHY and OSSE A2 TPCs. The first two land time series pairs are comparable except for minima and maxima amplitude differences. The SCIAMACHY and OSSE land TPC3 and TPC4 scores time series have differences in their seasonal variability. The TPC ocean time series show the $90°$ phase difference between the OSSE and SCIAMACHY SH tropical ocean scores time series observed also observed in the original principal components.

The subspace intersection used to align the spectral variability between two data sets and directly compare their corresponding temporal variability (e.g. Figure 2.32) can also be used for attribution. This spectral matching technique can be performed between two data sets, but it is ideal to have a database of hyperspectral reflectance spectra generated for a variety of scene types (e.g. varying amounts of absorbing gases, a range of solar zenith angles, and a variety of cloud types, etc). This spectral matching method would provide a direct link between observed spectral shapes in the SCIAMACHY measurements and the geophysical variables used as input to the radiative transfer model used to generate the database spectra. This efficient, linear spectral matching routine can be used to relate two data sets to one another, or to identify the physical variables represented by the variance-dominating spectral variables in a hyperspectral data set using a standard database.

One objective in climate model validation relative to hyperspectral observations is attribution of the difference between OSSE radiometric output and data to specific parameters in the model (e.g. cloud fraction, thickness, phase, height, etc.). Leroy et al., 2008b developed a spectral fingerprinting optimal detection technique to evaluate climate model output using direct measurements of hyperspectral infrared spectra. A *spectral fingerprint* is a signature that shows the spectral response to a change in a geophysical climate variable, such as water vapor, cloud amount, or the albedo of different surface types. Such spectral fingerprints were first calculated for the reflected shortwave portion of the spectrum by [Jin et al., 2011]. Spectral fingerprinting can also be used to attribute physical variables that contribute to

changes seen in the spectral shortwave signal.

An alternative method to radiative kernel spectral fingerprinting and traditional retrievals is the *randomForest* method. The *randomForest* technique is a machine learning algorithm which has been powerful in capturing non-linear dependencies in a wide-variety of problems [Breiman, 2001]. The *randomForest* method was successfully used by [Tett et al.,, 2013] to predict climate sensitivity. Future research in this area should investigate the possibility of using *randomForest* classification to build a hyperspectral *scene classifier* to obtain physical climate parameters from the information of measured and modeled hyperspectral reflectance.

2.8 In-orbit Reference Calibration Standard

In addition to the major advances in metrology over the last 20 years [Brown et al., 2006; Fox et al. 2011; Dykema and Anderson, 2006], there have been major advances in methodologies and techniques to inter-calibrate satellite sensors in-orbit. The critical need for sensor inter-calibration for research and applications in weather, climate, and natural resources, has led to an international effort called the Global Space-Based Inter-Calibration System (GSICS) [Goldberg et al., 2011]. The major limitation of these activities is lack of high accuracy reference radiometers to anchor the GSICS system. Inter-calibrating two instruments in-orbit is useful, but does not provide decadal change accuracy unless at least one of the radiometers can provide a reference with traceability in-orbit to international standards at climate change accuracy [Goldberg et al., 2011]. A second major challenge is that the reflected solar instruments all have very different spectral response functions (e.g. GOES, MODIS, AVHRR, CERES, GERB, Landsat). This means that the accuracy of even relative inter-calibration is typically limited to a few percent, as each instrument views a different part of the reflected spectrum. Unfortunately, this level of uncertainty is a factor of 10 worse than the $0.3\%(k = 2)$ accuracy requirement for reflected solar climate change observations discussed in Section 2.2. A third limitation is the inability to resolve issues with varying polarization sensitivity of reflected solar imagers like MODIS or VIIRS, especially since this sensitivity varies with instrument scan angle (i.e. scanning mirror angle) and therefore makes the usual use of Simultaneous Nadir Overpasses (SNO's) an incomplete inter-calibration approach. Unfortunately, the limits of orbit geometry, when combined with a fixed cross-track scan typical of satellite instruments, limits the ability to match time, space, and angle to nadir views only, so that the SNO approach is the current state-of-the-art capability for most instruments. The CERES instrument, having the ability to rotate the instrument in both azimuth and elevation directions (a bi-axial scan), demonstrated that angle, time, and space matched observations were possible for a wide range of conditions during satellite orbit crossings [Haeffelin et al., 2001; Clerbaux et al., 2009].

2.8.1 CLARREO Reflected Solar In-orbit Standard

Figure 2.33 shows an example of the CLARREO satellite orbit track (609 km altitude and 90° orbit inclination) crossing under the S-NPP or JPSS-1 satellite orbit track (827 km altitude, 13:30LT sun-syncronous orbit with 98.7° orbit inclination). The Figure also shows the ability to match elevation and azimuth directions across the cross-track scans of CERES, VIIRS,
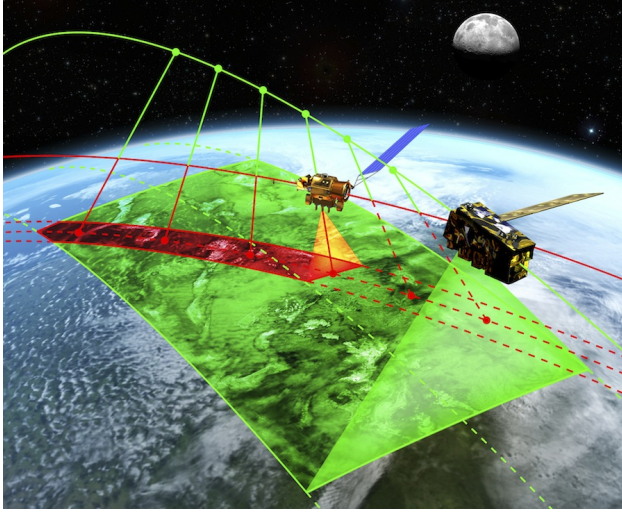
Figure 2.33: As the CLARREO orbit, at 609 km altitude (red), crosses that of a satellite such as Suomi NPP (green) with an operational sensor (e.g CERES, VIIRS), the CLARREO reflected solar spectrometer collects data matched in time, space, and view angles to provide a reference inter-calibration standard for the target sensors. To match viewing angles with the target instrument, and to maximize the inter-calibration sampling, the CLARREO reflected solar spectrometer has 2-dimensional pointing ability (roll over azimuth gimbal).

or CrIS. This is accomplished by setting the azimuth angle of the CLARREO instrument to match the NPP scan plane and then using the gimbal to slowly rotate the CLARREO RS spectrometer to match viewing zenith angles across the entire scan during the orbit crossing. The azimuth angle for this match varies from orbit crossing to orbit crossing, but is essentially constant for any single orbit crossing [Roithmayr and Speth, 2012].

A. Inter-calibration Sampling

The time available for the matching scan is directly proportional to the orbit altitude separation of the two spacecraft. If they are at the same altitude there are only a few seconds to obtain the entire scan swath, but several minutes are available for an orbit separation of 100 km or more [Roithmayr and Speth, 2012]. This difference is what leads to the CLARREO design orbit altitude of ∼609 km. The orbit is sufficiently high to minimize fuel use for orbit control, sufficiently low to minimize the launch vehicle requirement for mass to orbit, and well below the typical polar orbiter altitudes of ∼825 km (S-NPP, JPSS, METOP) to increase the matched scan angle inter-calibration time. Thus, the orbit selection and gimbal azimuth/elevation pointing capability will allow CLARREO to increase reference inter-calibration sampling by more than a factor of 100 compared to current GSICS capabilities, where typical SNOs restrict polar orbiting satellites to the polar regions and geostationary satellites to the equator.

Using existing data from SCIAMACHY, MODIS, CERES, and PARASOL, the CLARREO science team performed comprehensive simulations to derive requirements for inter-calibration sampling [Roithmayr, 2014b]. The CLARREO inter-calibration goal is to limit the statistical uncertainty contribution from data matching over a climate auto-correlation time period of 0.8 years, 0.3% ($k = 2$). Results of the estimated required sampling are summarized in Table 2.2 for inter-calibration of CERES and VIIRS sensors.

The most severe requirements are for the reflected solar inter-calibration, caused by the larger spatial and angular variability of reflected solar radiation. A study using AVHRR orbit crossings [Wielicki et al., 2008] showed that space/time/angle matching noise could be reduced to 1% relative for reflected solar inter-calibration if time simultaneity is 5 minutes or less, angle matching in viewing zenith and azimuth angles are within 1° or less, and spatial averaging areas are matched to within 5% of their diameter.

Sensor	Parameter	Time Scale	Variable	Error %($k = 2$)	N
CERES	Offset	monthly	scan angle	0.9	2.5×10^3
	Gain	monthly	scan angle	0.9	2.5×10^3
	Degradation of optics	seasonally	scene type	0.5	30×10^3
	Non-linearity	annually	all data	0.3	150×10^3
VIIRS	Baseline offset	monthly	P, scan angle	0.9	7.0×10^3
	Baseline gain	monthly	P, scan angle	0.9	7.0×10^3
	Sensitivity to polarization	seasonally	P, scan angle, χ	0.5	1.2×10^6
	Non-linearity	annually	P, scan angle	0.3	0.5×10^6

Table 2.2: Summary of high-priority inter-calibration tasks. Degree of linear polarization is denoted as P and angle of polarization as χ. Uncertainty contribution from inter-calibration data matching in % ($k = 2$) for corresponding time period and required inter-calibration sample number N.
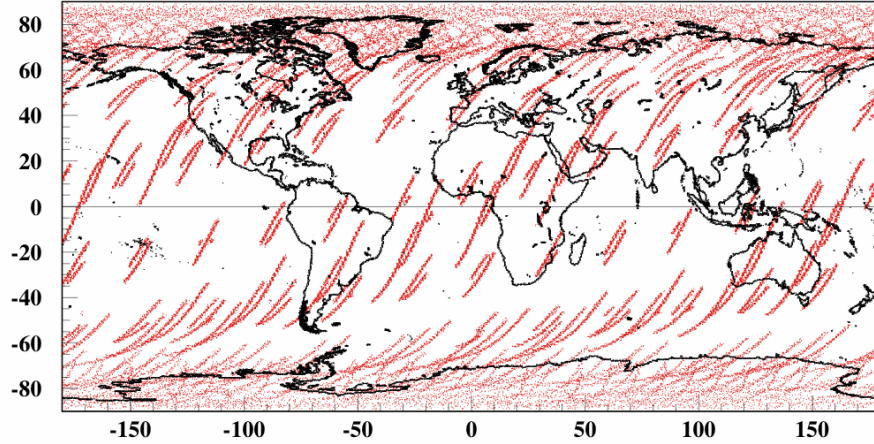
Figure 2.34: CLARREO RS BORESIGHT LOCATIONS MATCHING JPSS CROSS-TRACK DATA OVER A ONE YEAR TIME PERIOD. CLARREO OBSERVATORY IS IN 90° INCLINATION POLAR ORBIT WITH RAAN = 0°.

Orbital simulations of CLARREO orbit crossings, and instrument simulations of space, time and angle matching of the CLARREO RS spectrometer with cross-track scanning instruments like VIIRS and CERES, were then carried out to verify sufficient sampling and scene diversity [Roithmayr, 2014b]. The sampling requirements include the ability to verify offset (i.e. zero level), gain, nonlinearity (calibrate at different levels of dynamic range from dark to bright targets), and scan angle dependent polarization dependence (Table 2.2). Geo-location and distributions of inter-calibration opportunities for CLARREO inter-calibrating cross-track instruments on JPSS satellite over a one year time period are shown in Figure 2.34.

Since the CLARREO spectrometer has a FOV size of 0.5 km, the observations are spatially averaged. In estimating inter-calibration sampling with CERES, we took into account the size of CERES Point Spread Function at 2.6° in the along-track direction, and a data acquisition rate of 330 measurements in each 180° cross-track scan performed over 3.3 seconds [Wielicki et al., 1996]. In estimating inter-calibration sampling with VIIRS, we considered the area
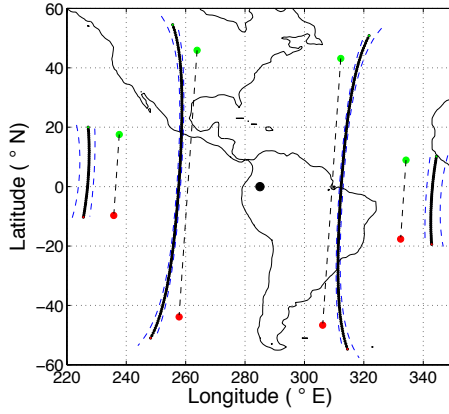
Figure 2.35: CLARREO AND GEO-BASED IMAGER MATCHED DATA FOR ONE DAY: CLARREO BORESIGHT GROUND TRACKS (SOLID BLACK CURVES) AND SWATH EDGES (DASHED BLUE LINES). SOLID BLACK CIRCLE INDICATES GEO SUB-SATELLITE POINT, AND BLACK DASHED LINES SHOW CLARREO GROUND TRACK DURING AN INTER-CALIBRATION EVENT. MULTIPLE INTER-CALIBRATION OPPORTUNITIES DAILY PROVIDE FLEXIBILITY IN CLARREO OPERATIONS.

included within 1° of elevation angle (10×10 km^2 at nadir) as a single inter-calibration sample. To estimate the total number of inter-calibration samples with independent spatial matching noise, we counted all possible samples in the matched data, shifting them in both directions (along and perpendicular to the ground track) for 0.1° (1 km at nadir). With the CLARREO RSS spatial sampling of 0.5×0.5 km^2 (nadir), such a shift ensures that only two boundary pixels are common for consequential samples.

The estimated achievable inter-calibration sampling for CLARREO RSS in a polar 90° inclination orbit meets the mission objectives and is sufficient to inter-calibrate CERES and VIIRS instruments monthly and seasonally, with the uncertainty required for measuring long-term climate change. Over a climate auto-correlation time period of 0.8 years, the statistical uncertainty contribution from data matching can be contained within 0.3% ($k = 2$). In the case of CERES monthly inter-calibration, the predicted sampling is below the required number for only one month out of the year.

Simulation and sampling estimates for inter-calibration imagers on a GEO satellite have been performed by Roithmayr et al., 2014b. Analysis has been performed for a GEO spacecraft stationed at a longitude of 75°W (GOES-East). During a typical day, CLARREO has four inter-calibration opportunities, as shown in Figure 2.35. Multiple inter-calibration events daily provide flexibility in CLARREO operations and guarantee plentiful sampling.

The International Space Station (ISS) is ideally suited to serve as a platform from which to obtain reflected solar radiance measurements that can be used to inter-calibrate instruments in sun-synchronous low Earth orbits (see Section 5.4 for the ISS mission concept). The ISS orbit provides coverage of a large part of the globe, which extends from 52.18° South to 52.18° North latitude. All scene types necessary for inter-calibration, including clouds, snow, clear-sky ocean, desert, and vegetation, can be found within the area of coverage. Results of orbital simulations show that the difference in ISS and sun-synchronous orbit plane precession leads to temporal uniformity in opportunities for inter-calibration [Roithmayr et al., 2014a]. Angular speed and angular acceleration required from a two-degree-of-freedom instrument gimbal for matching line of sight on ISS compares favorably to what is required for a dedicated CLARREO mission. Our estimates show that the numbers of samples that can be obtained from ISS are sufficient to inter-calibrate well-behaved sensors in sun-synchronous low Earth and geostationary orbits to the accuracy required for measuring long-term climate change.

In conclusion – A unique feature of the CLARREO RSS approach is an on-orbit 2-dimensional pointing ability; this allows planning and executing inter-calibration operations, and maximizing (optimizing) the amount of matched inter-calibration data for a given target sensor. CLARREO will collect inter-calibration sampling with CERES and VIIRS on JPSS satellites, AVHRR and follow-on imagers on MetOp, and imagers on geostationary platforms. We conclude that estimated inter-calibration sampling will limit the uncertainty contribution from data matching noise to 0.3% ($k = 2$) over the climate auto-correlation time period. The orbital modeling and inter-calibration event prediction developed here will serve as a framework for future mission operations.

B. Inter-calibration of Sensor Sensitivity to Polarization

Depending on the design of the optics for a spaceborne sensor, its measurements can be sensitive to the polarization of incoming light and have varying response as a function of the polarization state. Typical values of imager sensitivity to polarization are a factor of 2% to 5% depending on the spectral band, increasing for bands in the blue wavelength range [Sun and Xiong, 2007]. For the purpose of the CLARREO inter-calibration study reported in [Lukashin et al., 2013], we denote the imager reflectance factor as ρ^{imager}, and consider it without solar zenith factor. We introduce a sensitivity to polarization term to sensor calibration models in a way consistent with the definition by Sun and Xiong, 2007:

$$\rho^{imager} = \frac{\rho_0}{(1 + mP)} \tag{2.10}$$

where ρ^{imager} is the derived reflectance including correction sensitivity to polarization, ρ_0 is the reflectance factor corresponding to the imager calibration model for non-polarized light, P is the linear degree of polarization of reflected light at TOA, and m is the sensitivity to the polarization coefficient. The sensitivity to the polarization term is similar to the term for the correction of environment temperature. Both terms correct sensor effective gain. Generally, sensitivity to polarization is a function of sensor scan and polarization angles, $m(\theta, \chi)$. But in our case, Equation 2.10 is defined for fixed sensor scan and polarization angles. The advantage in this approach will be shown below in the clear error propagation analysis. For definition of the degree of linear polarization, P, and polarization angle, χ, see Appendix C.

Inter-calibration on orbit is achieved by comparison of the sensor measurement to observations by CLARREO that are coincident in time, space, and angle of view, as described above, and considered to be the reference or true observations. Generally, the inter-calibration process is iterative and consists of adjusting the calibration model of the target imager to minimize the differences with CLARREO. This process would most likely be a joint activity of both the inter-calibrated imager and CLARREO calibration teams. The reference inter-calibration process would start by determining the sensor calibration for the case of unpolarized scattered light (e.g. $P < 0.05$). The second step would be to attribute the differences caused by polarization (e.g. P range from 0.4 to 0.6) to a specific term in the calibration models, such as the inverse term *(1 + mP)* in Equation 2.10. The value of degree of polarization, P, is obtained by applying the Polarization Distribution Models (PDMs) as functions of viewed scene type and geometry. The concept and development of empirical and theoretical PDMs are described in Appendix C.

Because of the physical nature of polarization in an optical system and its linear response, it is reasonable to assume that inter-calibration offsets A_0 or A_p will be very similar, and that

the polarization effect will be contained in the difference of inter-calibration gains, G_0 or G_p. Obtaining inter-calibration gain for non-polarized and polarized cases, and attributing the difference to the polarization effect, then imager sensitivity to polarization and its relative uncertainty can be written as

$$m = \frac{(G_p - G_0)}{P} = \frac{\Delta G}{P} \; ; \qquad \frac{\sigma_m}{m} = \sqrt{\left(\frac{\sigma_{\Delta g}}{\Delta G}\right)^2 + \left(\frac{\sigma_p}{P}\right)^2} \qquad (2.11)$$

The first term, $\sigma_{\Delta g}/\Delta G$, is random relative error of inter-calibrated gain difference, dependent on inter-calibration sampling. The second term, σ_p/P, is the relative uncertainty of the degree of linear polarization, which we obtain by applying the PDMs (see Appendix C). It is important to emphasize that σ_p is the accuracy of P averaged over a large ensemble of inter-calibration samples, and not the instantaneous error of the PDMs.

After reference inter-calibration of the imager with CLARREO is performed, and the imager calibration model is tuned to minimize its difference with CLARREO observations, the PDMs are still required to provide polarization information for the imager's stand-alone operations. Sensitivity to polarization and its uncertainty are obtained from inter-calibration results (Equation 2.11). Imager reflectance is expressed by Equation 2.10, where m is the established sensor sensitivity to polarization and ρ_0 is the reflectance obtained from the baseline calibration model adjusted to CLARREO reference. We have demonstrated that the error contribution from polarization angles is small on average. For this study, we assume it to be negligible and that the covariance coefficients for angular parameters are zero. After performing error propagation analysis, we have target sensor relative radiometric uncertainty:

$$\frac{\sigma^{imager}}{\rho^{imager}} = \sqrt{\left(\frac{\sigma_0}{\rho_0}\right)^2 + \frac{P^2\sigma_m^2 + m^2\sigma_p^2}{(1 + mP)^2}} \qquad (2.12)$$

The uncertainty in the first term, σ_0, is radiometric uncertainty of inter-calibrated VIIRS reflectance for unpolarized measurements. A few steps are necessary to derive the σ_0:

(i) The CLARREO RS/Imager reference inter-calibration data products and the PDMs will be made available to the target sensor calibration team. Data products can range from original Level-1 inter-calibration matched data, matched inter-calibration samples, and CLARREO team recommendations on effective gain and offset differences, non-linearity, and sensitivity to polarization.

(ii) The target sensor team uses CLARREO reference inter-calibration data and PDMs to improve sensor calibration on orbit. This involves iterative tuning and validation of a complex instrument model to the reference observations and constraints. The goal is to achieve zero bias in the difference between CLARREO and the inter-calibrated sensor reflectances with additional random inter-calibration noise. For an ideal inter-calibration scenario, the uncertainty of the first term in Equation 2.12 can be written as:

$$\frac{\sigma_0}{\rho_0} = \sqrt{\left(\frac{\sigma^{clarreo}}{\rho_0}\right)^2 + \left(\frac{\sigma_{intercal}}{\rho_0}\right)^2 + \left(\frac{\sigma_{residue}}{\rho_0}\right)^2} \qquad (2.13)$$

where $\sigma^{clarreo}$ is the accuracy of CLARREO RSS, $\sigma_{intercal}$ is the error contribution from inter-calibration noise over an autocorrelation time period, and $\sigma_{residue}$ is error associated with

target sensor remaining error contribution (e.g. instrument month-to-month relative stability). These error sources are of different types: bias and random. If the difference between CLARREO and the imager measurements has remaining offset/gain, then Equation 2.13 will have additional error terms depending on the quality of performed inter-calibration (remaining inter-calibration offsets and gains).

The second term in Equation 2.12 is the error contribution due to inter-calibrated instrument sensitivity to polarization determined from inter-calibration with CLARREO, uncertainty of sensitivity to polarization, the degree of linear polarization and its uncertainty. When $P > 0$ (and $\sigma_p > 0$), sensor's radiometric error increases. For a fixed value of sensitivity to polarization, m, it is a function of P, σ_p, and σ_m. The mean m and uncertainty σ_m are obtained from inter-calibration with CLARREO as described above. The degree of polarization and σ_p are obtained from the PDMs.
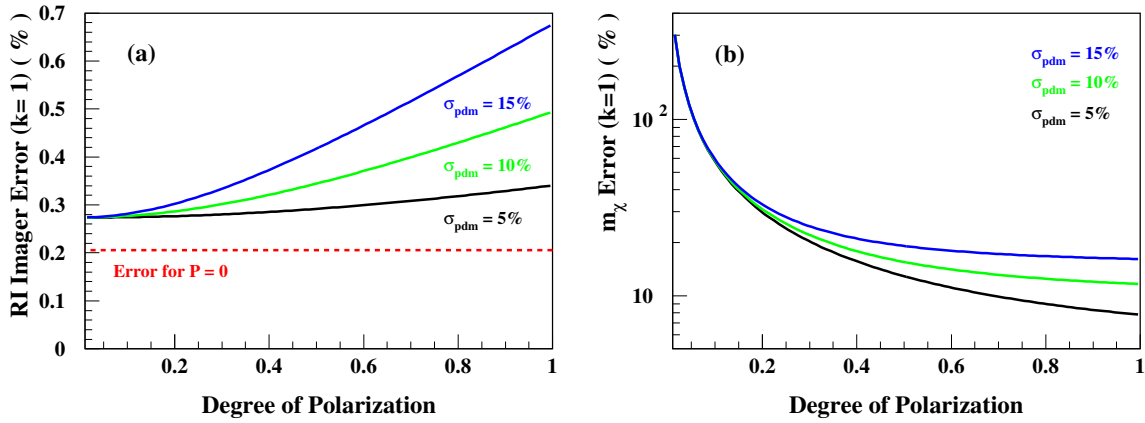
Figure 2.36: (A) RESULTING IMAGER RELATIVE RADIOMETRIC ERROR (K = 1) VERSUS DEGREE OF POLARIZATION. IMAGER SENSITIVITY TO POLARIZATION IS SET TO 3% (k = 1). COLORED CURVES SHOW CASES FOR DIFFERENT PDM UNCERTAINTY, σ_p: 5% (BLACK), 10% (GREEN), AND 15% (BLUE). RED DASHED LINE SHOWS THE ERROR LEVEL FOR UNPOLARIZED RADIANCES. (B) ESTIMATED RELATIVE ERROR OF SENSITIVITY TO POLARIZATION FOR PDM ACCURACY OF 5% (BLACK), 10% (GREEN), AND 15% (BLUE).

We performed numerical estimates for three different levels of PDM accuracy (σ_p): 5%, 10%, and 15%, using Equations 2.12 and 2.13, and estimated nominal polarized and not-polarized sampling uncertainties [Lukashin et al., 2013]. The resulting imager radiometric uncertainty is shown in Figure 2.36a as a function of degree of polarization. Colored curves show results for PDM accuracy at 5% (black), 10% (green), and 15% (blue). The red dashed line shows the uncertainty level for unpolarized reflectances. On Figure 2.36b, we show results for estimated relative error of inter-calibrated imager sensitivity to polarization and its dependence on the PDM accuracy: 5% (black), 10% (green), and 15% (blue) (Equation 2.11). The estimates show that reduction in PDM accuracy from 5% to 15% can cause an increase in uncertainty of inter-calibrated sensitivity to polarization by a factor of four for fully polarized light.

The CLARREO team has developed a formalism for estimation of the resulting uncertainty of CLARREO RSS reference inter-calibration with an imaging radiometer, such as MODIS,

VIIRS, AVHRR, or future imaging instruments on geostationary satellites. To address on-orbit instrument sensitivity to polarization and corresponding radiometric uncertainties, we developed Polarization Distribution Models, described in Appendix C. For the CLARREO RS mission requirements on accuracy, inter-calibration sampling, PDM errors, and under the assumption of inter-calibrated imager stable performance on orbit at 0.1 %(k=1), the estimated uncertainty is at a level of 0.3 - 0.4 %(k=1) over a climate autocorrelation time period of 0.8 years.

C. CLARREO RS Instrument Spectral Requirements

The goal of accurate inter-calibration of imaging multi-band instruments impacts spectral requirements for the CLARREO Reflected Solar instrument. We have determined sensitivity of inter-calibration uncertainty on key design parameters of the CLARREO spectrometer: its spectral range and sampling [Wu et al., 2015].

RS Instrument Spectral Coverage:

One of the objectives of the CLARREO mission is the calibration of broadband radiance for satellite sensors like CERES. For this endeavor, the required spectral coverage (i.e., the cutoff wavelengths at the low and high ends) is a critical parameter for the CLARREO instrument design. While the solar radiation spans a wide spectral range, over 99.5% of the total reflected energy from the Earth to space is within the spectral range from 300 nm to 2400 nm under virtually all real atmosphere-surface conditions, as shown in Figure 2.37a for selected surfaces and Figure 2.37b all-sky averages. Therefore, in terms of total radiation, measurements do not need to cover the entire spectrum but only the range in which sufficient reflected solar energy is enclosed. The minor correction from the uncovered spectral regions can be made using the radiative transfer calculations.
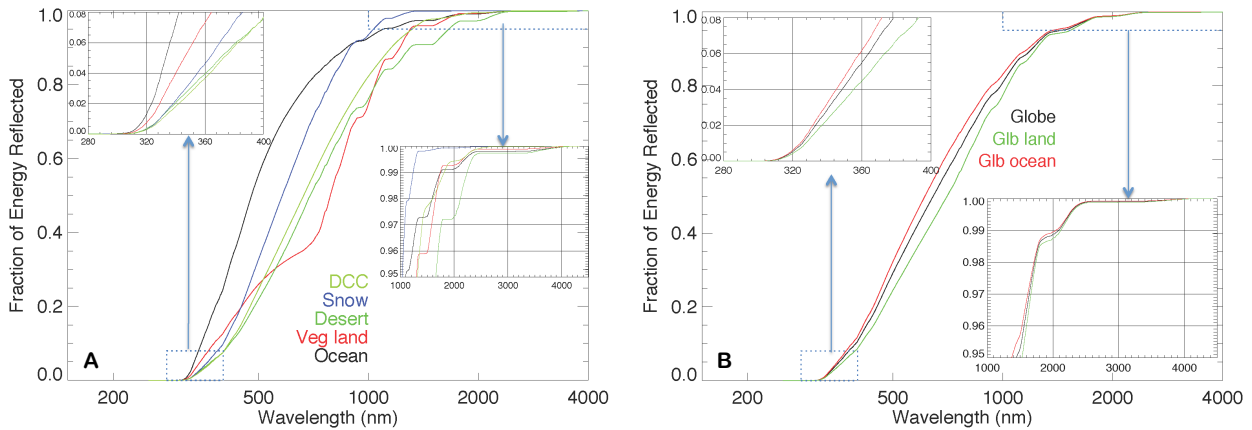
Figure 2.37: (A) THE CUMULATIVE DISTRIBUTION OF THE EARTH'S REFLECTED SOLAR ENERGY AT THE NADIR VIEW OF OCEAN, VEGETATION LAND, DESERT AND SNOW SURFACES UNDER CLEAR SKIES AND FOR THE DEEP CONVECTIVE CLOUD (DCC) WITH OPTICAL DEPTH OF 200. THE Y-AXIS SHOWS THE CUMULATIVE FRACTION OF THE REFLECTED SOLAR RADIATION. THE STANDARD MID-LATITUDE ATMOSPHERE IS USED IN THE CALCULATIONS WITH SOLAR ZENITH ANGLE AS 45°. (B) THE CUMULATIVE ENERGY DISTRIBUTION OF THE MONTHLY GLOBAL, OCEAN AND LAND MEAN RADIATION. THE CALCULATIONS USED THE OBSERVATIONAL DATA FOR AEROSOL, CLOUD AND SURFACE PROPERTIES FROM MODIS/CERES.

Summary of estimated error in total reflected solar energy is shown in Table 2.3 as function

of instrument spectral coverage globally and for selected scene types.

Scene Type	320 − 2300 nm	320 − 2400 nm	310 − 2300 nm	310 − 2400 nm
Global	0.09%	0.07%	0.05%	0.03%
All-sky Ocean	0.10%	0.08%	0.04%	0.03%
All-sky Land	0.08%	0.06%	0.05%	0.04%
Clear Ocean	0.16%	0.15%	0.05%	0.04%
Clear Desert	0.10%	0.07%	0.07%	0.04%

Table 2.3: ESTIMATED ERROR IN THE TOTAL REFLECTED SOLAR ENERGY.

RS Instrument Spectral Sampling and Resolution:

Signal aliasing arises when a signal is discretely sampled at a rate that is insufficient to capture the changes in the signal. In the case of inter-calibration, spectral reflectance aliasing will result in additional systematic uncertainty, which can be avoided with a proper sampling rate. The Nyquist-Shannon sampling theorem provides a prescription for the nominal sampling interval required to avoid aliasing. The oxygen molecular absorption in A-band at the 760 nm contains features, which change with wavelength faster than 0.1 nm. In comparison, the water absorption features include changes within wavelength intervals of 1 – 2 nm. The Earth's reflectance spectra, outside of molecular absorption, are relatively smooth, and these spectral regions are the high priority for the CLARREO inter-calibration objectives.

To estimate the expected biases due to CLARREO RS spectral sampling we used theoretical calculations (MODTRAN) and the SCIAMACHY Level-1B data product (SCI_NL_1P) is used to obtain nadir spectral reflectance with wavelength ranging from the 240 to 1750 nm [Bovensmann et al., 1999]. The impact of spectral resolution is tested using a number of reduced sampling frequencies from 1.0 to 8.0 nm. To produce each of the reduced sampling data sets, an integral of a Gaussian distribution (i.e., normal distribution) function with bandwidths being two times the sampling frequency (the Nyquist rate) is applied to the original high resolution spectral data. The MODIS band reflectances are computed by using Relative Spectral Response (RSR) functions.

In Figure 2.38a we show the spectral sampling with 4 nm frequency and 8 nm Gaussian FWHM bandpass (black), recommended for CLARREO RS instrument, and re-sampled all MODIS reflective solar bands (solid circle). The results are based on all-sky SCIAMACHY instantaneous data from July 2004, providing a general picture of how representative is the CLARREO RS type instrument in the inter-calibration of MODIS reflective solar bands. Figures 2.38b and 2.38c show expected reflectance aliasing at the same six MODIS bands for SCIAMACHY nadir sampling of deep convective clouds (DCC) with solar zenith angle (SZA) < 70°, and latitude within 60° North to 60° South. In this Figure, relative difference in spectral reflectance between calculated MODIS band reflectance from original high-resolution and re-sampled spectra is plotted as function of sampling frequency. For CLARREO recommended 4 nm spectral sampling the estimated biases are below 0.1% for wavelength outside absorption.

Results of our studies indicate that current concept of CLARREO RS instrument with a spectral range from 320 to 2300 nanometers, 4 nanometers in sampling and 8 nanometers in resolution will satisfy the inter-calibration standard requirements – errors in total reflected
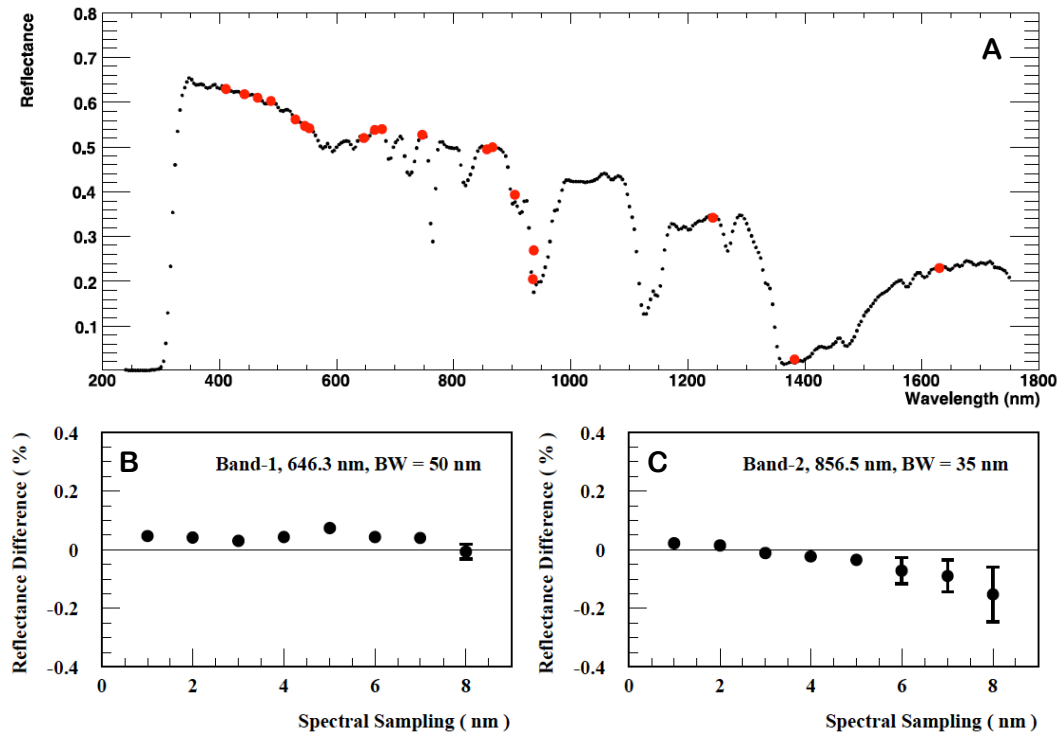
Figure 2.38: (A) SPECTRAL SAMPLING WITH 4 NM FREQUENCY AND 8 NM GAUSSIAN FWHM BANDPASS (BLACK), RECOMMENDED FOR CLARREO RS SPECTROMETER, AND RE-SAMPLED MODIS BANDS (RED CIRCLE). THE RESULTS ARE BASED ON ALL-SKY SCIAMACHY INSTANTANEOUS DATA FROM JULY 2004. (B) AND (C) EXPECTED REFLECTANCE ALIASING AT TWO MODIS BANDS AS FUNCTION OF SPECTRAL SAMPLING FREQUENCY. DEEP CONVECTIVE CLOUDS IN JULY 2004 SCIAMACHY INSTANTANEOUS DATA. THE ERROR BARS SHOW STANDARD DEVIATION OF THE DIFFERENCE (K=1).

energy can be corrected and estimated spectral biases are below 0.1% for wavelength outside absorption regions. For the water vapor absorption bands, challenge remains due to sensitivity to the spectral features of atmospheric water vapor.

2.8.2   CLARREO InfraRed In-orbit Standard

In addition to providing valuable data for benchmarking the Earth's climate and assessing climate models, the reference observations provided by CLARREO are also anticipated to be very useful for satellite inter-calibration. In fact, the relatively short-term inter-calibration benefits are anticipated to be a major contribution to a CLARREO mission. In order for the accuracy and traceability of CLARREO to be beneficial to other concurrent sensors, the inter-calibration methodology and resulting inter-calibration uncertainty must be robust and well understood. There are many approaches used for satellite inter-calibration [e.g. Chander et al. 2013]. This section describes the use of CLARREO to serve as a reference for infrared satellite inter-calibration and quantifies the uncertainty in determining radiometric biases observed between CLARREO and sun synchronous sounding sensors such as the Atmospheric InfraRed Sounder (AIRS), the Cross-track Infrared Sounder (CrIS), and the Infrared Atmospheric Sounding Interferometer (IASI).

The importance and various benefits of satellite inter-calibration are described in Goldberg et al. 2011 and Chander et al. 2013 and references therein, and are not repeated here. In addition to creating consistency among the global suite of satellite observations, inter-calibration aims to anchor observations to reference observations provided by a reference sensor. For infrared radiance, the Global Space-based Inter-Calibration System (GSICS) currently uses IASI and AIRS as reference sensors due to their wide spectral coverage, high spectral resolution, and relatively high radiometric and spectral accuracy. Measurements by CrIS on the operational Suomi-NPP and future JPSS platforms have similar characteristics and are also expected to be very useful for inter-calibration. In comparison to the IASI, AIRS, and CrIS data, which are useful for both weather and climate process applications, the CLARREO mission and sensor design are not focused on high spatial sampling and noise performance, but on obtaining the highest possible on-orbit accuracy, as well as on-orbit traceability of the calibration to SI units. CLARREO is designed to minimize potential radiometric calibration biases (due to radiometric nonlinearity, polarization, spectral calibration, and other contributions) and provide routine on-orbit verification/traceability of the radiometric accuracy, similar to what is traditionally done only in a laboratory environment prior to launch. The inter-calibration strategy utilizing CLARREO observations includes the inter-calibration of CLARREO with the sun-synchronous hyperspectral sounders (AIRS, CrIS, IASI), followed by the existing GSICS strategy of inter-calibration of these sensors with various broadband infrared sensors on sun synchronous and geostationary platforms. Therefore, CLARREO has the potential to provide high accuracy measurements with on-orbit SI traceability that will form the backbone of the satellite inter-calibration system, making the larger suite of satellite observations more useful for both weather and climate applications.
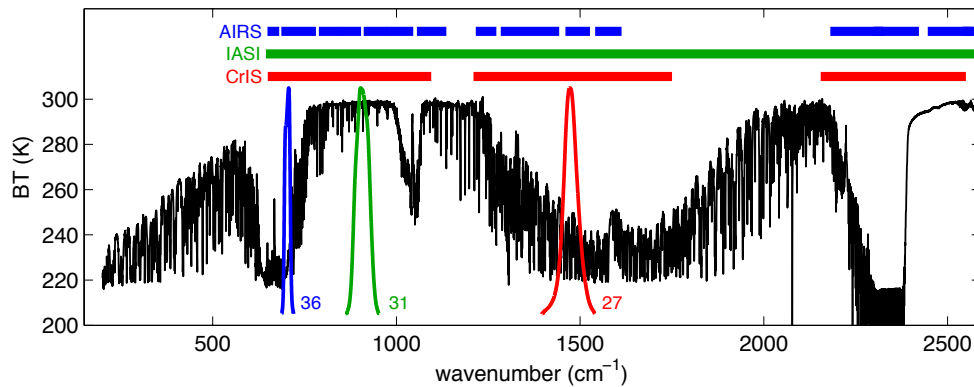
Figure 2.39: An example CLARREO brightness temperature spectrum (black) overlaid with Spectral Response Functions of MODIS bands 27, 31, and 36. The spectral coverage of AIRS, IASI, and CrIS are shown.

Characteristics of the CLARREO mission and infrared observations relevant to inter-calibration are described here. These include spectral coverage and resolution, radiometric accuracy and calibration traceability, radiometric noise performance, the satellite orbit, and the Earth view footprint size and sampling frequency. The spectral coverage and spectral resolution of CLARREO are well suited for inter-calibration. CLARREO is a Fourier Transform Spectrometer (FTS) with a combination of pyroelectric, HgCdTe, and InSb detectors providing continuous spectral coverage from 200 to 2800 cm^{-1}, with spectral resolution of 0.625 cm^{-1}. Spectrally, this allows robust comparisons with the IASI and CrIS FTS sensors by truncating

the observations to the lowest common spectral resolution, as well as high spectral resolution comparisons with AIRS. Additionally, the CLARREO spectra can be convolved with broadband sensor Spectral Response Functions to accurately simulate broadband infrared sensor observations. A sample CLARREO brightness temperature spectrum is shown in Figure 2.39 along with the spectral ranges of AIRS, IASI, and CrIS.
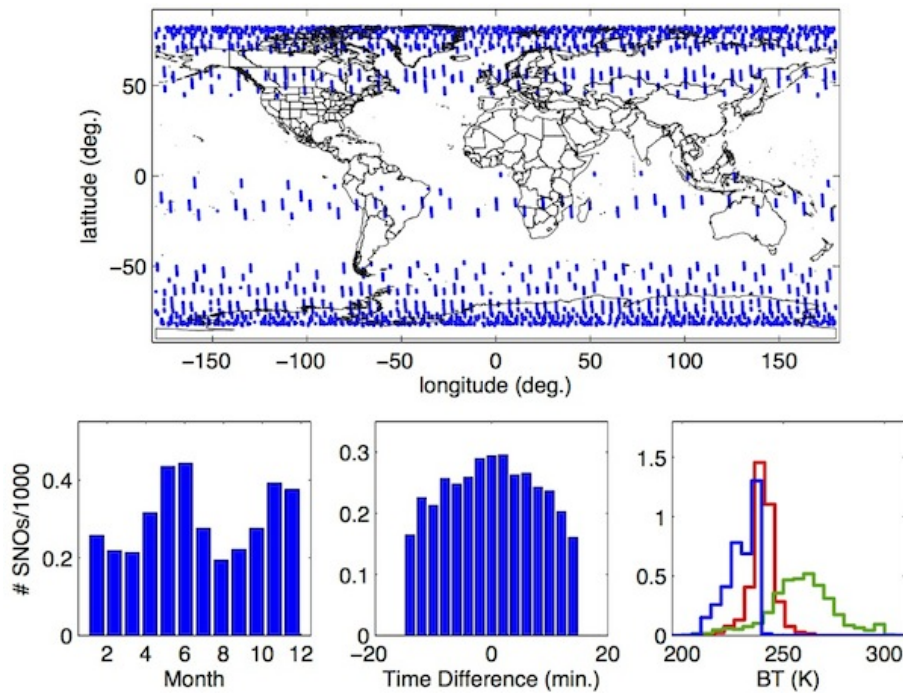
Figure 2.40: Characteristics of CLARREO/Sounder (sun-sync) SNOs for one year and 1 polar orbit CLARREO. One CLARREO FOV every 20 seconds. 3621 SNOs for the year. Top panel: SNO locations. Bottom left panel: SNOs per month. Bottom middle: SNO time differences (2 minute bins). Bottom right: SNO BT distributions for MODIS bands 27 (red), 31 (green), and 36 (blue) (5 K bins).

The on-orbit Radiometric Uncertainty (RU) of CLARREO is predicted to be 0.07 K (k = 3) or lower for all wavelength regions and all scene temperatures [Taylor et al., 2012] and has recently been demonstrated in laboratory vacuum conditions. Furthermore, CLARREO includes a sub-system which will allow the radiometric uncertainty to be routinely assessed on-orbit with SI traceability [Best et al., 2012]. This high accuracy and on-orbit traceability are the defining and unique characteristics of CLARREO for both climate and inter-calibration applications. This CLARREO RU is approximately 3 to 4 times better than the RU currently available from AIRS, IASI, and CrIS. The CLARREO orbit assumed for these inter-calibration studies is a 90° inclination polar orbit with an altitude of 600 km. Unlike a sun-synchronous orbit, this orbit drifts slowly with respect to the sun angle and provides coverage of the full diurnal cycle every six months. Characteristics of SNOs obtained with CLARREO and a sun-synchronous satellite are shown in Figure 2.40. From a 90° inclination polar orbit, CLARREO is expected to have a nadir view footprint diameter in the range of 25 to 100 km, with a likely value of 65 km. CLARREO does not include cross track scanning; the measurement sequence will produce one nadir Earth view footprint every 20 seconds, corresponding to adjacent nadir footprint spacing of 140 km.

To assess the ability to inter-compare and inter-calibrate a notional CLARREO sensor with IASI, AIRS, and CrIS, an inter-calibration simulation was performed. The study used real, global imager observations (MODIS) and orbital navigation tools to simulate a 90° inclination CLARREO orbit and SNOs with Aqua MODIS. SNO locations and times for CLARREO and Aqua are computed, and for each SNO we used MODIS observations and the observation geometries of CLARREO, IASI, and CrIS to produce simulated data for each sensor. The use of real MODIS IR observations and realistic SNOs provides a direct assessment of inter-calibration uncertainties, removes the unknown biases involved in typical inter-calibration studies using two real sets of observations, and allows the spatial and temporal colocation (or matching) errors to be examined. This is performed for three representative spectral regions (MODIS band 27 at 6.7 μm, band 31 at 11 μm, and band 36 at 14.2 μm). For a full year of SNOs, the range of SNO scene temperatures is shown in the bottom right panel of Figure 2.40. A large range of scene temperatures are sampled over the year ranging from 200 K to greater then 300 K. Not surprisingly, the more absorbing MODIS channels (27 and 36) are colder with less variability in the scene temperature. The sampling is relatively consistent with on average 200 – 400 SNOs per month with a total of 3621 SNOs for the year.
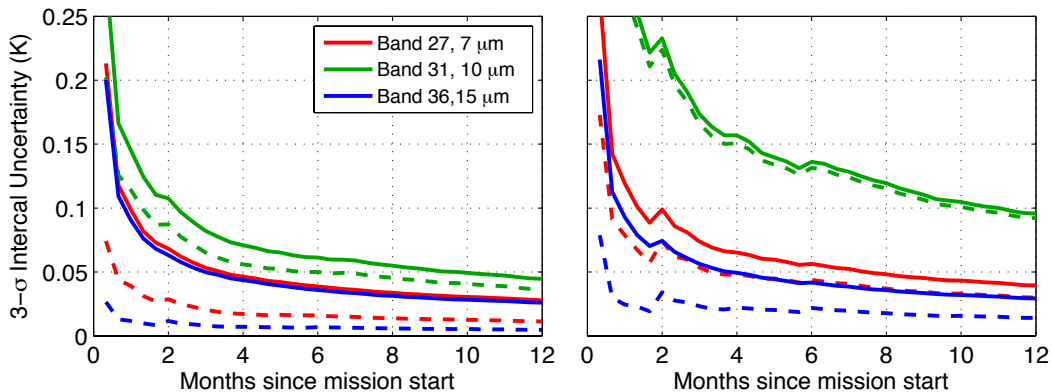
Figure 2.41: CLARREO INTERCALIBRATION UNCERTAINTY AS A FUNCTION OF MISSION LENGTH FOR SINGLE SPECTRAL CHANNELS IN THE 7, 10, AND 15 μM REGIONS FOR CLARREO/CRIS SNOS (LEFT PANEL) AND CLARREO/IASI SNOS (RIGHT PANEL). SOLID CURVES INCLUDE SPATIAL AND TEMPORAL COLOCATION ERRORS AND CLARREO AND SOUNDER DETECTOR NOISE; DASHED CURVES DO NOT INCLUDE CLARREO OR SOUNDER DETECTOR NOISE.

The SNO spatial and temporal colocation differences are combined with sensor detector noise contributions to estimate the overall inter-calibration uncertainty for ensembles of CLARREO and Sounder SNOs. The primary result is shown in Figure 2.41, which shows the $k = 3$ Inter-calibration Uncertainty (IU) as a function of CLARREO mission length for inter-calibration with CrIS or AIRS (left hand panel) and inter-calibration with IASI (right hand panel). Results are shown for a single CLARREO spectral channel in each of the three representative wavelength regions. For the CLARREO/CrIS inter-calibration, IU of 0.1 K ($k = 3$) is obtained after accumulating 1 month of SNOs for the 7 and 17 μm channels, and after 2 months for 10 μm channels. This implies that the radiometric calibration of CrIS or AIRS can be assessed at the 0.1 K ($k = 3$) level every 1 to 2 months using SNO inter-calibration with CLARREO. Alternately, using 12 months of SNOs, the absolute calibration can be assessed at the 50 mK level. For the 7 and 15 μm channels, the CLARREO/IASI IU results are similar to the CLARREO/AIRS/CrIS results due to the spatial homogeneity of the upper atmosphere. For

10 μm channels, however, the sparser spatial coverage provided by IASI results in larger IU, with an IU of 0.1 K (k = 3) obtained after 10 months of accumulated SNOs.

The CLARREO mission is an extended pre-Phase A study phase and options for demonstrating the CLARREO technologies and providing science benefit are being pursued. One option is to demonstrate prototype sensors on the International Space Station (ISS). In terms of satellite inter-calibration, the ISS would provide a similar number of SNOs per year ($\sim$3600) as compared to a 90° inclination polar orbit, but with the SNOs limited to the ±51.8° latitude range. Utilizing the same infrared sensor design would produce a 37 km diameter FOV from the ISS altitude. For CLARREO on the ISS, the CLARREO/AIRS/CrIS IU as a function of mission length has also been assessed. Due to the smaller footprint, the results are slightly degraded with respect to a 90° inclination polar orbit, but an IU of 0.1 K (k = 3) is still obtained with < 2 month (7 and 15 μm channels) and $\sim$4 month (10 μm channels) periodicity.

2.8.3 Current Inter-Calibration of On-orbit Sensors

The quantitative determination of global trends in the Earth's atmosphere, ocean, cryosphere, biosphere, and land surface depends significantly on the ability of the scientific community to construct multi-instrument/multi-platform data sets based on satellite observations covering periods of a decade or longer. This effort, global in scope, also constitutes a global challenge, as most, if not all, such data sets will rely on satellite programs from multiple agencies and/or nations, in particular, requiring the use of satellites primarily focused on research and operations. The "knitting together" of such data sets requires that the relative calibrations of the different sensors, their degradation over time, and the nature of the algorithms used to convert raw measurements into environmental parameters all be quantitatively understood. Given the diversity of sources of the instruments and algorithms, as well as the unique characteristics of each, a focused effort is needed in creating such combined data sets. This challenge has been widely recognized by satellite operators and the existing organizations through which they coordinate their activities, such as the CEOS, the WMO, the GSICS, and the Coordination Group for Meteorological Satellites (CGMS). In this Section, we describe relevant activities performed by the CLARREO SDT members and funded through the NASA ROSES 2011 solisitation "Satellite Calibration Interconsistency Studies".

A. Patrick Minnis (NASA Langley Research Center):
"Intercalibration of Satellite Imaging Channels to Facilitate Consistent Retrieval of Atmospheric and Surface Climate Data Records"

The CLARREO inter-calibration algorithms have greatly benefited from GSICS, CERES, and other NASA-Langley calibration studies. GSICS is an international collaborative effort to monitor, improve and harmonize the calibration of operational environmental satellites to provide consistent and accurate satellite retrievals [Goldberg et al. 2008]. The GSICS effort has been underway since the mid 2000's. CLARREO hosted the 2013 GSICS Research Working Group annual meeting and presented the CLARREO algorithms to measure instrument polarization, to calibrate operational instruments, and improvements in the CLARREO instrument design over current instruments. The GSICS community fully supports the CLARREO effort and is planning on using the future CLARREO visible and IR hyper-spectral radiances as a traceable absolute calibration reference to calibrate their operational imagers.

The current GSICS IR inter-calibration approach uses the IASI hyper-spectral radiances as a reference to inter-calibrate the operational IR imagers in GEO. The coincident instantaneous, angle-matched, and collocated GEO and IASI hyper-spectral data are convolved with the IR spectral response functions, radiance pairs and are linearly regressed weekly [Hewison et al., 2013]. The bias is monitored over time and the calibration correction factors are given in the GSICS operational products [*http://www.star.nesdis.noaa.gov/smcd/GCC/ProductCatalog.php*]. Similarly, GSICS efforts are underway to calibration microwave, UV, and visible bands.

Since there is no well-calibrated visible hyper-spectral satellite that covers the range of all visible operational sensors, the current GSICS visible calibration approach is to apply as many independent calibration techniques, where all are tied to the same reference calibration for traceability. Currently, the reference calibration instrument is Aqua MODIS and will shortly be replaced with NPP VIIRS. Eventually, the chain of visible reference instruments will be traceable to CLARREO. Consistency among the calibration techniques provides both the validation and the uncertainty analysis. The techniques include: clear-sky ocean (Rayleigh scattering), deep convective cloud (DCC), desert, polar-ice, lunar, and stellar invariant targets. Other techniques are matched directly to the reference instrument such as: coincident & collocated angle-matching, bore-sighting, or SNO radiance pair matching, or the use of predicted radiances from radiative transfer model (RTM), which use simultaneous surface, cloud, and atmospheric retrievals from the reference instrument. The target and reference instrument spectral band differences are resolved using Spectral Band Adjustment Factors (SBAF).
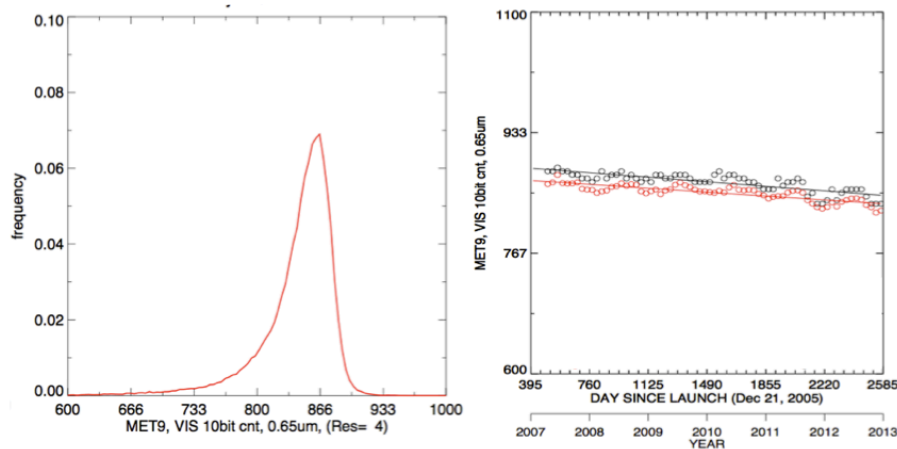
Figure 2.42: LEFT: THE PDF OF THE METEOSAT-9 PIXEL LEVEL DCC VISIBLE COUNTS, WHICH ARE PROPORTIONAL TO RADIANCE, FOR JULY 2012. RIGHT: THE METEOSAT-9 MONTHLY PDF MODES (BLACK CIRCLES) AND MEANS (RED CIRCLES) OF THE DCC COUNT ALONG WITH THE LINEAR TEMPORAL TRENDS.

NASA Langley pioneered the DCC calibration technique [Hu et al., 2003; Doelling et al., 2004]. DCC are the brightest nearly Lambertian Earth targets and are available over most of the tropics. Since the tops are located at the tropopause, the NIR SBAF correction is minimal because there is little water vapor above the tropopause. DCC are suited for wavelengths less than 1 μm since the ice particle habits can alter the reflectance for wavelengths greater than 1 μm. A simple IR threshold, usually less than 205 K, and if the surrounding 8 pixel level standard deviations in the visible and IR are less than 0.03% and 1 K, respectively, they are identified as pixel level DCC targets. A DCC bidirectional reflectance distribution (BRDF)

70

factor is applied for each pixel within 40° in both the solar zenith angle (SZA) and view zenith angle (VZA). A monthly probability distribution function (PDF) is computed from all of the DCC pixel radiances identified over the month (Figure 2.42). The mode of the PDF is found to be extremely stable over time. The temporal trend of the monthly mode DCC radiance is then used to monitor the calibration of the instrument. The Aqua MODIS 0.65 μm band, the GSICS calibration reference band, was found to have a linear calibration drift of 0.6% over a decade [Doelling et al., 2013a]. The monthly DCC mode radiance standard error about the linear trend was 0.5%. The two-year VIIRS record showed similar monthly standard errors. DCC calibration can confidently detect instrument calibration trends greater than 1%/decade in 5 years, whereas for Libya-4 desert the detection time will take 11 years [Bhatt et al., 2014a]. The current challenge with the DCC calibration technique is providing pixel level DCC radiances that are referenced to a traceable visible reference. The DCC BRDF radiance was found to be dependent on the IR threshold temperature. It is believed that most IR imagers that rely on blackbodies have IR calibrations that are stable in time, but the temperature may be biased according to the reference sensor IR temperature. This is especially true for historical imager sensors when well-calibrated IR sensors are not available.
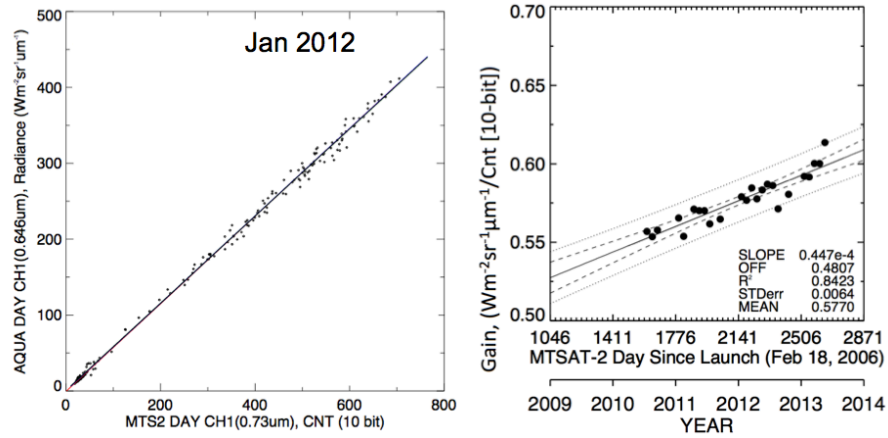
Figure 2.43: Left: The instantaneous coincident, collocated, and angle-matched MTSAT-2 visible counts and Aqua-MODIS radiances for January 2012, and linear regression that determines the gain. Right: The MTSAT-2 monthly gains along with the linear temporal trend.

CERES has calibrated 16 GEO imagers in preparation to process the synoptic product, which combines both CERES observed fluxes and GEO-derived fluxes to account for the change in the regional flux in between CERES measurements, which have been carefully normalized to the CERES observations to maintain the CERES instrument calibration. The GEO-derived broadband flux quality depends on the visible imager calibration and cloud retrievals and must be consistent across GEO imagers both spatially and temporally. The CERES project has used the MODIS/GEO ray-matched radiance pair technique to transfer the calibration of the superior calibrated MODIS instrument to the GEO visible imager, which to this date do not have onboard visible calibration [Doelling et al. 2013c]. The ray-match technique matches coincident collocated 50-km co-angled MODIS/GEO radiances and linearly regresses the instantaneous matches monthly (Figure 2.43). The gain is computed monthly based on the space observed radiance value. The monthly gains are monitored over time to capture the GEO visible degradation over time.

One of the greatest angle-matching uncertainties lie in the SBAF and monthly gain seasonal oscillations, which are mostly related to spectral band differences. In order to reduce this uncertainty, another angle-matching algorithm was developed using only coincident collocated co-angled radiance pairs over DCC targets. The GEO/MODIS angle-matched targets are not randomly located over the GEO domain, but are confined over specific locations since the MODIS sun-synchronous orbits are on a 16-day repeat cycle and the GEO satellites have a set-imaging schedule. Remarkably, enough DCC radiance pairs were obtained on a monthly basis. The monthly linear regression standard errors were reduced by 75% and the GEO record temporal trend error by 50%. Not only were the spectral response differences mitigated, the Lambertian nature of DCC reduced the effects of the angular mismatches.

Since the angle-matching technique sees the entire observed dynamic range monthly, any non-linearity in the GEO imager visible radiances can be detected by this method shortly after launch. The Multifunctional Transport Satellite (MTSAT)-1R imager, which was the operational GEO satellite at 140°E after July 2006, showed signs of visible radiance non-linearity during routine CERES angle-matching processing. After ruling out navigation, accounting for spectral band differences, and verifying the residual space offset, the non-linear behavior of MTSAT-1R visible radiances persisted. The Japanese Meteorological Agency (JMA) provided coincident MTSAT-2 commissioning images observed during December 2010. It was determined from comparisons of coincident MTSAT-1R and MTSAT-2 images that contamination in the optics slightly blurred the MTSAT-1R images. A small amount of the 1-km pixel radiance contribution was obtained from an area that extends over 800 km. An MTSAT-1R point spread function (PSF) was derived and the PSF correction reduced the blurring by 80% and improved the resulting MTSAT-1R derived broadband flux and cloud properties [Doelling et al., 2014a; Khlopenkov et al., 2014].

CERES uses GEO/Aqua-MODIS angle-matching as its primary calibration technique, and validates the calibration using GEO/Terra-MODIS angle-matching, where Terra-MODIS has been radiometrically scaled to Aqua-MODIS. Similar to GEO/MODIS angle-matching, Terra and Aqua MODIS coincident collocated co-angled radiance pairs can be regressed monthly during the summer to derive the Terra-scaling factor [Doelling et al., 2014b]. The instantaneous Terra and Aqua ground track intersect is commonly referred to as SNO. Also, invariant DCC and desert target calibration are used to verify the calibration. The desert target calibration employs the Diurnal Exothermic Radiance Model (DERM) [Bhatt et al., 2014b]. For each GEO domain, a reference GEO is identified and is calibrated using the angle-matched GEO/MODIS gains. Since a GEO imager scans according to well-maintained schedule, the daily local noon GEO SZA, VZA, and azimuthal angle over a particular site is repeated annually. The DERM is computed from the GEO reference daily local noon radiances over the desert site. It is assumed that the desert surface and atmospheric column varies seasonally, but the inter-annual variability is small. It was found that the 5-year daily inter-annual variability over the Libyan-4 desert was 0.74%. DERM then predicts the radiance for all future, current, or historical GEO imagers located at the same equatorial longitude location. The GEO DCC calibration method is similar to the MODIS calibration method. The Aqua-MODIS calibration transfer is based on the assumption that over the same DCC domain and GMT range that the GEO and MODIS DCC mode radiance should be equivalent if the same DCC identification thresholds are used [Doelling et al., 2011]. For GOES-13, it was found that Terra/GEO, Aqua/GEO angle-matching, DCC, and DERM calibration methods were consistent within 1.4% [Morstad et al., 2011].

With the launch of the SCIAMACHY visible hyper-spectral instrument, improvements in SBAF have been achieved to remove the visible band spectral response differences between the reference and the target instrument. SCIAMACHY footprint hyper-spectral radiances are collected over the calibration targets. The reference and target spectral response function are convolved with a single footprint of SCIAMACHY hyper-spectral radiances to compute a pseudo reference and target radiance pair. All of the footprint pseudo radiance pairs are regressed to derive the SBAF. Usually, a second order fit captures most of the radiance distribution. The standard error about the fit provides the uncertainty of the SBAF. To prove the effectiveness of the SCIAMACHY-derived SBAF, an all-sky ocean and all-sky land SBAF was computed over the GOES-12/Aqua-MODIS ray-match domain. The GOES-12/Aqua-MODIS ray-matched gains were computed with and without SBAF for both land and water. The SBAF application reduced the land/ocean gain difference by 4.5% and the offset by 41%. After the SBAF application, the land/ocean gain was within 0.1% and the offset was within 3.8% [Doelling et al., 2012]. NASA Langley has developed SBAFs over desert, polar-ice, DCC, and GEO/LEO equatorial domains.

A SCIAMACHY/GEO angle-matching technique was developed to transfer the calibration of SCIAMACHY to the target GEO sensor without the use of a SBAF. This technique can also be used by CLARREO to angle-match operationally scanned CLARREO/GEO radiances. The SCIAMACHY footprint is 240 by 30 km and if the angles between SCIAMACHY and a GEO sensor agree, all of the GEO pixel level radiances are averaged within the boundaries of the SCIAMACHY footprint. The SCIAMACHY hyper-spectral radiances are convolved with the GEO spectral response function to compute the reference radiance. The coincident collocated and angle-machted SCIAMACHY and GEO radiance pairs are then linearly regressed monthly. The Meteosat-9 calibration trend, using SCIAMACHY, was similar to the Aqua-MODIS angle-matching technique. However, the monthly standard error was reduced, inferring that the monthly noise from the Aqua-MODIS angle-matching may be due to band spectral response differences [Doelling et al. 2013b].

NASA Langley has nearly completed the uniform calibration of the entire AVHRR data record beginning with TIROS-N and ending with Metop-B. The greatest challenge in calibrating the AVHRR record is associated with the degrading NOAA satellites. They are launched into an afternoon or morning orbit and over time drift into a terminator orbit. For well-maintained sun-synchronous orbits, the angular viewing geometry over a particular region are replicated annually, so any angular bias in an invariant Earth target BRDF model are seen as noise. This is not the case for the NOAA orbits. Also invariant target models derived from MODIS do not have the full solar zenith extent needed to calibrate radiances observed near the terminator. The NASA Langley approach is to use NOAA-16 as the AVHRR reference instrument, which has been calibrated against Aqua-MODIS using SNOs. Desert and polar ice SZA-predicted radiance models are based on near nadir NOAA-16 radiance observations. Four desert, Libya-4, Libya-1, Arabia-1, Niger-1, and two polar ice targets, Dome-C and Greenland, are used to mitigate any reflectance natural variability over an individual site. An additional SZA correction is applied to the DCC approach, which has not been limited by a SZA threshold. Over the pre-MODIS time frame , a combined desert, polar-ice. and DCC calibration gain is used based on the inverse of the monthly gain temporal variability of the approach. During the MODIS time frame, the Aqua-MODIS/AVHRR SNO calibration gains are used and validated by the desert, polar-ice, and DCC approach. For most AVHRR instruments, the calibration gain difference among the methods are within 2%.
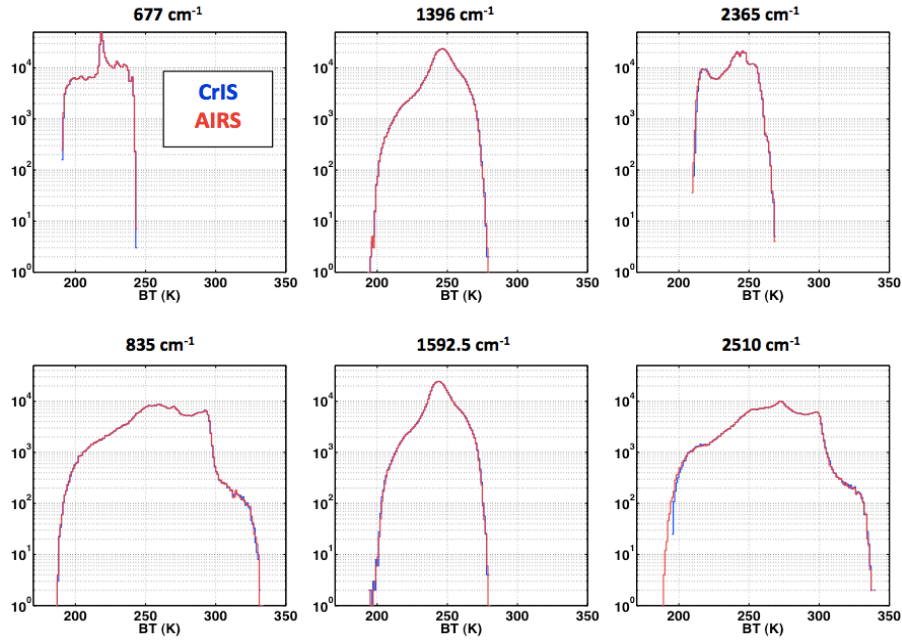
Figure 2.44: LOG-SCALE BRIGHTNESS TEMPERATURE DISTRIBUTIONS OF CRIS AND AIRS FOR SIX REPRESENTATIVE SPECTRAL REGIONS.

B. David Tobin (University of Wisconsin-Madison):
"Hyperspectral Infrared Satellite Inter-calibration Studies"

There are numerous inter-calibration investigations of today's infrared satellite sensors. These include inter-calibration of high spectral resolution sounders such as IASI, AIRS, and CrIS, broadband sensors such as MODIS, AVHRR, and VIIRS, as well as many other sensors including GOSAT, TES, and Geostationary imagers and sounders. These investigations utilize a wide range of inter-calibration methodologies which have recently been described in Chander et al., 2013, and inter-calibration results are routinely generated and reported via GSICS [e.g. Goldberg et al., 2011]. Here we present some examples of inter-calibation results for IASI, AIRS, CrIS, and VIIRS. In general, the agreement among state-of-the-art infrared observations is very good, on the order of a few tenths Kelvin for many sensors and bands. However, there are some sensors which display larger differences.

CrIS/AIRS Inter-calibration:

The inter-comparison technique involves collecting the CrIS and AIRS data found within 100 km of the SNO locations that occur with ±20 minute simultaneity. For each such case, the mean and standard deviation of the radiance spectra are recorded for both CrIS and AIRS. Because Suomi-NPP and EOS Aqua are in similar orbits, there are many SNOs distributed over a wide range of latitude and longitude. Sample results shown in Figures 2.44 and 2.45 indicate that the radiometric agreement between CrIS and AIRS is very good – less than ∼0.1K. The differences are also very stable with time, and do not show large dependence on scene brightness temperature.

CrIS/IASI Inter-calibration:

SNOs of CrIS and IASI occur at narrow latitude bands at approximately ±73.5°. Here we

74
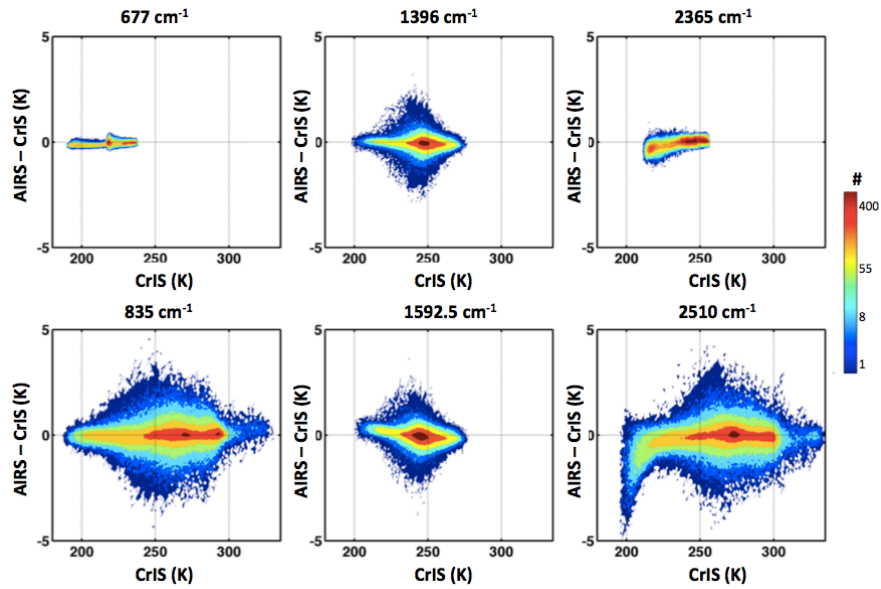
Figure 2.45: Log-scale distributions of brightness temperature differences as a function of scene brightness temperature. Dark blue is one count (one SNO) and dark red is 400.

show results comparing CrIS on Suomi-NPP to IASI on METOP-A and IASI on METOP-B, and also using CrIS as a transfer standard to inter-compare IASI on METOP-A to IASI on METOP-B. Using large ensembles of SNOs, it has been shown that the differences between all three sensors are less than approximately 0.2 K for the longwave and midwave spectral regions. Also, uncertainties in estimating the differences (the standard errors) are very small for this SNO comparison technique. Differences between IASI on METOP-A and IASI on METOP-B are also very small, being near zero for most of the midwave water vapor band and IASI-A approximately 0.1 K warmer than IASI-B throughout the longwave spectral band. These small differences demonstrate the excellent radiometric accuracy of both IASI and CrIS.

CrIS/VIIRS Inter-calibration:

Comparisons of CrIS and VIIRS on Suomi-NPP involves the spatial averaging of VIIRS pixels within CrIS footprints and the spectral convolution of CrIS spectra with the VIIRS spectral response functions. Using VIIRS bands where CrIS provides spectral coverage, the comparisons are computed for VIIRS bands M13 (4 μm), M15 (10.8 μm), and M16 (12 μm).

The VIIRS data is also used to assess spatial variability. Spatially uniform scenes are selected and differences between CrIS and VIIRS are computed. This results in approximately 500,000 collocated footprints suitable for comparison every day. Figure 2.46 shows a sample result: the time dependence of daily mean differences. VIIRS nonlinearity tests, performed quarterly, are evident in the time series. These differences are less than 0.1 K and are very stable with time (trends of -3.5, -2.1, and -3.6 mK/year), but with low-level seasonal patterns beginning to emerge. Also (not shown), the CrIS/VIIRS data comparison shows excellent behavior as a function of scan angle and scene brightness temperature.
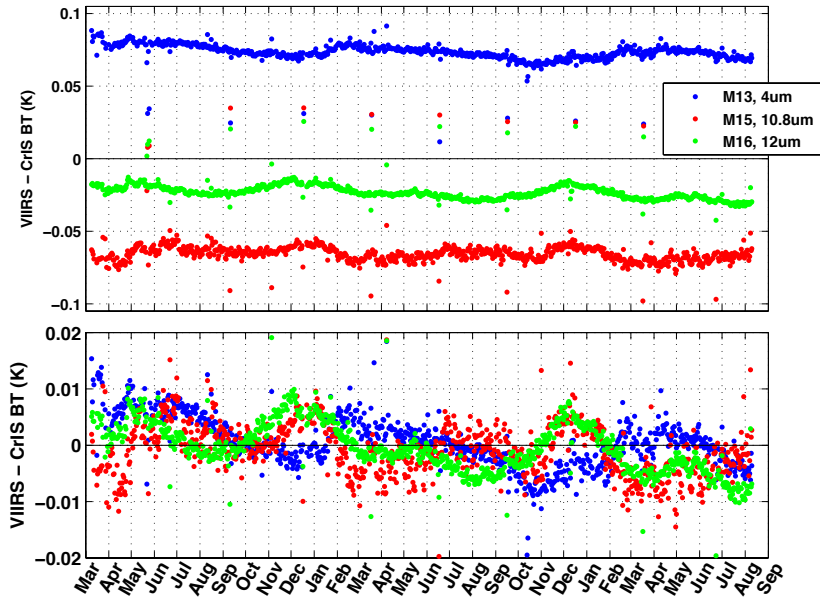
Figure 2.46: DAILY MEAN DIFFERENCES BETWEEN CRIS AND VIIRS. TOP PANEL: DAILY MEAN DIFFER-
ENCES. BOTTOM PANEL: DAILY MEAN DIFFERENCES WITH THE OVERALL BIASES SUBTRACTED OFF.

2.8.4 Multi-Instrument Inter-calibration Framework

Climate quality measurements require accurate calibration. Inter-calibration ties the cali-
bration of one instrument to a more accurate, preferably SI-traceable, reference instrument
by matching measurements in time, space, wavelength, and view angles. The challenge is
to find and acquire these matched samples from within the large data volumes distributed
across international data centers. For inter-calibration, typically $< 0.1\%$ of the data volume
are required for analysis. Software tools and networking middleware are needed to intelli-
gently select and acquire matched samples from multiple instruments on separate spacecraft.
Matched instantaneous observations are also used in cloud, aerosol, and model comparative
analysis studies.

The Multi-Instrument Inter-calibration (MIIC) Framework is a collection of software to sup-
port inter-calibration and inter-comparison studies within NASA and NOAA data systems.
Development of the MIIC framework started with ROSES ACCESS 2011 funding. The project
continued to be funded by the ROSES ACCESS 2013 program. Currently, the effort is fo-
cused on extending MIIC data access and analysis features, eploying MIIC web services, and
demonstrating cross-agency interoperability between NASA and NOAA data centers.

Inter-calibration between instruments is a central pillar of the calibration-validation strategies
of many national and international satellite remote sensing organizations. The GSICS, an in-
ternational collaboration focused on inter-calibration of space borne sensors, recommends a
variety of algorithm. Most are based on matching data from Earth targets or simultaneous
nadir overpasses. All organizations comparing observations from multiple instruments face the
same challenge, *how to access matched measurements from within large datasets distributed
across multi-agency international data centers?* The typical process is to spend months of
time downloading data from remote data centers onto TBs of expensive disk space. Custom
non-reusable software is written to read and process data on local client machines. Results
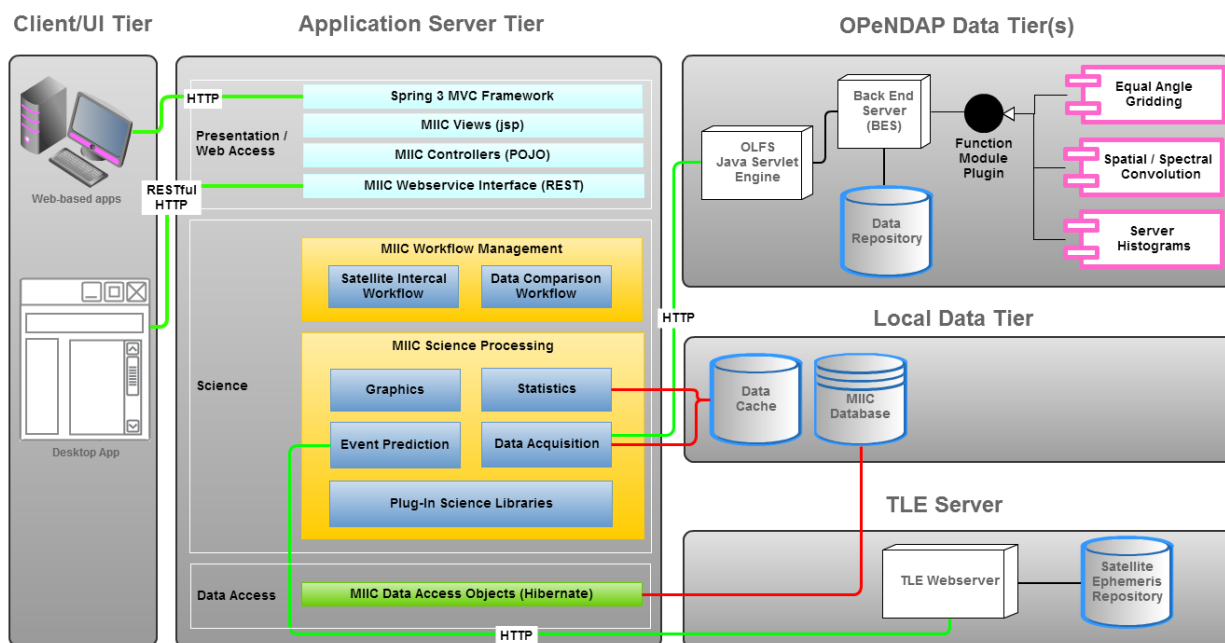
Figure 2.47: THE MIIC FRAMEWORK MULTI-TIER CONFIGURATION: CLIENT, APPLICATION, OPENDAP, AND LOCAL DATA TIERS.

are published, but code is typically poorly developed, maintained, and results hard to duplicate. Common reusable software helps to alleviate some of these problems. This project will demonstrate a collaborative IT solution between the NOAA National Climatic Data Center (NCDC) and NASA Atmospheric Science Data Center (ASDC) facilities to improve access to Earth science data for climate, weather, land use, and other scientific studies.

The MIIC framework is a collection of software designed to work in a distributed collaborative environment to support LEO-GEO and LEO-LEO inter-calibration and inter-comparison studies. The MIIC framework multi-tiered architecture is shown in Figure 2.47. The MIIC framework provides three main web services: Event Prediction, Data Acquisition, and Analysis. The Event Prediction service finds collocated near coincident measurements with similar view conditions based on viewing zenith, solar zenith, and relative azimuth angle differences. The framework uses an open source orbit propagator (SGP4) and custom Earth rotation, solar position, and instrument scan models to predict matched observations. This service is fast and efficient since no data products are read; instead only daily two-line-element (TLE) files are processed. The Event Predictor outputs Latitude-Longitude bounding boxes with instrument scan start/stop times for each matched event within the specified time period. Time periods can be days, months, or years so long as satellite TLEs exist. An example of inter-calibration event prediction is shown in Figure 2.48 for MODIS and GOES-13 for January 1, 2011, daytime. The Data Acquisition service then parses the Event Acquisition plan and communicates over the network using the OPeNDAP network protocol to acquire events from each remote data center. OPeNDAP server-side gridding, spectral and spatial convolution, and histogram functions are executed on remote servers. This combination of event prediction and server-side functions eliminates the need to transfer large volumes of data files in entirety, reducing both data center and user network bandwidth and disk storage consumption. Users can more efficiently access NASA and NOAA data through the RESTfull Application Programming

Interfaces (APIs) instead of point and click file selection order tools.

The LEO-GEO MODIS/GOES-13 inter-calibration use case, as illustrated in Figure 2.48, demonstrates a significant reduction in data transmission. One month, January 2011, of Aqua/MODIS L1B and GOES-13 imager data consists of 9672 files (1.4 TB). The Event Prediction algorithm, which finds time-matched simultaneous overpasses, reduces the number of files transmitted by a factor of 22X. Server-side equal angle spatial gridding reduces the data by an additional factor of 34X. The final matched gridded MODIS/GOES-13 samples are contained in 808 files (1.8 GB). This is consistent with other LEO/GEO inter-calibration algorithms that typically require only 0.1% of the total data volume.
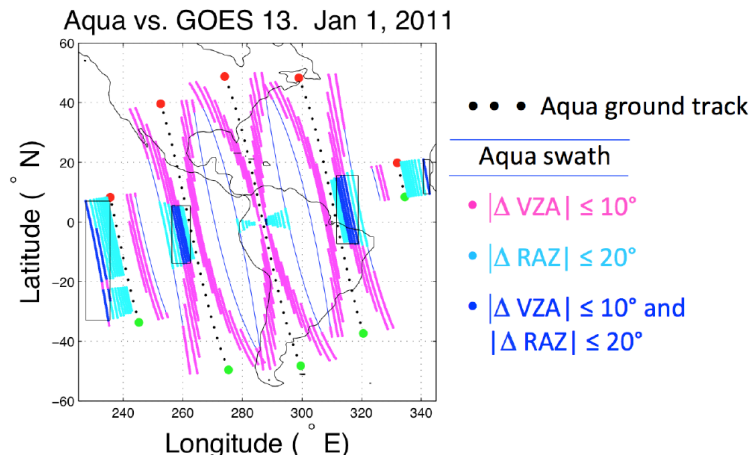
Figure 2.48: LEO-GEO EVENT PREDICTION MODIS/GOES-13 DAYTIME JAN. 1, 2011.

The LEO-LEO SCIAMACHY/MODIS inter-calibration server-side spectral and spatial convolution functions provide even greater reductions in data network transmission. SCIAMACHY Level-1B data have 5287 spectral bands, 240 − 1748 nm, and footprint sizes of 30 km × 240 km at nadir. Spectral convolution of MODIS Band 1 (0.65 μm) relative spectral response (RSR) values with hyperspectral SCIAMACHY data reduces the 5287 spectral values to one simulated reflectance value. Spatial convolution of 1 km MODIS pixels with 30 km × 240 km SCIAMACHY footprints accounts for a reduction factor of 7000 at nadir.

Histogram analysis and spectral and spatial resampling required for OSSE/observation comparisons have the potential for several orders of magnitude savings in data transmission. In addition to the substantial reductions in data transfer, there is a more important qualitative benefit provided by services such as the MIIC Framework. New collaborative research becomes more feasible as critical data centers such as NOAA's NCDC and NASA's ASDC support value added services along with remote access to their data.

Costs to transfer and store large volumes of data sets for inter-comparison studies are significant, especially when years of data and reprocessing are considered. Instead, acquiring only matched samples and performing more calculations at the data source enables better utilization of existing resources. Powerful event prediction and server-side processing simplifies data accessibility and enables researchers to focus more on analysis tasks. The MIIC Framework is based on demonstrated technology levels greater than TRL 6.

2.9 Improvement in Stability of EOS Retrievals

2.9.1 Retrievals in InfraRed

Climate change assessment depends on a long-term record of climate observations. Obtaining climate observations, however, remains challenging despite the now multi-decadal record of global observations from space. Climate observations need to discern small changes over large space-time scales (global, zonal, annual, seasonal, and decadal). To date, space-based Earth observing systems have been designed to detect small changes over space-time scales (local, hourly, and daily) associated with weather systems. Achieving observational accuracy and consistency at scales suitable for climate monitoring, such as to be obtained by the proposed CLARREO mission, remains one of the challenges in Earth system metrology.

Ultraspectral sounders measure the atmospheric column with relatively high vertical resolution. The ultraspectral resolution sounding concept [Smith et. al, 1979, 2009] is to measure a large portion of the infrared spectrum of Earth-atmospheric radiance to space in order to obtain a very large number of noise independent spectral channels of radiance for inferring atmospheric profiles of temperature, water vapor, as well as cloud altitude and trace gas concentrations. The high spectral resolution and large number of spectral channels both serve to optimize the vertical resolving power of the measurements. Having thousands of measurements, as opposed to tens of measurements, provides an order of magnitude improvement in signal-to-noise ratio, and this enables a much more precise inversion of the integral radiative transfer equation. The result is improved accuracy and higher vertical resolution of the retrieved profiles than can be achieved from prior generation multi-spectral radiance data.

With the first decade of accurate vertical atmospheric measurements now available, it is possible to determine their suitability for the assessment of climate change. There are four ultraspectral sounders in operational low-Earth orbit at present: AIRS on Aqua since 2002, IASI on Metop-A since 2006, and Metop-B since 2012, and CrIS on Suomi-NPP since 2011. Both IASI instruments are in morning orbits ($\sim$ 09:30 local crossing time), with AIRS and CrIS are in afternoon orbits ($\sim$ 13:30 local crossing time). The strength of ultraspectral sounders has been described by Smith et. al., (2009) and the accomplishments of AIRS and IASI data have been presented by Chahine et. al., and Hilton et al. (2012). The spatial resolution of the three instruments is similar (i.e., $\sim$ 13-km) but the spatial density of the AIRS and CrIS instruments is more than a factor of two greater than that for IASI. On the other hand, IASI possesses the highest spectral resolution and greatest spectral coverage. Although AIRS and CrIS are two different types of instruments (i.e., AIRS being a grating spectrometer while CrIS is an interferometer similar to IASI), they possess nearly the same spectral resolution and coverage.

The purpose of this research conducted by the University of Wisconsin-Madison (UW) members of the CLARREO SDT is to compare temperature soundings from three ultraspectral instruments in space in order to gauge their utility for climate change assessment. The objective is to characterize and quantify sources of systematic difference in soundings at climate scales (e.g., annual trends and averages at a 10-degree resolution) that contribute to the overall uncertainty in a continuous data record due to differences in instrumentation and sampling time, specifically. The main research questions are, (1) To what extent does the time of measurement affect long-term trend attribution ? (2) Given a single retrieval algorithm, and

similar diurnal sampling frequencies, do instrument differences affect the quality of retrieved geophysical parameters aggregated to coarse space-time scales? (3) Can a seamless long-term record of temperature profiles be assembled from multiple instruments? A more complete description of the study reported here is provided by the paper entitled "Climate Monitoring with Satellite Data Records – An investigation into the continuity among AIRS, IASI, and CrIS soundings" being submitted to the Journal of Climate and Applied Meteorology [Smith, N., W. L. Smith, E. Weisz, and H. E. Revercomb, 2014].

A. Geophysical Retrieval Method

In order to process long-term global records of ultraspectral radiance observations from multiple instruments, a fast, consistent and accurate algorithm is required. The UW's dual-regression (DR) retrieval method [Smith et al. 2012; Weisz et al. 2013] meets these requirements. Originally developed for operational use in real-time environments, it proves relevant also for climate-related research. It is a fast physical-statistical method for inverting ultraspectral radiance measurements into atmospheric profile, surface, and cloud parameters. It can ingest and process radiance measurements from any of the operational ultraspectral sounders: AIRS on Aqua, CrIS on SNPP, IASI on MetOp-A and MetOp-B. Apart from being a mature algorithm with proven operational stability and performance, a number of factors contribute to the relevance of DR to climate-related research: (1) The accuracy of the retrieval solution has no dependence on bias errors of weather prediction models. The information retrieved has a linear dependence on radiance measurement only, i.e., the retrieval solution is not influenced by the uncertainty of an *a priori* (or first guess). This means that the DR method maintains consistent retrieval accuracy across space (globally) and time (multi-generational, multi-decadal). (2) It is product-centric, which means it can be applied to any past, present, and future hyperspectral sounders in space or on aircraft to produce a consistent record of Earth system data records. (3) It retrieves atmospheric, cloud, and surface information simultaneously under clear-sky and cloudy conditions at instrument resolution.

The DR retrieval product contains profiles of temperature, humidity, and ozone, along with total column CO_2, surface- (temperature and emissivity) and cloud parameters (optical thickness, cloud top height, and temperature), as well as secondary derived properties (e.g., instability indices). The retrieved profiles described by 100 vertical quadrature levels of the atmosphere from the TOA to the surface. The vertical resolution of each of the retrieved profile quantities varies between 1 and 5 kilometers, depending on the parameter (i.e., temperature, water vapor, or ozone) and the altitude. Specifically, the atmospheric temperature profile vertical resolution ranges between 1-km near the surface to approximately 5-km within the stratosphere, the average tropospheric vertical resolution being about 2 kilometers. In the presence of clouds, the profiles describe the atmosphere from the TOA down to cloud top height, or to the Earth's surface, depending on the cloud fraction and optical depth. Retrieval consistency across instruments was found to be adequate for time-series analysis of short-term weather events, as well as in establishing a time-continuity across decades for trend analysis.

Five years of AIRS and IASI radiance measurements were processed, and one year of all three instruments – AIRS, IASI and CrIS. For a robust statistical measure of an annual cycle, global measurements from four months were processed for each year: February, May, August, and November. The five-year record spans February 2008 to May 2013, and the one-year record from August 2012 to May 2013. For brevity, these records are referred to as DR-AIRS, DR-

IASI, and DR-CrIS, respectively. In the absence of an objective truth, GDAS (Global Data Assimilation System) reanalysis data were used as a standard for comparison, or relative "truth." Global GDAS reanalysis temperature profiles are produced at 26 vertical levels, and 1-degree spatial resolution across the globe every six hours starting at time 00:00. The GDAS temperature field is interpolated in space and time to the instrument-specific configuration for AIRS, IASI, and CrIS, respectively. For the remainder of this text, we refer to these as GDAS-AIRS, GDAS-IASI, and GDAS-CrIS, respectively. Due to the high temporal frequency of model fields, the time difference between retrieval and its co-located model field is never larger than 3 hours. In addition, the 26 layers of model temperature interpolated to the 100 layers used in DR. Everything as described above for DR was repeated for the GDAS records.

The climate statistics used for comparison of the datasets were the annual and 5-year means as well as the 5-year temperature trend. These are useful for robust comparison of the impact of systematic differences. Temperature trend were calculated for each instrument across five years of data analyzed. A 5-year trend is computed as the slope of a linear fit to the annual average values for each grid cell. Thus, the slope of the linear relationship is the change per year (i.e., the annual trend). An annual mean is simply the average of the daily means. An equal area weighted global mean presents an effective way to summarize trends and differences in a single value.
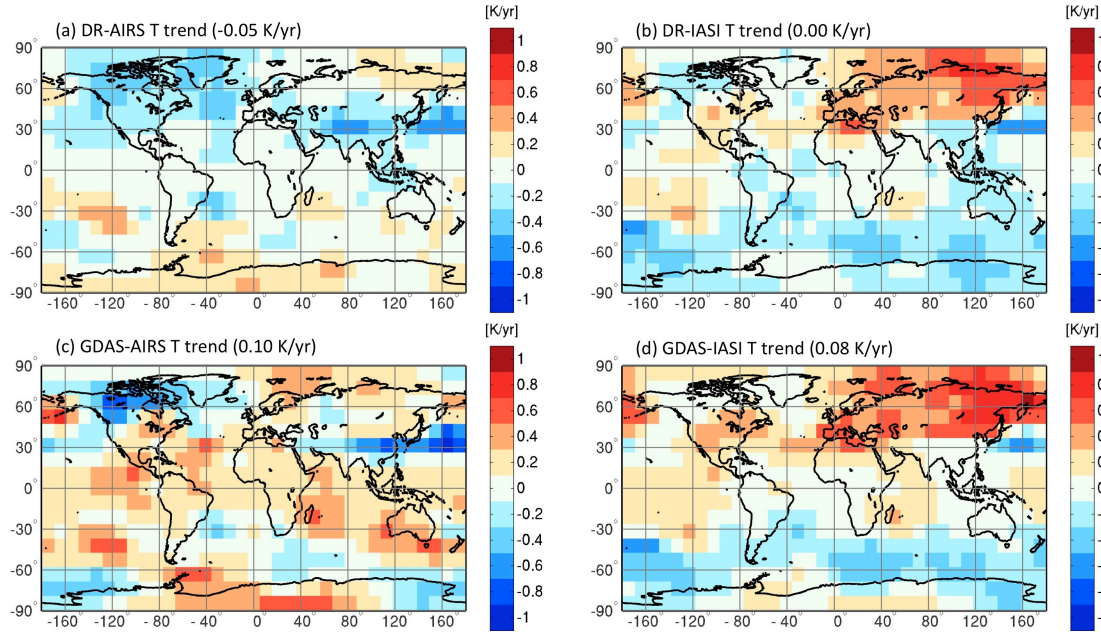
Figure 2.49: Five-year Temperature trend (2008 – 2012) at 300 hPa for (a) AIRS Dual-Regression (DR) retrievals, (b) IASI DR retrievals, (c) GDAS interpolated in space-time to the AIRS instrument grid, (d) GDAS interpolated in space-time to the IASI instrument grid. The global area-weighted mean trend is given in brackets.

B. Results and Discussion:

Data from three ultraspectral satellite sounders are compared with the goal to investigate whether they meet climate accuracy standards and to determine if the individual instrument datasets are sufficiently similar to form a continuous long-term data record. Some of the

major sources of systematic differences among data products arise from instrumentation. They include differences in calibration, signal-to-noise ration, and space-time sampling [Stubenrauch et al. 2013]. AIRS is in a PM orbit (13:30 LST) and IASI an AM orbit (09:30 LST). All measurements per 24-hour day that aggregate spatially to each grid cell are averaged into a daily mean. However, the diurnal sampling differences between AIRS and IASI persists over time and may present significant differences, even on a monthly scale. This diurnal sampling difference is equally strong in all latitudes despite the high latitudes receiving more frequent overpasses from polar-orbiting instruments. Thus, diurnal sampling can be expected to contribute to observed differences between data records from AIRS and IASI.

The most important climate change signal is the annual trend. Here temperature trends are calculated for AIRS and IASI across five years of data analyzed. An annual trend is computed as the slope of a linear fit to the annual averages for each grid cell. Thus, the slope of the linear relationship is the change per year (i.e., the annual trend). Weatherhead et al. (1998) determined that it will take several decades of high-quality data to detect climate trends, so the trend results presented here are preliminary and used to establish comparative relations only. We are interested in characterizing sources of uncertainty, not in quantifying accuracy.
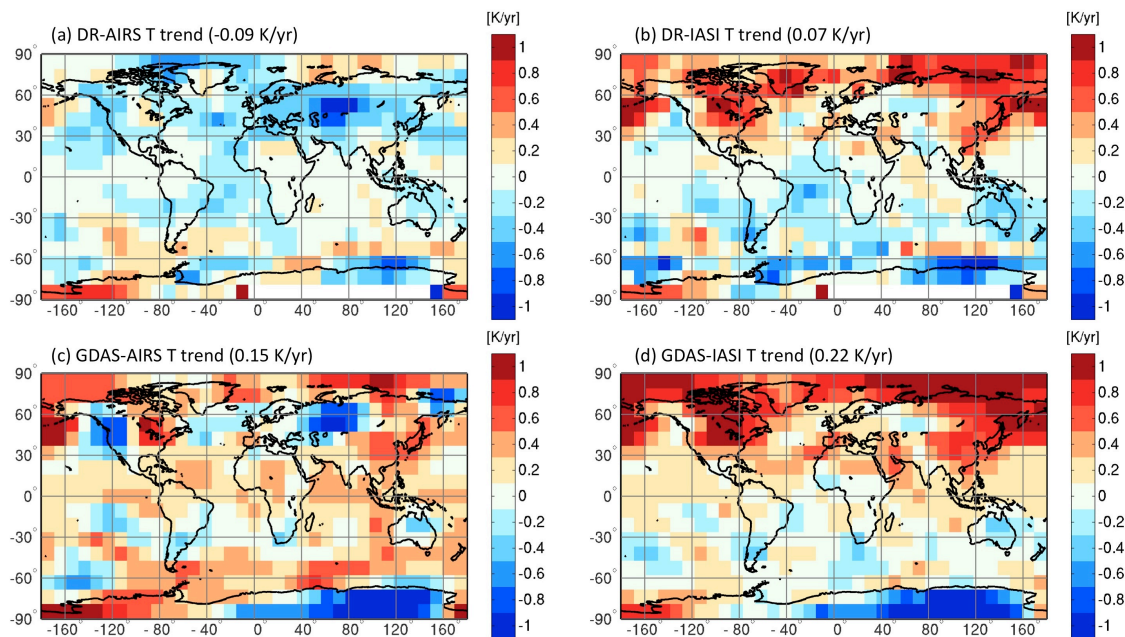
Figure 2.50: Temperature trend across five years (2008 – 2012) at 850 hPa for (a) Dual-Regression AIRS retrieval (DR-AIRS), (b) DR-IASI retrievals, (c) GDAS space-time interpolated to the AIRS instrument grid (GDAS-AIRS), (d) GDAS-IASI. The global area-weighted mean temperature trend is given in brackets.

The temperature trend for the PM records (i.e., DR-AIRS and GDAS-AIRS with 13:30 LST) at 300 hPa is given in Figures 2.49a and 2.49c, respectively. Similarly, the trend for the AM records (i.e., DR-IASI and GDAS-IASI with 09h30 LST) at 300 hPa is given in Figures 2.49b and 2.49d, respectively. Note the strong differences in trends between the Northern and Southern Hemispheres (NH and SH) for the AM records. Here, a strong warming trend is visible over the northeastern region of the globe, whereas a cooling trend is visible across the entire Southern Ocean. This contrasts sharply with the near random distribution of warming

and cooling zones in the PM records. Overall, the global area-weighted mean of DR trends (Figures 2.49a and 2.49b) is lower than for the GDAS trends (Figures 2.49c and 2.49d), with AIRS displaying an overall cooling effect over the five years (2008 – 2012). The model trends, GDAS-AIRS and GDAS-IASI, serve to indicate the global trend that would result from two datasets if the only difference between them is the time of measurement. It can be concluded that the uncertainty due to diurnal sampling in a mid-tropospheric temperature trend is 0.02 K/yr. Thus, the instrument dependent trend difference (i.e., DR-IASI minus DR-AIRS minus the difference 'GDAS-IASI' minus 'GDAS-AIRS') is much larger, being 0.07 K/yr, than the diurnal sampling produced trend difference.
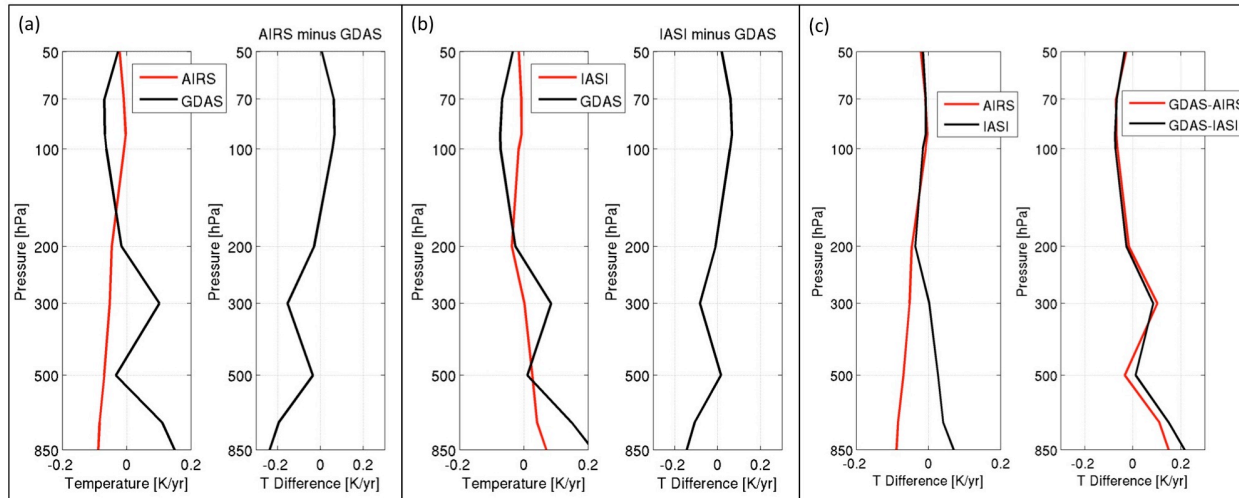
Figure 2.51: Profiles of global average temperature trends for Dual-Regression retrievals of AIRS and IASI as well as GDAS interpolated in space-time to the AIRS and IASI instrument grids, respectively. (a) AIRS DR trend compared to GDAS-AIRS trend (left), difference of the two profiles (right). (b) IASI DR trend compared to GDAS-IASI trend (left), difference of the two profiles (right). (c) Comparing the AIRS and IASI profile trends (left) and the GDAS-AIRS and GDAS-IASI trends on the right. This sheds light on height at which instrument and diurnal sampling biases start to matter.

This trend comparison was repeated for lower tropospheric temperature at 850 hPa (Figure 2.50). Here, the differences due to diurnal sampling are more pronounced. As before, there is a strong difference in trend between the NH and SH in the AM record. A strong warming trend extends across the full NH high-latitude zone for both DR-IASI and GDAS-IASI. Again, AIRS has a strong cooling trend globally that differs notably from the GDAS-AIRS trend. Despite the overall difference between DR-AIRS and GDAS-AIRS, they depict the same pockets of cooling trends over NH landmasses. From the global area-weighted average from each trend record in Figure 2.50, it can be concluded that the uncertainty due to diurnal sampling in a lower tropospheric temperature trend is 0.07 K/yr, 0.05 K/yr higher than in the mid-troposphere. Diurnal bias extends across the full latitudinal range, despite higher frequency observations in the high latitudes. This can be explained by the strong diurnal sampling difference between AIRS and IASI. The instrument dependent trend difference for this level is 0.09 K/yr, similar to the mid-tropospheric instrument dependent trend difference and also larger than that difference due to the diurnal sampling (i.e., 0.07 K/yr).

The global mean temperature trend calculated for 10 pressure layers gives a vertical profile as shown in Figure 2.51. The DR-AIRS and GDAS-AIRS trend profiles are compared in Figure 2.51a. Overall, DR-AIRS demonstrates a cooling trend at all layers (stratospheric and tropospheric). GDAS-AIRS has stratospheric cooling with a sharp increase towards a warming trend from 200 – 300 hPa and again from 500 – 850 hPa. With GDAS-AIRS as a reference, we can say that DR-AIRS has a low bias (> 0.1 K/yr) in the mid to low troposphere. This bias (or systematic difference) is larger than the predicted long-term trend in temperature (0.1 K/yr). The DR-IASI bias (Figure 2.51b) is much lower (< 0.1 K/yr) throughout the vertical atmospheric column except for the two lower tropospheric layers, 700 and 800 hPa. From this we can conclude that for stratospheric and upper tropospheric layers (< 200 hPa), systematic differences between the AIRS and IASI records are very low. With GDAS as a reference only (relative "truth"), we are unable to comment on the accuracy of the DR underestimation of both tropospheric warming and stratospheric cooling trends. This will be the focus of future work.

In considering the assembly of a long-term record from AIRS and IASI data, we can shed some light on this by comparing the DR trend profiles for AIRS and IASI against each other (Figure 2.51c, left). From this we are able to discern that, without any bias correction, DR records of AIRS and IASI can be assembled into a continuous long-term record for trend detection in the upper atmosphere (< 200 hPa). However, differences between these two records show a steady increase below 200 hPa, with maximum differences in the boundary layer (850 hPa). Thus, it is in the mid to low troposphere that improved inter-calibration between AIRS and IASI is most important if a continuous record is to be assembled. The contribution that diurnal sampling differences make to the observed disparities between the AIRS and IASI records is demonstrated in the comparison of GDAS-AIRS and GDAS-IASI trend profiles (Figure 2.51c, right). Differences due to diurnal sampling are overall quite low (< 0.1K) and impact global trends in the lower troposphere only (> 500 hPa). In other words, diurnal sampling affects only up to 50% of the differences observed between the DR-AIRS and DR-IASI records of temperature trend in the lower troposphere.

The bias introduced by instrumentation alone can be tested differently. For each instrument, a 5-year temperature mean is calculated, the difference of which indicates the continuity/disparity between long-term AIRS and IASI records. The relative contribution that instrument differences make to this calculated disparity can be tested by first removing the diurnal signal from the daily gridded mean before calculating a 5-year mean. This is done by subtracting the space-time interpolated GDAS daily mean from each instrument daily mean (DR-AIRS minus GDAS-AIRS and DR-IASI minus GDAS-IASI). Any remaining deviations in the 5-year mean of differences should be largely a result of instrument radiance measurement differences alone. At 300 hPa, we find that instrumentation accounts for 100% of the calculated disparity (the global area-weighted mean difference between the 5-year mean and mean difference is roughly the same at ~ 0.6 K). At 850 hPa, instrumentation accounts for only 50% of the calculated disparity (~ 0.6 K versus ~ 0.3 K). These results demonstrate the need for more accurate inter-calibration between AIRS and IASI, an expectant 0.25K improvement [Wielicki et al., 2013], if AIRS and IASI are to be assembled into a continuous record for long-term monitoring of the lower troposphere.

So far it has been shown that both diurnal sampling and instrument measurement characteristics matter. Now with the SNPP CrIS instrument, which is a Fourier Transform Spectrometer
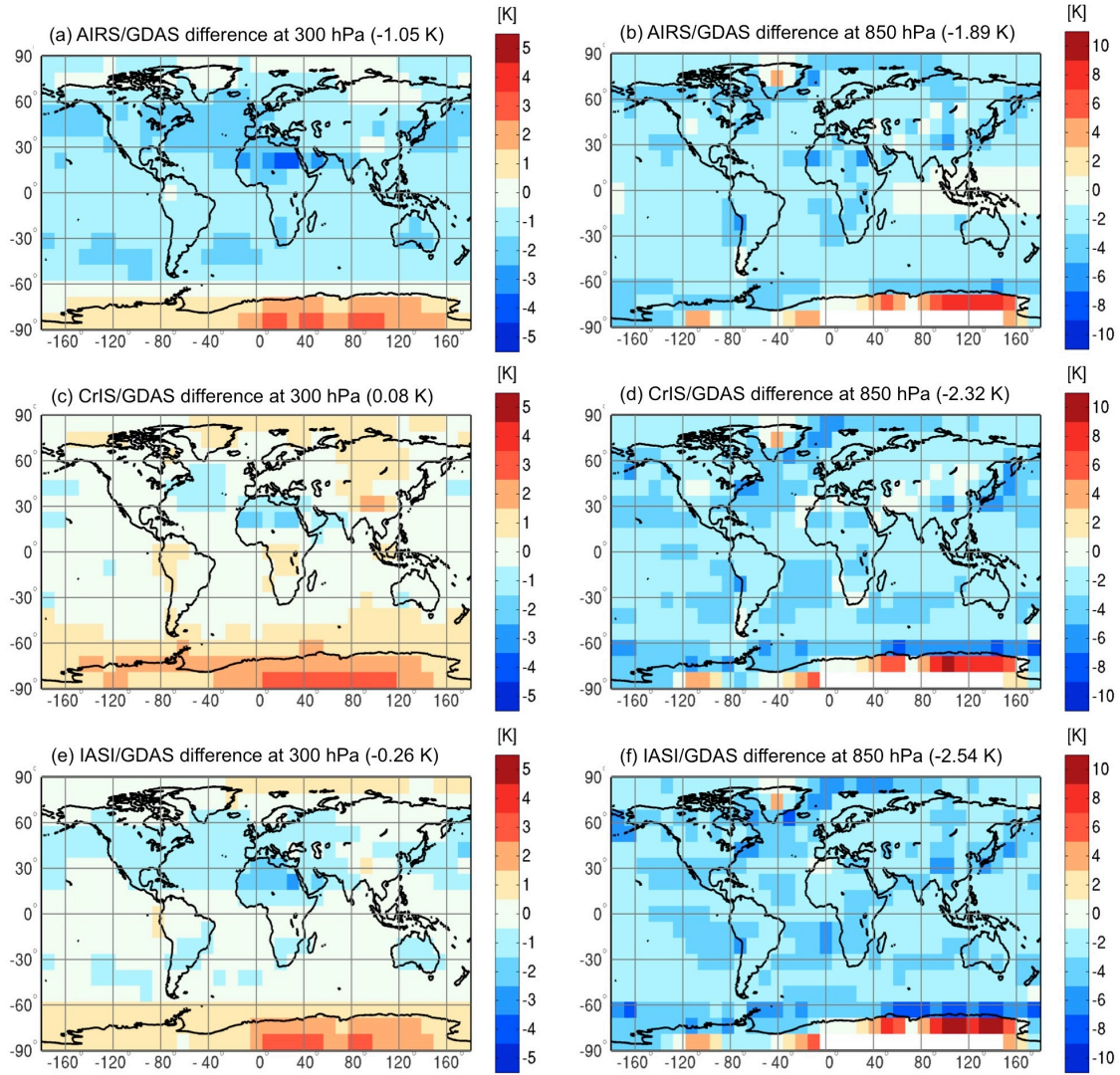
Figure 2.52: ANNUAL MEAN (2012 – 2013) OF DAILY TEMPERATURE (T) DIFFERENCE: DAILY MEAN OF $T_{instrument} - T_{model}$ AT TWO ATMOSPHERIC PRESSURE LEVELS, 300 HPA (LEFT) AND 850 HPA (RIGHT).

like IASI, in the same orbital planes as the Aqua AIRS, which is a grating spectrometer, it is possible to isolate instrument technology induced differences from diurnal sampling induced differences. The question is whether the CrIS record is similar enough to that of AIRS to allow CrIS to be used as a continuation so that a climate data record may be assembled, or instead, do the CrIS trends more closely resemble the trends depicted by IASI because they are both the same instrument type ? Which bias (i.e., diurnal sampling or instrument type) is greatest ? An answer to these questions is obtained by calculating the mean difference between satellite measurements and the model for a year of retrievals obtained from AIRS, IASI and CrIS (using the same four months for year 2012 – 2013). Results for the mean difference are shown in Figure 2.52 for 300 hPa and 850 hPa in left and right columns, respectively. For each instrument the GDAS reanalysis temperature field was space-time interpolated to the instrument grid before aggregation: (a) – (b) AIRS minus GDAS-AIRS at 300 hPa and 850 hPa, respectively. (c) – (d) CrIS minus GDAS-CrIS at 300 hPa and 850 hPa, respectively. (e) – (f) IASI minus GDAS-IASI at 300 hPa and 850 hPa, respectively. The global area-weighted

85

mean difference of temperature at each layer is given in brackets. CrIS shows a somewhat closer resemblance to IASI, which indicates that instrument characteristic differences are as significant as diurnal sampling differences. When comparing AIRS, IASI, and CrIS, we see a stronger similarity between IASI and CrIS at 300 hPa, confirming the significance of instrument bias in mean temperature statistics in the upper troposphere. However, at 850 hPa the instrument dependent differences are weaker, the differences being dependent on other sources such as diurnal sampling bias of the boundary layer.

C. Conclusions:

◇ Dual Regression provides climate quality all-sky condition retrievals from current hyperspectral sensors.
◇ IASI vertical temperature profile trend is in better agreement with GDAS than is the AIRS vertical temperature profile trend.
◇ IASI and GDAS show a typical CO_2 greenhouse warming signature; AIRS shows slight tropospheric cooling.
◇ In the mid to upper atmosphere, IASI and CrIS agree with each other better than either agrees with AIRS, indicating an instrument technology dependence. From this we can expect to make a better diurnal sampling bias study using IASI and CriS instead of IASI and AIRS, due to similar/lower instrument bias in the former.
◇ These results demonstrate the need for more accurate inter-calibration between AIRS and IASI, an expectant 0.25K improvement [Wielicki et al. 2013], if AIRS and IASI are to be assembled into a continuous record for long-term monitoring of the lower troposphere.
◇ Diurnal sampling affects up to 50% of the differences observed between the DR-AIRS and DR-IASI records of temperature trend in the lower troposphere. However, in the mid to upper atmosphere, diurnal sampling effects are negligible. This suggests that climate data records can be assembled for atmospheric parameters at layers < 300 hPa from multiple instruments, even if those instruments are not in complementary orbital planes.
◇ CLARREO is needed for cross-calibration of the operational ultraspectral sounders in orbit in order to be able to use the observations from these sensors to assess climate change.

2.9.2 Accuracy in RS and IR for Cloud Properties Change

Clouds play a complex role in the Earth's radiation budget, acting to cool or warm atmospheric layers and the surface depending upon their horizontal and vertical distribution and many other macrophysical and microphysical properties [Ramanathan et al., 1989, Stephens, 2005]. Cloud- and cloud feedback-induced differences in climate sensitivity – a measure of how the climate system changes relative to a sustained forcing — are the largest discrepancies among global climate models [Stocker et al., 2013]. Having a clear understanding of how observed cloud properties change over time is a requirement for constraining the cloud feedback differences among climate models. Because small changes in cloud properties need to be detected to understand the role of clouds in Earth's changing climate, both the cloud property retrieval algorithms and satellite instruments used to monitor clouds must be subject to stringent accuracy requirements.

Cloud properties that are retrieved from spectral reflectance (RS) and brightness temperature (IR) measurements include cloud optical thickness (τ_c), effective particle size, particle thermo-

dynamic phase, cloud fraction, and cloud altitude. Several instrument-based and algorithm-based factors need to be evaluated to understand how they may contribute to aliasing in the trends of cloud properties retrieved from reflected solar satellite measurements. *Aliases* are distortions of a true signal due to undersampling, errors, or biases. Instrument and algorithm errors or biases that alias into cloud property time series could potentially be mistaken for climate change variability and trends. As existing satellite data records continue to exceed beyond decadal scales, the scientific community needs to quantify the amount to which algorithm and instrument accuracy could impact decadal-scale cloud property trends.

The CLARREO intercalibration capability will improve the absolute calibration of operational cloud imaging instruments. For our initial studies we are using the CERES Cloud Property Retrieval System (CPRS), which ingests MODIS spectral reflectance for its input. Because the MODIS Atmosphere Group and the CERES Clouds Team use different bands and different algorithm methods in their retrievals of cloud properties, it is likely that these dependencies will be different between the two retrieval systems. We therefore plan to extend these investigations with the MODIS cloud retrieval algorithms in the near future.
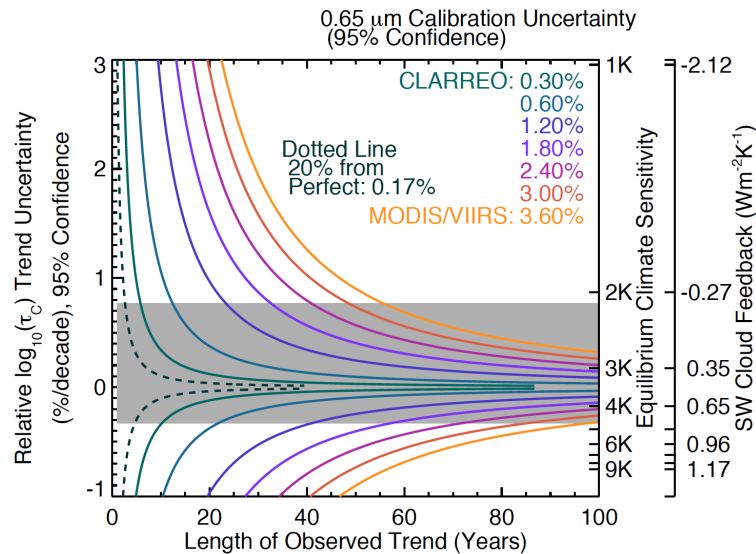
Figure 2.53: THESE RESULTS DEMONSTRATE THE IMPORTANCE OF STRINGENT ACCURACY REQUIREMENTS FOR CONSTRAINING THE TREND DETECTION TIME IN τ_c. RELATING THE τ_c TREND MAGNITUDE TO THE CMIP5 RANGE IN EQUILIBRIUM CLIMATE SENSITIVITY AND SW CLOUD FEEDBACK PROVIDES THE LIKELY RANGE OF τ_c TO FOCUS ON IN DETERMINING INSTRUMENT REQUIREMENTS.

Using the accuracy uncertainty factor, U_a (Equation 2.1), we can determine the needed instrument calibration uncertainty (the sole instrument uncertainty we are currently considering) for an instrument that is 20% from perfect (i.e. $U_a = 1.2$) for each cloud property, based on their natural variability. The units of the trend uncertainty (numerator of U_a) are dictated by the units of σ_{var} (natural variability of cloud property in question) and τ_{var} (autocorrelation time in years). We assumed a standard satellite instrument lifetime of 5 years for the calibration autocorrelation time τ_{cal}. With these known variables in hand, we solve for calibration uncertainty σ_{Vcal} in the units of the cloud variable.

The offline CERES Cloud Property Retrieval System (CPRS) was used to calculate the sensitivity of cloud properties to imposed gain and offset calibration changes to a subset of MODIS

reflectances (0.65 μm) and brightness temperatures (3.79 μm, 11 μm, 12 μm), respectively, ingested by the CPRS. From these calculations, we computed partial derivatives, providing the necessary relationship between the change in each cloud property and changes in MODIS reflectance and brightness temperature measurements for us to calculate σ_{cal} as a function of calibrated instrument units (i.e. $\partial\sigma_{Vcal}(\tau_c)/\partial\sigma_{cal}(\tau_c)$).

Figure 2.53 shows an example in which we used the natural variability of $log_{10}\tau_c$ to quantify calibration requirements in the 0.65 μm band. With the globally and annually CERES/MODIS anomaly time series, we calculated the relative uncertainty caused by natural variability and the natural variability autocorrelation time, and found the requirement for the 0.65 μm band to be 0.17% (2σ) for an instrument 20% from perfect. (Figure 2.53, dotted line) — nearly 50% more rigorous than the current CLARREO RS requirement of 0.3% (2σ). This stringent requirement calls for consideration to whether the goal for a RS instrument 20% from perfect is necessary for detecting climate change trends.

Using the conversion factor, $\partial\sigma_{Vcal}(\tau_c)/\partial\sigma_{cal}(\tau_c)$, and the numerator of the accuracy uncertainty factor, U_a (Equation 2.1), we calculate the time to detect trends in τ_c for a collection of instruments with a range of calibration uncertainties (Figure 2.53). There is another piece of information that will help to put these results into context: the range of τ_c trend magnitudes that we might expect for some range of SW cloud feedback. We estimated the relationship between τ_c trend magnitude in relative $log_{10}\tau_c$ per decade (left y-axis) and SW cloud feedback (far-right y-axis) using the τ_c contribution to the SW feedback [Zelinka et al., 2012] and radiative kernels. Then we estimated the relationship between SW cloud feedback and Equilibrium Climate Sensitivity (ECS) (internal right y-axis) with the relationship between the sum of climate feedbacks, global surface temperature trend, and globally averaged radiative forcing with estimates from [Zelinka et al., 2012] and [Stocker et al., 2013].

These relationships provide context within the CMIP5 ECS ensemble range (Fig. ??, shaded gray). Intersections between the shading and trend uncertainty curves gives the time needed to begin detecting trends of $log_{10}\tau_c$ that are likely for climate sensitivities within the CMIP5 range for instruments with different calibration uncertainties. For a perfect instrument taking measurements of Earth with an ECS on the less sensitive end of the boundary (2.1K), it would take about 5 years to detect a $log_{10}\tau_c$ of 0.8%/decade; however, it would take MODIS/VIIRS more than 12 times that long. A CLARREO RS instrument with a 0.3% requirement would take three years longer to detect a $log_{10}\tau_c$ trend than an instrument 20% from perfect.

In addition to examining the potential impacts of instrument calibration, several characteristics of cloud retrieval algorithms need to be evaluated to quantify their potential contributions to aliasing in climate change signals. Satellite cloud retrieval algorithms have been developed and rigorously validated to minimize the retrieval errors and uncertainties at the instantaneous pixel level; however, the accuracy of these retrieval algorithms on the longer temporal and spatial scales used in climate studies remains to be tested. Large spatial and temporal averages of cloud variables retrieved at the pixel level are essential for cloud parameterization development and climate change studies [King et al., 2003].

Several assumptions need to be made in cloud property retrieval algorithms such as the plane-parallel assumption and the estimation of ice particle shapes (habits). Errors, biases, or uncertainties that alias into climate signals based on these assumptions within the retrieval process may be sufficiently insignificant on smaller scales for process studies but in climate

change studies involving larger temporal and spatial scales, those errors may easily become large enough to mask or distort true climate signals, which are expected to be quite small.

In the near future, we will be focusing on the climate change scale impact of the cloud retrieval plane-parallel assumption. Many previous studies have evaluated the inability of 1D cloud retrievals to resolve 3D radiative effects, but such studies focused on small scales of individual cloud fields. Our studies will extend this previous work by looking at the impact of 3D τ_c bias for different ISCCP cloud top pressure-τ_c bin cloud types over climate change scales (e.g. global, annual averages). These studies will help resolve whether current cloud retrievals are able to discriminate domain-aggregated, long-term trends from inherent aliasing errors. However, the climate change scale impact of other retrieval error sources need to be quantified as well.

2.9.3 MODIS Degradation and C6+ Calibration Improvement

Aging of Earth observing sensors begins as soon as they start on-orbit operations. This happens for a number of reasons, the main being exposure to the solar and cosmic radiation. MODIS has been the primary pioneering sensor of the Earth Observing System on the Terra and Aqua platforms. Of the two, MODIS on Terra has had a more rapid on-orbit degradation accompanied with changes in the response vs scan angle (RVS) and increased polarization sensitivity. Until $\sim$ 2007, these changes were not detected through MODIS calibration, and they were not obvious in MODIS Terra science products. The latest analysis has demonstrated [Levy et al., 2010; Wang et al., 2012] and quantified [Lyapustin et al., 2014] trends in different MODIS C5 Terra and Aqua products including aerosol and cloud properties, as well as surface reflectance and vegetation index (NDVI/EVI). Figure 2.54 shows systematic negative trends in global monthly mean Terra Aerosol Optical Depth (AOD) over land from the Dark Target [Levy et al., 2007] algorithm (27 %/decade) and Terra ($\sim$ 13 – 17 %/decade) and Aqua (4 – 5 %/decade) Cloud Optical Thickness (COT) [Platnick et al., 2003; King et al., 2013] over both land and ocean. Lyapustin et al., [2014] demonstrated surface reflectance trends in MODIS visible-near-IR bands resulting in a negative NDVI trend of $\sim$ 0.01/decade. This is equivalent to the global Gross Primary Production (GPP) change of 1 PtG carbon (annually) and has significant implications for the global carbon modeling. Due to its longer record, MODIS Terra Collection-5 data (with stronger calibration-related trends) are often used to uncover long-term changes in the Earth system, which raises the importance of improved calibration and removal of trends in geophysical products.

Calibration of the MODIS solar reflective bands relies primarily on the solar diffuser (SD) and solar diffuser stability monitor (SDSM), which tracks SD degradation over time [Xiong and Barnes, 2006]. The standard MODIS calibration protocol tracks response at two angles of incidence (corresponding to SD and Moon view) out of the full RVS function. By the Collection-6 (C6) timeframe, enough evidence had accumulated to indicate that the MODIS/Terra RVS change is non-linear and that the previous Collection-5 (C5) approach was not sufficient [Sun et al., 2012]. To track RVS change, the MODIS Calibration Science Team (MCST) C6 calibration algorithm introduced the Earth View (EV) monitoring of stable desert calibration sites, recommended by the CEOS [*http://calval.cr.usgs.gov/sites_catalog_map.php*]. In this case, all Angles Of Incidence (AOis) can be characterized independently via surface BRDF. The new C6 calibration approach removes major calibrations trends in MODIS Level 1B data.
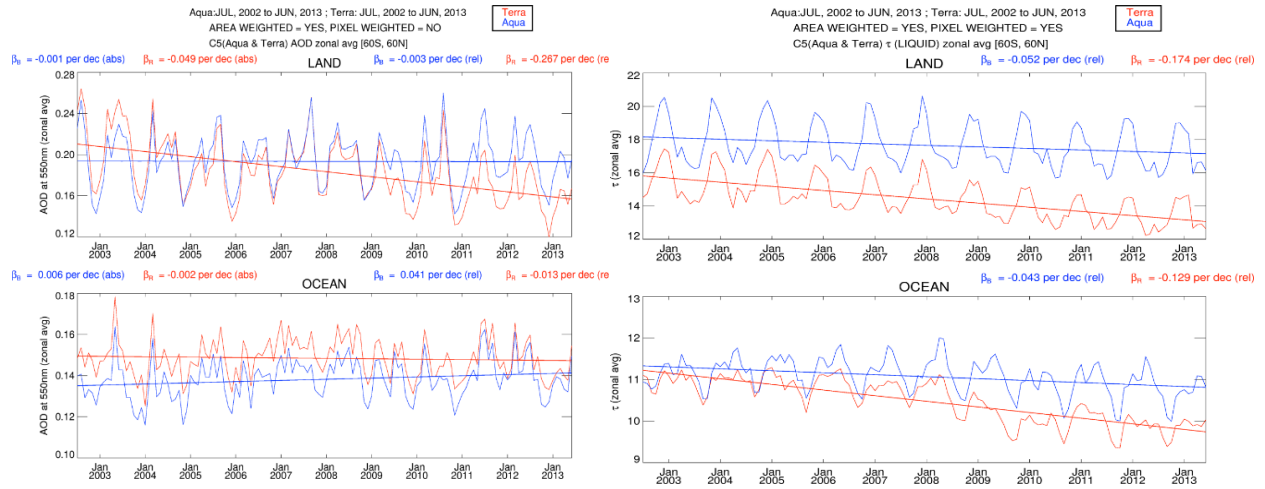
Figure 2.54: TIME SERIES OF C5 "DARK-TARGET" MONTHLY GLOBAL MEAN AOD AT 0.55 μM (LEFT) AND LIQUID-PHASE CLOUD OPTICAL THICKNESS (COT) (RIGHT) OVER LAND (TOP) AND OCEAN (BOTTOM) FOR MODIS TERRA (RED) AND AQUA (BLUE) DURING JULY 2002 – JUNE 2013. THE SHOWN LINEAR TREND SLOPES ARE GIVEN IN UNITS OF AOD OR COT PER DECADE (β_B) AND PERCENT/DECADE (β_R). DATA ARE OBTAINED FROM MONTHLY LEVEL 3 MODIS PRODUCTS.

At the same time, analysis by the ocean biology processing group (OBPG) detected changes in the MODIS Terra polarization sensitivity [Franz et el., 2008], and developed a polarization correction method through Terra/Aqua cross-calibration over clear-sky ocean scenes [Meister et al., 2012; Kwiatkowska et al., 2008]. This method uses Level 3 ocean color and aerosol products from MODIS/Aqua to compute expected TOA radiance for the Terra overpass time and view geometry. This "theoretical" radiance is related to Terra measurements via elements of its Mueller matrix where polarization is assumed to be from Rayleigh scattering and Fresnel reflectance from the ocean surface. The OBPG produces the time-dependent set of coefficients for MODIS Terra polarization correction (PC), which also depends on the mirror side, band, detector number, and scan angle. This correction removes the 10 km striping from the AOT product along with spectral distortions of surface Red-Grenn-Blue (RGB) Bi-directional Reflection Functions (BRF).

Band	Δ_T	σ	Δ_A	σ	Gain	σ
B1	0.0048	0.0020	-0.0046	0.0022	1.0200	0.0024
B2	0.0035	0.0019	-0.0062	0.0027	1.0060	0.0016
B3	-0.0082	0.0015	-0.0048	0.0016	0.9910	0.0013
B4	0.0049	0.0022	-0.0021	0.0023	1.0090	0.0031
B8	0.0094	0.0015	-0.0015	0.0013	0.9960	0.0015

Table 2.4: AVERAGE TREND PER DECADE PER UNIT OF REFLECTANCE FOR MODIS C6 TERRA (Δ_T) AND AQUA (Δ_A), AND MODIS TERRA GAIN ADJUSTMENT WITH CORRESPONDING STANDARD DEVIATIONS.

While the new C6 calibration approach and PC-correction of MODIS/Terra provided a much needed improvement, we found it insufficient for the climate applications. Our further Multi-Angle Implementation of Atmospheric Correction (MAIAC) based analysis [Lyapustin et al., 2011; 2012] over CEOS desert calibration sites revealed the presence of residual calibration

trends of several tenths of one percent TOA reflectance in the visible-near-IR MODIS bands of both Terra and Aqua sensors. Figure 2.55 (left) shows the time series of daily TOA reflectance (R_n^{TOA}) in MODIS Band-3 (B3, 0.47 μm) and near-IR (B2, 0.87 μm) bands for the normalized view geometry (VZA = 0°, SZA = 45°). R_n^{TOA} was computed using MAIAC-retrieved parameters including cloud mask, column water vapor, aerosol properties, and spectral surface BRDF. The TOA normalized reflectance R_n^{TOA} provides the required de-trending (slope) coefficients for each band as shown in the left and middle plots for Terra and Aqua. After an application of de-trending, Figure 2.55 (right), the geometry-normalized R_n^{TOA} provided the means to assess Terra-Aqua calibration gain difference. As MODIS Aqua has been a more stable and better characterized sensor, the derived gain adjustment is applied to MODIS Terra. The summary of de-trending coefficients and gain adjustment factors, with respective standard deviations for MODIS bands B1 – B4, B8 is presented in a summary Table 2.4.
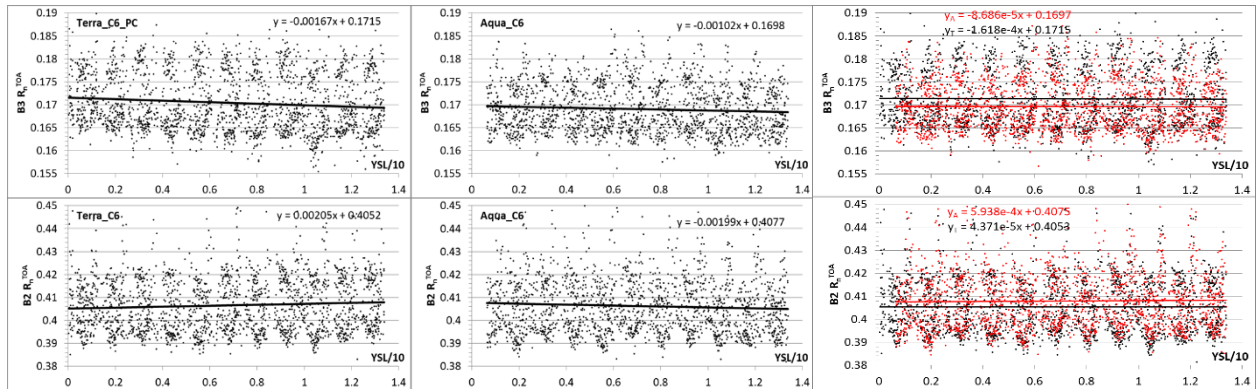
Figure 2.55: Left: Derivation of de-trending coefficients over Libya-4 site for MODIS Terra and Aqua bands B2 and B3. The vertical axis shows clear-sky daily reflectance R_n^{TOA} computed for the normalized geometry, and the horizontal axis shows Years Since Launch (YSL)/10. Right: Clear-sky daily reflectance R_n^{TOA} after de-trending illustrating possibility of Terra-to-Aqua cross-calibration.

Effectively, this very extensive analysis has led to the new C6+ MODIS dataset augmenting C6 calibration with PC for MODIS Terra bands B8 – B10 and B3. This removes the residual scan angle, mirror side, and seasonal errors from aerosol and surface reflectance records, followed by de-trending of both sensors and by an additional gain adjustment for MODIS Terra to match the Aqua TOA record.

The MAIAC-based science analysis over the southern USA shows that the C6+ version will provide the most reliable MODIS record with the best consistency between Terra and Aqua measurements. The latter will significantly benefit multiple algorithms which rely on the time series analysis and which use or may use the combined MODIS Terra – Aqua record. This would include the BRDF/albedo algorithm [Schaaf et al., 2002], change detection [Roy et al., 2002], MAIAC etc. The removal of additional negative decadal trend artifacts from Terra ΔNDVI ~ 0.01 (ΔEVI ~ 0.02) has implications for the global carbon modeling and analysis of vegetation dynamics, especially over the tropics where morning Terra provides on average about a 30% more cloud-free observations [Hilker et al., 2012]. Specifically, this result may explain some recently reported trends in gross and net primary productivity or vegetation greenness [e.g., Zhao and Running, 2010]. As a result, implementation of the C6+ calibration

may help address the problem of "missing carbon sink" [e.g., Myneni et al., 2001; Pan et al., 2011].

Present work is an evolution of cross-calibration techniques which rely on the stability of one of the sensors, in this case, MODIS Aqua. This principle is central for both polarization correction and for gain adjustment of MODIS Terra. At the same time, MODIS on Aqua is in its 12th year of operation showing calibration trends as demonstrated in our vicarious calibration analysis (VCA) over deserts. While we were able to remove major trends, the accuracy of VCA is limited and will be harder to maintain with further sensor aging. This argument strongly advocates for the independent on-orbit science facility for cross-calibration of the Earth's Science sensors, which would help create the well-calibrated long-term Earth's Science records of essential climate variables. CLARREO holds promise to achieve this goal with accuracy unprecedented for our current fleet of Earth viewing instruments.
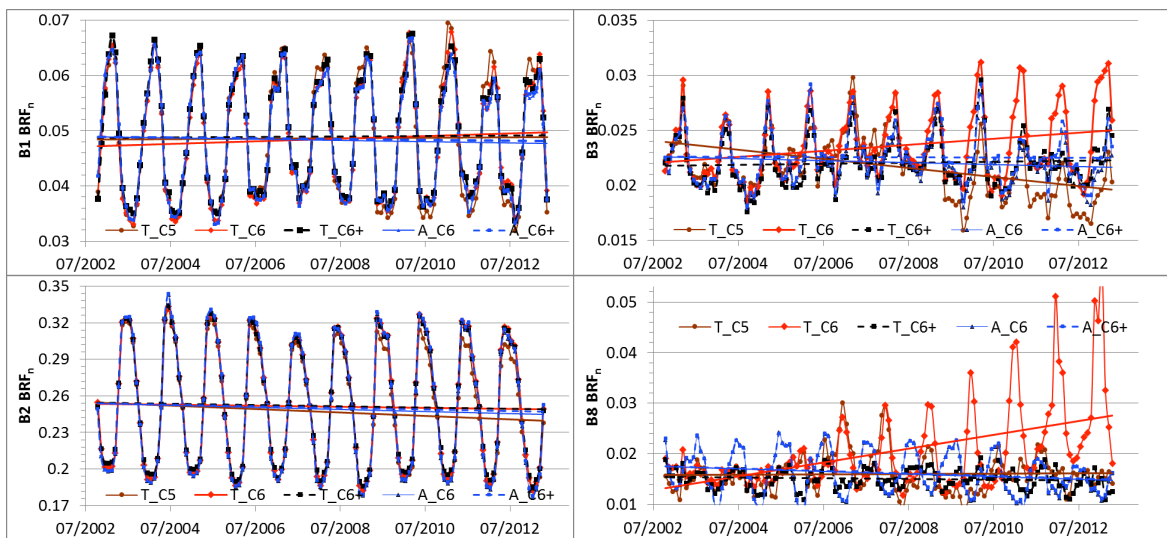
Figure 2.56: TIME SERIES OF MAIAC CLEAR-SKY MONTHLY BRF_n FOR GEORGIA (USA) REGION.

While aging of the "reference" sensor is the dominant issue, aging of the calibrated sensor becomes a growing technical challenge as well. For instance, current calibration procedure starts with MCST analysis including SD, Moon view, and desert Earth view targets trending. The OBPG group uses the resulting C6 Level-1B dataset to derive PC coefficients. These two procedures can be effectively de-coupled when both RVS and polarization changes are relatively small, but it can become unstable with further sensor degradation. Figure 2.56 shows MAIAC-based geometrically-normalized surface reflectance (BRF_n) in bands B1 – B2 and B3, B8 processed with different versions of calibration including C5, C6 and C6+ for Terra, C6, and C6+ for Aqua. Plots for bands B3 and B8 show the over-correction in the C6 Level-1B version from the introduced RVS trending over the desert sites. In B8, this procedure results in unstable growth of the BRF_n seasonal amplitude over time, which is then cancelled by the OBPG's polarization correction. The main reason for this instability is the lack of accounting for the sensor's polarization sensitivity during the C6 RVS trending. This emphasizes the need for an on-orbit, high accuracy calibration reference such as CLARREO [Wielicki et al., 2013], and further improvement of the MCST calibration routine which should simultaneously account for the changes in RVS and in polarization sensitivity of the sensor.

92

2.10   Near Term Impacts on Earth Science

While the primary focus of the CLARREO mission is on high accuracy decadal change observations, there will be a wide range of benefits to many other aspects of Earth science. These benefits can be realized in the first few years of the mission and do not require the decades needed to detect climate change.

2.10.1   Spectral Far-InfraRed Observations

Earth is a far-infrared planet [Harries et al., 2008]. The energetically significant range of infrared emission spans the region from 100 to 4 μm (100 to 2500 cm^{-1}). The far-infrared (far-IR) portion spans 100 to 15.5 μm (100 to 650 cm^{-1}) and was last observed from space by the Interface Region Imaging Spectrograph (IRIS) instrument [Hanel et al., 1971] on the Nimbus IV spacecraft in 1970 over a period of 9 months. The far-IR includes 50% of the Earth's infrared energy emitted to space and contains most of the Earth's water vapor greenhouse effect [Mlynczak et al. 2006]. The free troposphere cools to space almost entirely in the far-IR [Clough et al., 1992]. As a result, the far-IR dominates the physics of the water vapor feedback in climate, but has yet to be observed from space to verify climate model simulations of these processes. The effect of clouds in the far-infrared also remains unobserved in high-resolution spectra, and radiative transfer model discrepancies have been identified in the limited number of far-infrared measurements (from aircraft) that have been made in the presence of clouds [Cox et al. 2010]. Thus, the far-infrared spectrum plays a crucial role in the energy balance of the Earth. Accurate observations of the far-IR remain a frontier of Earth system and climate science.

CLARREO will provide the first accurately calibrated full infrared (50 to 4 μm; 200 to 2500 cm^{-1}) spectral observations from space, including the first accurate spectral observations of the far-IR from 50 to 15.5 μm (200 to 650 cm^{-1}). There are no extant high accuracy, near-global, spectral data to simultaneously validate radiative physics across the entire IR spectrum, mid-IR, and far-IR. CLARREO provides that dataset for the first time to achieve the following leading-edge scientific discoveries:

(1) Determine the Earth's spectral greenhouse effect across the entire IR spectrum, including the far-IR, for clear-sky and all-sky conditions.
(2) Determine spectral cloud radiative forcing (CRF) across the entire IR spectrum, including the far-IR.
(3) Determine the atmospheric radiative cooling rate profile consistent with the entire IR spectrum, including the far-IR.
(4) Verify climate model performance across the entire IR spectrum, including the far-IR.
(5) Measure Earth's surface emissivity in the far-IR in polar regions where the water vapor burden is < 1 mm and the surface can partially radiate to space in far-IR windows [Feldman et al., 2014b].

3 CLARREO Economic Value and Societal Benefits

Climate science, as science in general, is an economic investment by the public. However, we currently have no national or international climate observing system, nor a plan to create one. Should we invest in one? Is it worth it? What is the economic value of an advanced climate observing system? And, how to estimate it?

We have a few traceable estimates of the economic value of weather prediction for severe storms, hurricanes, floods, and droughts. Climate scientists often say that the results from their research *"will inform societal decisions with trillion dollar impacts."* But is this statement verified and traceable in any way? How could we quantify an economic value to climate science? Recall that climate change science value exists decades into the future. Its value has to be treated as a risk/benefit economic analysis. A rigorous analysis must take into account the uncertainties in climate science, economic impacts, and policy (see Figure 3.1).
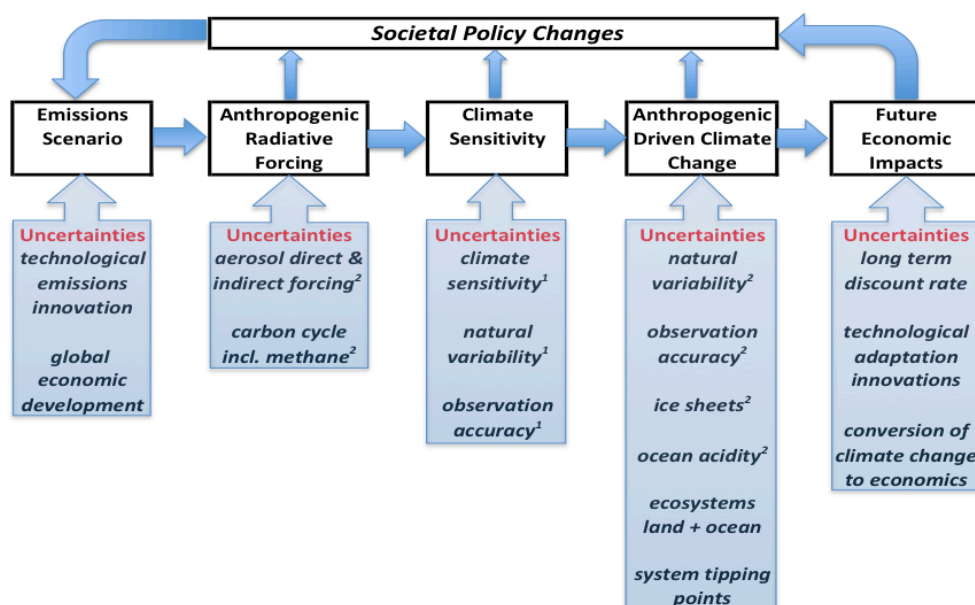
Figure 3.1: VALUE OF CLIMATE SCIENCE OBSERVATIONS.

Science value and economic frameworks are potentially valuable for strategic planning of the Earth observing system, as well as communicating climate research value to society. We present in this Section a new methodology to estimate the economic value to society of advanced climate observing systems.

3.1 Value of Information Approach

The uncertainty of societal decisions on climate change is strongly affected by the uncertainty in the future predictions of climate change. For example, the 90% confidence bound for equilibrium climate sensitivity is a factor of 4 [IPCC, 2013]. Climate sensitivity defines the relationship between an increase in carbon dioxide in the atmosphere and the amount of global surface air temperature change. Studies of the economic impacts of climate change [Interagency Social Cost of Carbon Memo, 2010, hereafter SCC] suggest a quadratic relationship

between amount of global temperature change and the magnitude of economic impacts. *In this case, the factor of 4 uncertainty in climate sensitivity causes a factor of 16 uncertainty in long term economic impacts, which leads to inefficient and uncertain solutions for climate change.*

Society (and climate science) views past climate change through two sets of "fuzzy" lenses. The first is natural variability in the climate system which acts as noise to confuse early signals of anthropogenic climate change. The second is uncertainty in our observations of climate change, including drifting calibration of instruments or orbit sampling uncertainties, described in Section 2.2. Figure 2.4b shows an example of these uncertainties for observing one of the critical measures of climate sensitivity: changes in the amount of global mean solar energy reflected back to space by clouds as climate changes.

CLARREO is designed to serve as reference calibration spectrometers for the entire reflected solar and thermal infrared spectrum. Its orbit is designed to underfly all geostationary and low Earth orbit satellites with matched time/space/angle of view observations, and thereby provide the SI standard reference calibration system in orbit to allow instruments such as CERES, MODIS, VIIRS, CrIS, IASI, Landsat, and others to maintain highly stable calibration over decades, even if gaps in observations occur [Wielicki et al., 2013].

The IPCC climate model range of trend values are shown in the green arrow at the lower left of Figure 2.4b. *Figure 2.4b shows that advances in accuracy can advance by 20 years the ability to observe cloud feedbacks and thereby narrow uncertainty in climate sensitivity.*

Figure 2.4a shows a similar example for observations of global mean temperature trends from space-borne instruments. The conclusions are similar.
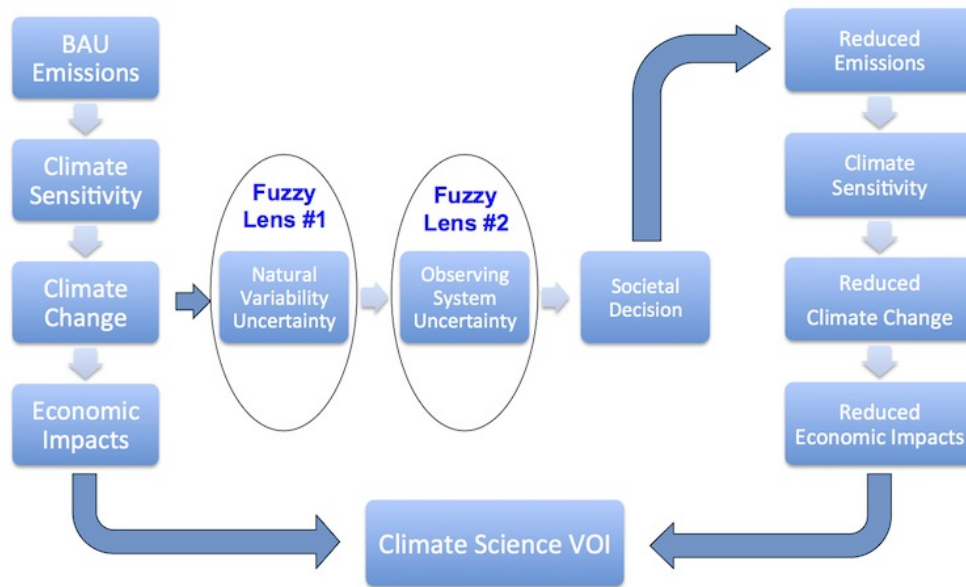
Figure 3.2: VOI ESTIMATION METHOD.

Given these results, what would an advance of 15 to 20 years in climate change knowledge mean in terms of economic impacts of climate change? The schematic in Figure 3.2 shows how to test such a concept. The concept uses the climate accuracy framework from Wielicki

et al. 2013 developed for the CLARREO mission, and combines it with the SCC 2010 estimates of future climate impacts for varying levels of warming, and the DICE 2009 integrated assessment model [Nordhaus, 2008], which links models of climate physics, economic development, and economic impacts. The Figure 3.2 shows the dependence of economic impacts from climate change on societal decision points, which are in turn dependence on the accuracy of climate observations. The Dynamic Integrated Climate-Economy (DICE) model is run for 1000s of simulations varying climate sensitivity (SCC 2010 distribution), natural variability realizations, and emissions scenarios.

3.2   Economic Impact of Climate Observations

Before we discuss the results, we need a quick version of Economics 101. First, the global Gross Domestic Product (GDP) per year is about $70 Trillion US dollars. Second, economics calculations use a concept called Net Present Value (NPV) to equate investments and returns over long time intervals. To do this, a Discount Rate is used, which varies in the SCC 2010 report from 5% to 3% to 2.5%. The effect of using the nominal 3% Discount Rate is that the economic benefits gained in the future are discounted by 3% per year, so that benefits gained 50 years from now are "discounted" by a factor of 1.0350, or a factor of 4.4. This means that economic benefits 50 years into the future are decreased by a factor of ~ 4.4, while benefits 100 years into the future are decreased by a factor of ~ 20. Finally, the recent financial crisis affected worldwide GDP by a few percent. This is similar to the economic impacts of climate change in the second half of this century, which are expected to range from 0.5% to 5% of GDP per year depending on climate sensitivity and the amount of warming realized. *Therefore, future climate change impacts can range from $0.4T to $3.5T per year.*

The calculations in this study use a baseline scenario of a societal trigger when 95% confidence is reached for a global average temperature increase of 0.2°C/decade, and an advanced full climate observing system begins in 2020. All initial calculations use a simple switch from higher to lower emissions scenarios.

Discount Rate	NPV of VOI
2.5%	$17.6 T
3.0%	$11.7 T
5.0%	$3.1 T

Table 3.1: The NPV in US 2015 dollars for CLARREO improved climate observations.

Table 3.1 summarizes the results for CLARREO improved climate observations, and shows a NPV of $11.7 Trillion U.S. dollars for the nominal 3% discount rate. While the CLARREO example of advanced accuracy has been used in this initial estimate, society would never base a decision on any one set of instruments, so this economic value should be viewed as that of an advanced full Climate Observing System, which CLARREO would be a key part of. If we estimate that such a system would cost 4 times the current investment in world climate research of about $4B/yr, then over 30 years, the additional cost in NPV would be about 1/50th of the benefits shown in Table 3.1. Every $1 invested returns $50. We also examined sensitivity of the results to the assumed baseline parameters by changing the warming rate from 0.2°C to 0.3°C/decade for the societal decision trigger, by varying the

statistical confidence required (80 to 99%) and the severity of the emissions reduction scenario (moderate or severe). In all cases, the economic value remained within about 30% of the values in Table 3.1. The results of this study have been published in the Journal of Environment, Systems, and Decisions [Cooke et al., 2013].

In a second paper [Cooke et al., 2015] several improvements are made to the original VOI estimates of an advanced climate observing system. First, a more realistic relationship between carbon emissions and global GDP following shifts between different emission scenarios was implemented. This change increased the VOI. Second, the cost of carbon emission reductions was added, which reduced VOI. Third, the economic concept of Real Option Value was included in the analysis. Real Option Value explicitly models the impact of current economic investments on the future flexibility and efficiency in changing economic conditions. Following all three of these improvements, the economic value of an advanced more accurate climate observing system changed from the initial estimate of $12 Trillion to $9 Trillion. Both estimates are for the nominal discount rate of 3% used in the U.S. Social Cost of Carbon Memo (2010). The improved VOI value remains within the +/- 30% uncertainty of the original VOI result as determined by a sensitivity analysis that varied several assumed parameters.

3.3   CLARREO Societal Benefits

The Decadal Survey [NRC, 2007] recommendations were strongly based upon the societal benefits of the missions. The primary benefit from CLARREO will be in strengthened decision support from improved climate predictions. The creation of a benchmark climate record that is global, accurate in perpetuity, pinned to international standards and that can be used to develop trusted, tested climate forecasts is necessary for the decision support structure for responding to climate change. CLARREO will provide this by measuring solar reflected and infrared emitted high spectral resolution benchmark radiance climate data records that can be used to test climate model predictions, improve climate change fingerprinting, and attribution. These climate records will be augmented and complemented by the GNSS RO refractivity data record. By reducing climate prediction uncertainties, CLARREO impacts: civil Government and military planning (i.e., Navy bases), disaster mitigation, response, and recovery (i.e., insurance industry), and U.S. international policy decisions.

CLARREO will also provide climate-accuracy calibration for operational sensors, making its measurements a cornerstone of the Earth observing system. CLARREO data will be used to calibrate other solar and infrared space-borne sensors and thereby improve climate accuracy of a wide range of sensor measurements across the Earth observing system. This is in alignment with the recommendations of the Achieving Satellite Instrument Calibration for Climate Change (ASIC3) and the GSICS, both of which call for benchmark instruments in space with appropriate accuracy, spectral coverage, and resolution to act as a standard for inter-calibration (see Section 2.8).

The CLARREO mission will also help to address a major issue of our current observing system. Climate data records that are not tied to the accuracy standards of CLARREO cannot produce long-term climate data records without substantial overlap between successive instruments. Without overlap, long-term data records, such as the Earth radiation budget, will be irretrievably broken if a new instrument cannot be launched prior to the failure of

the current instrument. The requirement for redundant and overlapped missions has a great impact on the cost of the entire observing system. The absolute accuracy of CLARREO, when used to calibrate other sensors in orbit, can dramatically reduce the impact of data gaps on decadal change data records across many climate variables.

CLARREO will also provide the first space-based measurements of the Earth's far infrared spectrum. This opens a new window to 50% of Earth's IR spectrum, with key information on water vapor feedback, cirrus radiative forcing, and the natural greenhouse effect (see Section 2.10.1).

3.4   International Partnering

Efforts are underway for international collaboration in CLARREO-like missions. Establishing SI traceable standards in orbit is similar to establishing metrological standards here on Earth. International standards require independent verification. Therefore, the long-term vision for CLARREO-like missions includes a US version, along with at least one international version, for independent verification. In support of this goal, the CLARREO team has been collaborating with two mission proposal groups in Europe: the Traceable Radiometry Underpinning Terrestrial- and Helio- Studies (TRUTHS) mission [Fox et al., 2011] for high accuracy solar reflected spectra, and the Far-Infrared Outgoing Radiation Understanding and Monitoring (FORUM) mission for high accuracy thermal infrared spectra. This collaboration is the key to achieving the required accuracy for global climate change data. These missions represent a new era of climate change accuracy viewing the entire globe, and provide a foundation for the first true global climate observing system. Hopefully, we can have the foresight to provide that accuracy to future climate science, and thereby facilitate an improved understanding of the trajectory of the climate system among future climate scientists.

4 CLARREO Measurements and Instrumentation

4.1 Measurement Requirements

Table 4.1 provides a summary of the CLARREO instrumentation and mission requirements. The requirements were used to develop instrument designs, with the additional goal of reducing instrument size to minimize mass, power, and cost. The CLARREO instruments at the Mission Concept Review (MCR) are about 18kg (RO), 76kg (IR), and 69kg (RS), much smaller than typical weather instruments such as VIIRS (252 kg), CrIS (152 kg), or IASI (210kg). This allows flight on small spacecraft and launch vehicles. The entire suite of CLARREO instruments would require a satellite with mass of only 1/3 to 1/6th that of the flagship missions Terra, Aqua, or NPP. The instrument designs leverage almost a decade of investments by the NASA Earth Science Technology Office (see Section 4.5).

4.1.1 Requirements for InfraRed Measurements

CLARREO shall obtain infrared radiance spectra of the Earth and its atmosphere using nadir views from orbiting satellites. The benchmark and reference inter-calibration measurements require:

A. Broad spectral coverage of the Earth's emitted spectrum, including the far-infrared, that captures climate trend information about atmospheric structure, composition, clouds, and surface properties;
B. Spectral resolution chosen for greenhouse gas species separation and for vertical structure information;
C. Radiance measurement systematic error that corresponds to < 0.1 K brightness temperature radiometric calibration uncertainty ($k = 3$ confidence, excluding random noise) for the range of expected Earth scene temperatures and wavelengths relevant to climate;
D. Spatial and temporal sampling sufficient to provide global coverage and reduce sampling errors to levels that degrade the measured climate trend accuracy by less than 15%, and that degrade the time to detect climate trends less than 10%. The degradation of trend accuracy is relative to the limits of accuracy caused by climate natural variability.

4.1.2 Requirements for Reflected Solar Measurements

CLARREO shall obtain the solar spectral nadir reflectance of the Earth and its atmosphere relative to the solar irradiance spectrum. The benchmark and reference inter-calibration measurements require:

A. Broad spectral coverage of the Earth's shortwave reflected spectrum, that captures climate trend information about atmospheric structure, composition, clouds, and surface properties;
B. Spectral resolution chosen to resolve atmospheric structure, composition, clouds, surface properties, and to allow reference inter-calibration of the solar reflected spectral bands of climate relevant operational sensors;
C. Reflectance measurement with an absolute uncertainty of 0.3% relative to global mean reflected solar energy ($k = 2$ confidence excluding random noise) for the range of Earth

InfraRed (IR) Spectrometer	Reflected Solar (RS) Spectrometer	GNSS Radio Occultation	Spacecraft Orbit
Systematic error $< 0.1K$ ($k = 3$)	Systematic error $< 0.3\%$ ($k = 2$) of Earth mean reflectance	Systematic error $< 0.03\%$ refractivity ($k = 1$) for 5–20 km	$90 \pm 0.1°$ inclination for full diurnal sampling twice/year
200–2000 cm^{-1} spectral coverage	320–2300 nm spectral coverage	GPS and Galileo GNSS frequencies	Global Coverage
0.5 cm^{-1} unapodized spectral resolution	4 nm spectral sampling, 8 nm spectral resolution	5 to 20 km altitude range refractivity	609 ± 0.2 km altitude 61-day repeat
NeDT<10K for 200-600 cm^{-1} and >1600, all others <2K	S/N>33 for 0.3 scene reflectance at SZA 75°, S/N>25 for $\lambda > 900$ nm	>1000 occultations per day to control sampling noise	RAAN of 0° or 180° to optimize inter-calibration
20–100 km nadir footprint	0.5 km nadir pixels, 100 km swath		5 yr initial mission record length
<200 km between successive FOVs along ground track	Polarization sensitivity $< 0.5\%$ ($k = 2$) for VIS and NIR		Repeat exactly each year to avoid diurnal/seasonal cycle aliasing
Nadir pointing with systematic error $< 0.2°$	Pointing in azimuth and elevation for solar, lunar, and inter-calibration views		RS and IR fly on same spacecraft or in close formation
Prototype design: 4 port FTS, 76 kg mass, 124 W avg. power, 2.5 Gbytes/day	Prototype design: Dual Grating Spectr., 69 km total mass, 96 W avg. power, 30 Gbytes/day	Prototype design: TriG Receiver, 18 kg mass, 35 W avg. power, 1.2 Gbytes/day	IR/RO or RS fueled spacecraft mass 370 kg, can fit on small launch vehicles

Table 4.1: The science team mission studies were used to derive the mission and instrument requirements. Those requirements are summarized for the 3 instrument types as well as the mission orbit. Prototype designs were developed for all of the instruments, with similar designs being used to verify calibration accuracy tests in collaboration with NIST. A wide range of mission orbits, spacecraft, and launch vehicle designs were considered, and judged against a science value/cost matrix (see Section 5.2) to optimize these requirements.

reflected solar energy at the wavelengths relevant to decadal climate change.

D. Spatial and temporal sampling sufficient to provide global coverage and reduce sampling errors to levels that degrade the measured climate trend accuracy by less than 10%, and that degrade the time to detect climate trends less than 7%. The degradation of trend accuracy is relative to the limits of accuracy caused by climate natural variability.

4.1.3 Requirements for GNSS-RO Measurements

The radio occultation instrument of CLARREO is intended to capture a snapshot of the state of the atmosphere with uncertainty in that state, determined empirically, that can be used to accurately determine change on decadal timescales. By comparing a retrieved quantity derived from well calibrated, reproducible observations from one epoch to the next using a common retrieval algorithm, the change of the atmosphere as revealed in a retrieved quantity is determined without contribution from retrieval error. Consequently, retrieval error is irrelevant to CLARREO radio occultation. However, all errors that directly affect the observation of the SI-traceable observation are relevant; these are "individual sounding" errors. Moreover, because CLARREO seeks accurate snapshots of the state of the global atmosphere, errors due to sub-sampling in space and time are also relevant; these are "climatological averaging" errors.

Atmosphere Occultation Individual Sounding Measurement: CLARREO shall measure the phase delay rate of the GNSS transmitted signal occulted by the atmosphere from low Earth orbit:
A. Over altitudes from 5 km to 20 km at 200 m vertical resolution.
B. With an uncertainty in the phase delay rate (from all error sources) of 0.5 mm s^{-1}.

Atmosphere Occultation Climatological Averaging Measurement: CLARREO shall measure the averaged microwave refractivity of the GNSS transmitted signal occulted by the atmosphere from low Earth orbit:
A. Over 1 year, in 10° latitudinal zones, over all longitudes.
B. Over altitudes from 5 km to 20 km at 200 m vertical resolution.
C. With an uncertainty in refractivity (from all error sources) of 0.03%($k = 1$).

4.2 Reflected Solar Instrument Concept

4.2.1 CLARREO RS Instrument Description

Requirements for the CLARREO RS observation are summarized in Section 4.1 and Table 4.1, with details behind how these requirements have been derived given in Section 2. The sensor concept design, as shown in Figure 4.1, is based on the required derivation of an at-sensor reflectance over the spectral range from 320 to 2300 nm with 4 nm spectral sampling, with 0.5 km ground-field-of-view (GFOV), and a 100 km swath width. The two separate focal planes cover spectral ranges of 320 – 640 and 600 – 2300 nm, and are implemented as two individual "blue" and "red" spectrometers. CLARREO's measurements of radiance, while viewing the Earth's surface, will be converted to a reflectance through ratios to solar- and lunar-based measurements [Wielicki et al., 2013]. The measurement signal will vary by

factors of 2 to 10 because it is functionally dependent on solar zenith angle, wavelength, atmospheric gas absorption that changes with altitude and wavelength, and scene type that ranges from dark (clear-sky ocean) to bright (deep convective clouds). The RS instrument must be designed to account for these effects to include a calibration approach that allows accurate retrieval of the reflectance in the mid-visible wavelength range, and be traceable to SI standards at a level better than 0.3% ($k = 2$). Such a required accuracy provides a data set that, when collected globally, reduces sampling biases for climatologically significant spatial and temporal averages over annual means. The instrument spectral range and spectral sampling requirements are motivated by inter-calibration of the broadband (CERES) and narrowband radiometers (VIIRS), respectively. The spatial sampling 0.5 km ground-field-of-view is for achieving a quality cloud masking, and spatial coverage is motivated by the CLARREO RSS "benchmark" global sampling at nadir. In order to achieve the reference inter-calibration mission objectives, the CLARREO RS instrument will be designed to allow the boresight to be pointed along selected lines of sight within the fields of view of orbiting target sensors, as illustrated in Figure 2.33.
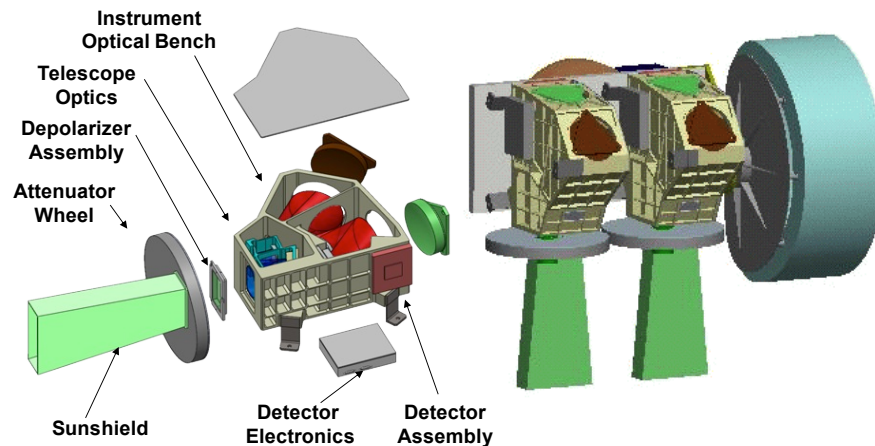
Figure 4.1: CLARREO RS SPECTROMETER CONCEPT DESIGN, SHOWING DETAILS OF A SINGLE SPECTROMETER AS WELL AS THE TWO-SPECTROMETER SYSTEM AS IT MIGHT APPEAR ON THE SPACECRAFT.

The primary data product from the RS instrument is spectral reflectance. The current operational plan for the RS instrument is to determine the ratio of the output of the instrument while viewing an Earth scene, to that of the instrument while viewing the Sun. Taking into account the geometry differences between a radiance measurement (while viewing the Earth scene) and an irradiance measurement (the solar measurement) permits the retrieval of a directional-hemispheric reflectance. Thus, the RS sensor will function like a band-ratioing radiometer. The instrument is based on an Offner imaging spectrometer design, which is capable of limiting spectral smile on the focal plane. The instrument will operate as a push-broom imager with a reliance on heritage hardware, reduction of sensor complexity, and solar- and lunar-source based calibration.

The most critical parameter of CLARREO instrument design is the radiometric calibration accuracy requirement of 0.3% of reflectance integrated across all wavelengths and for individual bands. Such a requirement is nearly an order of magnitude improvement over past and existing sensors. The sensor SNR values for a single sample are defined for a typical radiance based on a reflectance of 0.3 and incident solar zenith angle of 75°. The required
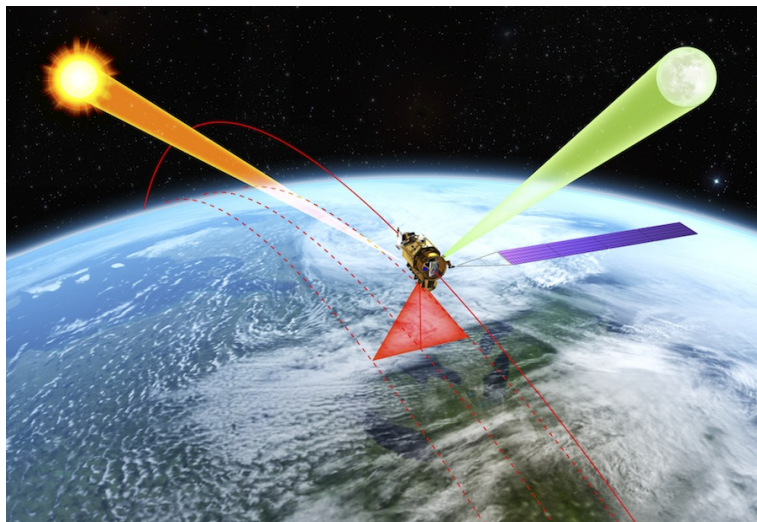
Figure 4.2: CLARREO RS INSTRUMENT CALIBRATION CONCEPT: VERIFICATION OF NADIR SPECTRAL REFLECTANCE ACCURACY RELIES ON ROTATING THE ENTIRE INSTRUMENT TO VIEW THE MOON AT CONSTANT PHASE ANGLE AS A STABLE REFLECTANCE SOURCE (SIMILAR TO THE SEAWIFS), THE SUN IN COMBINATION WITH FILTERS AND PRECISION APERTURES FOR NONLINEARITY DETERMINATION, AND THE USE OF DEPOLARIZERS TO CONTROL POLARIZATION SENSITIVITY.

SNR is > 33 for wavelengths 380 – 900 nm and an SNR > 20 for other wavelengths. Figure 4.2 demonstrates the approach for the reflected solar spectrometer and its use of the Moon as a reference for stability in orbit, the Sun with multiple attenuators to verify instrument nonlinearity of gain across the Earth viewing dynamic range, and ability to directly scan deep space to verify instrument offsets [Espejo et al., 2011; Fox et al., 2011]. Spectral response is verified using solar spectral absorption line features. One of the critical differences of this instrument relative to others in orbit is its ability to point the entire instrument at Earth, Sun (every 2 weeks), Moon (monthly at 5 to 10 degree phase angle), or deep space. This eliminates the need for scanning mirrors with angle dependent calibration uncertainties, and allows the use of depolarizers to reduce polarization sensitivity to the required levels of < 0.5% (k=2) over entire spectral range [Lukashin et al., 2015]. Scanning the instrument view across lunar and solar disks provides images suitable for verifying stray light performance. Finally, any future improvements in the absolute reflectance of the lunar surface can be used to tie the CLARREO solar spectrometer results to future improvements in calibration beyond CLARREO, even should these improvements come 10 or 30 years from now [Kieffer, 1997; Kieffer and Stone 2005]. Note that the calibration of the reflected solar is in terms of reflectance units. Conversion to absolute radiance can be done using the spectral total solar irradiance provided by instruments, such as TSIS, with expected absolute accuracy of 0.25% [Richard et al., 2011].

4.2.2 CLARREO RS Instrument Calibration

The instrument design relies on a direct solar view as the primary calibration approach while on orbit. The data from a solar view are coupled with the Earth view data and knowledge of the sensor optical geometry to retrieve at-sensor reflectance. Calibration SI-traceability is the cornerstone of the success of CLARREO's mission. Demonstration of SI-traceability requires both a detailed preflight calibration and then a transfer of that calibration to orbit. It is expected that the primary sources of error in transferring the prelaunch calibration to orbit will be changes in stray light behavior and sensitivity to polarization.

In order to observe both Earth's reflected radiance and solar irradiance (to have both signals in the same dynamic range), the RS instrument must be able to reduce the incident solar irradiance to a level comparable to the Earth-viewing radiance, approximately a factor of

50,000. The attenuator approaches being evaluated include a single pinhole aperture, neutral density filters, a collection of pinhole apertures, or combinations of these three. The reason that three attenuator approaches are currently under study is that an additional goal of CLARREO is to rely on multiple and independent calibration approaches. The attenuators require extremely careful evaluation during ground testing, and are also a source of uncertainty on orbit if the attenuators degrade in some fashion. Evaluation of the attenuators on-orbit takes place through coordinated views of the Sun and the Moon. The brightness of the Moon is low enough to permit measurements without the attenuators in place, allowing the coupled lunar and solar views to determine if the attenuators are operating properly. Instrument nonlinearity is determined using a range of attenuators while observing the Sun.

The solar irradiance, measured by CLARREO, can be written in terms of the sensor output while viewing the Sun, $S_{i,\lambda}^{solar}$, and $R'_{i,\lambda}$, which is the responsivity of i-th detector and wavelength, λ, as

$$E_{solar,\lambda} = \frac{\sum_{x'_{solar}} \sum_{y'_{solar}} S_{i,\lambda}^{solar}(x'_{solar}, y'_{solar})}{R'_{i,\lambda} T_{attenuator} A_{attenuator}} \ , \tag{4.1}$$

where $T_{attenuator}$ is the transmittance of the attenuator used to allow direct view of the solar disk, and $A_{attenuator}$ is the entrance pupil of the sensor when viewing the solar disk. The summation over x'_{solar} and y'_{solar} integrates the output from a single detector over the entire solar disk needed to measure the solar irradiance.

The Earth-view radiance measured by CLARREO can be written as

$$L_{i,\lambda}^{earth} = \frac{S_{i,\lambda}^{earth} A_{sensor} \Omega_{sensor}}{R_{i,\lambda}} \ , \tag{4.2}$$

where A_{sensor} is the area of the entrance pupil of the sensor while viewing the Earth, Ω_{sensor}, $R_{i,\lambda}$ is detector response, and $S_{i,\lambda}^{earth}$ is the signal from the given detector at the specific wavelength while viewing the Earth.

The Bi-directional Reflectance Distribution Function (BRDF) can be written in terms of the measured radiance from a surface of interest relative to the incident solar irradiance. Note that Equation 4.2 can be written in terms of the solar irradiance through substitution of the detector response using Equation 4.1. The resulting BRDF is

$$BRDF_{i,\lambda}^{sensor} = \frac{S_{i,\lambda}^{earth} A_{sensor} \Omega_{sensor}}{R_{i,\lambda}} \frac{R'_{i,\lambda} T_{attenuator} A_{attenuator}}{cos\theta_\circ \sum_{x'_{solar}} \sum_{y'_{solar}} S_{i,\lambda}^{solar}(x'_{solar}, y'_{solar})} \ , \tag{4.3}$$

where $\theta_\circ$ is the solar zenith angle at TOA. It is assumed that any temporal changes in response between the solar and the Earth views, $R'_{i,\lambda}$ and $R_{i,\lambda}$, are minimal, and changes in solar irradiance between the Earth and solar views are also minimal. If these difference are negligible, detector responses for the Sun and Earth views cancel out. In this case, the absolute radiometric calibration is not used for BRDF retrieval, but it is required for establishing SI-traceability.

Ensuring SI-traceability and adequate accuracy requires evaluation of sensor performance on-orbit and a traceable error budget. The basis of the CLARREO traceability is via a high-fidelity sensor model developed from prelaunch characterization data coupled with on-orbit
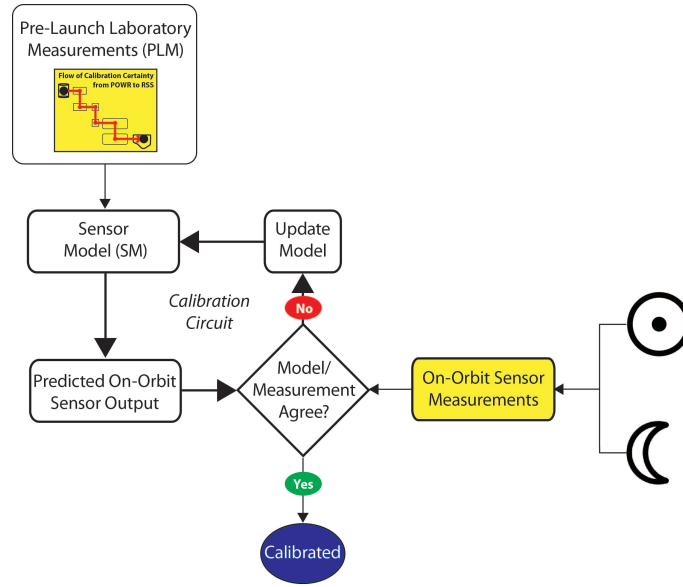
Figure 4.3: Flow diagram for CLARREO RS instrument calibration.

absolute solar irradiance measurements to show the sensor did not change going to orbit. Disagreement between reported solar irradiance and predicted values mean that the sensor model requires modification. Stellar and lunar views provide information regarding the optical quality of the sensor. Temporal changes in the sensor are evaluated using these techniques as well. The sensor model can be thought of as the numerical abstraction of the physical instrument, encapsulating knowledge of both optical physics and empirical results gained from laboratory analysis. Disparities between laboratory results and model predictions guide model improvements. This is a continuous process that ultimately yields a sensor model ready for use after launch as illustrated in Figure 4.3.

A critical part of the calibration is developing SI-traceable data by characterizing the sensor to SI-traceable, absolute radiometric quantities during pre-launch calibration to the electric Watt (prelaunch calibration box shown in Figure 4.3). Pre-launch absolute calibration includes both irradiance and radiance modes as well as the determination of geometric factors for conversion to reflectance. The end result of the prelaunch calibration is sufficient data to develop a sensor model that predicts the solar, lunar, and planetary/stellar sources planned for on-orbit calibration. Agreement between prelaunch and on-orbit (as shown in Figure 4.3) means the system is calibrated, and, by analogy, traceable to the pre-launch SI measurements. Disagreement means the sensor model requires improvement based on the on-orbit data, including an additional set of characterization measurements. Solar and lunar views provide information regarding temporal changes in the sensor once on-orbit traceability is established. Thus, the key to the RS on-orbit calibration is the prelaunch, SI-traceable calibration.

Evaluation of sensor performance on-orbit uses combined calibration, validation, and verification activities. One approach planned for validation of the RS on-orbit calibration is comparison to on-ground measurements propagated through the atmosphere to predict at-sensor radiance. Another radiometric calibration/validation activity will be comparisons to other sensors including airborne sensors. The main difficulty with validation for CLARREO RS will be ensuring that the validation data sets have sufficient radiometric quality.

4.2.3 Operational Requirements for CLARREO Lunar Verification Observations

The CLARREO Reflected Solar (RS) instrument concept calls for monthly observations of the Moon to verify the radiometric calibration stability on orbit (Section 4.2.2). The primary RS calibration relies on direct measurements of the Sun, which must be obtained with attenuators in place to reduce the solar irradiance input. No attenuation is required when viewing the Moon, therefore lunar observations will be used throughout the mission to evaluate the performance of the solar attenuators in orbit. This capability derives from the inherent stability of the lunar surface reflectance.

The operations plan for the RS lunar verification observations specifies that the Moon shall be acquired at phase angles between 5° and 10°. Although this is a relatively small range, the lunar irradiance cannot be considered constant across it. As an example, Figure 4.4 shows irradiance spectra produced for one night of ground-based observations, where the phase angle changed from 6.6° to 9.5° over about 9 hours. The difference between the two spectra ranges from 10% to 12%, dependent on wavelength. Generally for Moon views acquired from orbit, there are dependencies on the hemispheres of the Moon that are illuminated and viewed; these are referred to as the *lunar librations*. Consequently, CLARREO RS measurements of the Moon must be normalized to remove any geometry-driven differences in brightness before they can be used to assess instrument calibration stability. Normalization is done using the reference lunar spectral irradiance generated for the particular conditions (phase and librations) of the RS Moon observations, by the USGS ROLO model [Kieffer and Stone, 2005]. These model-generated reference spectra can be used to develop normalization factors, or to correct the observations to a standard geometry, such as 7° phase and zero librations.
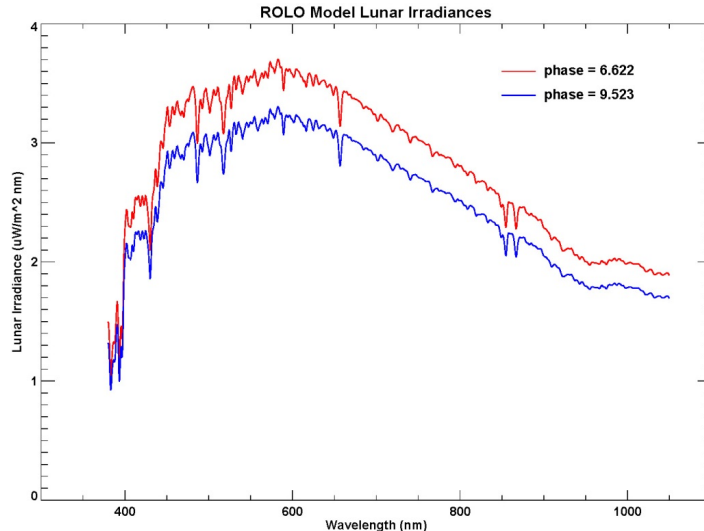
Figure 4.4: ROLO MODEL-GENERATED LUNAR IRRADIANCE SPECTRA PRODUCED FOR A GROUND-BASED SPECTROMETER. THE OBSERVATION TIMES DIFFER BY 9 H 21 M, AND THE PHASE DIFFERENCE IS 2.9°. THE IRRADIANCES DIFFER BY 10% TO 12%, SPECTRALLY DEPENDENT.

As described in sections 4.1.2 and 4.2.1, the CLARREO RS instrument is an imaging spectrometer with 100 km swath, or ∼10° cross-track field of view (FOV). From low Earth orbit, the Moon presents a disk about 0.5° in diameter. To make a lunar irradiance measurement, the entire disk must be spatially sampled, which for an imaging spectrometer typically means

scanning it in the along-track direction. Generating the irradiance from the scan data involves concatenating the scan lines into a spectral image, then spatially summing the (radiance) pixels and multiplying by the pixels' instantaneous field of view (IFOV):

$$E_m = \Omega_p \sum L_i \ , \tag{4.4}$$

where E_m is the measured irradiance, Ω_p is the pixel IFOV expressed in steradians, L_i is the radiance measure of pixel i, and the summation is over all pixels on the Moon's disk. Recommended best practices call for oversampling the Moon in the along-track direction, while underfilling the cross-track FOV. To obtain accurate irradiance measurements, correction factors for the disk oversampling must be determined carefully. This requires accurate knowledge of instrument pointing and the spacecraft position, velocity and attitude, sampled at frequencies higher than the scan line acquisition rate. The Moon must be scanned at a uniform rate over the lunar disk, so that the oversampling rate is constant for the entire scan. This imposes stability requirements on the slew rates of the instrument gimbal and the spacecraft attitude during Moon imaging. The corrections for oversampling typically are applied to the irradiance measurements from (spectral) images prior to normalization by the lunar model results.

CLARREO MCR engineering studies identified several considerations for acquisitions of the Moon by the RS instrument, directed toward obtaining the highest accuracy lunar irradiance measurements. To avoid the effects of reflected sunlight from the spacecraft and scattering in the Earth's atmosphere, lunar scans are to be acquired in the eclipse parts of the CLARREO orbit and at elevation angles $> 7°$ above the local horizon. At the lunar phases specified for CLARREO lunar verification operations, the Moon is available to all low-Earth orbits. However, other limitations on the observability of the Moon may be imposed by the mission configuration, such as the instrument's location on the ISS (Section 5.4).

The summation of spectral images to irradiance (Equation 4.4) works with radiometrically calibrated radiance pixels, having corrections applied for detector artifacts such as dark level and bias offsets, flatfielding, and response linearity. Because the Moon is an extended source viewed against the near-zero radiance background of deep space, in many cases detector dark level offsets can be evaluated independently and verified using the overscan regions of the observations. Additionally, the high-contrast edge of the illuminated Moon limb can be used to evaluate light scattering by the instrument optics, which must be accounted for in the image processing to irradiance. Given the CLARREO RS spatial footprint of 0.5 km at nadir (and presuming an orbit altitude ~609 km), the nominal Moon diameter will cover ~11 pixels in the spatial direction, substantially underfilling the cross-track FOV. Accurate irradiance measurements therefore depend on precise pixel response equalization, or flatfielding. Depending on the duration of the orbit eclipse periods, multiple views of the Moon may be acquired for each observation opportunity, possibly scanning with different parts of the detector array. However, it is not operationally practical to acquire a complete spatial sampling of the Moon in every spatial element (i.e. all detectors). Since the Moon is a relatively dark target (mean reflectivity ~0.11 at 550 nm), lunar irradiance measurements are sensitive to detector response linearity at the lower end of the dynamic range. Thus a thorough characterization of sensor linearity is essential for successful lunar calibration operations. It is possible to use the Moon to assess linearity on orbit; however, there are a number of complicating aspects to this type of analysis.

In practical application, the lunar irradiance measurements acquired by the CLARREO RS

instrument, when compared with the corresponding lunar reference values, each constitute a snapshot radiometric calibration of the RS sensor. Collecting these comparisons into time series can reveal the temporal stability of the instrument radiometric calibration, completely independent of the performance of the solar attenuators. Given a long enough time series, the uncertainty in this temporal trending can be reduced to under 0.1% per year (e.g. Sea-WiFS, [Eplee et al., 2012]). This metric is evaluated from fitting the measured vs. reference irradiances as a function of time, where each measurement and model value has an associated error. Error in the irradiance measurements are developed from characterizations of the scan sequence, the pixel conversions to radiance, and the spectral image processing to irradiance. The reference value errors arise from residual geometric dependencies in the lunar model; for the phase angle range $5 - 10°$, this error is no more than a few tenths percent, relative. Sensor response trends derived in this way are not affected by the absolute accuracy of the lunar model as a first-order dependency.

To use the RS lunar irradiance measurements for on-orbit evaluation of the instrument's solar attenuator performance requires knowledge of the absolute reflectance of the Moon, spatially integrated over the lunar disk, for the specific conditions corresponding to the Moon views. This can be done using the USGS lunar irradiance model (ROLO), combined with a solar spectrum. However, a major caveat of this process is the uncertainty in the ROLO model absolute scale, which currently cannot be verified against radiometric standards to better than $5 - 10\%$. However, the absolute offsets of the lunar model are consistent across its spectral and geometric ranges. This enables a verification strategy that references a set of baseline lunar measurements acquired at the earliest opportunity upon CLARREO achieving orbit. These initial observations are used to establish a spectrally resolved offset to the lunar model that can be considered constant through the mission lifetime. The validity of this method is substantiated by the invariance of the lunar reflectance (with time).

It should be noted that future improvements to the lunar model absolute scale can be applied retroactively to the operational RS lunar measurement datasets, and several projects for refining the USGS lunar model are currently ongoing and planned, with the common goal of improving and/or verifying the model's absolute accuracy and assuring SI traceability. In a longer view, it is recognized that a lunar observation dataset acquired by CLARREO could potentially contribute to a future characterization of the Moon's absolute reflectance, presuming the RS instrument operates within its absolute accuracy specifications for reflectance measurements (Section 4.1.2). This supplemental CLARREO task would require expanding the range of lunar phase angles observed by the RS instrument, and developing a corresponding set of operational requirements to support these observations.

4.3 InfraRed Instrument Concept

Calibration is central to the design of the infrared sensor, and the CLARREO calibration approach differs in a fundamental way from previous missions. Flight instruments are typically calibrated on the ground before launch, and then post-launch performance is validated through intensive calibration/validation field campaigns and by comparison with existing instruments. The approach for the CLARREO infrared sensor is to include a verification suite that provides SI-traceable calibrations on-orbit. The verification suite shown in Figure 4.5 includes: a variable temperature deep cavity blackbody to check radiance calibration accuracy over a range of

target temperature; phase change cells to provide SI-traceable temperature sensor calibration; heated collars to verify blackbody cavity emissivity; a quantum cascade laser and integrating sphere to verify instrument lineshape and provide an independent blackbody emissivity check; and a second deep space view to quantify instrument polarization sensitivity [Anderson et al., 2004; Dykema and Anderson, 2006; Gero et al., 2008, 2011; Best et al., 2008]. We present below the full capability instrument concept that was developed for Mission Concept Review (MCR) in November 2010. Work is also ongoing to develop a reduced capability design that could be implemented at significantly lower cost.
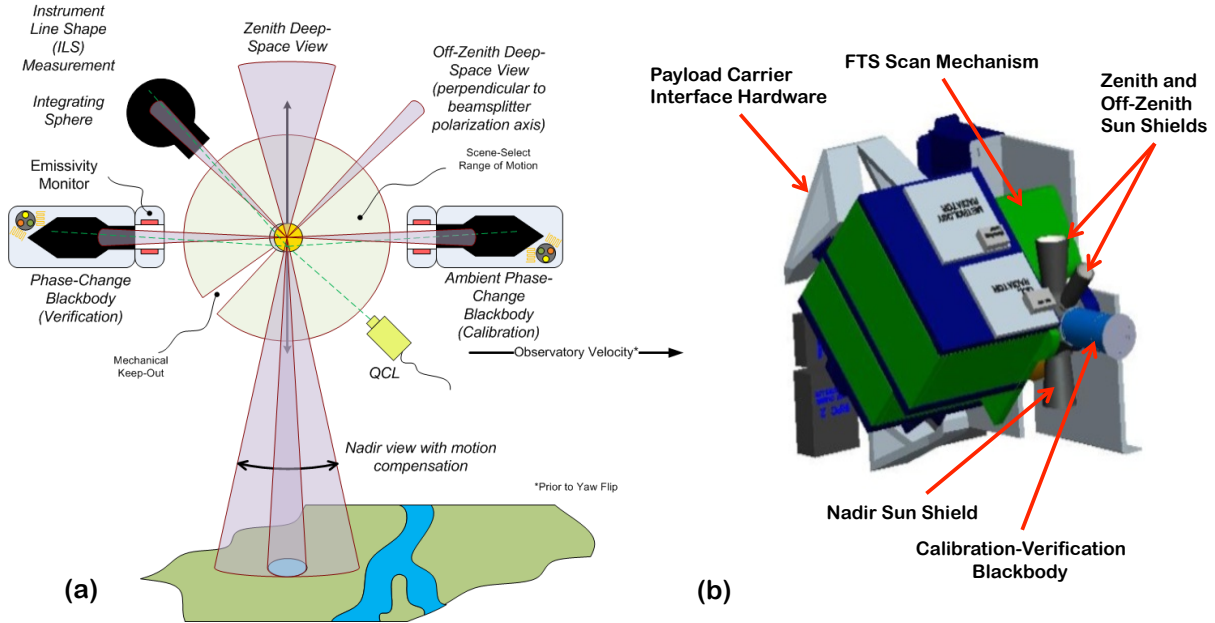
Figure 4.5: (A) CLARREO IR MEASUREMENT CONCEPT WITH VERIFICATION SUITE. TYPICAL OBSERVATION SEQUENCE IS ZENITH SPACE VIEW, CALIBRATION BLACKBODY, NADIR-ZENITH SPACE VIEW, CALIBRATION BLACKBODY, AND VERIFICATION VIEW, WHERE THE VERIFICATION VIEW MAY BE THE VERIFICATION BLACKBODY, INTEGRATING SPHERE, OR OFF-ZENITH SPACE VIEW. THE QUANTUM CASCADE LASER (QCL) PROVIDES A MONOCHROMATIC SOURCE FOR ILLUMINATION OF THE INTEGRATING SPHERE AND A HIGH INTENSITY SOURCE FOR CHECKING THE BLACKBODY CAVITY REFLECTIVITY. (B) THE IR INSTRUMENT PACKAGING CONCEPT.

The basic measurement concept uses a Fourier transform spectrometer (FTS) to create target scene spectra that are subsequently calibrated using observations of deep space and an internal ambient-temperature deep-cavity blackbody source. Because verification is so important for CLARREO, the target scene alternates between nadir views of the Earth and observations of the verification system, typically the onboard variable temperature blackbody. The calibration spectra of deep space and the ambient blackbody emitted radiance are recorded at 1/4 spectral resolution (1/4 scan time) to maximize the time spent observing targets of interest. Results from laboratory systems (see below) show that this does not compromise performance since the calibration spectra are essentially smooth Planck functions without sharp spectral features. Observations of other verification system components, including the integrating sphere and alternate deep space view, are made at regular intervals for instrument performance trending.

The FTS is a four port design that uses cube corner retroreflectors to offset the two inputs
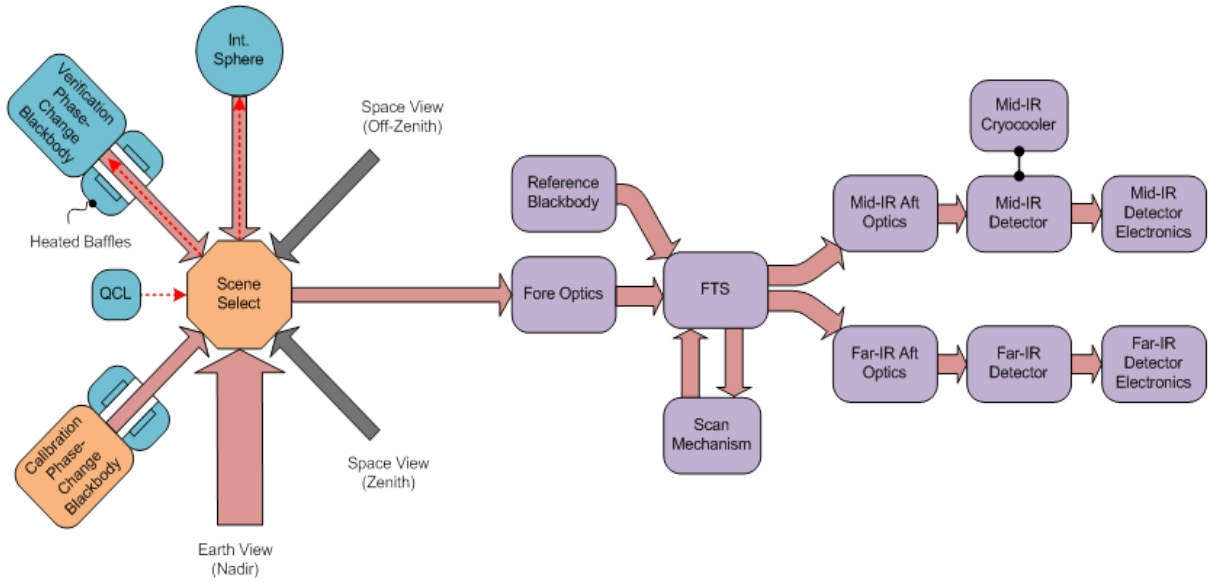
Figure 4.6: THE CLARREO IR INSTRUMENT FUNCTIONAL DIAGRAM: ELECTRO-OPTICAL (PURPLE), COLLECTION AND CALIBRATION (ORANGE), AND VERIFICATION (BLUE).

from the two outputs. One input is coupled to the Scene Select Mirror (SSM) and the other input is coupled to a stable internal reference blackbody as shown schematically in Figure 4.6. One output is coupled to an uncooled pyroelectric (Far-IR) detector while the other output is coupled to a pair of cooled photovoltaic (Mid – IR) HgCdTe detectors. The pyroelectric detector covers roughly $200 – 650$ cm^{-1}, while the photovoltaic (PV) detectors cover $650 – 1000$ cm^{-1} and $1000 – 2000$ cm^{-1}. The input pupil is placed at the calibration blackbody aperture and is imaged onto the cube corner vertex to minimize the size of the interferometer optics. The pupil is reimaged at the two FTS outputs where camera optics subsequently reduce the image size to fit onto the detectors. Pupil and field stops are included in the aft optics to control stray light. Emission from the stops does not produce modulated light and so does not contribute to instrument background.

Interferograms are recorded while scanning the FTS retroreflector towards the beamsplitter, and the SSM is repositioned to target scenes or calibration sources during FTS flyback. Frequent calibration views are used to minimize the effect of instrument drift, so that a standard observation sequence would be: space view, ambient blackbody, nadir view, space view, ambient blackbody, and verification system view. The full resolution target scans of ±1 cm in optical path difference take 8 seconds, the 1/4 resolution scans take 2 seconds, and the flyback takes 1 second between each, so that the full cycle including nadir and verification views takes 30 seconds. At the nominal orbital altitude (~ 700 km) this provides a nadir sample interval of approximately 200 km.

The SSM provides nadir views only with no cross-track scanning capability since science studies have shown that nadir views are adequate for both climate benchmark measurement and inter-calibration. The SSM rotates slightly during interferogram acquisition to compensate for in-track spacecraft velocity as shown in Figure 4.5. The four primary view ports (primary deep space view, ambient blackbody, verification blackbody, and nadir view) are orthogonal to each other and are oriented at $\pm45°$ with respect to the instrument polarization axis (de-

fined primarily by the FTS beamsplitter) to minimize sensitivity to polarization caused by the reflection off the rotating SSM mirror.

The radiance scale for the observed scenes is defined by the radiance model for the ambient blackbody calibration source, as can be seen from the calibration equation:

$$L'_e = \frac{L_{ABB}(S_e - S_{SV})}{S_{ABB} - S_{SV}} \; , \tag{4.5}$$

where L'_e is the calibrated scene radiance, L_{ABB} is the modeled ambient blackbody radiance, and S_e, S_{SV} and S_{ABB} are the uncalibrated (but linearized) scene, space view, and ambient blackbody spectra, respectively. We made the simplifying assumption that the space view radiance is negligible so that $L_{ABB} - L_{SV} \approx L_{ABB}$. The blackbody radiance model is dominated by the emission from the cavity with a small component due to the reflected radiance from the environment:

$$L_{ABB}(\bar{\nu}, T) = \frac{\epsilon a \bar{\nu}^3}{1 - e^{b\bar{\nu}/T}} + (1 - \epsilon)B_{env} \; , \tag{4.6}$$

where $a = 2hc^2$, h is Planck's constant, c is the speed of light, $b = hc/k$, k is Boltzmann's constant, ϵ is the blackbody cavity emissivity, and B_{env} is the radiance incident on the cavity from the external environment. For high cavity emissivity, the blackbody radiance is insensitive to the environment, and for low contrast between the blackbody temperature and the effective environment temperature, the radiance is insensitive to the cavity emissivity. The verification blackbody radiance can be modeled similarly and compared to the calibrated spectra produced by the spectrometer to estimate residual radiometric bias during flight.

If the temperature and emissivity (and to a lesser extent the environmental radiance) of a blackbody are known, then the radiance can be calculated using Equation 4.6. Similarly, the uncertainty in the modeled radiance can be estimated from the uncertainty in the estimated emissivity, temperature, and environmental radiance. The CLARREO project has partnered with NIST to develop traceable standards for characterizing the calibration and verification blackbodies, and especially for quantifying the cavity emissivity over the full 200 to 2000 cm^{-1} wavenumber range. This effort involves both spectral measurements of surface diffuse and specular reflectance properties that are extended to cavity emissivity using models such as Virial STEEP3 Software, and measurements of cavity reflectance at discrete wavelengths to provide end-to-end checks of the model results.

Maintaining SI traceability requires the ability to characterize the calibration and verification blackbodies. The temperature sensors are recalibrated on orbit using embedded phase change cells that provide a repeatable SI-traceable temperature reference. The cavity emissivity is measured both by using a heated collar to provide a spectral measurement of cavity reflectivity for off-axis illumination, and by using a QCL to provide a monochromatic measurement of nearly on-axis cavity reflectivity.

The total estimated systematic error in observed radiance, when expressed in brightness temperature units, depends on scene temperature, wavenumber, and detector channel, but in general the uncertainty is dominated by uncertainty in calibration blackbody source thermometry and residual errors in the detector nonlinearity correction. For example, the estimated uncertainty at 1000 cm^{-1} for a scene temperature of 250 K is 54 mK ($k = 3$). For this case,

the uncertainty due to uncertainty in the calibration blackbody radiance is 31 mK, and the uncertainty due to detector nonlinearity is 29 mK. The estimated uncertainty from all other sources combined is 33 mK.

The estimated technology readiness level (TRL) at MCR of the blackbody with phase change cells, the $200 - 2000$ cm^{-1} FTS, and the photovoltaic (PV) focal plane were assessed at 4 to 5, with the rest of the instrument subassemblies at TRL 6. Risk reduction work since MCR has matured all technologies to TRL 6, with the exception of the PV focal plane subassembly consisting of side-by-side detectors having different cutoff wavelengths.

4.4 GNSS-RO Instrument Concept

4.4.1 Radio Occultation Measurement

The GNSS-RO instrument is a traditional GPS receiver system nominally used for satellite navigation augmented with the capability to perform Radio Occultation (RO) using data tracked from multiple GNSS satellites. The basic concept of the RO measurements is shown in Figure 4.7. The CLARREO GNSS-RO instrument uses occulting GNSS satellites to measure atmospheric refractivity through Doppler shifts. It observes the change of delay of the transmitted GNSS constellation satellite signal through the atmosphere as it sets or rises behind the Earth's limb. The change of delay, measured as a Doppler frequency shift, is a function of the slowing and bending of the GNSS signal, and so it is translated to a bending angle, α, as shown in Figure 4.7. A vertical refractivity profile is created at the tangent point, and allows for reconstruction of the temperature, pressure, and humidity in the neutral atmosphere.
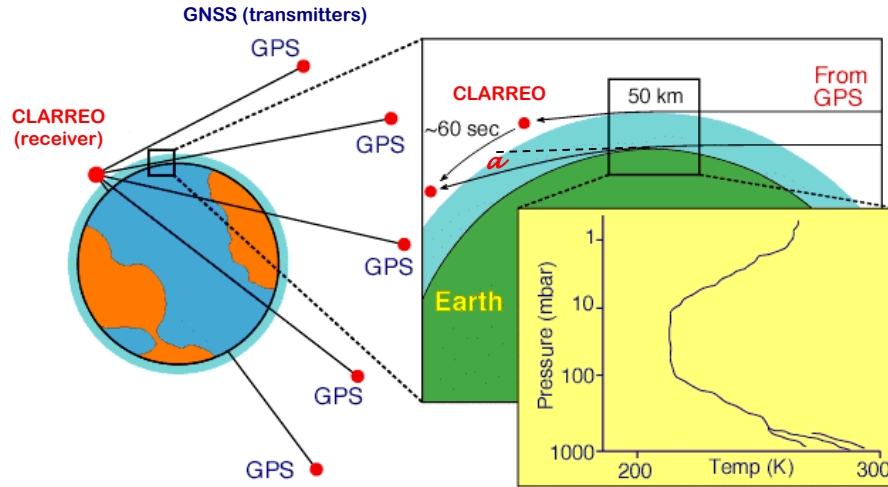
Figure 4.7: Concept of the CLARREO GNSS-RO measurements.

The CLARREO MCR Baseline mission concept (Section 5.3) uses two types of observatories, an IR Observatory and a RS Observatory. The IR Observatory carries the infrared spectrometer, and the GNSS-RO instrument. The RS Observatory carries only the reflected solar spectrometer there is no GNSS-RO instrument on the RS observatory. The MCR version of the IR Observatory concept and the GNSS-RO instrument's general arrangement is shown

in Figure 4.8. The antenna Field of Regards (FOR) are set such that: a) the zenith Precise Orbit Determination (POD) antenna has simultaneous access to a sufficient number of GNSS reference satellites; and b) the ram and wake occultation antennas have a Field-of-View (FOV) over the Earth's limb to acquire rising (ram antenna) and setting (wake antenna) occulting GNSS satellites. Every six months, yaw flips of the observatory will reverse the ram and wake directions for the other half of the year.

POD Choke Ring Antenna:
Located on zenith deck of spacecraft for views to GNSS satellites

IR Instrument Suite

GNSS Receiver:
RF receiver with additional capability for radio occultation processing (located inside spacecraft bus)

Ultra-stable Oscillator:
Provides high-precision frequency reference for zero-differencing (inside bus)

Laser Retro Reflector:
Located on nadir side of spacecraft for Precise orbit determination (POD) validation using satellite laser ranging

Phased Array RO Antennas:
Located on ram and wake faces with fields-of-view oriented towards the Earth's limb to view GNSS constellation Earth-occulting satellites (rising and setting)

Figure 4.8: General arrangement of the CLARREO GNSS-RO instrument suite.

To meet the CLARREO baseline science requirements, it will be necessary to acquire a total of 2,000 occultations per day. The threshold science requirements will be met if a total of 1,000 occultations per day are collected, which could either be met by two observatories tracking only GPS or Galileo, or by one observatory tracking both constellations (see Section 2.3.2 for more detail). To allow for validation of the GNSS-RO data, it will be necessary to use Satellite Laser Ranging (SLR), a mission activity that will provide precise observatory range/position information. For this purpose, the CLARREO observatory will be fitted with a Laser Retro Reflector (LRR) located on the nadir side of spacecraft (Figure 4.8). The laser ranging operations will be coordinated with the International Laser Ranging Services (ILRS), hosted by the NASA GSFC [*http://ilrs.gsfc.nasa.gov/about/index.html*].

4.4.2 GNSS-RO Instrument Description

Currently, only the GPS constellation is operational using the L1 and L2 frequencies. Tracking at only these two frequencies using the GPS constellation provides sufficient sampling density to meet CLARREO's threshold science objectives with two CLARREO observatories. However, when additional frequencies become available with new GNSS constellations, such as Galileo, then CLARREO would benefit by using these new frequencies to increase sampling density and thereby achieve the science objectives in a shorter time scale. The frequency availability of the GPS and Galileo constellations are described in Table 4.2. Using both GPS and Galileo, CLARREO would achieve its threshold science objectives with just one observatory and the baseline science objectives with two observatories. Including the capability to track the Galileo constellation also provides a contingency in case currently existing GPS frequencies are phased out over time (e.g. the potential exists for the L1 and L2 P(Y) codes to be phased out perhaps as early as 2020).

GNSS-RO Receiver: The receiver is a traditional "GPS receiver," nominally used for satellite

navigation but augmented with the capability to perform RO measurements using data tracked from the GPS and Galileo constellations.

Constellation	Frequency Availability	Initial Availability	Full Availability
GPS IIA	L1 P(Y) and C/A, L2 P(Y)	∼1984	Dec 1993
GPS IIR	L1 P(Y) and C/A, L2 P(Y)	∼1984	Dec 1993
GPS IIR-M	L1 P(Y) and C/A, L2 P(Y) and L2C	Sep 2009	∼2016
GPS IIF	L1 P(Y) and C/A, L2 P(Y) and L2C, L5, plus higher accuracy clocks	∼2010	∼2018
GPS III	L1 P(Y) M-Code C/A and L1C, L2 P(Y) M-Code and L2C, L5	∼2014	∼2021
Galileo	E5a, E5b, E1 (TBC)	∼2010	∼2013

Table 4.2: GNSS GPS AND GALILEO CONSTELLATION FREQUENCIES AND PLANNED AVAILABILITY.

In order to mitigate the issues related to codeless tracking (L2 signal only), noisiness, and defocusing of occultation signal below 10 km altitude, the CLARREO receiver will have the ability to track both L2 and L2C frequencies. The L2C frequency is modulated, but with a public sector P-code that receivers should be able to track as well as L1, thus eliminating the need for codeless tracking. The capability to track L2 would be retained since it is beneficial in providing ionospheric correction capability in the troposphere (< 10 km). Only the Block IIR-M GPS satellites currently broadcast L2C. All future GPS satellites, beginning with Block IIF, will broadcast L2C.

The CLARREO GNSS-RO receiver is currently envisioned to be a derivative of the TriG receiver being developed by the Jet Propulsion Laboratory. The Current Best Estimate (CBE) receiver dimensions are $30{\times}30{\times}20$ cm^3. This volume does not include accommodations for an Ultra-Stable Oscillator (USO), which is described below. The receiver may be placed on the observatory in a location of convenience, however, the distance between the receiver and all antennas should be as short as practical to minimize RF losses due to cable transmission. An example receiver is shown in Figure 4.9a, which depicts the JPL/Broad Reach Integrated GPS Occultation Receiver (IGOR) receiver that is currently flying on each of the six COSMIC (Constellation Observing System for Meteorology, Ionosphere, and Climate) satellites. The mass of the receiver has been estimated at 4.76 kg total.

The power consumption of the receiver is dependent on two factors: 1) the degree to which the receiver can simultaneously track multiple occulting satellites and process the data; and 2) whether the occultation antennas are static (fixed) phased array antennas or electronically steerable phased array antennas. Based on CLARREO's orbit and occultation antenna field-of-view, it has been determined that the receiver will be required to simultaneously track up to four occulting satellites. In addition, the current system design calls for static phased array occultation antennas. Considering these two parameters, orbit average power consumption is estimated at 31.9 W.

Occultation Antennas: The CLARREO GNSS-RO system utilizes two occultation antennas in the ram and wake directions, respectively (see Figure 4.8), which acquire the signals from the occulting GNSS satellites. The occultation antennas are static phased array antennas. A

phased array antenna is made up of a series of patch antennas that, together, act as a single, larger patch antenna, and provide higher gain and better suppression of local multi-path in RO tracking than a single conventional patch antenna. The CLARREO antennas are baselined to each have six individual elements in a 2×3 array. In a static phased array antenna, the data from all patches is electronically summed on-orbit. The required on-board processing and the data rate are the same as for a single patch antenna because the signals of the antenna elements are combined in electronics before passing an A/D converter. An example of a contemporary static phased array occultation antenna is shown in Figure 4.9b. It is the GRASS antenna manufactured by Rüstungs Unternehmen Aktiengesellschaft (RUAG) which is being used for radio occultation measurements on the METOP mission.
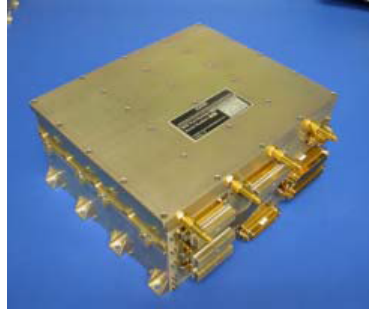
(a) IGOR receiver (COSMIC RO satellites).

(b) RUAG GRAS occultation antenna.
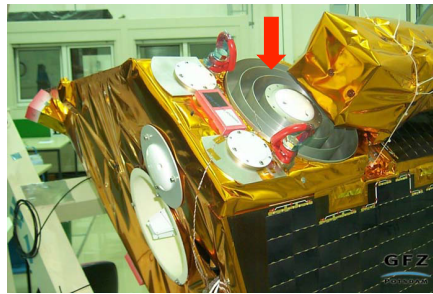
(c) CHAMPS Choke Ring POD antenna.

(d) GRACE APL ultra-stable oscillator.

Figure 4.9: THE GNSS-RO SUITE COMPONENTS WITH HERITAGE: A) IGOR RECEIVER USED ON THE COSMIC RADIO OCCULTATION SATELLITES, B) GRASS OCCULTATION ANTENNA, C) CHOKE RING POD ANTENNA ON CHAMP OBSERVATORY, D) APL ULTRA-STABLE OSCILLATOR FOR GRACE MISSION.

The occultation antennas are located on the ram and wake faces of the observatory to: a) provide a clear field-of-view to occulting GNSS satellites; b) minimize local multi-path, the reflection of GNSS signals off of other structures and into the antenna; and c) reduce RF interference with the S- and X-Band communication systems. The baselined static phased array occultation antennas on the ram and wake faces are oriented vertically (in the nadir-zenith direction), and have a clear ±45° FOV in azimuth. This orientation and FOV were selected to provide sufficient access to GNSS constellation Earth-occulting and non-Earth-occulting satellites. Performed analysis show that the antennas would track approximately 1,000 occultations per day using both the GPS and Galileo constellations, assuming that the GNSS-RO receiver is capable of tracking up to four occultations simultaneously. Section 2.3.2 discusses the sufficiency of this sampling capability.

The CBE occultation antenna dimensions are 45×30×6 cm³. These dimensions were estimated

from a variety of existing phased array antenna configurations that have already flown on space-borne radio occultation missions or are currently under development. The mass of each occultation antenna was estimated using the GRAS occultation antenna (Figure 4.9b) as a basis. The CBE mass estimate for each of CLARREO occultation antenna has been established as 2.0 kg.

Precise Orbit Determination (POD) Antenna: The POD antenna is a choke ring antenna that was selected because a choke ring provides better suppression of local multi-path in POD tracking than a single patch antenna. Similar antennas have flown on previous radio occultation missions. Figure 4.9c shows the choke ring antenna that was used for the radio occultation system on the CHAMP observatory.

The POD antenna is located on the zenith face of the observatory to provide as much unobstructed field-of-view as possible to the GNSS reference satellites and to mitigate the potential of local multi-path introducing errors into the POD measurement (Figure 4.8). The CLARREO baseline is for the POD antenna to have a minimum unobstructed view of $\pm 75°$ relative to zenith. To derive the CLARREO observatory position to sufficient precision, the POD antenna is required to track six reference satellites at least 80% of the time, and it is acceptable for only three reference satellites to be in view for short periods of time.

The CBE POD antenna dimensions are 31 cm diameter $\times$ 10 cm height. These dimensions were estimated from a variety of existing choke ring antenna configurations that have already flown on space-borne radio occultation missions or are currently under development. The CBE mass of the POD antenna is based on the Antcom 123GM1215AXT1F choke ring antenna, and is estimated at 2.0 kg.

Ultra-stable Oscillator: The internal clock of the TriG receiver is currently planned to have a frequency stability of 10^{-12}, which is not sufficient to meet CLARREO's zero-differencing measurement requirement for achieving SI traceability. To provide a reference frequency with the needed 10^{-13} stability, an external USO will be incorporated into the GNSS-RO instrument system. Similar USOs have flown on previous missions, with the USO used for the GRACE spacecraft depicted in Figure 4.9d. This USO was developed by the Applied Physics Laboratory (APL). The frequency of the USO is planned to be 10.228 MHz to serve as a reference oscillator for the TriG receiver. The mass and volume of the USO have been estimated using typical USO specifications provided by APL. The CBE mass and average power of the USO are 2.3 kg and 3.0 W, respectively.

Parameter	Value	Parameter	Value
Mass	17.9 kg	RO Science Data	111.1 kbps
Orbit Average Power	35.0 W	POD Science Support Data	0.8 kbps
Peak Power	40.0 W	Engineering Data	5 kbps

Table 4.3: THE GNSS-RO SYSTEM COMBINED MASS, POWER, AND DATA RATE.

4.4.3 GNSS-RO Calibration and SI-Traceability

The CLARREO GNSS-RO will use multiple calibration pathways in order to provide robust and independent SI traceable data sets. This will include 3 pathways to the realization of independency and 2 precise orbit determination (POD) pathways. They need not be incorporated at all times, but CLARREO will pursue a schedule of RO data that occasionally collects

all pathways of clock data to verify the accuracy of GNSS and CLARREO clocks, and both pathways of orbit data to verify the accuracy of orbit determination. Moreover, CLARREO can verify that sampling requirements are being met by sub-sampling an atmospheric analysis at the sounding locations of the RO data.

The RO measurement's traceability to the international standard of the second[4] is achieved by the three independent realizations of atomic clocks that can be used to make an observation or calibrate an observation:

1) On-board USO: the realization of the second is on-board and accurate to 10^{-13} over 1-second intervals; no breaks in traceability between the measurement and the scale realization of the second.

2) Reference GNSS satellite: The phase of a reference, non-occulted, GNSS receiver is observed at the same rate as the phase of the occulted GNSS receiver. The reference GNSS clock has a stability of 10^{-14}. The reference GNSS is tracked at L1 and L2 and an ionosphere-removing linear combination (LC) is formed immediately. The lone break in traceability derives from propagation of the reference GNSS signal through the ionosphere to the occultation receiver, thus incurring orbit errors and slight ionospheric residual.

3) Reference ground network: Both a reference GNSS satellite (see previous item) and the occulted GNSS satellite are observed during an occultation event by a receiver on the ground using a clock with stability 10^{-15}. Reference ground networks are provided by special, independent services such as the International GNSS Service (IGS). Breaks in traceability are propagated through the ionosphere and atmosphere of the signals observed on the ground, in addition to the breaks in traceability listed for the previous item. The ionosphere can contribute residual in the LC phase, and necessary removal of the delay induced by the atmosphere is imperfect.

Inferring the atmospheric path delay rate from an SI-traceable measurement of phase rate on-board CLARREO requires the removal of the influence of the satellites' trajectories; therefore, not only does the observation of phase on-board CLARREO need to be accurate, but so also does the orbit determination of all satellites involved in the occultation. As such, precise determination of the orbits of the CLARREO observatories must be provided and determined by CLARREO. The two POD pathways are

1) Precise Orbit Determination is the method wherein overhead GNSS satellites are observed throughout the CLARREO orbit. Because orbit trajectories are easily predictable over short time intervals - Keplerian trajectories are very strong approximations over several seconds - it is unnecessary to collect POD data more frequently than every 10 seconds, but it is necessary to collect POD data from multiple GNSS satellites at any given time. The POD data over each 24-hour period are then considered in a ground calculation that simultaneously considers the data and orbital dynamics, complete with terms that approximate the physical effects responsible for drag on the satellites, to yield a best estimate of CLARREO's orbits. While tracking ≥ 4 GNSS satellites at any given time is considered a best practice, the nature of the orbit calculation does not demand it explicitly. Consequently, it is permissible to track just 3

---

[4]The international definition of the second is the time required for 9,192,631,770 cycles of the radiation emitted by a hyperfine transition of the ^{133}Cs atom. The standard is maintained by the U.S. National Institutes for Standards and Technology (NIST) in Boulder, Colorado; by the U.S. Naval Observatory; and by the Bureau des Poids and Msures in Paris.

GNSS satellites for POD for limited time intervals. Precise orbits of the GNSS satellites are also provided by special, independent services such as the IGS, and may be used to compare against the CLARREO collected POD data.

2) International Satellite Laser Ranging is the practice of obtaining a precise range to a satellite when it overflies a ground station with SLR capability. The ground station produces laser pulses directed toward the satellite as it flies overhead, and the satellite reflects the laser pulses back to the ground station from an attached corner cube retro-reflector. The retro-reflector is attached directly to the CLARREO spacecraft bus (Figure 4.8). This data by itself is insufficient to fully obtain CLARREO's orbits, but it is independent of POD calculations and sufficiently accurate to serve as a strong check on the overall accuracy of POD. The International Laser Ranging Service, hosted by the NASA GSFC, provides this service and the resultant data.

4.5 CLARREO Technical Readiness

The CLARREO Infrared Spectrometer, Reflected Solar Spectrometer, and GNSS Radio Occultation instruments are mature, achieving Technology Readiness Level 6. The high technology readiness was achieved by competing successfully multiple NASA Earth Science Technology Office (ESTO) Instrument Incubator Program (IIP) projects, establishing close relations with the NIST, and developing the Calibration Demonstration Systems (CDS) for reflected solar and infrared spectral measurements at NASA GSFC and NASA LaRC, respectively.

4.5.1 NASA Investments in CLARREO Technology

For nearly a decade, the NASA ESTO carefully managed technology projects, built, and validated early versions of the instruments and components needed for such a mission. In many ways, the development of these early investments enabled the designation of CLARREO as a mission concept in 2007. The ESTO investments since 2007, adopted by the CLARREO Science Definition Team, are summarized in Figure 4.10, and amount to $\sim$ \$18M total. The earlier ESTO investments relevant to the CLARREO mission, amount to $\sim$ \$8M total. What follows is the list of these key technologies, focused specifically for CLARREO mission requirements.

$\diamond$ The Far-Infrared Spectroscopy of the Troposphere (FIRST) instrument, an early airborne precursor to CLARREO, was demonstrated in 2005 on a high-altitude research balloon and provided the first-ever high resolution measurement of the complete infrared emission spectrum of the Earth, including the key far-infrared region from 15 to 100 μm that contains over 50% of Earth's infrared radiation. More recently, FIRST was installed at 17,500 feet atop the Cerro Toco Plateau in Chile as part of the Radiative Heating in Underexplored Bands Campaign - II (RHUBC-II). Principal Investigator: M. Mlynczak, NASA LaRC, IIP 2001 and 2004.

$\diamond$ The In-Situ Net FLux within the AtMosphere of the Earth (INFLAME) project has developed a Fourier Transform Spectrometer to measure upward and downward radiation fluxes simultaneously in the lower atmosphere. INFLAME was successfully demonstrated on a LearJet in 2010 and may provide calibration/validation data for CLARREO. Principal Investigator: M. Mlynczak, NASA LaRC, IIP 2004.
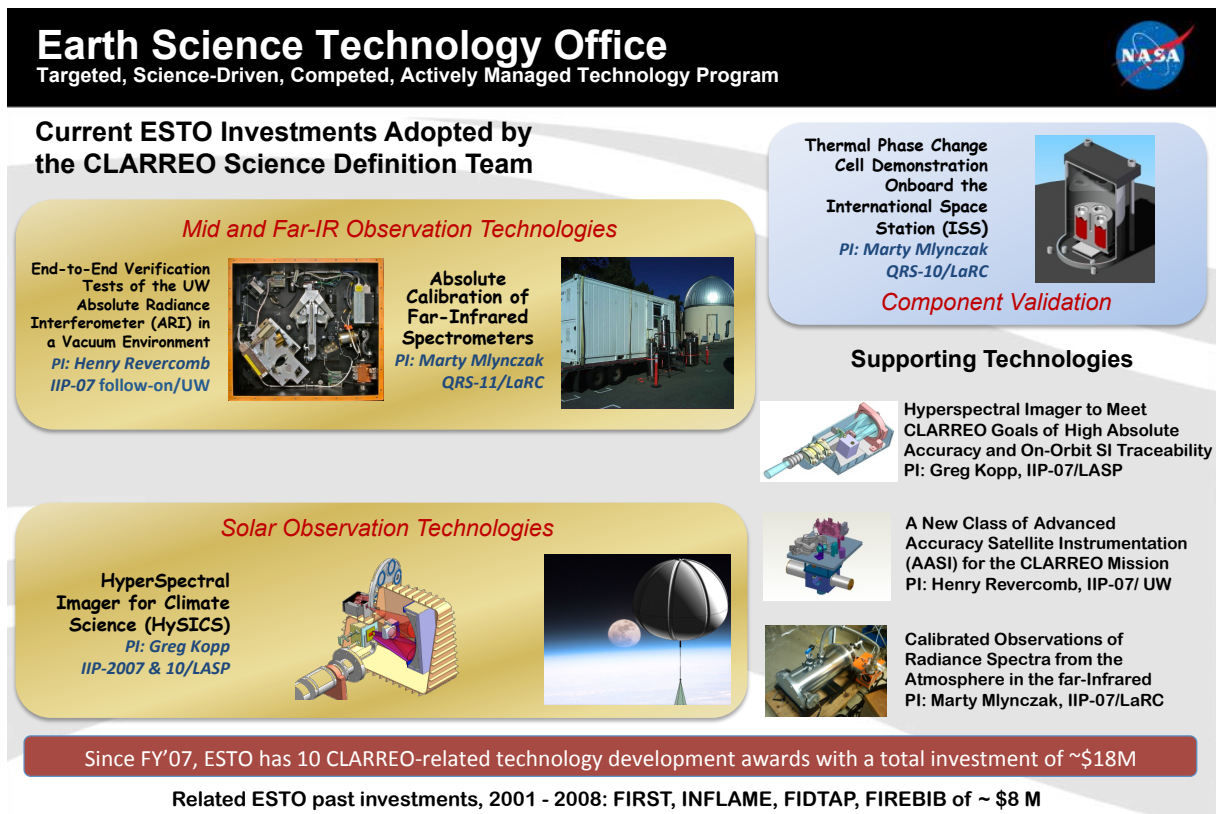
Figure 4.10: THE NASA ESTO INVESTMENTS IN CLARREO RELATED TECHNOLOGIES.

⋄ Initiated in 2008, the Hyperspectral Imager to Meet CLARREO Goals of High Absolute Accuracy and On-Orbit SI Traceability project seeks to design and construct an advanced, high accuracy hyperspectral imager, investigate attenuation methods, and validate the solar cross-calibration approach for the CLARREO mission concept. Principal Investigator: G. Kopp, Univ. of Colorado, IIP 2007 and 2010.

⋄ The Advanced Accuracy Satellite Instrumentation for the CLARREO mission project, seeks to develop and test several key calibration subsystems, such as temperature calibration for the blackbody cavity, dual absolute radiance interferometers, and an emissivity module. Principal Investigator: H. Revercomb, University of Wisconsin, IIP 2007.

⋄ Instrument integration activities are also ongoing in the Calibrated Observations of Radiance Spectra from the Atmosphere in the far-InfraRed (CORSAIR) project. CORSAIR combines a set of technologies central to the CLARREO mission: infrared detector elements, blackbody radiance standards, and robust optical beamsplitters with continuous high efficiency over the full spectral range. Principal Investigator: M. Mlynczak, NASA LaRC, IIP 2007.

⋄ A new effort began in 2010 to Demonstrate Thermal Phase Change Cells Onboard the International Space Station (ISS). The CLARREO mission proposes to use phase change reference standards (melt cells) to recalibrate its on-board temperature sensors; however, these standards have never been flown in space. This project will achieve in-space testing of two melt cell designs, provided by University of Wisconsin and The Space Dynamics Laboratory at Utah State University, in 2011 onboard the ISS. Principal Investigator: M. Mlynczak, NASA LaRC.

◇ For the 3-year term of CLARREO Science Definition Team, selected for funding from 2011 to 2014, the Calibration Demonstration Systems (CDS) in the RS and IR were funded in NASA GSFC and NASA LaRC, respectively. The total funding amounts to ∼ \$3M. The scope of both CDSs is to design technology demonstrators for the spectrometer components of the CLARREO mission concept, and to achieve the same instrument performance specifications. The calibration process and its SI-traceability was developed in collaboration with the National Institute of Standards and Technology (NIST).

◇ From 2010 to 2014 time period, the NIST supported CLARREO mission development, focusing on establishing high-accuracy calibration and SI-traceability of relevant measurements from space. These activities were supported in part through NASA funding agreements ∼ \$650K, and in part through NIST climate initiative internal funding ∼ \$1.2M. The NIST group also reviewed the CLARREO CDSs design and performance in 2013 for both RS and IR spectral measurements.

4.5.2 InfraRed Technology Development at NASA Langley

The development of infrared and far-infrared (far-IR) measurement technology at NASA Langley began in 1999 with seed funding from NASA's Upper Atmosphere Research Program to initiate science studies of the far-infrared spectrum and its role in climate. At the nearly same time, the first papers on infrared spectral fingerprinting were being published [Haskins et al., 1997; Goody et al., 1998]. These and other studies [Harries, 1996; Harries, 1997] rapidly led to the realization that far-IR measurements were a frontier of atmospheric science and measurement technology [Mlynczak et al., 2002]. For the next decade, NASAs Earth Science Technology Office (ESTO) invested heavily in the measurement technology for the infrared and far-infrared, via competed proposals through its Instrument Incubator Program (IIP). Three IIP proposals from Langley were selected (beginning in 2001) and work was carried out over the ensuing decade to develop systems and components necessary to accurately measure the infrared and far-infrared spectrum. Scientific field campaigns and additional calibration activities were carried out in recent years, supported by ESTO and the NASA Radiation Sciences Program. All these will be described in the following Section, with specific discussion of their relevance to building the scientific and technical knowledge base needed to accomplish the CLARREO mission.

4.5.2.1 The Far-Infrared Spectroscopy of the Troposphere (FIRST) Instrument

The FIRST project was proposed to and selected in the IIP solicitation in 2001. The FIRST project was a partnership between NASA Langley, the Space Dynamics Laboratory (SDL) of the Utah State University, and the Harvard Smithsonian Astrophysics Observatory (SAO). The FIRST project built and demonstrated a Michelson Fourier transform spectrometer (FTS) covering the range from 100 to 2000 cm^{-1} although the initial specifications were 100 to 1000 cm^{-1} (100 to 10 μm).

FIRST developed and demonstrated three separate technologies, all of which were demonstrated by the successful measurement of upwelling, top-of-atmosphere Earth radiance. The first technology was a high throughput FTS system capable of daily global sampling from low earth orbit. The second was a broad bandpass beamsplitter capable of passing the entire infrared spectrum so as to enable measurement with a single focal plane. Prior technologies only

passed portions of the spectrum, necessitating multiple focal planes for different wavelength regions, complicating the optical design and necessitating calibration of multiple focal planes or detectors. The third technology was a large format focal plane array capable of housing 100 detectors (coupled to Winston cones) to enable global coverage with a relatively small instrument.

Shown in in the Figure 4.11a is the FIRST broad bandpass beamsplitter developed by the SAO. The beamsplitter is picture in the laboratory at SDL prior to insertion in the FIRST instrument. The beamsplitter is a germanium coating on polypropylene and is approximately 18 cm (7 inches) in diameter. Figure 4.11b shows the assembled FIRST interferometer core. The ring holding the beamsplitter is in the center of the figure at a 45° angle. The moving mirror drive of the FTS is the assembly to the left of the beamsplitter and the fixed mirror is the assembly below the beamsplitter.
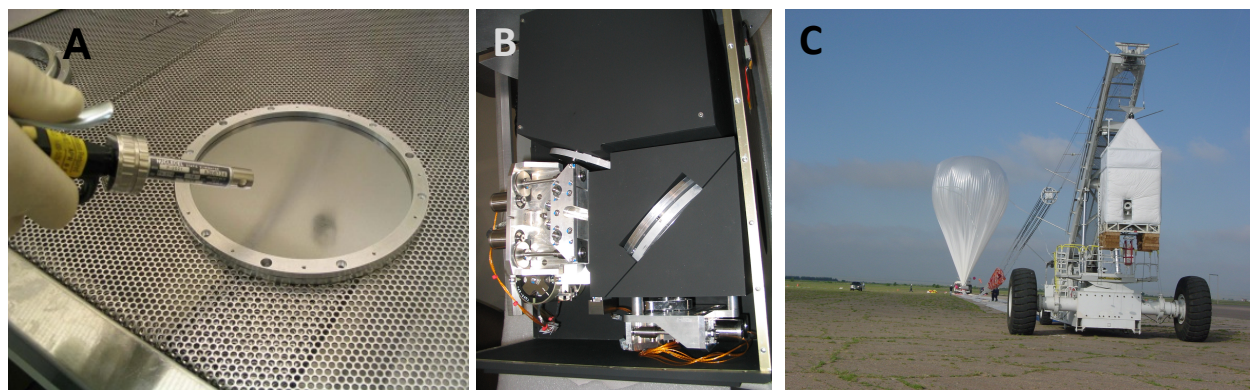
Figure 4.11: a) The FIRST broad bandpass beamsplitter. b) The FIRST interferometer core. The beamsplitter is positioned and held by the silver colored ring at 45° in the center of the picture. The moving mirror of the FTS is operated by the mechanism at the left of the figure. The stationary mirror of the FTS is located in the fixture visible below the beamsplitter. c) The FIRST instrument is visible through the side of the gondola held aloft by the crane in the foreground of this picture. The 11 million cubic foot balloon that carried FIRST to 105,000 feet is visible in the distance. The payload was launched shortly after this picture was taken.

A key requirement of the IIP is that the technologies be tested and verified in a relevant environment. For FIRST, the relevant environment is that of an orbiting satellite. As a space flight demonstration was well beyond the budget of the IIP, FIRST was housed in a stainless steel vacuum canister to simulate the vacuum of space and flown on a high altitude balloon to enable simulation of the measurement of top-of-atmosphere radiance. FIRST was carried aloft to approximately 33 km (∼108,000 feet) on June 7, 2005 for its technology demonstration flight. Figure 4.11c shows the FIRST instrument through the side of the gondola in which it was housed for the demonstration flight. Clearly visible in the figure is the space view port of the instrument that serves as one of two calibration views (the other is an ambient blackbody not visible in this picture) used by FIRST to accurately calibrate its measured radiances. FIRST was launched shortly after the picture in Figure 4.11c was taken. After roughly 1 hour FIRST had reached a stable float altitude near 33 km and operated for about 5 hours before the flight was terminated in late afternoon to allow sufficient time for the recovery team to locate and secure the payload, its parachute, and the balloon prior to nightfall.

The demonstration flight was a technical success with the instrument returning quality spectra across the infrared from 10 to 1600 cm^{-1} (1000 to 6.7 μm). Figure 4.12a shows a sample calibrated "first light" spectrum recorded by FIRST. This is the first measurement of the entire energetically significant portion of the Earth's infrared spectrum at high (0.64 cm^{-1}) spectral resolution from a space-like vantage point. Clearly visible are the CO_2 15 μm band in the center of the spectrum centered at 670 cm^{-1} and the ozone 9.6 μm band near 1000 cm^{-1}.
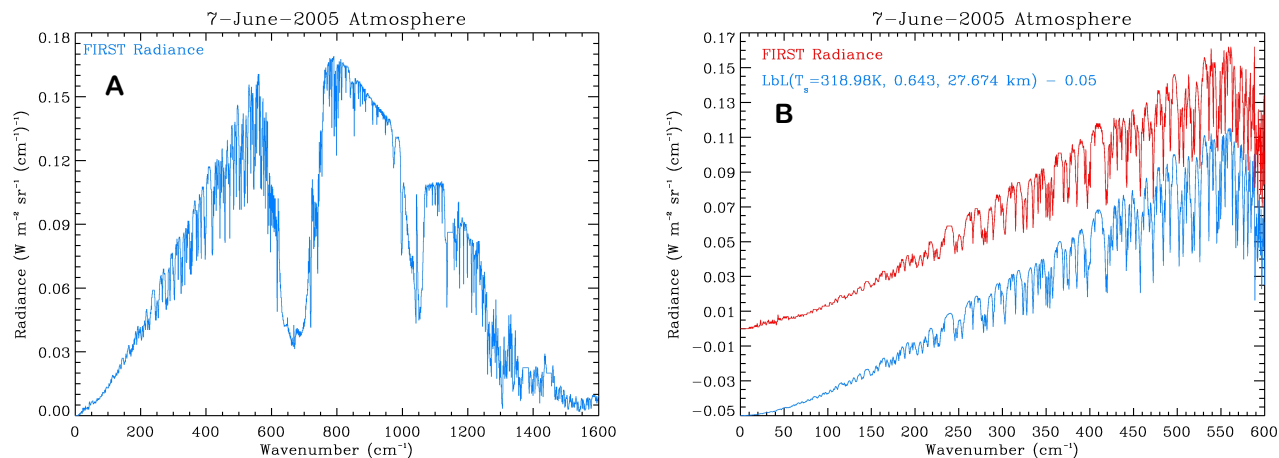
Figure 4.12: a) First light spectrum from the FIRST instrument. The spectrum demonstrates instrument performance from 10 to 1600 cm^{-1} (1000 to 6.7μm). b) Comparison of measured FIRST radiance (red curve) and computed radiance based on a near-coincident radiosonde profile. The two curves are offset by 0.05 radiance units. This figure illustrates the exceptional spectral fidelity of the FIRST instrument as evidenced by the comparison of observed and calculated spectral structure.

While the FIRST instrument was flying, radiosondes were launched to provide measurements of the atmospheric temperature and moisture vertical profiles. These are then used to compute the anticipated radiance that would be measured by the instrument. Figure 4.12b shows a comparison between the FIRST measured spectrum (red curve) and that computed from a line-by-line model of the radiance (blue curve). To facilitate comparison of observed and modeled spectral structure, the two curves in Figure 4.12b are offset by 0.05 radiance units. The comparison shows that FIRST replicates the anticipated spectral structure of the far-infrared to a remarkable degree of fidelity.

During the flight the Aqua satellite passed over the FIRST instrument at around 2:25 p.m. local time. A goal of the FIRST project was to compare its measurements with those of other sensors in order to validate the calibration. The Atmospheric Infrared Sounder (AIRS) instrument on the AURA satellite records infrared spectra between 4 and 15 μm and thus measures the mid-infrared portion of the spectrum coincident with FIRST. Comparisons between FIRST and AIRS in this region of the spectrum illustrate excellent agreement, especially considering the vast difference in scope of the two projects. The results from this flight of the FIRST instrument are given by Mlynczak et al. [2006].

FIRST flew again from Fort Sumner in September 2006 in support of CALIPSO validation. The instrument again performed nominally and recorded several thousand more spectra over

a flight lasting again about five hours. As in 2005, the Aura satellite and the rest of the A-train" of satellites overflew the FIRST balloon shortly after 2:00 p.m. local time. Again the comparison of infrared spectra shows excellent agreement between AIRS and FIRST.

After the two successful technology demonstration flights at Ft. Sumner, the FIRST instrument was modified to operate as a ground based instrument that would make measurements of downwelling atmospheric infrared radiance at Earth's surface. In exceptionally dry environments the far-IR spectrum has substantial development and ground based observations under these conditions could provide exceptional tests of our understanding of far-IR spectroscopy and radiative transfer.
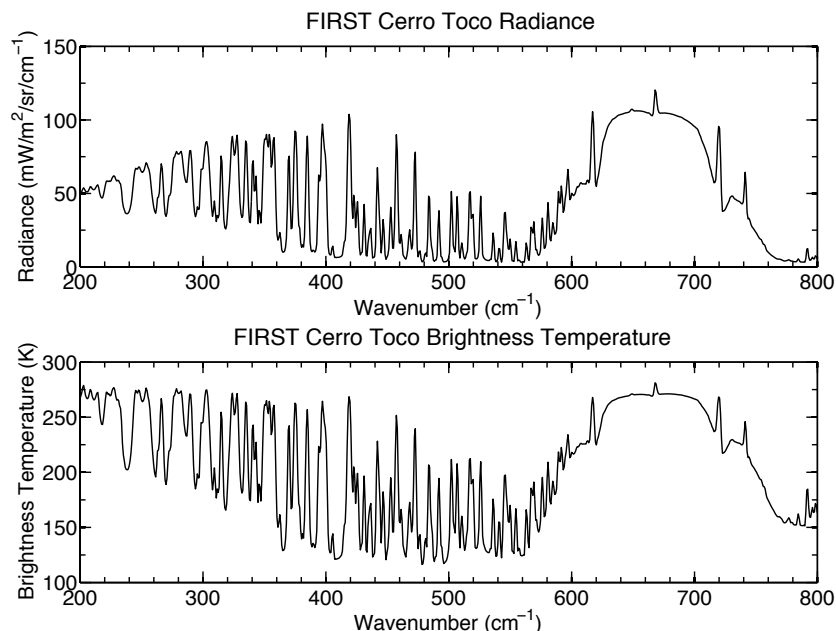
Figure 4.13: FIRST RADIANCE RECORDED AT CERRO TOCO, CHILE UNDER EXCEPTIONALLY LOW PRE-CIPITABLE WATER VAPOR CONDITIONS (PW < 1 MM).

The FIRST instrument participated in a ground-based science campaign, the Radiative Heating in Underexplored Bands Campaign, part II, or RHUBC-II, sponsored by the Atmospheric Radiation Measurement (ARM) program of the Department of Energy. The campaign took place from August to October of 2009 in Chajnantor, Chile in the Atacama desert. From a location on top of a mountain at approximately 5.2 km (17,000 ft) FIRST and a host of other instruments observed the atmosphere in the zenith view. FIRSTs participation in RHUBC-II was sponsored jointly by NASA through a competitive proposal to the NASA Radiation Sciences Program (Far-Infrared Observations of the Radiative Greenhouse Effect (FORGE). During this campaign, FIRST and other instruments recorded the entire infrared spectrum of Earth's atmosphere at the planet's surface for the first time [Turner et al. 2012].

Figure 4.13 shows a FIRST spectrum taken during the RHUBC-II campaign in Chile during conditions of exceptionally low precipitable water vapor (< 1 mm). The spectra show full development of the far-IR spectrum from 200 to 600 cm^{-1}. Also of note are the low radiance values from 350 to 575 cm^{-1} that are a consequence of the low water vapor values. The lower plot in the figure shows the measured radiances expressed in brightness temperatures, which reach a low of 115 K between 400 and 500 cm^{-1}.

In 2012 NASA Langley won a competition for funding by ESTO with a proposal to calibrate the FIRST instrument with standards fully traceable to NIST. The Long Wave Infrared Calibration Source (LWIRCS) blackbody, built for the purpose of calibrating the FIRST instrument, was (for a separate project) calibrated at NIST in their Low Background Infrared (LBIR) facility. This tied the LWIRCS to NIST standards for the first time. The FIRST instrument was then shipped from Langley to SDL and calibrated using the LWIRCS. FIRST was calibrated in its ground-based observing mode with an ambient and warm blackbody source. The results of this calibration are reported in Latvakoski et al., [2013]. The instrument was also calibrated in the mode used on high altitude balloons with an ambient blackbody and a cold source simulating the space view. These results are reported in Latvakoski et al., [2014].

Subsequent to the calibration at SDL, the FIRST instrument was taken to Table Mountain, California to conduct a radiative closure experiment. The site is approximately 7200 feet above sea level. Water vapor amounts are often below 1 cm and during the deployment water vapor amounts under 0.3 cm occurred. FIRST observed the downwelling radiances while radiosondes were launched to provide temperature and moisture date necessary for computing the expected radiances to compare with FIRST.
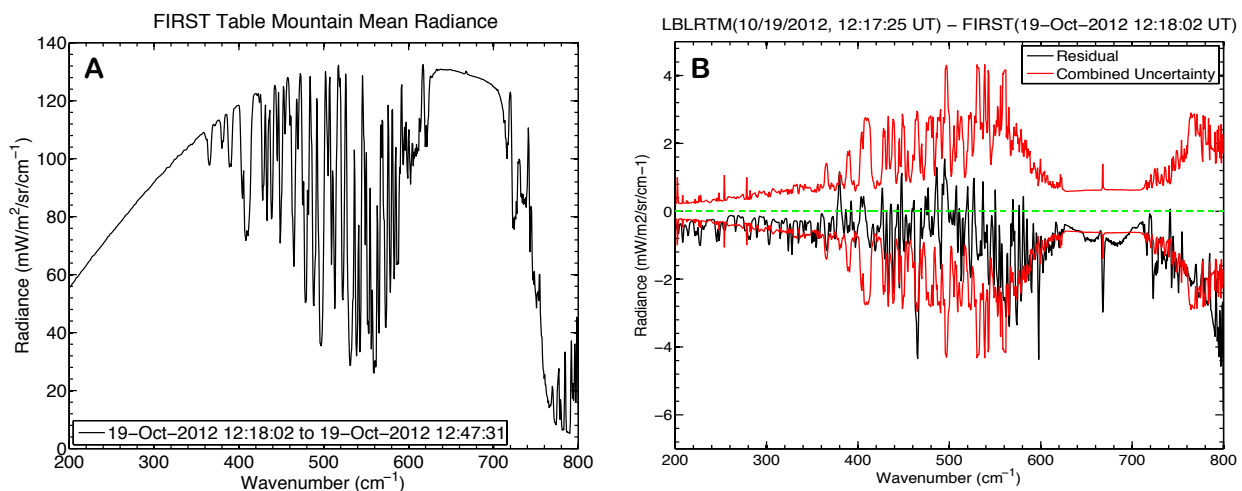
Figure 4.14: a) FIRST radiance spectrum recorded at Table Mountain on 19 October 2012. Precipitable water vapor amounts were 0.28 cm. b) Difference between FIRST measurements and radiative transfer calculations (Residual, black curve) and the uncertainty in the difference (Combined uncertainty, red curve), for spectra recorded at Table Mountain California, October, 2012.

Figure 4.14a shows a spectrum measured by FIRST with 0.28 cm precipitable water at Table Mountain. Unlike the Cerro Toco spectrum shown in Figure 4.13, spectral development does not begin until 350 cm^{-1}. The radiance levels are also much higher at Table Mountain than Cerro Toco, which is 10,000 feet higher than Table Mountain.

Figure 4.14b shows the results of the closure experiment conducted at Table Mountain in late 2012. The black curve is the difference between the downwelling radiance measured by FIRST and line-by-line radiative transfer model calculations. The red curve is the total uncertainty of the difference between measurements and models. The results indicate that FIRST

measurements largely agree with radiative transfer calculations across the spectrum to within the uncertainties in the measurements and models. Results from this field campaign including the figure shown below are in preparation for submission to the Journal of Quantitative Spectroscopy and Radiative Transfer.

In summary, the FIRST project has helped to open a new measurement window on the infrared spectrum of the Earth. It has developed technology (FTS systems; beamsplitters; focal planes) that will enable routine space-based observations of the far-IR during the CLARREO mission. Measurements made by the FIRST instrument are in agreement with model calculations, to within known uncertainties.

4.5.2.2 INFLAME

A fundamental problem in atmospheric science is the computation of the rates at which visible and infrared radiation heat and cool the atmosphere. As important as the measurement of infrared spectra is at the top of the atmosphere and from the surface looking up, it is also crucially important to understand radiation fields within the atmosphere. The divergence of the net flux of radiation determines the rate at which the atmosphere heats or cools by radiative transfer. However, measuring radiative heating rates within the atmosphere is perhaps the last remaining (and most difficult challenge) in atmospheric radiation measurement.

To address this long-standing problem, NASA Langley proposed the In-situ Net Flux within the Atmosphere of the Earth (INFLAME) project to the IIP competition held in 2004. The goal of INFLAME was to build and demonstrate small sensors that could directly measure the net flux of radiation at a given altitude within the atmosphere from an airborne platform (such as a conventional aircraft or UAV). The aircraft would fly in a spiral pattern from the surface to the tropopause, measuring the net flux of radiation at ~ 1 km intervals. The derivative of the vertical profile of net flux with respect to altitude is the net flux divergence, which, through provision of atmospheric temperature and density, yields the rate at which the atmosphere is heating or cooling due to radiation. Two sensors were proposed, one for the visible spectrum, one for the infrared spectrum. INFLAME was selected in late 2005. A successful technology demonstration flight was conducted over the Atlantic Ocean off of Virginia Beach, VA in January, 2010.

The fundamental equations solved in every atmospheric model include the momentum and continuity equations and the thermodynamic equation or equivalently, the first law of thermodynamics. The main terms in the first law that must be determined are the rates of atmospheric heating and cooling due to absorption of solar radiation and emission of infrared radiation. The radiative heating rate dT/dt is determined from the expression

$$\frac{dT}{dt} = \frac{-1}{\rho \, C_p} \frac{dF_{net}}{dz} \, , \tag{4.7}$$

where ρ is atmospheric density, C_p is the heat capacity at constant pressure, and F_{net} is the net radiative flux at altitude z. The net flux is simply the difference between the energy flowing upward and downward through an aperture of unit area, or $F_{net} = F_{up} - F_{down}$. The change in net flux with altitude is the net flux divergence, dF_{net}/dz, and is proportional to the rate dT/dt at which radiation heats or cools the atmosphere. The net fluxes are usually separately determined for the visible (solar) and the infrared (thermal) parts of the spectrum. Determining the net radiative flux, the flux divergence, and heating rates remains

a fundamental goal of many NASA projects. For example, the CERES project, presently operating on the EOS Terra and Aqua satellites, produces net flux and flux divergence data products for several broad atmospheric layers. It is also an emerging goal of the CLARREO mission.
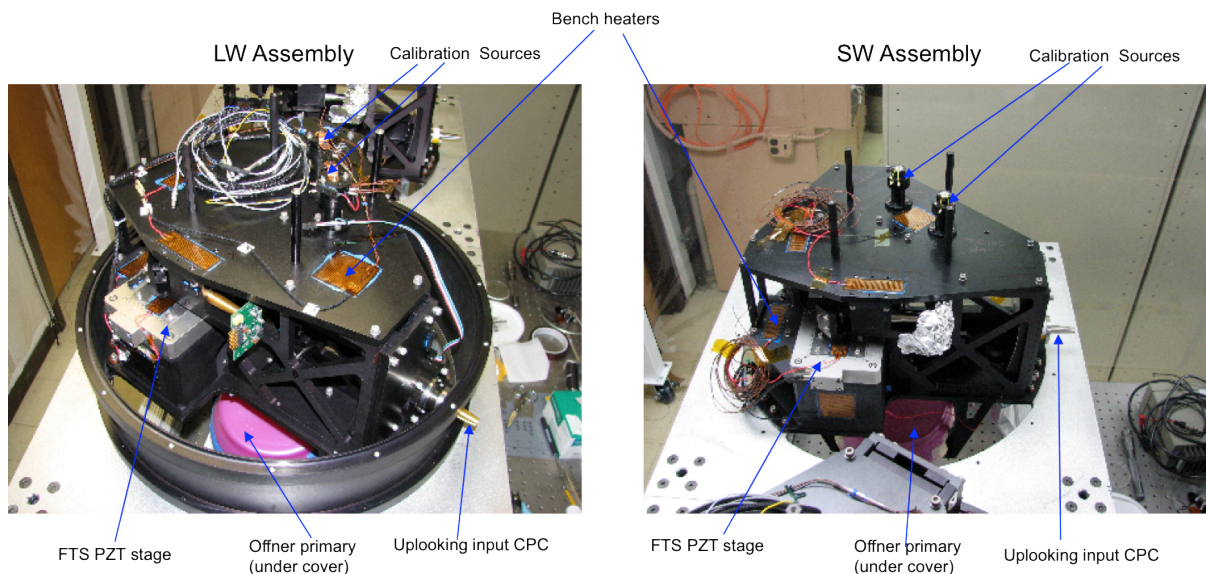
Figure 4.15: THE INFLAME SPECTROMETERS: INFRARED (LEFT) AND VISIBLE (RIGHT).

The measurements objectives of INFLAME are to measure the shortwave and longwave net flux with sufficient stability to derive tropospheric heating rates in 1 km layers that are accurate to within 10%. This requires measuring the net flux with a stability of 0.2% per km and 0.8% per km in the shortwave and longwave spectral regions, respectively. It is important to note that while measuring the net flux divergence requires that the instrument response be very stable, it does not require a similar level of absolute accuracy in measuring the net flux. If the calibration errors are stable and independent of altitude then the relative uncertainty in the net flux divergence will be no greater than the relative uncertainty in the net flux measurement.

The INFLAME instruments measure the net flux by using a low-resolution Fourier transform spectrometer (FTS) to observe the upward and downward flux simultaneously using the two inputs of the same instrument. The two complementary outputs of the FTS can be transformed to produce spectra proportional to the difference between the two inputs. The contribution of INFLAME to the CLARREO mission is the demonstration of extremely stable 4 port FTS systems and the establishment of science measurement capability to measure directly within the atmosphere processes that CLARREO will be determining from outside of the atmosphere.

The net flux will be measured directly in the atmosphere by deploying the INFLAME instruments on a Lear Jet. The instruments will be mounted in the wing tip tanks. The aircraft will slowly ascend from near the surface to approximately 40,000 feet in altitude, recording the profile of net flux. As indicated by Equation 4.7, the derivative of the vertical profile of net flux gives the rate at which the atmosphere is heated. INFLAME employs one spectrometer for measuring net flux in the visible portion of the spectrum to determine heating rates

Figure 4.16: ONE INFLAME INSTRUMENT (IN THE GOLD COLORED HOUSING) MOUNTED IN A LEARJET WING TIP POD JUST PRIOR TO FLIGHT DEMONSTRATION IN JANUARY 2010.

due to the absorption of solar radiation and one spectrometer for the infrared to determine the radiative cooling rates due to emission. Using two separate spectrometers allows us to optimize the mirror coatings, beamsplitter, and detectors for each wavelength range.
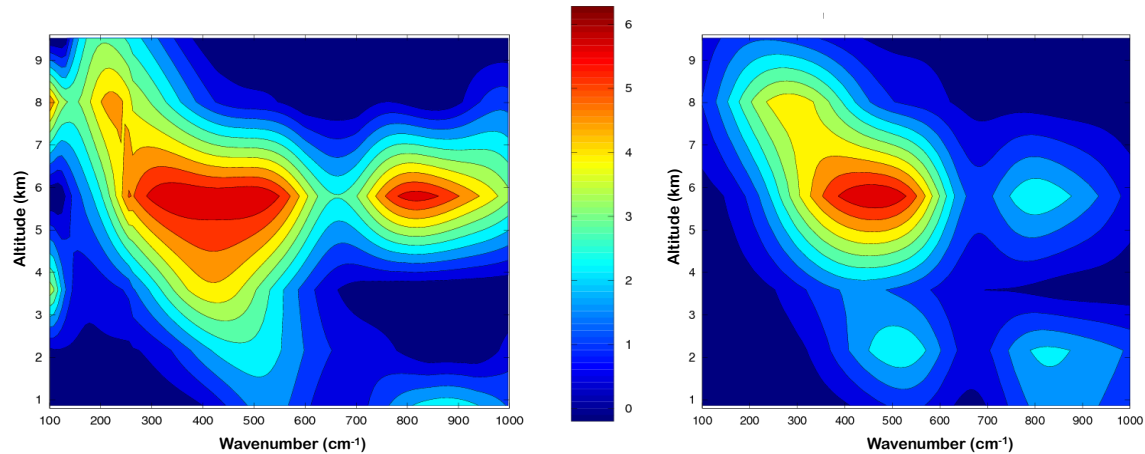
Figure 4.17: INFRARED COOLING RATE RESULTS FROM THE INFLAME TECHNOLOGY DEMONSTRATION FLIGHT IN JANUARY, 2010: CALCULATED INFRARED COOLING RATES (MK/DAY/CM^{-1}) (LEFT), AND MEASURED INFRARED COOLING RATES (RIGHT).

Figure 4.17 shows the spectral infrared radiative cooling rate (mK day^{-1} cm) measured by INFLAME during its demonstration flight (right plot) as compared with the calculated spectral heating rates based on measured atmospheric conditions near the flight track (left plot). The flight took place over 2.5 hours just off the Virginia coastline. INFLAME made the first-ever measurement of the spectral infrared cooling rate within the atmosphere.

The INFLAME project successfully completed in 2010 and has met its goals of developing the technology to measure the spectral radiative heating and cooling rates within the atmosphere. The INFLAME instruments are unique and are ready for science deployment.

4.5.2.3 CORSAIR

As CLARREO related technology development moved forward, it was apparent that there were still some technical challenges to be addressed. With this in mind ESTO competed another Instrument Incubator Program call in 2008 specifically targeted at the upcoming CLARREO mission. NASA Langley proposed the Calibrated Observations of Radiance Spectra of the Atmosphere in the Infrared (CORSAIR) project to address three outstanding technical hurdles: high sensitivity infrared and far-infrared detectors operating near room temperature; broad bandpass beamsplitters with high throughput; and SI traceable blackbody radiance standards for wavelengths beyond 15 μm. Selected partners for the CORSAIR effort included The National Institute for Standards and Technology (NIST), Raytheon Corp., Space Dynamics Laboratory, and ITT. NASA selected CORSAIR for implementation in 2009.

First, Raytheon Corporation carried out the uncooled detector work. The approach was to use small antennas efficiently coupled to diodes to rectify the antenna current which could be readily measured. Two different fabrication runs were developed in which Shottky diodes were coupled to millimeter-wave antennas. An intensive test program was undertaken, with NASA Langley playing a major role in the design and fabrication of the test set up at Raytheon. Despite several months of testing and analysis, the devices yielded no measurable signals. The antenna coupled devices remain at TRL-2.

Then, ITT Corporation, carried out the work related to development of high throughput, broad bandpass beamsplitter. The approach involved detailed modeling of optical properties of multi-layer coatings on cesium iodide substrates. A three-phase program was developed and implemented, including design and vendor selection; beamsplitter fabrication; and testing. However, issues still remained with moisture performance and optical flatness. The TRL progressed from 2 to 4 during this task.

Figure 4.18: The CORSAIR blackbody upon delivery to NASA LaRC.

The third task under CORSAIR was the development of a blackbody that would serve as a prototype for the CLARREO mission. The requirements included high (> 0.999) emissivity from 5 to 50 μm, temperature operation from 200 K to 325 K, phase change cells for accurate temperature monitoring, and incorporation of a quantum cascade laser for emissivity monitoring. The CORSAIR blackbody designed and built by SDL, pictured in Figure 4.18 upon its delivery to NASA Langley, advanced from TRL 3 to TRL 6. The apparently large volume of

the blackbody is necessitated by the requirement to cool the blackbody down to 200 K to cover the range of scene temperatures to be observed by CLARREO. The cooling is accomplished by the use of liquid nitrogen, which must surround the actual blackbody contained within the pictured housing. The CORSAIR blackbody was put to use immediately at Langley as an integral part of the Infrared Calibration Demonstration system for CLARREO.

4.5.3 InfraRed Calibration Demonstration System at NASA Langley

The Infrared Calibration Demonstration System (IR CDS) is specifically designed to be a technology demonstrator for the infrared spectrometer component of the CLARREO mission concept, and is intended to achieve the same instrument performance specifications. The IR CDS consists of two major subsystems: the infrared spectrometer subsystem, including associated ambient and cold calibration blackbodies; and the variable temperature blackbody (VTBB) subsystem. The IR CDS is operated in a dedicated vacuum chamber, both for improved thermal control and to enable the use of a liquid nitrogen (LN_2) cooled blackbody without having a window in the optical path. Each subsystem is described in detail below.

(a) InfraRed CDS layout.　　　　　(b) InfraRed CDS assembly.
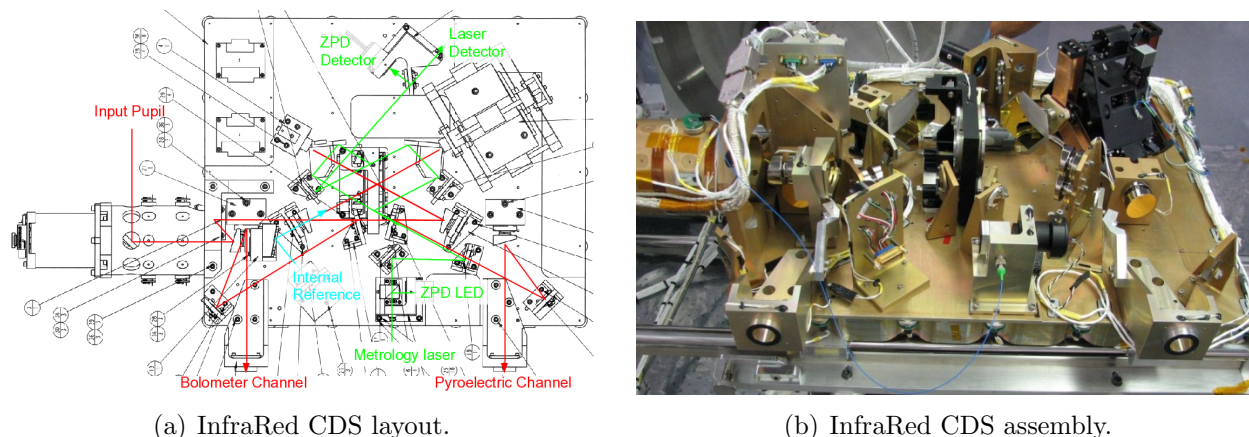
Figure 4.19: INFRARED CDS AT NASA LARC: TEMPERATURE-CONTROLLED OPTICAL BENCH.

Following light from input to output, the spectrometer subsystem shown in Figure 4.19 consists of a rotating SSM that switches between viewing the ambient temperature calibration blackbody (ABB), the cold source calibration blackbody (CSB), and the VTBB; fore optics; FTS; aft optics; and detector subsystems, including camera optics. All components from the SSM to the exit pupil stops are mounted to a temperature-controlled optical bench inside the main vacuum housing. The calibration blackbodies, VTBB, and detector subsystems with camera optics are mounted to external ports on the vacuum housing for ease of access.

The FTS is a Michelson design with cube corner retroreflectors used to separate the input and output planes, making both inputs and both outputs accessible. One input is coupled to the fore optics and SSM, and the second input is coupled to a thermally-stabilized internal reference blackbody. Both outputs are coupled through aft optics and field and exit pupil stops to the vacuum housing output ports, and one or both outputs can be used interchangeably with available detector subsystems. For the present work, one output is coupled to a 4 K

silicon bolometer, while the other output is coupled to an uncooled pyroelectric detector. The 20 mm input pupil is imaged onto the cube corner vertex and re-imaged onto the exit pupil with unit magnification and a beam divergence of 2.38°. The optical system is all reflective with the exception of the cesium iodide beamsplitter and compensator substrates. A stabilized diode-pumped 1064 nm Nd:YAG laser is currently used for FTS metrology, including velocity control and interferogram sampling. The metrology beam passes through the same beamsplitter/compensator and retroreflectors as the infrared beam, but uses different input and output optics. A broadband 870 nm LED source is used to provide a zero path difference reference signal.

The optical bench temperature is maintained at 303 K by a multi-zone heater control system. Calibrated thermistors are mounted on all optical components so that drifts in instrument background can be estimated and compared to any observed measurement bias. For the measurements presented here, the internal reference blackbody is thermally tied to the optical bench, but the instrument can also be operated in an alternate configuration with the internal reference blackbody temperature controlled independently with a thermoelectric cooler.

All electronics were designed and built in-house, with the exception of the temperature readout electronics for the calibration sources and the internal reference. The system is modular and makes extensive use of serial interfaces to simplify debugging, modification, and upgrading of subsystems if needed.

The ABB and CSB are both deep cavity specular traps, although they have different designs. The ABB is an angled flat plate design painted with gloss black PT-401, while the CSB is an inverted cone, painted with Z302, that forms the bottom of a LN_2 tank. Both sources share a vacuum with the main vacuum housing, are thermally-isolated from the laboratory environment, and are instrumented with calibrated temperature sensors. Neither source has active temperature control, although the CSB is cooled by the LN2 in the reservoir. Specular and diffuse reflectance has been measured for paint witness samples for both sources by both NIST ($2 - 20\,\mu$m) and Surface Optics Corporation (SOC; $5 - 50\,\mu$m.). NIST has also measured the cavity reflectance of both sources at 4 μm and 10 μm, with the result that both sources have an effective cavity emissivity better than 0.999.

The VTBB is also a deep cavity Z302 specular trap, but one that is LN_2 cooled and has active temperature control [Latvakoski et al., 2010]. The VTBB can be operated from 200 – 320 K, although at present the temperature sensor calibration has only been verified over the more restricted range of 233 – 308 K. The VTBB operates completely independently from the IR spectrometer subsystem, although they share a vacuum. Temperature data is communicated to the IR spectrometer control computer through a simple Ethernet interface.

A typical measurement sequence starts with warming the optical bench and internal reference blackbody and letting their temperatures stabilize at 303 K; cooling the CSB and letting its temperature stabilize near 78 K; and filling the VTBB LN_2 reservoir, letting it cool, then turning on the heaters and waiting for its temperature to stabilize at the desired operating temperature. The CDS is operated in the same way as was proposed for the MCR concept. Interferograms are recorded while scanning the FTS in one direction, then the SSM changes views during FTS flyback. VTBB "scene" interferograms are recorded at full resolution (± 1 cm max OPD), while calibration ABB and CSB are recorded at 1/4 resolution ($\pm$ 0.25 cm max OPD) to maximize the time spent observing the VTBB. This also tests the assumption that
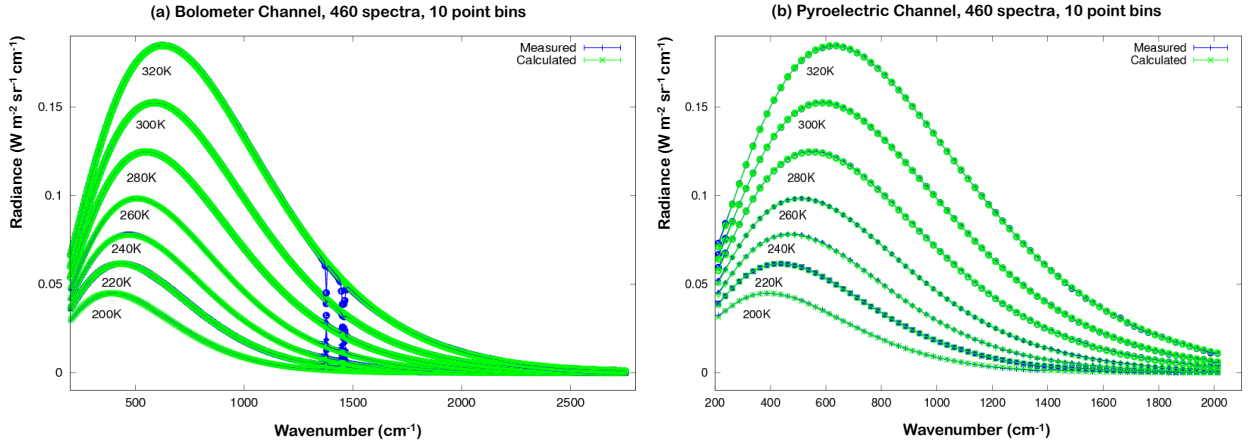
Figure 4.20: AVERAGE CALIBRATED RADIANCE FOR BOLOMETER (A) AND PYROELECTRIC (B) CHANNELS. APPROXIMATE VTBB CAVITY TEMPERATURE IS INDICATED BY THE LABELS.

instrument background and responsivity have no sharp spectral features that would prevent use of this strategy on orbit. One observation cycle of ABB, CSB, and VTBB takes roughly 15 seconds. Once sufficient data are obtained, the VTBB is stabilized at the next temperature plateau and the cycle is repeated.

The bolometer interferograms are corrected for detector nonlinearity using a simple correction with no free parameters based on the DC detector voltage. The pyroelectric interferograms are corrected for gain fluctuations resulting from FTS scan velocity variations using fringe crossing times that are recorded with each detector sample.

The IR spectrometer has proven to be sufficiently stable to do background subtraction in the interferogram domain. However, since laser fringes are not counted during flyback, each interferogram needs to be properly indexed before calibration, using the broadband LED signal to locate the proper sample index. Once the interferograms have been co-aligned, ABB and CSB interferograms, I'_{ABB} and I'_{CSB}, are estimated for the time of the VTBB observation using linear interpolation within a sliding window centered on the VTBB observation. The normalized response R is given by:

$$R = \frac{FT(I_{VTBB} - I'_{CSB})}{FT(I'_{ABB} - I'_{CSB})}\,, \tag{4.8}$$

where the FT operator represents a complex Fourier transform. The calibrated VTBB spectrum is given by:

$$L'_{VTBB} = L_{CSB} + (L_{ABB} - L_{CSB}) \times R\,, \tag{4.9}$$

where L_{ABB} and L_{CSB} are the ABB and CSB cavity radiance, respectively, estimated from the measured temperatures using a cavity model that incorporates the measured specular and diffuse paint reflectance measured by SOC.

The observed radiance L'_{VTBB} is compared to the modeled radiance L_{VTBB} in Figure 4.20, where L_{VTBB} is estimated from available VTBB temperature and paint reflectance data as was done for the calibration sources. The comparison is done as a difference in brightness temperature from L_{VTBB} in Figure 4.21 by inverting the Planck functions for L' and L.

131
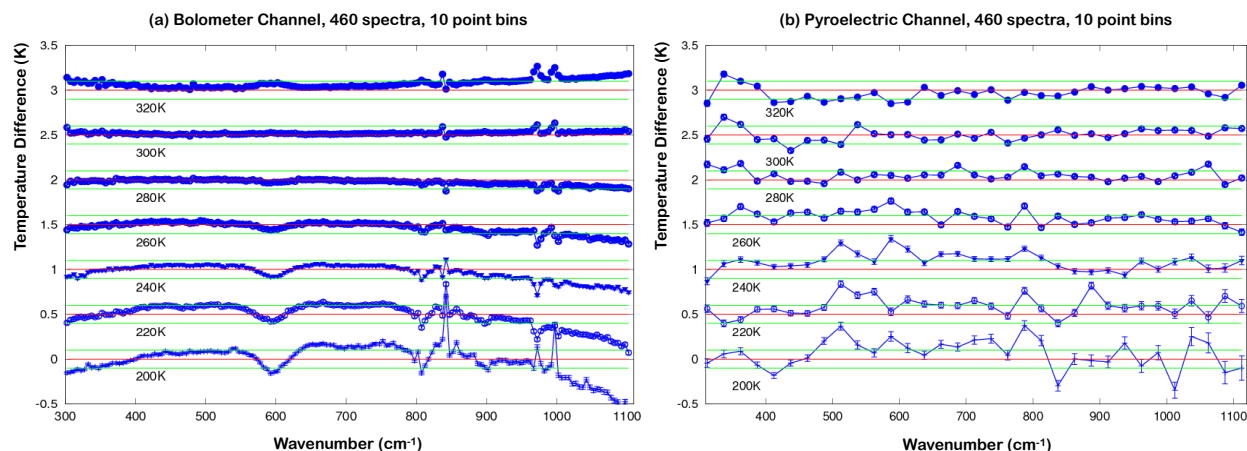
Figure 4.21: Difference between measured and calculated brightness temperature for bolometer channel (a) and pyroelectric channel (b). Red line indicates origin for each offset plot; green lines indicate 0.1K. Approximate cavity temperature is indicated by the labels.

Preliminary results suggest that the demanding instrument performance required to quantify long-term climate change is within reach. Brightness temperature differences in the region 300 – 1100 cm^{-1} are generally less than 0.2 K for scene temperatures 200 – 320 K and appear to be dominated by uncorrected distortion of the interferogram, possibly resulting from residual detector nonlinearity. Temperature differences increase for higher wavenumbers as radiance decreases. Band-limited shortwave detectors, including PV HgCdTe detectors, will be added in the future to improve our ability to diagnose measurement bias above 1100 cm^{-1}. Once a number of promising cost and weight saving modifications to the original MCR design have been identified, the CDS will further be used to quantify the performance impact of these design modifications.

4.5.4 Infrared Prototype Instrument Development at UW-SSEC

NASA ESTO supported the development of the Absolute Radiance Interferometer (ARI), a flight-like prototype of the CLARREO IR instrument, developed by the University of Wisconsin-Madison, Space Science and Engineering Center, who teamed with the Anderson Group at Harvard University [Revercomb, 2013a]. The ESTO has now designated the entire ARI, consisting of a Calibrated Fourier Transform Spectrometer (CFTS) and an On-orbit Verification and Test System (OVTS) with several new technologies, to be at TRL 6 as required for a flight program.

The ARI instrument concept is very similar to the infrared sensor concept from the CLARREO MCR presented in Section 4.3. That design included the UW/Harvard concepts for on-orbit verification and test, and the same generic FTS and detector choices. However, there were some different specific implementation choices made for our IIP design, including the use of an FTS with strong, recent flight heritage; an optical design with different requirements and approach; and a somewhat different operational scenario and sampling. These differences will be highlighted in the section describing the CFTS.
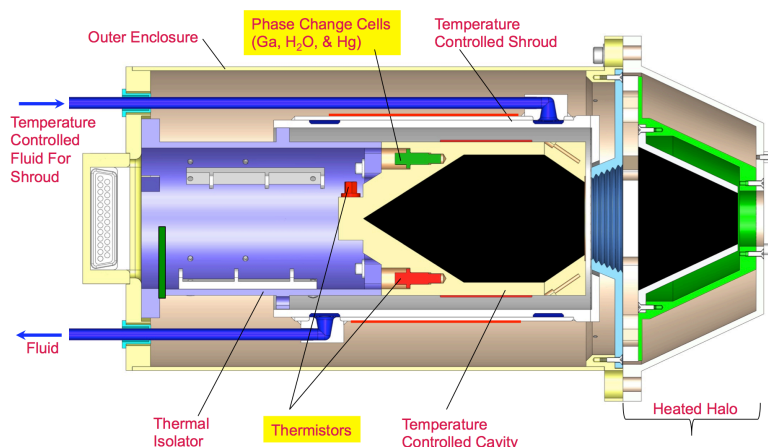
Figure 4.22: A SECTION VIEW OF THE LABORATORY VERSION OF THE OARS DEVELOPED UNDER THE IIP FOR CALIBRATION VERIFICATION OF ARI. FOR THIS LABORATORY VERSION, THE TEMPERATURE CONTROLLED SHROUD USES A FLUID LOOP TO MAINTAIN THE COLD-BIASED TEMPERATURE ENVIRONMENT FOR THE CAVITY. CAVITY TEMPERATURES FROM $-60\degree$C TO $+60\degree$C ARE POSSIBLE WITH THIS DESIGN.

4.5.4.1 Key New Technologies for On-orbit Verification

1. On-Orbit Absolute Radiance Standard (OARS)

The OARS is a high emissivity blackbody cavity (> 0.999) with accurate absolute temperature knowledge of better than 0.045 K ($k = 3$). On-orbit, the OARS is operated over a wide range of temperatures to provide independent infrared radiance accuracy verification of the CFTS that is calibrated frequently with an independent ambient blackbody and a space view [Taylor et al., 2010; 2012]. In the laboratory, calibration is done with an ambient (295 K) and a hot (330 K) blackbody.

Figure 4.22 shows a section view of the laboratory version of the OARS that was built and demonstrated through end-to-end testing of the ARI system under the UW IIP [Best et al., 2012]. The light-trapping cavity shape is coated with Aeroglaze Z306 diffuse black paint. The heated cavity temperature is measured with five Thermometrics SP60 thermistors, with absolute temperature calibration provided by three imbedded phase transition cells (mercury, water, and gallium). The heated halo located in front of the cavity is used for measuring cavity emissivity to within an accuracy of 0.0006 ($k = 3$), as described later in this section.

2. Absolute Temperature Calibration Using Phase Change Cells

The thermistors of the OARS are calibrated to an absolute temperature scale established on-orbit with miniature phase change cells. Figure 4.23 (left) shows typical transient temperature responses of one of the blackbody cavity thermistors during a gallium melt event, where it can be seen that the melt plateau is clearly discernable to within 5 mK of the known melt temperature [Best, 2008]. First, the blackbody cavity is brought to thermal stability in the constant temperature mode about 50 mK under the expected phase change temperature. Then, the blackbody controller is switched into constant power mode using the power level that would bring the cavity to about 100 mK above the expected phase change temperature.

Significant testing has been conducted to explore the melt plateau repeatability, and to characterize the relationship between the time taken to go through the melt and the melt plateau (mid-melt) temperature. Figure 4.23 (right) illustrates that as the time to go through the melt is increased, the mid-melt temperature asymptotically approaches the known gallium melt temperature. The inset plot illustrates the excellent melt plateau repeatability for three different runs taken before and after exposure to accelerated life testing.
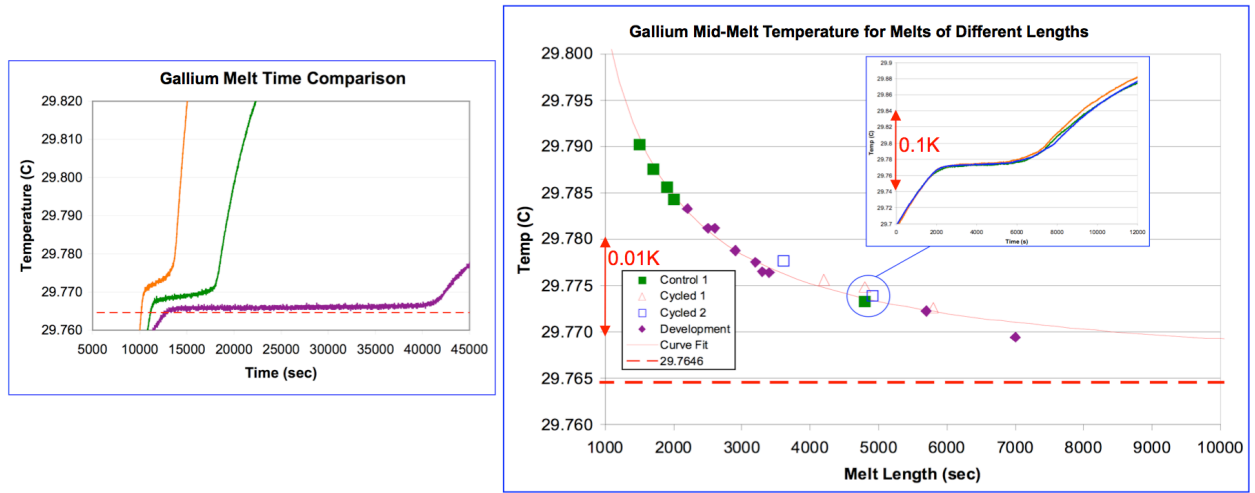
Figure 4.23: THE PLOT ON THE LEFT SHOWS THREE MELTS OF DIFFERENT DURATION. THE LONGER THE MELT THE CLOSER THE PLATEAU APPROACHES THE THEORETICAL MELT TEMPERATURE. THE LARGE PLOT AT RIGHT ILLUSTRATES THIS BY PLOTTING MID-MELT TEMPERATURE VS. MELT LENGTH EACH DATA POINT CORRESPONDS TO A SINGLE MELT. THIS CHARACTERISTIC ASYMPTOTIC BEHAVIOR HAS SHOWN TO BE INVARIANT FOR A GIVEN PHYSICAL CONFIGURATION.
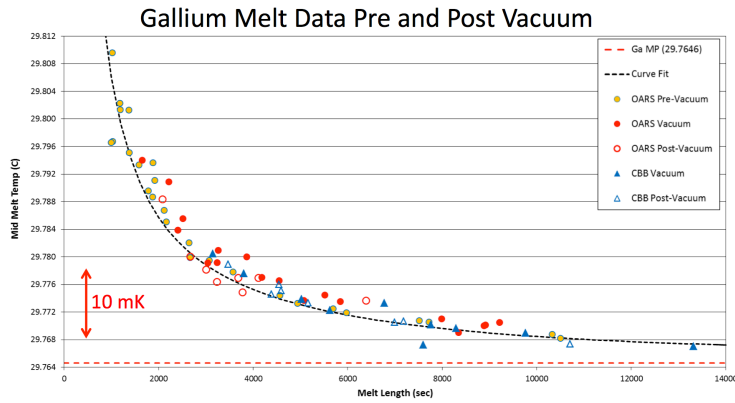
Figure 4.24: CHARACTERISTIC MELT BE-HAVIOR PLOTS FOR GALLIUM INTEGRATED INTO THE OARS AND COLD BLACKBODY, FOR BOTH PRE- AND POST-VACUUM TEST-ING. SIMILAR RESULTS WERE OBTAINED FOR WATER AND MERCURY. THE SIGNA-TURE PLOTS FOR EACH MATERIAL SHOW THAT THE MELT BEHAVIOR IN A VACUUM ENVIRONMENT IS VERY CLOSE TO WHAT WAS DEMONSTRATED IN ATMOSPHERE.

The accelerated life test subjected each of the three phase change materials (gallium, water, and mercury), individually contained in sealed phase change housings, to the full number of deep temperature cycles expected prior to and throughout a mission lifetime [Best 2010]. The test also subjected the phase change cells to an equivalent expected dissolution environment by exposing them to an elevated temperature for a far shorter period than a mission lifetime. The equivalency was established through the Arrhenius reaction equation. Melt signatures were compared both before and after the accelerated life test to verify that there was no change in performance. Also, careful inspections using scanning electron microscopy were conducted on the housings to show that there were no mechanical failures or melt material migration from the housings. Selected destructive testing was also done to check that the gallium or mercury liquid metals had not migrated into the grain boundaries of the housing, a condition that leads to liquid metal embrittlement.

Phase change signatures for each of the reference materials were conducted in the vacuum environment, using the OARS as configured in Figure 4.22 [Revercomb, 2013b]. Mid-melt temperature vs. melt length for each of the three materials is plotted in Figure 4.24 for both

the OARS and cold blackbody, for both pre- and post-vacuum operation. The data are fit with a previously determined characteristic curve that has been shown to be invariant for a given reference material and melt cell housing configuration.

The overall temperature uncertainty budget for the OARS in the laboratory, on-orbit, and for the Ambient Blackbody on-orbit are 45, 40, and 45 mK respectively. This budget includes the 3-sigma uncertainty contributions from the temperature calibration standard, the readout electronics, the temperature transfer process during calibration, the cavity temperature uniformity (during use), the long-term stability, and the determination of the thermistor weighting factors used to calculate the blackbody effective radiometric temperature. These are the values used in the end-to-end uncertainty budget for the ARI instrument.

3. Emissivity Measurement Using a Heated Halo

The heated halo is used to measure the OARS broadband spectral emissivity. The configuration of the heated halo in front of the OARS is presented in Figure 4.22. The method used to make the cavity emissivity measurement is illustrated in Figure 4.25 (left), and described in detail in [Gero et al., 2012]. The heated halo is heated 70 to 90°C above the blackbody cavity that is at ambient temperature. The halo is baffled so that the spectrometer only sees it via reflection from the cavity. The equation in Figure 4.25 (left) defines the radiance measured by the CFTS sensor. All the terms on the right side of the equation are known except for the emissivity. $B(T_{BB})$ is the Planck radiance emitted directly from the blackbody cavity. The cavity emissivity is ε. The view factor from the cavity to the heated halo is F and can be accurately calculated. $B(T_{Halo})$ is the Planck radiance from the halo, $B(T_{room})$ is the background radiance, and $R_{background}$ is the term enclosed in square brackets.
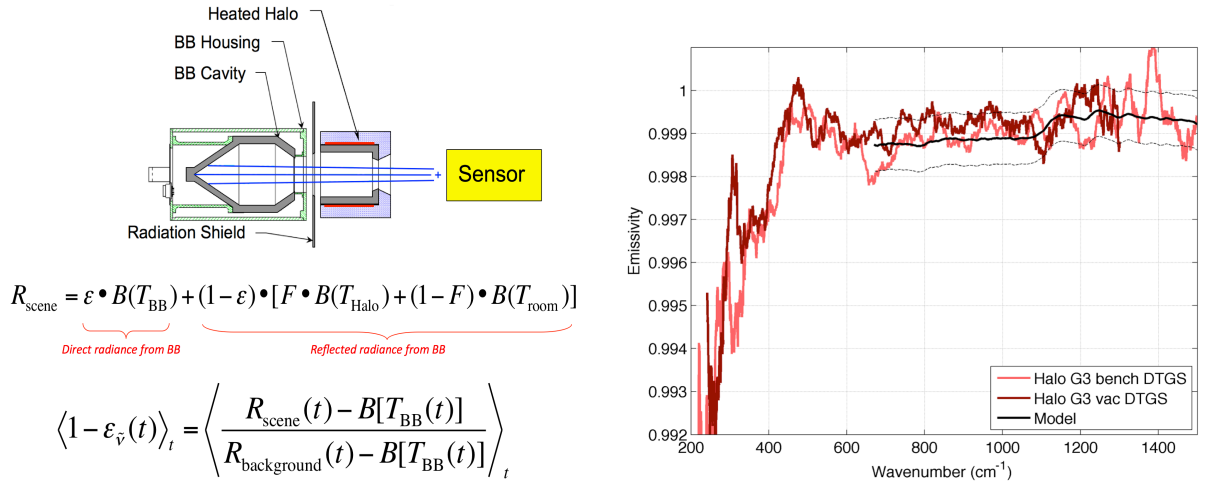
Figure 4.25: Left: Heated Halo emissivity measurement scheme. The bottom equation shows the inverted equation used to calculate emissivity. Right: Spectral emissivity measurements of the OARS using the Far-IR deuterated triglycine sulfate (DTGS) detector, comparing measurements taken in the laboratory with those taken under vacuum.

An important aspect of this measurement is that each time the OARS is viewed during a calibration cycle, the emissivity is calculated, so long-term temperature stability is not required. Stability is only required over the relatively short instrument calibration cycle. By

making the measurements in this way, the individual emissivity measurements can be averaged over long periods to reduce noise in the measurement.

Spectral emissivity measurements made of the OARS cavity are shown in Figure 4.25 (right): Monte-Carlo ray-trace modeled cavity emissivity with $\pm 3\sigma$ error bars are shown in black. All heated halo data are smoothed using a Savitzky-Golay filter which creates artifacts in regions where the noise is high (e.g., 1200 –1500 cm^{-1}).

The laboratory measurements show excellent agreement with the model. These results also compare very well with other emissivity measurements made with similar blackbody targets using the UW Atmospheric Emitted Radiance Interferometer (AERI) ground-based and Scanning High-resolution Interferometer Sounder (S-HIS) aircraft instruments [Best et al., 2009]. The lower emissivity between 200 and 400 cm-1 is expected to be largely eliminated by impregnating the Z306 paint with graphene.

4. On-Orbit Instrument Spectral Response Measurement Using a CO_2 Laser

The Instrument Line Shape (ILS) of the spectrometer is defined as the output response to a purely monochromatic input. The truncation of the interferogram is the most fundamental limit for the FTS instrument line shape, and ultimately limits the achievable spectral resolution. Other possible contributors to instrument line shape for IR FTS instruments are finite source size [Genest, 1999 and 2008, Desbiens, 2002], diffraction, mirror misalignment, and optical aberrations [Genest, 2002 and 2003].
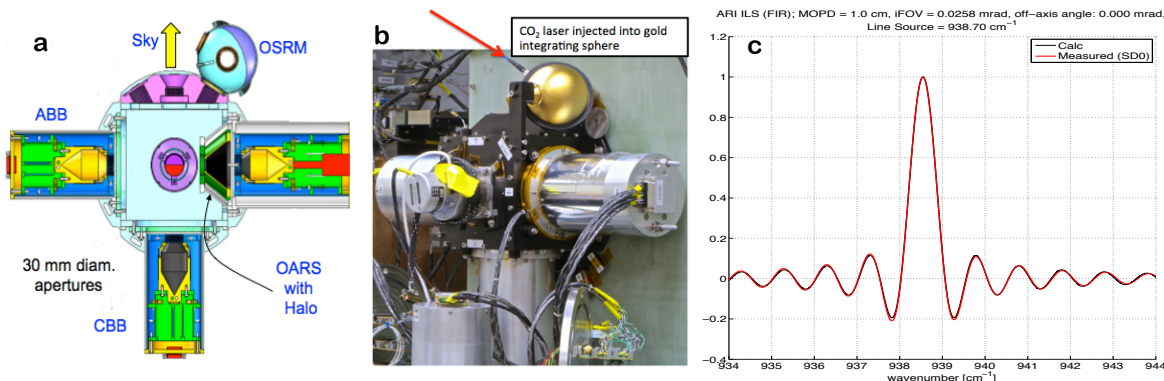
Figure 4.26: ARI INSTRUMENT LINE SHAPE MEASUREMENT CONFIGURATION DIAGRAM (A), TEST SET-UP PHOTOGRAPH (B), AND (C) DTGS RESULTS (RED) COMPARED TO CALCULATIONS (BLACK).

Figure 4.26 illustrates the laboratory measurement of the CFTS ILS, made using a gold integrating sphere and a fiber coupled 10.6 μm CO_2 laser (a QCL laser is planned for flight – see next subsection), and compares the measured to the calculated instrument ILS. The calculation assumes the as-designed angular field-of-view in interferometer, an on-axis detector, perfect optical alignment, and perfect laser beam filling of the instrument field of view. The results show good agreement between the calculated and measured instrument line shape, confirming that the measured line shape is well understood.

5. Blackbody Emissivity and Spectral Response Measurement Using a QCL

A monochromatic infrared light source with linewidth, power stability, and wavelength stability well-suited for complementary monitoring of the emissivity of the CLARREO calibration
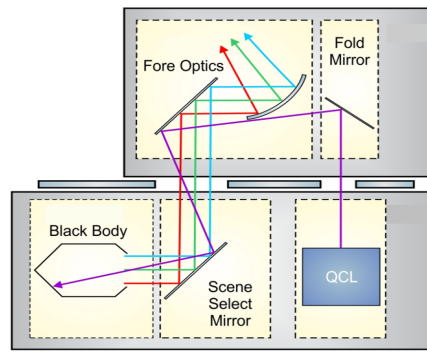
Figure 4.27: MONOCHROMATIC RADIATION FROM THE QCL (PURPLE) IS INJECTED INTO THE BLACKBODY UNDER TEST. REFLECTED QCL RADIATION IS RETURNED ALONG WITH BLACKBODY THERMAL RADIATION (RED, GREEN, CYAN).

blackbodies, was developed under IIP-07. This infrared payload subsystem utilizes a QCL, a unipolar semiconductor device that takes advantage of recent developments in semiconductor technology to provide compact, non-cryogenic, single mode laser light. QCL's are capable of reaching high powers (>100 mW) at moderate temperatures (accessible from thermoelectric coolers) with narrow linewidths (< 1 cm^{-1}). These characteristics are ideal not only for implementing on-orbit analogs of laser-based optical materials measurements performed by institutions such as NIST, but also for creating uniform, monochromatic sources for optical system testing. This allows an on-orbit analog to laboratory testing of the ILS with a CO_2 laser.

The concept of operations for the emissivity measurement is to illuminate the blackbody with the QCL beam off-axis and to measure the reflected laser light with the infrared FTS sensor (Figure 4.27). By injecting the QCL into the blackbody from a reflection off of the scene select mirror, a single QCL device can be used for both a calibration and a verification blackbody. The reflected laser light appears as a clearly distinguishable narrow spectral peak superimposed on the blackbody spectrum.

The radiometric calibration of the FTS sensor allows the accurate determination of the radiance associated with this spectral peak. Changes in this radiance over time are indicative of changes in the blackbody emissivity. The power of the laser that is injected into the blackbody is determined using a calorimetric approach that makes use of the blackbody temperature sensors to measure the rate of temperature rise. Optical modeling analysis, taking into account the illumination and viewing geometry of the complete system, allows an independent quantitative determination (with an explicit uncertainty estimate) of blackbody cavity emissivity.

A compact, integrated housing was developed for the QCL that is compatible with LEO environmental requirements and utilized design heritage from systems deployed on aircraft flights in the lower stratosphere. This housing provides thermal, optical, and electrical accommodations sufficient to meet performance requirements for on-orbit monitoring of blackbody cavity emissivity. The housing provides thermal stability adequate to maintain sufficient output power stability and linewidth. It provides integrated collimation optics to collect light from the QCL device and collimate the light into a well-defined beam with waist much smaller than the blackbody aperture. It provides electrical interfaces for low-noise current supply to the laser diode itself as well as to the integrated thermo-electric cooler (TEC) used to actively control the diode temperature setpoint. This system has undergone vacuum testing in Harvard's test chamber, showing that it is capable of meeting requirements both in vacuum and ambient conditions after many vacuum test cycles.

4.5.4.2 Absolute Radiance Interferometer (ARI) Instrument

The two major components of ARI, the calibrated FTS sensor and a novel On-orbit Verification and Test System (OVTS) that contains the sub-system technologies described above are shown in Figure 4.28 [Taylor, 2014]. The CFTS is the familiar combination of an FTS and calibration blackbody, with a space view and Earth view, analogous to a standard hyperspectral IR sounder, but much simpler. The OVTS confirms accurate calibration over a wide range of source temperatures by providing an independent IR radiance standard to meet the requirements for proven on-orbit SI traceability.
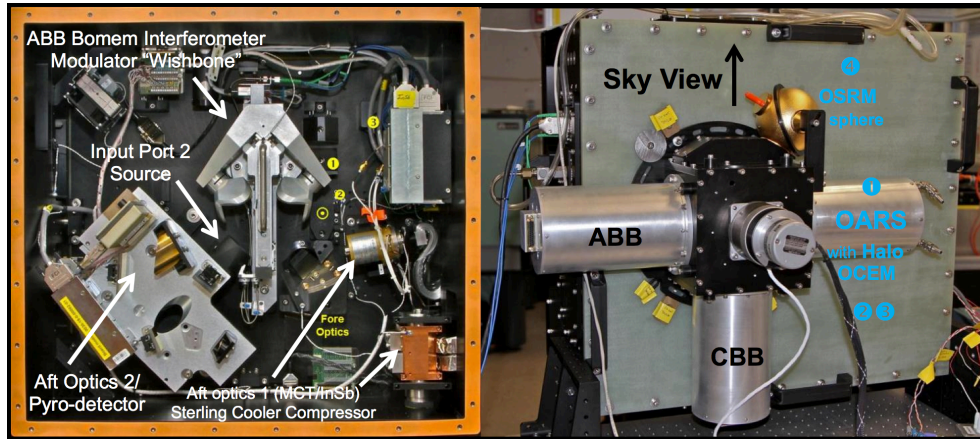
Figure 4.28: Absolute Radiance Interferometer (ARI). The back of the instrument is shown (left) with key elements of the calibrated FTS. The front of the instrument is shown at right with an ambient blackbody and cold blackbody (replacing the space view), along with elements of the OVTS and the integrating sphere for ILS measurement.

The heart of the ARI, and a key to its relative simplicity, is a well-characterized ABB Bomem interferometer module that has flight heritage [Taylor, 2012]. The FTS approach is ideal for satisfying the IR spectrometer requirements because it naturally provides: (1) broad spectral coverage with a small number of detectors, (2) a well-defined instrument line shape that can be monitored on-orbit, (3) the spectral resolution needed to accurately calibrate the spectral scale using well-known atmospheric absorption lines, and (4) Nyquist spectral sampling that allows rigorous spectral matching to other coincident instruments and to future climate benchmark observations. These properties eliminate some of the largest calibration errors traditionally associated with IR instruments based on filters or gratings for spectral separation.

1. On-Orbit Verification and Test System (OVTS)

The OVTS is both a unique and an essential element of the ARI design that will be used for the on-orbit equivalent of SI-traceable preflight thermal/vacuum calibration testing. It also makes possible the objective demonstration of the accuracy on-orbit. The OVTS incorporates the subsystem technologies demonstrated under the IIP that were described above.

2. Calibrated FTS (CFTS)

The FTS subsystem takes input radiance from a scene mirror and modulates the energy with a 4-port interferometer. If then directs the shorter wavelength spectrum to an InSb detector and two Mercury Cadmium Telluride (MCT) detectors, and the longer wavelength

spectrum to a pyroelectric detector. The InSb and MCT detectors cover different portions of the 3.5 – 15 micron band, and the pyroelectric detector covers the overlapping far IR (10 – 50 microns) band. The scene mirror allows the interferometer to view the atmosphere, an ambient temperature calibration blackbody, the OARS, or deep space, all at 90° with respect to each other to minimize polarization effects.

Interferometer Module. The FTS for ARI is built by ABB Bomem. It uses corner-cube reflectors with a wish-bone drive mechanism and a single self-compensating CsI beamsplitter [Buijs, 2008]. The 4-port design prevents double-pass artifacts and gives spectral band separation without the need for an additional beamsplitter. This well-proven ABB Bomem design limits interferometric artifacts to a negligible level.
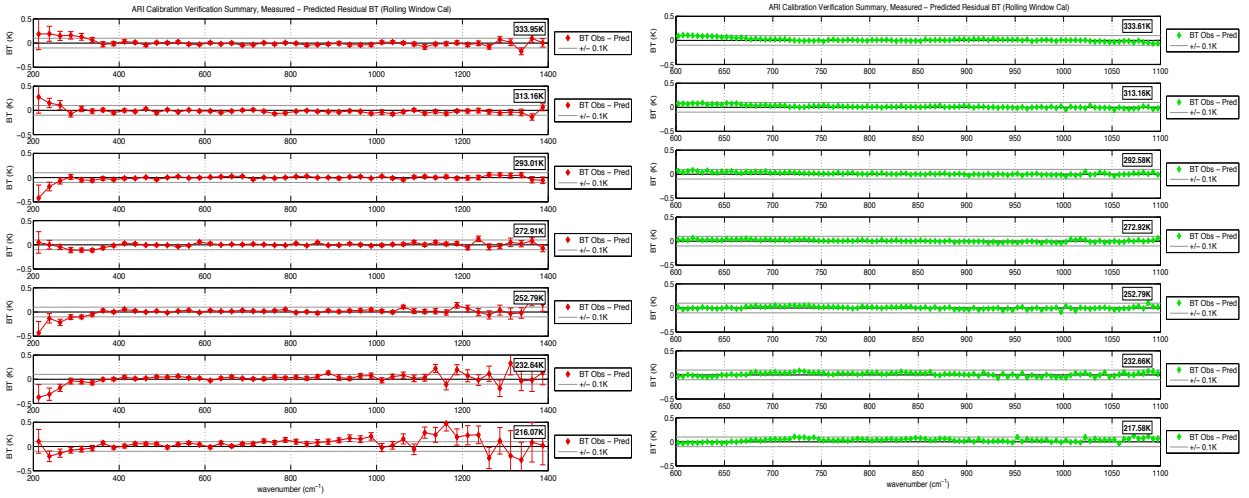
Figure 4.29: ARI CALIBRATION VERIFICATION. OBSERVED – PREDICTED OARS BRIGHTNESS TEMPERATURE RESIDUALS AVERAGED OVER 25 CM^{-1} FOR NOISE REDUCTION FOR THE DTGS DETECTOR (LEFT) AND AVERAGED OVER 5 CM^{-1} FOR THE MCT (RIGHT). THE DIFFERENCES GENERALLY FALL INSIDE THE ±0.1 K BOUNDARIES SHOWN. IN THE FARIR, FROM 200 – 300 CM^{-1}, THE LOW SIGNAL-TO-NOISE DUE TO THE LESS THAN OPTIMUM BEAMSPLITTER COATING CAUSES A SMALL BIAS. THE COLDEST SHORTWAVE REGIONS ALSO SHOW SOME SMALL BIASES DUE TO LOW SIGNAL-TO-NOISE (THE NOISE LEVEL OF THE TESTS IS A FACTOR OF 4 LARGER THAN THE ON-ORBIT NOISE SPECIFICATION DUE TO SHORTER DWELL TIMES).

Optical Design. The ARI optical system uses all-reflective optics on the front end and long-wave band (except for the FTS beamsplitter), and reflective and refractive optics on the shortwave bands [Schwarz, 2011]. The design optimizes interferometer throughput by imaging the aperture stop at the corner-cube vertices, while keeping the calibration blackbody and OVTS system small (30-mm diameter apertures). It also provides well-defined stops. Stray light and instrument background are managed by: stable temperature shielding of detector cavities; use of low-scatter mirrors; proper baffling; and an optical design that ensures no vignetting occurs. Separate focusing optics are used for each output port. The entrance aperture is focused on the detectors for all channels, thereby eliminating non-uniform scene signal dependence from non-uniform response regions of the detectors.

Detectors. ARI uses standard single-element detectors that are readily available. The longest wavelength energy, 10 – 50 microns, uses a DTGS pyroelectric detector. The short- and mid-wave IR energy is detected by an InSb detector responding from 3.5 to 5.5 microns, an

MCT detector responding from 5.5 to 9 microns, and a second MCT responding from 9 to 15 microns. These detectors are housed in a single dewar and maintained at 77 K by a tactical cryocooler.

On-orbit Testing. In addition to radiometric verification, the ARI instrument demonstrated the capability for several types of testing that can be conducted on-orbit. These tests include (1) blackbody emissivity, (2) instrument line shape, (3) response linearity, and (4) polarization sensitivity. Blackbody emissivity is measured with both broadband and laser sources. The same laser will be used with a small integrating sphere for ILS. Linearity is measured both using the variable temperature OARS and by analyzing out-of-band harmonics [Revercomb, 1994; Taylor, 2009].
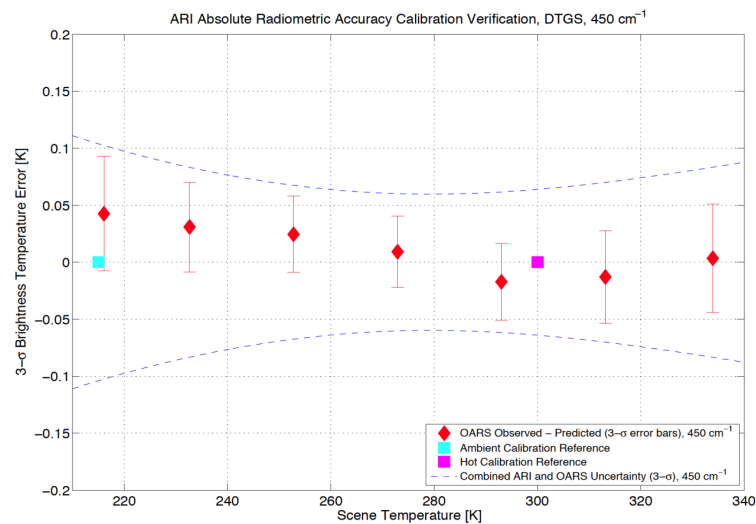
Figure 4.30: ARI CALIBRATION VERIFICATION, 450 CM^{-1}; DTGS. MEETING THESE UNCERTAINTY BOUNDS IN THE VACUUM ENVIRONMENT DEMONSTRATES THE CAPABILITY TO MEET THE 0.1 K ($k = 3$) UNCERTAINTY REQUIREMENT ON-ORBIT.

4.5.4.3 ARI Key Performance Results

Calibration verification was completed in the vacuum calibration configuration and environment using the OARS at temperature set points of approximately 216 K, 233 K, 253 K, 273 K, 293 K, 313 K, and 333 K. The differences between measured and predicted radiances for all OARS setpoints are shown for the ARI DTGS (left) and MCT (right) channels in Figure 4.29.

A sample at 450 cm^{-1} of the results of the calibration verification versus OARS temperature is shown in Figure 4.30. These uncertainties were calculated using a perturbation analysis of the instrument calibration equation [Revercomb, 1988 and 2013b, BIPM, 1995].

Calibration verification with similar results was also completed under a transient thermal environment exceeding the specified maximum thermal transient over a calibration cycle.

4.5.4.4 ARI Summary

The Absolute Radiance Interferometer is a prototype of the CLARREO IR instrumentation with a short path to production of a flight model. The NASA ESTO has judged that all new technology issues have been addressed thoroughly and has assigned a TRL 6 to all of the new

subsystems and to the complete instrument. The demanding CLARREO radiometric accuracy requirement of better than 0.1 K ($k = 3$) brightness temperature at scene temperature has been met by comparing calibrated radiances from the Calibrated Fourier Transform Spectrometer with radiances calculated from the proven characteristics of the On-orbit Verification and Test System. The IR instrumentation for CLARREO is ready for a mission.

4.5.5 SOLARIS Calibration Demonstration System at NASA GSFC

The Reflected Solar Calibration Demonstration System (CDS) is specially designed for the Reflected Solar (RS) spectrometer component of the CLARREO mission concept, and is intended to achieve the same instrument performance specifications (summarized in Table 4.1). The RS CDS consists of two major subsystems: (1) the SOlar, Lunar for Absolute Reflectance Imaging Spectroradiometer (SOLARIS), and (2) the associated calibration support equipment needed to evaluate the spectrometer's calibration. Considering both as part of the CDS emphasizes that reducing the risk of achieving on-orbit CLARREO calibration requirements, described in Section 4.2, relies on both the sensor design as well as developing the laboratory characterization. The goals of the SOLARIS CDS is to create and check calibration protocols and methods, demonstrate the path to SI-traceability (source and detector standards), and prove the ability to derive reflectance via a view of the Sun and Earth's scene. The instrument build and testing takes place primarily at the NASA Goddard Space Flight Center.

A silicon-based detector coupled with an Indigo 9803 640×512 pixel read-out integrated circuits (ROIC) is the current baseline for the sensor for the wavelength range from 320 to 640 nm. The "red" spectrometer is based on MgCdTe detectors coupled to the same ROIC and samples the 600 to 2300 nm spectral range. Polarization sensitivity is minimized for both systems to levels below 0.5% through depolarizers placed in front of the telescope. Solar irradiance is attenuated through the use of a single pinhole aperture, neutral density filters, a collection of pinhole apertures, or various combinations of the three. A silicon-based detector has been fully evaluated (as described below) and has been integrated with a completed telescope and spectrometer to develop the SOLARIS "blue" box. The HgCdTe detector is awaiting further quality control of its integration into its housing. The delay is a result of reduced funding and smaller size of the SOLARIS team, as CLARREO remains in extended pre-formulation phase. Delaying the HgCdTe integration has permitted the smaller SOLARIS team to continue testing of the calibration approaches and protocols with the "blue" spectrometer. Inclusion of the "red" spectrometer SOLARIS will eventually be required to demonstrate the detector-based calibration approaches at longer wavelengths.

4.5.5.1 CLARREO RS Calibration & Characterization Approach

The CLARREO RS spectrometer measurements and calibration approach is provided in Section 4.2. A critical part of the calibration is developing SI-traceable data by characterizing the sensor to SI-traceable, absolute radiometric quantities during prelaunch calibration to the electric Watt (prelaunch calibration box shown in Figure 4.3). Prelaunch absolute calibration includes both irradiance and radiance modes as well as the determination of geometric factors for conversion to reflectance. The end result of the prelaunch calibration is sufficient data to develop a sensor model that predicts the solar, lunar, and planetary/stellar sources planned for on-orbit calibration. Agreement between prelaunch and on-orbit (as shown in Figure 4.3)

means the system is calibrated, and, by analogy, traceable to the pre-launch SI measurements. Disagreement means the sensor model requires improvement based on the on-orbit data, including an additional set of characterization measurements. Solar and lunar views provide information regarding temporal changes in the sensor once on-orbit traceability is established. Thus, the key to the RS on-orbit calibration is the prelaunch, SI-traceable calibration.

Figure 4.31: SIRCUS TRACEABILITY OF THE CLARREO RS AND SOLARIS CALIBRATION.

The required 0.3% uncertainty is fully traceable to the electric Watt by applying tunable laser sources and detector-based standards. Calibration systems, such as NIST's Spectral Irradiance and Radiance Responsivity Calibrations using Uniform Sources (SIRCUS) facility, provide such standards and a capability to understand stray light, spectral response, and polarization sensitivity at the level necessary for CLARREO [Brown et at., 2000]. The basis of SIRCUS is a well-understood tunable laser source that can be coupled to a fiber optic system providing both radiance and irradiance sources. The output of the source is determined via detector standards characterized against the Primary Optical Watt Radiometer (POWR). The planned calibration traceability to SIRCUS is shown as a stepwise sequence in Figure 4.31. It begins with a substitution radiometer that is used to calibrate the tunable laser source, known as the POWR Laser. In a second step, the POWR unit is moved and replaced by the CLARREO Transfer Radiometer (CXR) based on a silicon-trap detector for the visible and near infrared and indium-gallium arsenide detectors at longer wavelengths. The stated accuracy to calibrate a transfer radiometer in irradiance mode using POWR is 0.09%($k = 3$). The upper portion of Figure 4.31 shows these steps.

The accuracy of such a radiance-based calibration has been demonstrated in NIST facilities to an expected accuracy of 0.2% for k=3. Once the CXR is calibrated, it is moved to the CLARREO Calibration Laboratory to calibrate the output of the sources used in the calibration of the RS instrument.

4.5.5.2 SOLARIS Test Plan

The SOLARIS test plan evaluates all parts of the CLARREO calibration process, described in Section 4.2 and summarized in Figure 4.3, with emphasis on the laboratory-based absolute radiometric calibration. The SOLARIS test plan is shown in Figure 4.31. Attention is paid to developing credible uncertainties for characterizing possible degradation of the attenuator system. Emphasis of the laboratory testing is on the radiometric and spectral characterizations since the current state of the art of geometric and spatial calibration approaches are sufficient for CLARREO mission requirements, assuming that stray light, scattered light, and ghosting analysis are radiometric properties. The importance of stray light in the reflectance retrieval makes characterization and modeling of stray and scattered light critical for SOLARIS, and the field-based measurements of the Sun and surface reflectance retrievals essential to demonstrate understanding of the error budgets.
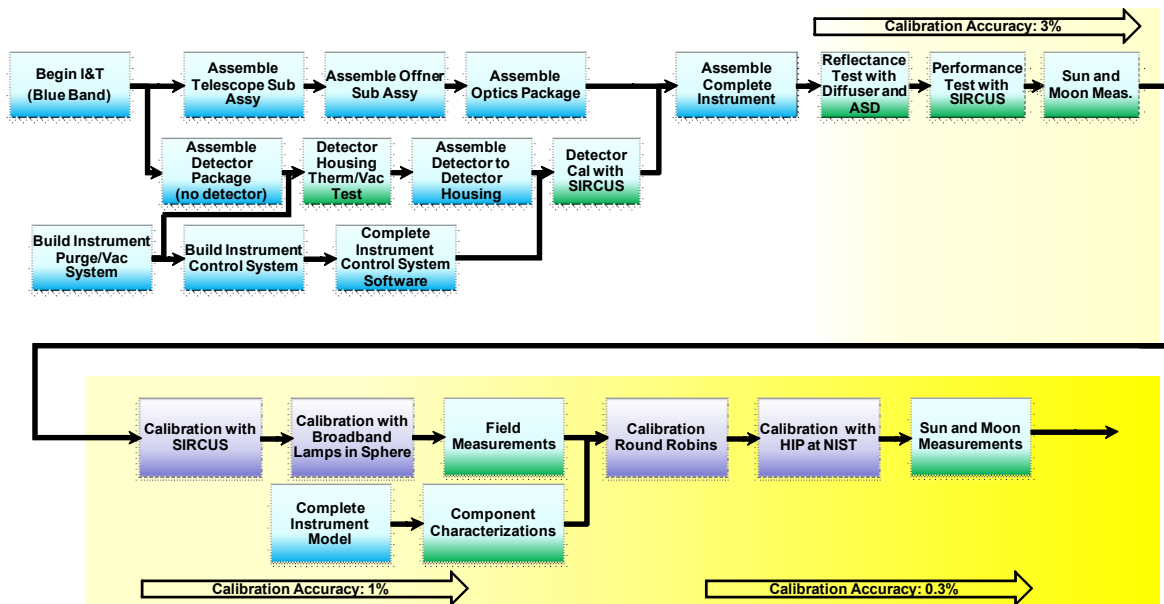
Figure 4.32: SOLARIS INTEGRATION AND TEST PLAN.

SOLARIS testing will lead to an end-to-end instrument performance model and error budgets with measured uncertainty magnitudes and peer reviewed measurement accuracy traceability chains, all of which are applicable to CLARREO. The path to an SI-traceable error budget leads to the CLARREO-required absolute uncertainties of $0.3\%(k = 2)$. Figure 4.32 shows the three phases of SOLARIS integration and testing that leads to this level of accuracy: (1) 3% absolute uncertainty; (2) 1% absolute uncertainty; and (3) 0.3% absolute uncertainty. Current budgetary restrictions result in limitations on the available calibration and sensor hardware such that the CDS goal is to demonstrate $< 1\%$ absolute uncertainty with a path to 0.3%. SOLARIS will show these uncertainties for reflectance retrieval using direct solar irradiance to demonstrate SI-traceability of reflectance through both source- and detector-based standards.

The testing in each of the three phases is described below. All three phases follow the general philosophy to accomplish the following: (1) Develop and evaluate calibration protocols leading to an SI-traceable calibration of the SOLARIS; (2) Develop a physically-based spectrometer

model; (3) Create a defensible error budget; (4) Implement a tunable laser facility with sufficient spectral coverage to cover the full CLARREO spectral range; (5) Evaluate broadband stray light; (6) Understand depolarizer technology; (7) Determine the impact of thermal control uncertainties of attenuators and detector; (8) Field collections with SOLARIS to provide a check on instrument models; (9) Inter-comparisons with other systems; (10) Characterization of solar and lunar irradiance; and (11) Retrieval of reflectance via direct solar view comparison. While this list is strictly not in order of priority or importance, the first three items are considered to be the most important to the CLARREO project, and strictly speaking, ensure that the others occur.

Included in the Phase 1 was evaluation of SOLARIS hardware at the component and subsystem level prior to assembly of the sensor. The key components under consideration were the optical elements including the slit and grating, the detector package, and attenuation and depolarizer elements. The assembled instrument was used in the laboratory as part of preliminary detector-based calibrations [Brown et al., 2000] and in the field with solar- and diffuser-based reflectance retrievals and lunar measurements to demonstrate the 3% absolute uncertainty. The error budget demonstrating the 3% level of uncertainty was evaluated in November 2013 as part of a CLARREO internal review that included the Science Definition Team and NIST evaluators. Phase 2 of the testing is achieving uncertainties $< 1\% (k = 2)$ absolute by improving knowledge of the transfer radiometers that are part of the detector-based methodology. Additional component-level testing takes place to improve the knowledge of the instrument model leading to the 1% uncertainty error budget for the reflectance retrieval. Phase 3 concentrates on taking the uncertainties to the 0.3% level and concludes with an independent review of the error budget by NIST.

4.5.5.3 SOLARIS Initial Testing Results

Initial testing of SOLARIS took place at the component and subsystem level prior to assembly of the sensor. The key components characterized were optical elements including the slit and grating, the detector package, and attenuation and depolarizer elements. Preliminary results of these tests are provided below. Also provided are early results from the laboratory testing of radiometric and spectral parameters, with concentration on the stray and scattered light characteristics needed to develop the optical model or to provide guidance for modifications to the SOLARIS optical system to limit these effects. The SOLARIS calibration demonstration is of the retrieved reflectance, and as such must include field-based measurements of the sun and surface reflectance retrievals. Lunar collections are also coupled with the field work to evaluate SOLARIS repeatability using the Moon.

Detector tests: Component-level testing of the detectors, both Silicon and HgCdTe, were used to select optimal wafers from multiple production runs that traded spectral response at shorter wavelengths against spectral coverage. Testing took place in the detector characterization laboratory at GSFC and included measurements of relative spectral response (RSR), detector-to-detector uniformity, noise, and temperature sensitivity. Physical measurements of pixel pitch and orientation of array relative to fiducials were also made. The next stage of detector evaluation occurred after assembly of the focal plane within the detector housing to protect the detector from contamination. Performance characterization followed with evaluation of RSR from 300 to 1200 nm to define the point at which detector response reaches the noise floor. Testing occurred with the housing at ambient temperature conditions with the detectors cooled to their operational levels. Testing was repeated in cold operational conditions.

The data collected permitted evaluation of detector noise, dark current level and stability, relative spectral response, conversion efficiency (CE) level and stability, detector-to-detector uniformity, and linearity. Testing of the relative spectral response for the detectors was via a standard monochromator approach.
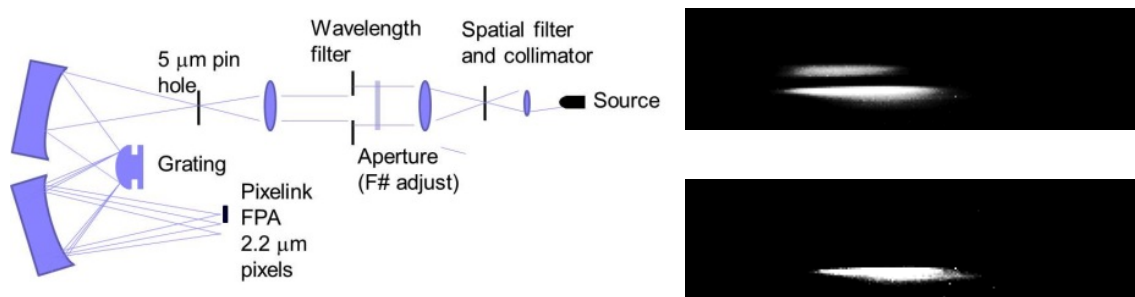
Figure 4.33: Test configuration for testing the optical and spectral quality of the blue spectrometer grating. Test results are shown on the right corresponding to pre- (upper) and post-baffling (lower) to eliminate a manufacturing artifact.

Grating Characterization: Characterization verified grating performance and its dimensional metrology. Dimensional metrology determined the size, shape, radius of curvature, and conic constant. The metrology also permitted assessing the optical quality of the grating through direct microscopic means. Optical characterization made use of the test configuration shown in Figure 4.33. Spectral evaluation made use of narrowband interference filters permitting determination of key spectrometer performance variables. Sample images from the high resolution imager at the end of the optical train are provided in Figure 4.33 as an example of the utility of these data. The horizontal and vertical size of the image provides the spatial and spectral quality of the grating. The top image demonstrates the effect of a manufacturing artifact that was observed during the direct metrology of the grating. Altering the positioning of the grating, proper baffling and slit design mitigated the impact of this artifact in the integrated system, as shown in the bottom image of Figure 4.33.

Optical Elements: The telescope and spectrometer optics were evaluated in like fashion to the grating. Dimensional metrology at the end of fabrication determined the size and shape of each element, including radius of curvature and conic constant. The metrology also evaluated the mechanical aspects of the elements and their associated mounts.

Performance characterization evaluates the quality of the surface finish and reflection efficiency as a function of wavelength. Surface figure of the optical elements was evaluated using standard optical interferometry techniques to evaluate wavefront error, and this was done under varying thermal conditions to understand the mirror's behavior with temperature. Our results indicate the high-quality of the telescope elements. The relatively good agreement with the model indicates that the optical elements were properly aligned and the optical model is an adequate representation of the sensor.

Further comparison of the optical performance of SOLARIS relative to predictions from optical modeling is shown in Figure 4.34. The upper portion of the figure shows the spot diagrams for a point source located at $-5°$, $0°$, and $+5°$ from the optical axis. The lower portion of the figure shows imagery obtained by a high-spatial resolution camera placed behind the SOLARIS telescope and illuminated with a collimated source at the same angles as modeled.
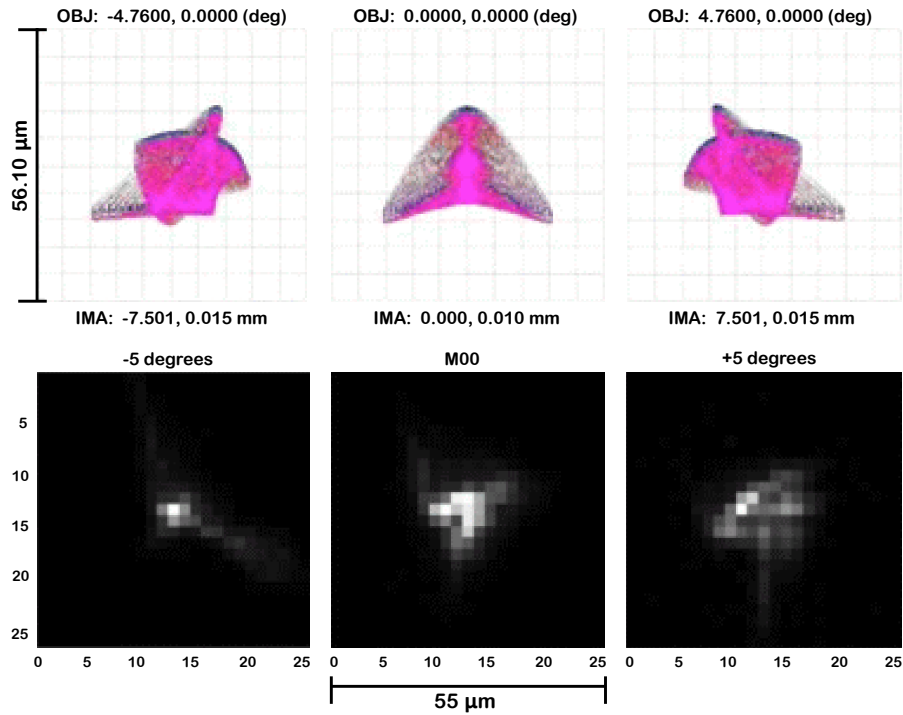
Figure 4.34: Top: modeled spot diagram results for SOLARIS telescope for sources at −5°, 0°, and +5°, and Bottom: measured camera output from a collimated source at the same angles illuminating the telescope.

The imagery and model output are remarkably similar, save for slight rotational differences in the orientation of the patterns.

The spectral reflectance of the coatings of the mirrors was also measured to allow prediction of the sensor signal to noise. The spectral resolution of the reflectance measurements was sufficient to allow it to be combined with grating and detector response. Initial characterizations of the mirrors demonstrated that the coatings did not meet the required spectral reflectance at shorter wavelengths. The mirrors were recoated to ensure that the signal-to-noise would be sufficient in the ultraviolet while being as free as possible from spectral absorption features in the coating.
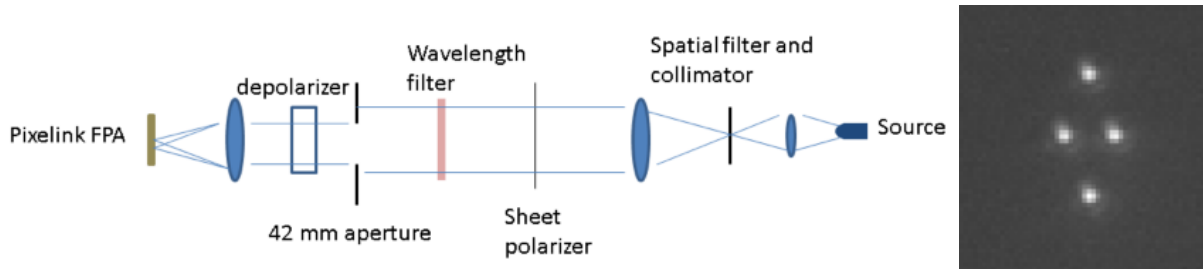
Figure 4.35: Schematic of experimental set up used to evaluate the performance of the SOLARIS depolarizers along with the image recorded by a commercially available, high resolution camera system of a collimated source. Each point is the result of the two wedges producing two polarization states. The ensemble of four points is smaller than the size of the SOLARIS pixel pitch.

Depolarizer: The quartz-quartz wedge depolarizer approach was selected for SOLARIS due to its compactness and its wide use in similar applications. Figure 4.35 shows a schematic of the experimental set up that was used to evaluate the performance of the SOLARIS depolarizers. The source in the figure consisted of a spherical integrating source coupled with a collimator that allowed $\pm 5°$ of tilt incidence at different f-stop numbers. A Moxtek wire-grid style broadband polarizer mounted within a rotation stage that allowed rotation through 360° acted as a reference calibration polarizer or "analyzer." The analyzer was incrementally rotated through 360° to characterize the degree of polarization of the light exiting the assembly. A set of narrow-band filters provided spectral selection.

The collimated source passed through the depolarizers to be imaged on a commercially available, high resolution camera system. The image shown on the right side of Figure 4.35 shows the results from a single analyzer position at a wavelength of 490 nm (through a 10-nm bandpass filter). The source was stopped down by a 5 μm pinhole. Each point in the image is the result of the two wedges producing two polarization states for a total of four points. The brightness of each point varies with the overall polarization of the source. The result matches analytical predictions with the left to right spot separation being 22 μm and the top to bottom spot separation being 60 μm. Collecting the light from all four points would ensure that integrated measurement is polarization insensitive. Ensuring that the size of the four-spot diamond fits within the SOLARIS detector would lead to a polarization-insensitive sensor.

Attenuators: The RS measurement requirement to obtain spectral reflectance relative to the solar irradiance drives the need to view the Sun and requires attenuation of up to a factor of 1:50,000 relative to a typical Earth scene. The baseline design of the attenuator system includes a pinhole aperture, a perforated plate, and neutral density filters. The nominal size of the pinhole aperture would need to be 500 μm for the CLARREO application, but apertures of this size are associated with significant diffraction effects that vary strongly with wavelength. Characterization of the neutral density filters has followed standard approaches using monochromator measurements to determine the spectral transmittance.

The perforated plate is a grid of over 300 discrete pinholes attenuating through blockage and diffraction. A random hexagonal grid of pinholes with a random phase of 0.6 μm reduces artifacts from the system. The size of the perforated area and number of pinholes is designed to be large enough to produce a uniform beam across multiple detectors while avoiding edge effects. The pinhole density is uniform so that each detector in the focal plane sees the same number of pinholes. Randomizing the grid by varying pinholes prevents problems associated with the geometric regularity of mesh attenuators. Similarly, vignetting is avoided through both the random grid design and the operations concept of nominal 90° solar incidence angle.

Characterization of the pinholes to date has relied on measurements performed by the manufacturer as well as preliminary measurements with a laser-based system [Brown et al., 2000]. Future measurements will include imaging approaches using electron microscopy or similar approaches to evaluate the shape, size, and total area of the pinholes.

Instrument-level laboratory testing: Instrument-level testing follows basic testing protocols for most passive, hyperspectral, imaging sensors. Collimated sources are used to evaluate spatial characteristics of the sensor and extended sources for the radiometric characterization. Inclusion of new sources is planned such as RF lamps to enhance blue light output [Arechi

et al, 2011]. The approach to establish SI-traceability is to the standard Watt via NIST's POWR facility and through development of SIRCUS-like sources [Brown et al., 2000].
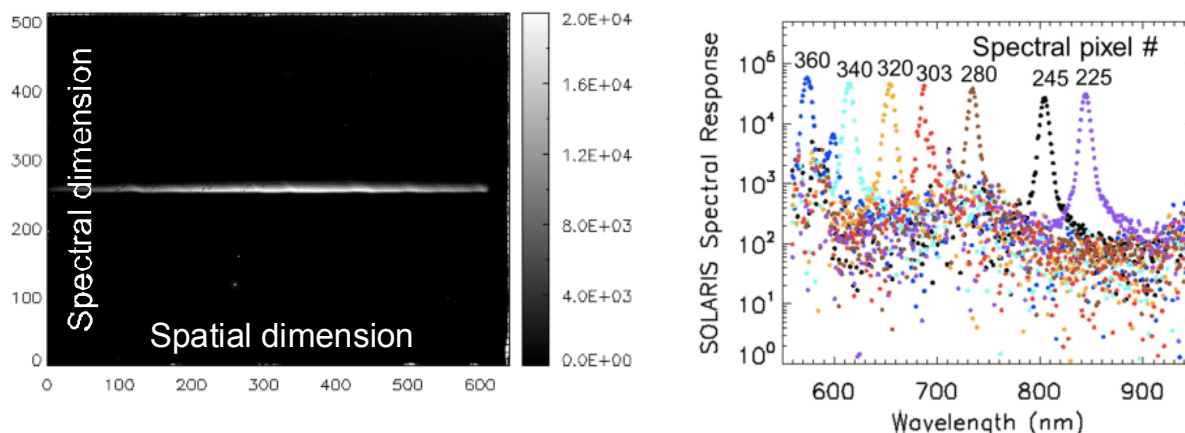
Figure 4.36: THE SOLARIS OUTPUT RESULTING FROM THE ILLUMINATION BY A MONOCHROMATIC, WIDE-FIELD SOURCE (LEFT IMAGE), AND THE RESULTS FROM SEVERAL HUNDRED SUCH IMAGES TO PRODUCE ABSOLUTE SPECTRAL RESPONSE OF SOLARIS FOR SEVEN REPRESENTATIVE BANDS (RIGHT IMAGE).

Absolute Radiometry Tests: The use of SIRCUS is the key to achieving calibration against both NIST standards and with respect to SI-traceable standards. The difficulty with a SIRCUS-based approach for absolute spectral response is the time-consuming nature of the measurements.

Figure 4.36 (left) shows the SOLARIS image from a single SIRCUS wavelength from a wide field spherical integrating source. The narrow vertical extent of the image is indicative of the near-monochromatic nature of the incident source. The wide spatial extent is the result of the wide field illumination. Each individual data point in Figure 4.36 (right) is the result of a single image as demonstrated in the left image. It should be noted that these data required several days to collect. The advantages of such data are the high accuracy of the absolute calibration, excellent knowledge of out-of-band response, and SI-traceability. The results shown in Figure 4.36 indicate that the spectrometer portion of SOLARIS is behaving as expected. There are no significant sources of out-of-band light except for higher order diffraction effects that can be corrected by appropriate filtering techniques. One key lesson learned to date from the SOLARIS absolute calibration collections is the need for improved lasers within the SIRCUS system to increase signal levels at the sensor, increase spectral coverage, and decrease the time needed to scan through the full spectrum under study.

The benefit of a nearly monochromic source is that collimating that source will provide a singular point on the imaging spectrometer's output. Figure 4.37 shows this singular point (labelled "Point source image" in the figure). Two other features are noticeable in the image as well. The lower feature is the result of higher-order diffraction effects in the grating and the fact that there is no filter in SOLARIS to remove this effect. The feature to the left of the point-source image is a result of an un-baffled reflection from the spectrometer's slit. The image shown in Figure 4.37 resulted in a modification to the SOLARIS optical train to add a baffle that removes this feature.

Relative Radiometry Tests: Parameters covered under the relative radiometry term include
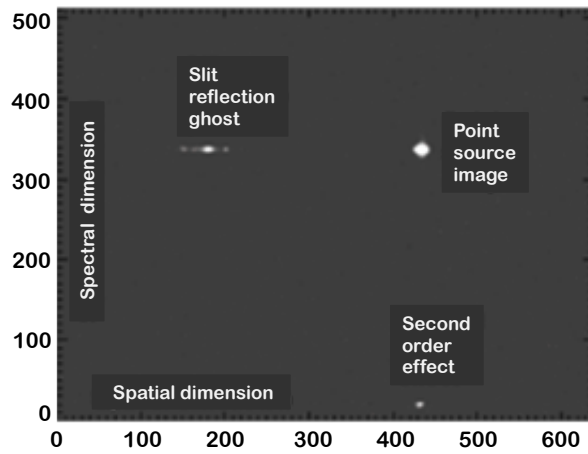
Figure 4.37: IMAGE SHOWS THE SOLARIS OUTPUT FROM A COLLIMATED, MONOCHROMATIC SOURCE INDICATING A SPATIAL STRAY LIGHT FEATURE RESULTING FROM A REFLECTION FROM THE SLIT.

signal-to-noise ratio (SNR), noise characteristics, and detector-to-detector variability. These will make use of full-field, full-aperture sources and thus include all detectors in the evaluations. Thus, a portion of the relative radiometry process will be assessment of the temporal stability and spatial uniformity of the sources.

An initial evaluation of SOLARIS noise characteristics included data collected in three sweeps with 50 frames collected for exposure times varying from 5 to 900 ms. Collections at 5, 10, 15, 20, 25, and 30 ms were made at 10 frames per second, while those at 50, 100, 150, 200, and 250 ms were done at 3 frames per second. The last four exposure times of 300, 500, 700, and 900 ms included SOLARIS images at 1 frame per second.

Determining the dominant noise types is important for CLARREO because the climate record relies on averaging thousands of spatial data points over time to remove short-term reflectance variations in the Earth-atmosphere system. This allows the SNR requirement for CLARREO to be significantly lower than process-based missions, but requires that noise in the sensor be random. The low SNR of SOLARIS makes assessing the noise characteristics a challenge. Evaluation of the data relied on averages of all 50 frames per integration time as well as averages of sets of 10 frames. Mitigation of the relatively high noise of SOLARIS was accomplished by averaging 4×4 detectors. The ROIC used by SOLARIS relies on four separate amplifier chains, and the detectors were separated and evaluated by each amplifier chain.

The results indicate that the noise decreases by a factor of $5^{1/2}$ when comparing 10 frames versus 50 frames. This is as expected for a Gaussian- or shot-noise case and is the goal of the CLARREO design as it means that increased sampling will improve the overall signal-to-noise characteristics without creating a measurement bias. The averaging of the 16 spatial detectors did not, however, lead to a factor of four improvement in signal-to-noise. The result is still under evaluation since one possible cause would be a lack of independence between the 16 detectors being averaged as a result of a flaw in the focal plane electronics. A set of newer electronics that are closer to flight-like quality have recently been implemented, and its noise will be characterized in future.

Sensor Linearity Tests: The fact that SOLARIS should have a highly non-linear sensor response, as a result of selecting a detector and electronics package that provides the dynamic

range needed for a solar and Earth view approach, prompts for treating linearity as a specific item. Linearity characterization is done via three methods: (1) varying integration time; (2) varying source output via multiple apertures; and (3) varying source output via inclusion of attenuating filters. The first approach is necessary to allow characterization of the 9803 ROIC behavior at low-light levels.

Evaluation of the noise characteristics, described above, was also used to determine sensor linearity. The approach is very similar to that developed for the Thermal Infrared Sensor (TIRS) on the Landsat 8 platform [Montanaro et al., 2013], which uses an identical ROIC as in SOLARIS. The linearity correction developed for SOLARIS has been shown to be more accurate than that for TIRS, but is still at an error level too large for the CLARREO mission. Evaluations are currently underway to determine whether an alternate correction approach can reduce the errors or whether a different electronics design is needed for CLARREO.

Sensitivity to Polarization Tests: The same source and linear polarizer, as used to evaluate the depolarizer optics, is deployed at the instrument-level tests – the polarizer is rotated while recording the output of SOLARIS. The measurements are complicated by the fact that the polarized source must be known in a relative fashion to better than 0.5% to allow determination of the SOLARIS polarization sensitivity at levels required for CLARREO. Efforts to date have concentrated on understanding the polarization of the SIRCUS laser coupled to the spherical integrating source and the polarizer filter. Evaluations using a non-imaging field spectrometer, the SOLARIS sensor, and the transfer radiometers used to calibrate the SIRCUS output indicate that the sphere source is depolarized to better than the 0.5% level. While such results would typically lead to the conclusion that the source is effectively unpolarized, the strict requirements for SOLARIS means that further evaluation of the polarization test set up is needed.

Instrument-level Field Testing: The baseline approach to on-orbit radiance knowledge is that the Sun provides a reliable source for transfer to orbit and for maintaining calibration on-orbit. The goal of field measurements is to develop the techniques needed to ensure an accurate transfer to orbit while at the same time demonstrating that a direct solar view can be used to determine surface reflectance. Lunar data are to be collected to verify the calibration of the attenuators.

Demonstration of SOLARIS in the field took place in early 2012 with measurements of an Earth scene converted to reflectance via inclusion of a reflectance standard in the image. Analyses of these data pointed to several issues related to portability, sensor frame rate, and stray light features. This led to the implementation of a field portable version called Suitcase SOLARIS. The design made use of an additional set of optics, grating, and housing coupled to an off-the-shelf silicon charge-coupled device (CCD) array package. This system is not intended to retrieve solar-Earth view ratios, thus can rely on detector packages with smaller well depths. The data from Suitcase SOLARIS rely on the laboratory radiance calibration before and after deployment.

The Suitcase SOLARIS was completed in March 2013 and deployed in April 2013 in the southwest deserts in Arizona, California, and Nevada as part of early on-orbit evaluation of the Landsat-8 Operational Land Imager. The goal of the deployment was to evaluate inter-calibration approaches proposed for CLARREO, and included ground-based measurements of surface-leaving radiance by Suitcase SOLARIS timed to coincide with overpasses of Landsat-

7, Landsat-8, and an airborne imaging spectrometer. The data set will provide an ability to test the robustness of the SOLARIS design as well as traceability protocols since all of the sensors used during the field measurements can be traced to the SIRCUS-like calibration approach.

4.5.6   Reflected Solar Prototype Instrument Development at CU-LASP

The HyperSpectral Imager for Climate Science (HySICS), developed by Greg Kopp and the team at the University of Colorado's Laboratory for Atmospheric and Space Physics (LASP), is a testbed demonstrating improved techniques for future space-based radiance studies, and result from the ESTO funded IIP projects of 2007 and 2010. The calibration method developed by the HySICS team improves the SI-traceable accuracy by the factor of ∼10 to the required levels for the CLARREO Scientific Objective of measuring the solar radiation reflected or scattered by the Earth. This hyperspectral imager will trace its calibration on-orbit through the solar spectral irradiance recommended in the Decadal Survey [NRC, 2007]. Solar irradiance is known to better radiometric accuracy than any other calibration source available on-orbit. By cross-calibrating a hyperspectral imager with solar spectral irradiance, using techniques LASP has proven on other spaceflight instruments, the Earth-viewing imager can be calibrated, validated, and tracked on-orbit to the required accuracy and traceability levels. A polarization insensitive design, plus polarimetry capabilities, help achieve CLARREO radiometric accuracies needed for climate benchmarking and cross-calibration.

(a) The high-altitude balloon that carried the HySICS instrument to the outermost part of Earth atmosphere was inflated with helium.

(b) Spatial/spectral scans of the Sun enable HySICS's accurate radiometric calibrations.
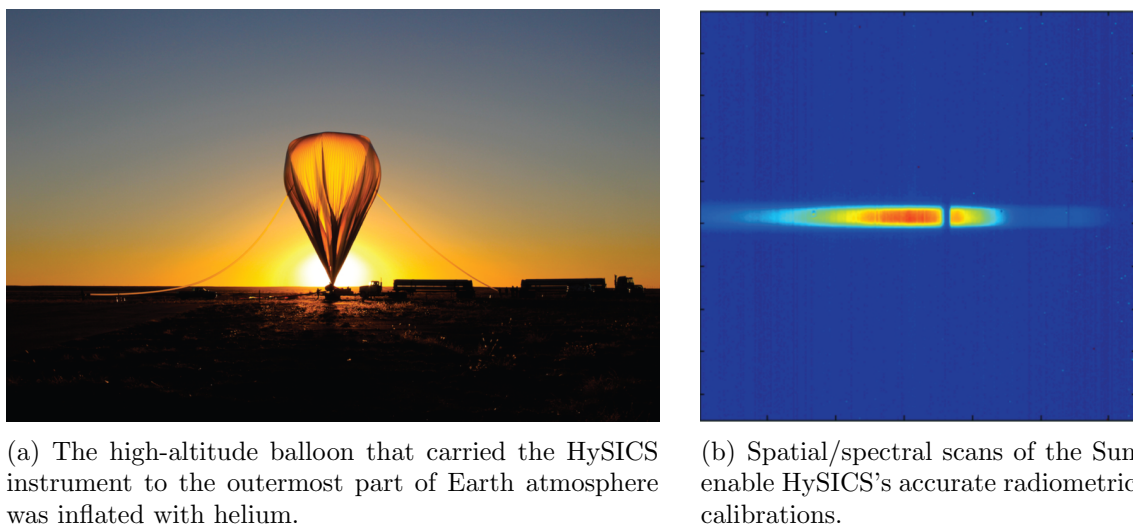
Figure 4.38: THE HySICS DEMONSTRATION IN SEPTEMBER 29, 2013.

In September 2013, HySICS made its inaugural engineering flight on a high-altitude balloon from Fort Sumner, NM (Figure 4.38a). Balloon flights provide realistic, space-like conditions at a fraction of the cost of launching an instrument into space, and therefore an ideal means of testing new technologies. From 125,000 feet and above most of Earth's atmosphere, HySICS, aided by the pointing precision of the NASA Wallops Arc Second Pointer (WASP), was able to make measurements of the Earth, Sun, and Moon during both daylight and night hours. The instrument performed as expected on the eight and a half hour flight, collecting radiance data and periodically calibrating itself with highly accurate radiance scans of the Sun (Figure

4.38b) and Moon. The data collected during the engineering flight will be used to improve the instrument over the next year and to further advance the science algorithms used to process the data. HySICS images scenes onto a single focal plane array at wavelengths between 350 and 2300 nm, covering the extremely important solar and near infrared spectrum containing most of the Sun's emitted energy. Using only a single array allows HySICS to be smaller and lighter than many imagers, a feature necessary for cost-effective space-based Earth observing missions.

A second balloon flight was made in September 2014. After a successful mid-morning lift-off and reaching an altitude high enough to provide the imager with nearly a 7-kilometer field-of-view of the ground, HySICS collected science data and self-calibrated by periodically taking radiance measurements of the Sun and Moon. The calibration against the Sun's known emitted energy provides the instrument with a reference point that allows it to collect such high-accuracy data of the Earth.

The precision pointing that is critical to calibrations using HySICS three differing targets – the Earth, Sun, and Moon – during one short flight was made possible by WASP, a balloon-based tool originally developed for planetary scientists to aim their instruments at distant items of interest. WASP, developed at NASA's Wallops Flight Facility in Virginia, took its first balloon test flight in 2011 and another engineering flight in 2012. After extensive testing, WASP was partnered with its first science instrument, HySICS, for the radiance instrument's inaugural engineering flight.

From liftoff to landing, HySICS and WASP were airborne for nearly nine hours. When the team had collected enough data to test the accuracy of the instrument, the balloon payload was separated from the balloon itself and was safely carried back to the ground via parachutes, landing between two threatening thunderstorms. The payload landed east of Holbrook, Arizona. The flight was deemed both an operational and science success. The HySICS team was able to collect high-quality radiance measurements throughout the flight and has now returned the instrument to Boulder to process and analyze the on-board data. When this analysis is completed, the HySICS team will learn if they have reached their goal of collecting the most accurate shortwave radiance measurements ever taken of the Earth.

4.5.7   NIST Calibration Activities for CLARREO

In Section, the NIST activities in support of the NASA CLARREO mission are summarized, covering time period from 2010 to 2014. During the first two years, the NIST activities were fairly evenly divided between the CLARREO RS and IR instruments, multiple ideas for collaboration between NIST and NASA were proposed, and some were pursued. In the CLARREO extended pre-formulation phase, starting in 2011, the NIST tasks were more tightly directed toward the RS and IR Calibration Development Systems (CDS).

A. Activities in Support of the RS Instrument

The primary technical activities between NASA Goddard and NIST were centered around the use of the NIST Spectral Irradiance and Radiance Calibrations with Uniform Sources (SIRCUS) technique for pre-flight RS calibration. In this technique, the flight instrument views the radiance from an integrating sphere that is illuminated by a tunable laser. The

laser can be tuned across the RS spectral range, and the radiance calibrated by a NIST-calibrated detector substituted in the position of the RS instrument. This technique was seen from the outset as a promising method of characterizing the RS instrument for stray light and perhaps for ultimately calibrating the RS instrument. To facilitate its use for CLARREO, NIST procured a portable version of the SIRCUS hardware and provided it to NASA Goddard on long-term lone. NIST staff also trained NASA Goddard staff on the operation of the SIRCUS instrument at Goddard, assisted NASA with the specifications for procurement of the reference detectors, and calibrated the reference detectors.

Additional (NIST-funded) activities at NIST related to the RS instrument included development of an absolute detector-based source (ADbS) and the Hyperspectral Image Projector (HIP). Each of these uses a spectral light engine to provide broadband, programmable spectra. The output of the ADbS is calibrated using a broadband detector by tuning one-by-one through each monochromatic spectral channel. The ADbS developments used a commercially-available lamp-based spectral light engine. Two papers were written on the ADbS (2010 SPIE and a manuscript headed for J. Res. NIST). The HIP uses a commercially-available supercontinuum source and is otherwise a custom instrument. It presents realistic spatial and spectra scenes to the sensor being tested many SPIE papers were written on the HIP. The HIP prototype was used in 2011 with a CLARREO-relevant hyperspectral imager prototype developed by the University of Colorado Laboratory of Atmospheric and Space Physics (LASP) under an NASA IIP project to provide an initial test of the concept. A hyperspectral image was projected by the HIP into the LASP sensor and measured at the end of a two-week visit of the LASP sensor to the NIST HIP facility, but there has not been time to pursue more detailed tests. (The LASP sensor has since been busy with balloon-based testing). As of this writing, both the development of the ADbS and HIP are ongoing but at a relatively low-level compared with a few years ago. There are plans at NIST to continue with development of both concepts, and in particular to use the HIP hardware to test the ADbS concept.

B. Activities in Support of the IR Instrument

Initially, the activities at NIST in support of the IR instrument centered around the development of a facility at NIST known as the Controlled Background Spectrophotometry and Spectroradiometry System CBS3. The idea was to extend NIST's spectral calibration capabilities for blackbodies and their components to 50 μm (rather than the 14 μm limit that existed at that time) and to enable all of the measurements to be made in a reduced-IR-background vacuum environment facility rather than simply a dry, scrubbed purge (as is done now). A new vacuum-compatible Fourier transform spectrometer was purchased, and a contract to design the CBS3 was performed. However, the cost to build the CBS3 per the design that was developed was considerable, and when the CLARREO mission was directed to remain in pre-formulation, NIST did not have the funding to build CBS3 so it has not been pursued further.

Since 2011, the IR instrument NIST efforts were descoped to be more specific in two directions. The first direction (see B.1 and B.2 below) was to provide measurements of IR CDS blackbody cavities and blackbody paint witness samples to support the IR CDS demonstration. These were done using existing NIST facilities and outsourcing where necessary, but since the NIST spectral range did not extend to 50 μm, measurements were also made at Surface Optics Corporation for comparison. The second direction (see B.3 and B.4 below) was to continue to work on long-term projects to push the NIST blackbody and component measurement
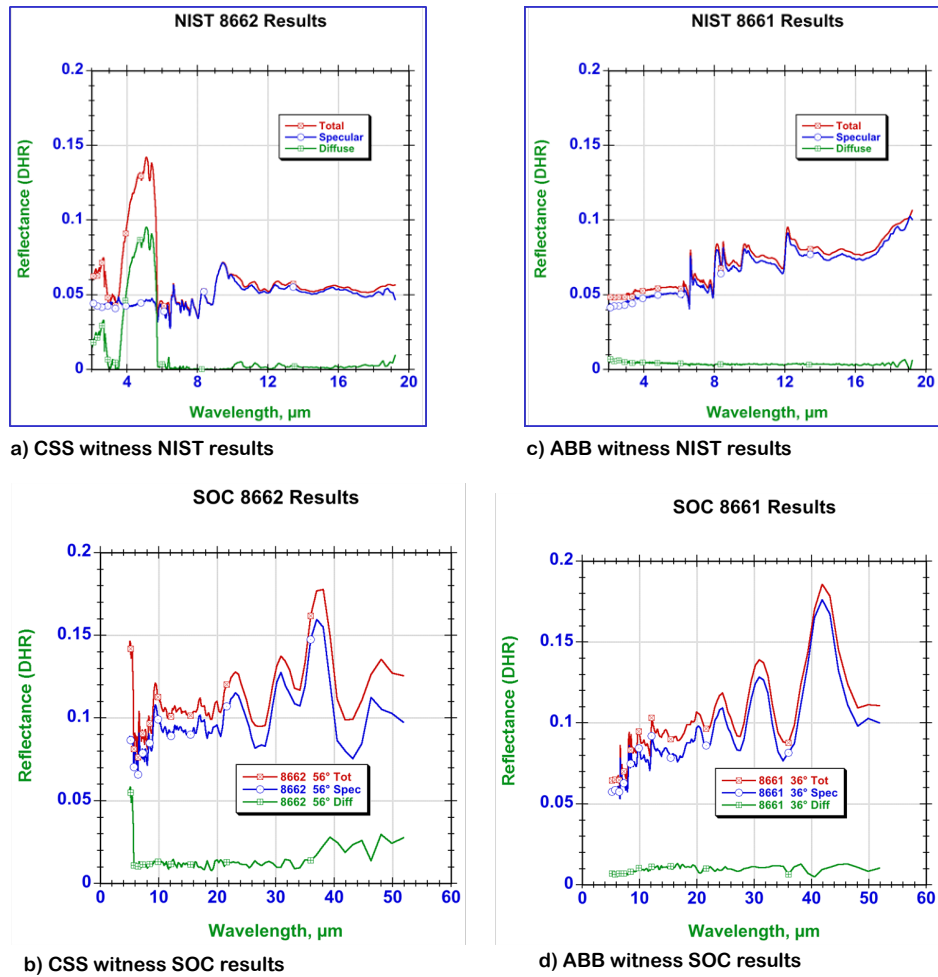
Figure 4.39: NIST DIRECTIONAL/HEMISPHERICAL MEASUREMENTS ON WITNESS SAMPLES OF CLARREO CDS BLACKBODY COATINGS.

capabilities out to 50 μm.

B.1 Surface Reflectance Measurements on Blackbody Paint Witness Samples

Three paint coupons were measured. Example data are shown in Figure 4.39. The coupons were numbered 8661 for the ABB Ambient-temperature Blackbody (PT-401), 8662 for the CSS Cold Scene Source blackbody (Z302), and 8663 for the VTBB Variable temperature (CORSAIR) blackbody (Z302). The ABB and CSS are integral components of the IR CDS, and the data of Figure 4.39 were used in the analysis of the CDS test results.

Measurements coordinated by NIST were made at Surface Optics Corporation (SOC) using their SOC100 measurement system, which measures the angle-dependent hemispherical-directional reflectance factor (HDRF) of samples. Data provided includes the s- and p-polarized spectral reflectance as well as average values over the spectral range of 5 μm to 50 μm. In addition, diffuse-only measurements were performed, which enables the breakdown of reflectance into specular and diffuse components. Each coupon was measured at the angle of incidence corresponding to the angle of viewing of the rear surface of the blackbody cavity when in use.

Measurements were also made at NIST using the Infrared Reference Integrating Sphere (IRIS) system, which measures near-normal (8°) directional-hemispherical reflectance (DHR), which is equivalent via reciprocity to HDRF. Data provided includes spectral reflectance values over the spectral range of 2 μm to 18 μm. In addition, diffuse only measurements were performed, which enables the breakdown of reflectance into specular and diffuse components. Each coupon was measured at 8° incidence. The CSS sample was also measured at 8° incidence by SOC, enabling a direct comparison.

The spacing and amplitude of the interference fringes in the spectra at wavelengths beyond 20 μm indicate that additional thickness of the coating would likely reduce the reflectance and hence enhance the emittance of both the coatings and cavities. The diffuse components of samples 8661 and 8662 in the 3.5 to 5.5 μm range is indicative of thinner coatings, and disappear for thicker ones. The roughly constant diffuse level for sample 8663 is likely due to the numerous visible bubble defects in the sample. The comparison of SOC and NIST results in Figure 4.39 show general agreement for the spectral reflectance. However, the SOC data contains an extra nearly constant diffuse component as compared to the NIST data. There may be a source of error leading to the higher SOC results, since the measurement geometry of the SOC100 and NIST are very similar. Hence the other SOC data may also overstate the diffuse components at large incidence angles.

In addition to the above measurements, and to get a better idea of the scatter of the black samples, measurements of the Bidirectional Reflectance Distribution Function (BRDF) of the same three paint witness samples were made at 5 μm and 10.6 μm and delivered to NASA.

B.2 The CSS and ABB Emissivity Measurements Using the NIST CHILR Facility

The CSS and ABB were delivered to NIST from NASA Langley and set up at the Complete Hemispherical Laser-Based Reflectometer (CHILR) facility. Measurements of its reflectance were made at 10.6 μm using a CO_2 laser, Figure 4.40, and later at 4.0 μm using a quantum cascade laser (QCL). Measurements were performed with both s- and p-polarized light, the average of which represents the unpolarized light result, and were compared to additional measurements using circularly polarized light (10.6 μm) and 45° linearly polarized light (4.0 μm). Due to the small spot of the laser, the cavity was scanned across its aperture at normal incidence. The resulting reflectance map is averaged to produce an effective emissivity versus viewed spot size result.

An interesting result of the CHILR measurements is that the reflectance at 4.0 μm is a factor of 10 greater than that at 10.6 μm. This is due to a difference in the cavity coating reflectance at the two wavelengths (as seen in Figure 4.39). In both the SOC and NIST results, there is a "bump" in the diffuse component of reflectance from 3.5 μm to 5.5 μm of 0.08 at 8° and 0.05 at 56°, compared to near 0 at 10.6 μm (NIST results at 8°, and likely near 0 at 56°). If the coupons are truly representative of the cavity, then the strong diffuse component at 4 μm can account for the lower effective emissivity seen in the cavity measurements. And, according to the coupon measurements, the reflectance should be even higher (and the emissivity lower) at 5.0 μm. Beyond 5.6 μm it appears that the diffuse component remains smaller.

Although comparatively low in value, the reflectance of the ABB cavity was found to be twice as large at 4.0 μm than at 10.6 μm. There was not a significant difference in the paint coupon reflectances between the two wavelengths. Perhaps the cavity coating contains a
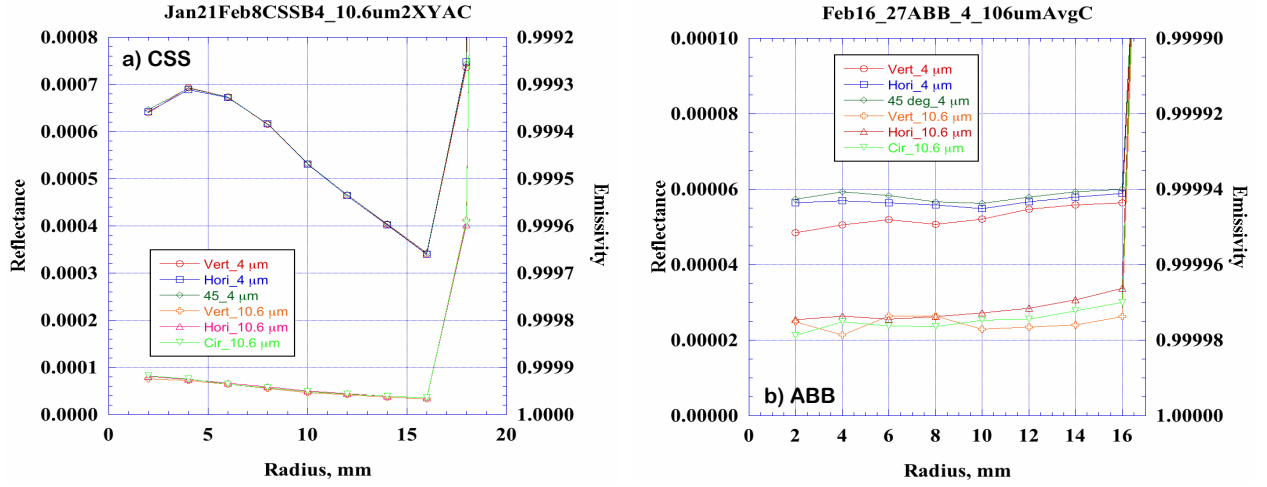
Figure 4.40: NIST CHILR cavity reflectance versus position at a wavelength of 10.6 μM provided to NASA for (a) CSS and (b) ABB. For reference, the right hand scale for each plot shows emissivity computed from $1 -$ reflectance.

greater density of bubble defects, which could result in a greater diffuse component at shorter wavelengths. Despite the wavelength dependence, the effective emissivity is very high at both wavelengths.

B.3 Evaluation of the 23 μm Quantum Cascade Laser for use on CHILR Systems

Initial tests of the 23 μm Quantum Cascade Laser (QCL) obtained in 2011 were able to verify lasing, but also revealed a number of issues that needed to be overcome before effective use in a measurement system. These issues have now been addressed. The temperature stabilization scheme has been improved enabling continuous measurements over several hours. By modulating the pulsed laser output at a slow 10 Hz rate and phase-locked-loop detection, the laser output is separated from the ambient background radiation. The QCL output angular and spatial distributions were measured, from which the optimum collection optics were determined and procured. The average output power of the laser was measured to be 25 μW (± 5 μW). To maximize the signal-to-noise ratio for CHILR cavity reflectance measurements at 23 μm, a blocked impurity band (BIB) *Si:As* cryogenic detector was utilized. It is cooled to 10 K and has a spectral range that extends to 28 μm. A custom dewar was purchased, the mounting hardware and temperature control and signal handling wiring was been designed and fabricated. A wire mesh optical filter was also installed for use in the detector to the reduce background signal.

B.4 Extension of IR Reflectometry Spectral Range to beyond 25 μm

Extension of the NIST's infrared reflectometry capability for diffuse materials to wavelengths beyond 14 μm was achieved in two stages. The first stage involved modification of the existing IRIS system, by replacement of the 14 μm MCT detector unit with a second MCT capable of measurement out to 18.5 μm. Each MCT used with IRIS is custom designed employing a cooled compound hyperbolic concentrator and lens for high effective throughput. The new MCT has a longer hold time dewar (> 24 hr versus 12 hr) enabling longer measurement times to compensate for the lower NEP associated with the longer wavelength cutoff. After construction of the new MCT, and its performance validated, the IRIS system was re-calibrated

for the expanded wavelength range. The upgraded setup is fully operational and has been used to calibrate customer samples.

The second stage, expanding the spectral range to 25 μm, involved construction of a second integrating sphere, motorized rotation stages, an extended spectral range high sensitivity detector, and a reconfigured layout of the measurement system (which includes the FTIR spectrometer, interface optics and sphere setup). After completion of the system and component designs, all required parts were produced or procured. Setup of the system is in progress as of writing.

In parallel to this, NIST began to pursue an alternative approach to extend the diffuse reflectance scale to 50 μm that uses a hemi-ellipsoid and a room-temperature pyroelectric detector instead of an integrating sphere. Several iterations were performed to procure the large-area detector required. Currently the hardware is in place but full-scale testing has not begun yet.

5 CLARREO Mission Concepts

5.1 CLARREO Concept Timeline

5.1.1 Release of the Earth Science Decadal Survey

In 2007, the CLARREO mission was recommended by the National Research Council's Earth Science Decadal Survey as one of four "Tier 1" missions and identified as a critical element of the climate observing system [NRC, 2007]. The NRC ranked the "Tier 1" missions based on considerations of the scientific merit, contributions to the long-term observational record, societal benefits, affordability, and technological readiness. Two of the four missions recommended for earliest implementation were the Soil Moisture Active-Passive (SMAP) and the Ice, Cloud, and land Elevation Satellite (ICESat-II) with launch readiness dates (LRD) of 2012 and 2015, respectively. The remaining two "Tier 1" missions, CLARREO and the Deformation, Ecosystem Structure, and Dynamics of Ice (DESDynI), were recommended for slower implementation and assigned a projected LRD of 2017.

Consequently, NASA began a systematic approach to advancing the CLARREO mission. Shortly after release of the DS, NASA Headquarters identified Langley Research Center (LaRC) as the lead for CLARREO. Working with the Program Scientist and Program Executive at NASA Headquarters and the Earth Systematic Missions Program Office at Goddard Space Flight Center (GSFC), the LaRC team has defined an integrated Pre-Phase A mission study plan. From 2008 – 2010, NASA conducted Pre-Phase A science and mission planning for CLARREO.

5.1.2 CLARREO Mission Concept Review

CLARREO conducted a Mission Concept Review (MCR) on November 17, 2010. The assessment of the review board was that the CLARREO mission successfully demonstrated MCR maturity and should proceed into Phase A. The Board was chaired by Dennon Clardy of MSFC and included members from Langley, Goddard, Marshall, Glenn, NIST, and JPL.

The review panel identified 10 notable strengths relative to the proposed CLARREO mission concept and the project team personnel. In addition, three Requests for Action were identified, related to working with HQ and the Program Office on project categorization, risk class, and the budget profile. The Board concluded that the RFAs did not identify additional work not already planned in Phase A. The MCR Board panel praised the project for "exploring a variety of mission concepts and [having] done an excellent job of defining a feasible concept within a constrained funding profile and launch date." Mr. Clardy, MCR Chair, further commended the team for the strong working relationship between science, project management, and engineering, and noted that the project did an excellent job of defining a feasible mission concept within a constrained funding profile and schedule. Finally, he noted that CLARREO was well beyond MCR maturity in many areas.

The project began working with HQ and the Earth Systemmatic Missions Program Office on a schedule to hold the KDP-A meeting, as early as February 2011.

5.1.3   The President's Budget

On February 14, 2011, the President's FY 2012 budget was released and it removed $1.2B from the $2.1B FY 2011 proposed Earth Science Climate Initiative in years 2012 – 2015. As a consequence, the original NASA funding profiles for CLARREO and DESDynI missions were eliminated. Immediately following the release of the budget, Michael Freilich (Earth Science Division Director) stated the following (March 11, 2011): "I know unequivocally that the decision to focus these cuts on CLARREO [and DESDynI] was not based in any way on perceptions of under performance of the teams or lack of value of the mission for the country. The cuts are purely budgetary."

The new budget guidance directed the CLARREO mission to enter into an extended Pre-Phase A and to examine other ways to achieve some portion of the CLARREO science in the near term through alternative mission concepts (i.e., International Space Station), instruments of opportunity, international collaboration, inter-agency collaboration, or other mission implementations. The alternative mission concepts are described in greater detail in Sections 5.4 and 5.5.

5.1.4   Extended Pre-Phase A

Currently, the CLARREO mission remains in extended Pre-Phase A. During this time period, the team has had three overarching goals:

◇ *Advance the CLARREO RS, IR, and RO climate change science.*
◇ *Further reduce the development risk of the RS and IR Instruments.*
◇ *Determine the impact of alternate mission concepts on CLARREO science and thereby enable science value/cost trades through use of the Science Value Matrix approach.*

The first of these three overarching goals joins the science expertise of an external Science Definition Team (which was competed in January 2011) with the LaRC and GSFC internal science expertise to advance the CLARREO science goals. Over the past 3+ years, the science studies have focused on the following: (1) instrument-specific SI traceability in the IR, RS, and RO, (2) climate change Observing System Simulation Experiments (OSSE's), (3) climate change spectral fingerprinting, (4) Reference inter-calibration of a range of spaceborne IR and RS sensors at climate change accuracy, (5) GNSS RO algorithm improvements for climate change at altitudes below 5 km and above 20 km altitude, (6) new studies on the stability of satellite retrieval algorithms for decadal change, and (7) orbital sampling impacts on accuracy of climate change spectral fingerprints and on reference inter-calibration.

At the time of the MCR, most of the CLARREO science studies were in the early stages of development. During the intervening 3+ years, the Science Definition Team has extended these studies to more rigorous and complete levels. In addition, they have been extensively documented in peer review literature.[5]

The second of the three overarching goals is to greatly broaden the science trade space from

---

[5] 26 journal papers published or in press in 2013; 15 papers submitted or in review, and 42 papers in preparation. (13 journal papers were published in 2012). In total, 72 papers (to date) have been included in http://esdpubs.nasa.gov.

that considered for the original CLARREO Decadal Survey mission. The guidance received in 2011 directed the team to focus on much smaller elements of the CLARREO science and not the full mission. The guidance focused on other ways to achieve parts of the CLARREO science by means of a small mission, an instrument of opportunity, international collaborations, or even a sub-orbital campaign. To support these possibilities, the team explored a wider range of less capable, but also less expensive, orbits and platforms including the International Space Station, Iridium, sun-synchronous orbits of opportunity, and shared launch options with either other U.S. agencies or international collaboration. It's important to note that these options required even smaller instruments than the MCR defined IR or RS spectrometers (mass of ∼75kg each) leading to the evaluation of much smaller, lighter, lower power, but less capable options (again) to achieve a portion of the CLARREO science. Examples of such reductions in instrument capability considered, included: decreased spectral resolution and spectral coverage, increased instrument noise, and decreased SI-traceable absolute accuracy.

The final of the three overarching goals focuses on reducing development risks by demonstrating CLARREO-like infrared and reflected solar spectrometer calibration performance. In 2013, research teams at LaRC and GSFC completed testing of the IR and RS Calibration Demonstration Systems (see Section 4.5), including completion of the absolute calibration verification activities with NIST peer review. In addition, the team completed a mapping of instrument properties to accuracy sensitivities and made available the CLARREO calibration systems as a resource to be shared among multiple Earth science missions (e.g., VIIRS, CrIS, Landsat, and CERES). The Calibration Demonstration Systems have completed Phase I: build, test, and verify calibration accuracy levels. They now enter Phase II of utilization for instrument optimization (FY14) and accuracy improvements (FY15).

5.2   Science Value Matrix Approach

The CLARREO science value matrix (SVM) is a concept that has been used to clarify for NASA Headquarters and the CLARREO team the value of various mission trade studies during our pre-phase A work. It has helped the team clarify its thoughts on the wide range of climate science that might be impacted by CLARREO observations. The CLARREO mission is unusually broad in this regard: most NASA missions are focusing on one or two climate variables, and therefore a science value matrix is of less use. CLARREO's breadth of science impact is a strength, but it can also complicate derivation of the mission priorities and requirements. The science value matrix is just one of the tools used to help.

For a science value matrix to be a useful tool, the "value" needs some method of quantification. Our science value matrix approach is based on the CLARREO team's work and discussions in Section 2. The Science Value of a Science Objective, SV_{so}, is computed as product:

$$SV_{so} = F_{si} \times F_{cv} \times \sqrt{F_{crl}} \times F_{ta} \times F_r \tag{5.1}$$

where F_{si} is science impact factor, F_{cv} is calibration verification factor, F_{crl} is climate record length factor, F_{ta} is trend accuracy factor, and F_r is risk factor. If any objective has zero science impact, there is no value in measuring it, no matter how accurate or low risk. If the climate record length is too short, the data has little utility and is lost in natural variability.

CLARREO MCR Baseline: 2 IR/RO (2018), and 2 RS (2020).								
CLARREO Science Objective	**Related Climate Change Variable**	F_{si}	F_{cv}	$F_{crl}^{1/2}$ (75%)	F_{ta} IR	F_{ta} RS	F_{ta} RO	SV_{so}
Cloud Feedback SW	Reflected SW flux, albedo RS Cloud Properties	**2**	1.9	2.2	0	1.05	0	**8.8**
Cloud Feedback LW	Earth Emitted LW flux IR Cloud Properties	**1**	1.8	2.2	1.03	0	0	**4.1**
Cloud Feedback Net	Net Cloud Radiative Forcing	**5**	1.8	1.7	1.03	1.05	0	**16.1**
Temperature Response & Lapse Rate Feedback	Temperature Profile	**3**	1.9	2.2	1.03	0	1.0	**12.9**
Water Vapor Response & Water Vapor Feedback	Water Vapor Profile	**3**	1.9	2.2	1.03	0	0.2	**2.6**
Aerosol Direct Radiative Forcing	Aerosol Radiative Forcing Aerosol Properties	**1.5**	1.9	2.2	0	1.0	0	**6.3**
Snow & Ice Albedo Feedback	Reflected SW flux, albedo Snow/Ice & Cloud Cover	**1.5**	1.9	2.2	0	1.05	0	**6.6**
Land Albedo Change & Radiative Forcing	Reflected SW flux, albedo	**0.5**	2.0	2.2	0	1.05	0	**2.3**
Vegetation Index Change	Vegetation Index	**1**	2.0	2.2	0	1.05	0	**4.6**
Sum of Mission Science Value								**64.3**
Total Mission Science Value relative to MCR Baseline								**100%**

Table 5.1: SCIENCE VALUE MATRIX FOR THE MCR CLARREO BASELINE MISSION (SECTION 5.3).

If the accuracy is too poor, CLARREO adds little value over existing sensors. As a result, the overall science value is dependent on the multiplicative (not additive) total of the above factors. In this section, we briefly discuss the definition of each factor in the Equation 5.1. Note that in all cases, the factors used in this equation are a relative measure of value. In general, our CLARREO MCR Baseline Mission is assigned "100% Science Value", as shown in Table 5.1, and the value of other mission options will be scaled to this option.

5.2.1 Science Impact Factor

The science impact factor, F_{si}, attempts to capture both the importance of the science objective as well as the uniqueness of the CLARREO contribution to it. We assign to each science contribution a relative numeric weight. We use equal value for forcing, response, and feedback science objectives. This fits well with IPCC discussions of decadal to century climate change, as well as the diagram summarizing CLARREO science objectives, shown in Figure 2.1.

The science impact factors, third column from the left in Table 5.1, are based on the IPCC uncertainties in forcing, response, and feedback components [IPCC, 2007a]. Cloud feedback uncertainty is roughly twice as large as water vapor/lapse rate feedback uncertainty [IPCC, 2007a; Bony, 2006, Soden and Held, 2006; Roe and Baker, 2007]. Cloud feedback uncertainty is roughly 3 times as large as snow/ice albedo feedback uncertainty [IPCC, 2007a; Bony, 2006, Soden and Held, 2006; Roe and Baker, 2007]. As a result, we give a total science impact weight to cloud feedback of 4, to water vapor/lapse rate feedback of 2, and to snow/ice albedo feedback of 1.5. Consistent with our earlier discussion of giving equal value to feedback and response, we add a science impact value of 4 to climate change responses relative to cloud feedback (fluxes, cloud properties), so that the total impact value is 8. Given the importance of the temperature and water vapor profile response in the NRC decadal survey, we also give a total value of 4 to the temperature/water vapor response. The resulting cloud feedback/response impact totals 8 (4 feedback + 4 response), and the resulting temperature/water vapor impact totals 6 (2 feedback + 4 response).

Since the CLARREO information content is very different in the RS, IR, and RO observations, we further divide the science impact among the individual observational components. This allows the CLARREO mission to consider the relative impact of different components of its observations. For cloud feedback, we separate LW, SW, and Net components. Climate sensitivity is linked most directly to Net cloud feedback, which is the combination of SW and LW cloud feedbacks [Soden et al., 2008]. Of the total impact of 8 for cloud feedback, we assign 5 units to Net. The remaining science impact is 2 for SW, and 1 for LW cloud feedback. The larger impact score for SW is based on the largest IPCC uncertainty in cloud feedback having been identified as low cloud feedback [Bony et al., 2006, IPCC, 2007a]. Low clouds are dominated by SW cloud radiative effect, which has much smaller LW effects. Therefore, we assign SW cloud feedback an impact of 2 and LW feedback an impact of 1. SW impact is assigned to the RS spectrometer and LW impact to the IR spectrometer. Net impact requires both RS and IR spectrometers.

For temperature and water vapor, we split the 6 units of science impact equally, 3 for temperature lapse rate feedback and response, and 3 for water vapor feedback and response. For water vapor, the science impact is kept in the IR spectrometer, while for temperature it is

split between the IR spectrometer and the RO instrument.

For radiative forcing, a factor of 4 is given to the uncertainty in aerosol direct and indirect radiative forcing. However, CLARREO is assumed to contribute only an impact of 1.5 out of the full aerosol uncertainty. Land albedo change is a much smaller radiative forcing uncertainty than aerosols and the factor of 0.5 science impact reflects this reduction [IPCC, 2007a]. Finally, vegetation index change as a metric of biosphere changes is also given a relatively low weight of 1. At this time, it is more difficult to quantify this weight than the others.

5.2.2   Calibration Verification Factor

The current matrix defines this factor, F_{cv}, as follows: a value of 2 is given to independent verification of the CLARREO observation and a value of 1 is given to a CLARREO observation without independent verification. Clearly there can be an open and lengthy discussion about the independent verification that will serve this purpose for each observation. As for the science impact value, this metric will not be as simple as the trend accuracy or length of climate record metrics. Nevertheless, given the CLARREO task of high confidence in decadal change, it seems inescapable that CLARREO include such a metric.

Current values of this metric are very rough. The tables assign a verification factor of 2 to a science objective if there is a 1-year overlap of two CLARREO instruments in-orbit to verify consistent performance and calibration within uncertainty of the instrument or instruments used for that science objective. If there is no overlap, then the verification factor depends on an evaluation of the usefulness of aircraft underflights, comparisons of RO and IR (temperature only), etc. If a partial verification is possible, it is given a factor of 1.5 in the current tables (e.g. temperature and water vapor profile verification using aircraft underflights). The likelihood of achieving in-orbit instrument overlap is taken into account by using the probability of obtaining overlap as a weighting function. For example: for a 2017 and 2020 launch of a single IR spectrometer on each spacecraft, there is a 70% probability of 1 year of overlapping data. If the verification factor for no in-orbit overlap is 1.5 (aircraft verification), while having overlap is 2.0, then we use the probability of overlap in orbit to obtain a verification factor weighted between the 1.5 and 2.0 values, in this case $1.5 + (0.7) \times (2.0 - 1.5) = 1.85$. If, however, as for LW cloud feedback, the far infrared spectrum is critical and is unlikely to be verified at the required accuracy using aircraft underflights, then the verification metric would be $1.0 + (0.7) \times (2.0 - 1.0) = 1.7$. This is a very simple and crude method that allows some accounting for the relative value of instrument overlap in-orbit, as well as the likelihood of obtaining it based on launch schedules and instrument and spacecraft reliability.

5.2.3   Trend Accuracy Factor

By trend accuracy we mean the relative accuracy for CLARREO determination of decadal change trends. The metric here is determined by the accuracy relative to a perfect climate observing system limited only by natural variability [Leroy et al., 2008b]. The metric is quantification of the effect of instrument absolute accuracy on the uncertainty of trend detection, as well as the effect on time to detect climate change trends at a given level of confidence. Climate trend accuracy is key to testing climate model predictions of decadal change, while

time to detect trends is key to societal decision making processes. The extension of the Leroy et al. [2008b] results include all CLARREO sources of uncertainty, such as instrument noise and orbital sampling, and summarized in Appendix A.

Equations A.1 through A.5 provide a simple but powerful understanding of how observing system uncertainties will affect decadal climate change trends. The most important result is that observing system errors should be viewed relative to natural variability as a reference. As the magnitude of uncertainties fall below that of natural variability, they will rapidly become insignificant for climate trend errors. As the time scale for uncertainties becomes shorter than natural variability, they also become less significant. The formalism above provides a method to rigorously consider a wide range of error sources: calibration, accuracy, orbit sampling, reference inter-calibration uncertainty, and instrument noise. Mission design can then successfully trade cost/value across these error sources. Finally, Equations A.3 and A.5 show that climate trend accuracy, U_a, and time to detect trend, U_t, are tightly related. For values of U_a near 1, their relationship simplifies to

$$(U_t - 1) \sim 0.67 \times (U_a - 1) . \tag{5.2}$$

Another way of saying this is that if the CLARREO observing system goal is for decadal trend accuracy no worse than 20% larger than a perfect observing system, then the time to detect trends will be no worse than $0.67 \times 20\% = 13.4\%$ longer than a perfect observing system. There is a simple relationship between the two science goals. For CLARREO, our Level 1 requirements specify trend accuracy within 20% of a perfect observing system, and time to detect trends within 15% of a perfect observing system.

The final decision is how to use climate trend accuracy as a metric in the science value matrix. Given the science value equation at the beginning of this document, we require a metric that increases with increasing accuracy, and a metric that reduces to zero as accuracy becomes so poor that CLARREO's value to the climate observing system is lost. We currently use a value of 1.0 for the accuracy factor if the Level 1 Requirement of accuracy within 20% of a perfect observing system is met. We take this accuracy as the 100% capability value. As accuracy in decadal change trends reduces below this, we reduce the accuracy value factor proportional to the loss of accuracy. In particular, we use this as an trend accuracy value factor:

$$F_{ta} = \frac{1.2 \times U_a}{U_{clarreo}} . \tag{5.3}$$

As the CLARREO Level 1 requirement goal is to be within 20% of a perfect observing system, $F_a = 1.0$ when the trend accuracy requirement is met, $F_{ta} > 1.0$ when CLARREO's measurements achieve trend accuracy better than requirement, and $F_{ta} < 1.0$ when CLARREO's measurements exceed the 20% accuracy limit.

The accuracy values used in Table 5.1 are determined from the CLARREO SDT studies and include calibration absolute accuracy, orbit sampling error, and instrument noise. The accuracy factor is the same independent of whether CLARREO uses a spectral benchmarking approach or reference inter-calibration. Reference inter-calibration error can be added, but the studies indicate that this error is equal to or lower than orbit sampling error. In general, the CLARREO decadal change accuracy is dominated by the instrument absolute accuracy for global annual time scales. Orbit sampling error becomes more important at zonal and regional spatial scales and at seasonal time scales. This difference is a result of the fact

that calibration error is independent of the space/time scale, while the errors from natural variability and sampling both increase as space/time scale reduces. Orbit sampling studies have shown that natural variability and orbit sampling error increase roughly proportionally. For example, natural variability at zonal annual time scales are three times larger than global annual. As a result, the effect of calibration uncertainty is largest for global annual time/space scales. For many purposes, however, the global annual values are some of the most critical measures and are the first to show anthropogenic signals given their lower natural variability: this is true for everything from global average surface temperature, or for the impact of feedbacks on climate sensitivity. As a result, our accuracy metric use in the Science Value Matrix uses global annual trend accuracy.

The trend accuracy factor is shown separately for each instrument: spectral RS, spectral IR, and RO. This allows us to account for different calibration accuracy, orbit sampling, and instrument noise in each instrument and mission design. The factor is slightly greater for the IR than for RS because of lower fractional sampling errors in IR as well as a somewhat smaller absolute calibration error. For calculation of each science objective's science value we use the maximum trend accuracy factor out of the three CLARREO measurement types: spectral IR, spectral RS, and RO.[6]

5.2.4 Climate Record Length Factor

The trend accuracy metric in Section 5.2.3 is relative to a perfect observing system. While this is a critical part of climate trend accuracy, Equation A.2 shows that the length of the climate record is also a key factor in determining the accuracy of trends – for both a perfect observing system and for CLARREO. As follows from Equation A.2, the uncertainty of climate trends, δm, will scale as $(\Delta t)^{3/2}$. As explained in Leroy et al. (2008), the reduction in trend error with length of record is a result of two very different factors. First, a linear dependence on record length occurs as a result of increasing climate trend signal magnitude with length of record. Second, there is a $\sqrt{\Delta t}$ that is a reduction in natural variability as we are able to average over an increasing number of autocorrelation time periods.

The first CLARREO missions will contribute to the linear component by achieving the absolute accuracy needed to overcome gaps in the climate record. For example, a 30-year trend could be achieved by using the first 5 years of the CLARREO record, followed by another 5 years of equivalent data 30 years later. In this sense, the linear record length component is dependent on getting the first CLARREO up to start the record, but is then dependent primarily on whether follow-on missions are flown. In that sense, the first mission record length is independent of this linear component. The second $\sqrt{\Delta t}$ component, however, is relevant to the first CLARREO mission. Consider, for example, if we launched the first CLARREO and only achieved 1 month or 1 year of data: even though highly accurate, it would not anchor the long-term record well because of high natural variability. As a result, in our Science Value Matrix for the first two CLARREO missions, we include the square root dependence of record

---

[6]For RO water vapor science objective, the accuracy is listed as low, primarily because of low information content. The science value for this observation is from the IR instrument with a much smaller contribution from the RO observation.

length. In particular, we choose as our science value metric

$$F_{crl} = \sqrt{\Delta t} \,, \tag{5.4}$$

where Δt is the number of years of CLARREO data with a 75% likelihood of survival on-orbit. Using this metric, the length of the initial CLARREO record will be accounted for in determining the accuracy of the climate trends that can be achieved by the mission, even in the long term. The value of Δt is determined using the normal engineering estimates of the likelihood of launch success, spacecraft survival, and instrument survival. The failure rates of instruments and spacecraft are controlled by the amount of redundancy built into the systems, especially for key electronics components. For example, single string electronics will be less reliable than redundant electronics. This allows a cost/value trade for the CLARREO mission for instrument and spacecraft reliability, especially selected redundancy of key components. As for other missions, the CLARREO failure rates of instruments, spacecraft, and launch vehicles are assumed to be independent.

For many CLARREO science objectives, only one of the CLARREO instruments is required (e.g. the IR spectrometer for water vapor profile), while for others (e.g net cloud feedback) both reflected solar and infrared spectrometers are required. The value of Δt is calculated accordingly, with independent failure rates assumed for each instrument. When more than one CLARREO spacecraft is in orbit (e.g. 2020), the value of Δt accounts for the joint probability that multiple spacecraft and instruments survive if the science objective requires it. Alternatively, if only one instrument is required to survive, then the value of Δt accounts for the fact that one instrument of either spacecraft is sufficient. For all record length calculations used in the SVM Tables we assume the following reliabilities[7]:

◇ Launch vehicle success rate: 97% (mature launch vehicle such as Delta 2).
◇ Spacecraft survival for 3 years: 95% (98.3% survivability per year).
◇ Instrument survival for 3 years: 90% (96.6% survivability per year).

Using these reliabilities, the 75% likelihood in the CLARREO Baseline mission (Table 5.1) that at least one of the IR spectrometers survives, is 5 years. This gives a value of $F_{crl} = 2.2$. It is less likely that both one IR spectrometer and one RS spectrometer will survive, therefore Net Cloud Feedback has a 75% likely record length of only 3 years and hence a value of $F_{crl} = 1.7$.

5.2.5 Risk Factor

Any science value estimation should consider risk as an element of its science value metrics. One example of risk is technological risk. All new instruments, including those on CLARREO, will have some level of risk in demonstrating the viability of new technologies in-orbit. One of the key objectives in the ESTO IIP investigations related to CLARREO is to reduce this risk from moderate to low values. The CLARREO engineering team has evaluated the risks in our current IR, RS, and RO instrument designs and has not found a large difference in the risk factor of these instruments. As a result, this factor, F_r, is currently left at 1.0 for all instruments, but could be adjusted in the future.

---

[7]The values used are for moderately reliable instruments and spacecraft. These can be varied with levels of instrument and spacecraft redundancy, or launch vehicle maturity. Costs will increase as reliability increases. They can be made higher or lower by increasing or decreasing electronics and other key component redundancy.

5.3   CLARREO in 90° Inclination Polar Orbit

The NRC 2007 Decadal Survey (DS) called for an early launch of CLARREO (LRD 2017) to provide the measurements needed by society to make informed decisions about responding to climate change. The original concept called for 11 high-absolute-accuracy instruments, 3 spacecraft at 90° inclination orbits, and 3 separate launches [NRC, 2007]. The CLARREO mission study team began by reviewing the science objectives outlined in the DS, initiating science and engineering studies to fill in any gaps, and looking for opportunities to reduce the overall cost of the mission. Utilizing the mission concept defined in the DS as a starting point, the study team conducted multiple Design Analysis Cycles (DAC), from DAC1 to DAC5. The goal was to formulate a mission that provided the maximum science benefit while remaining within NASA's defined programmatic constraints. Throughout this process, the team focused on maintaining internal consistency, flow down, and traceability from the end instrument measurements back to the original NRC objectives [*http://www.nap.edu/catalog/11820.html*].

5.3.1   CLARREO Mission Requirements

The top-level science requirements were established to ensure that CLARREO fulfills the primary science objective to provide accurate, broadly acknowledged climate records that can be used to validate long-term climate projections. The top-level science requirements which had the most influence on the MCR design for the CLARREO mission were:

1. Baseline Accuracy in Climate Trends: Benchmark observations shall achieve an accuracy in decadal trends of within 20% of a perfect observing system for the combined uncertainty sources of SI-traceable calibration, orbit sampling, and instrument noise, at annual global and annual zonal time/space scales.

2. Climate Record Length: Sufficient sampling needed to average over climate system natural variability cycles and provide the initial benchmark records for long term climate trends. The IPCC uses 5-year or 10-year running means to reduce natural variability (e.g. ENSO). Therefore, it was required that CLARREO shall obtain each observation type with a record length of at least 5 years, with likelihood of 70% or greater.

3. Measurement Overlap: Coincident measurements were recommended for the infrared and reflected solar to better characterize cloud response and feedback, and infrared with radio occultation for temperature/water vapor response and feedback.

4. Cross-instrument Verification: Multiple copies of each instrument type (IR, RS, and RO) were recommended by the DS for cross-instrument verification in-orbit. This also supports confidence in SI-traceable accuracy results.

5. Reference Inter-calibration: CLARREO shall provide data to climate-relevant orbiting sensors (similar to VIIRS, CERES, CrIS, and IASI) that will be used to improve the accuracy of their measurements.

The top-level science requirements flow down to commensurate measurement requirements that dictate the needed accuracy, spectral range, and resolution of CLARREO's infrared and reflected solar spectrometer measurements, and the altitude range, resolution, and accuracy

of the GNSS radio occultation refractivity profiles. The science requirements also drive the number of instruments in-orbit and the selection of the orbits (altitude and inclination).

The CLARREO MCR mission concept followed programmatic constraints on the launch dates, the budget profile provided by NASA Headquarters, and budgeting for Minotaur IV launch vehicle costs. The mission design objective was to formulate a mission that provides the most science benefit while adhering to these programmatic constraints.
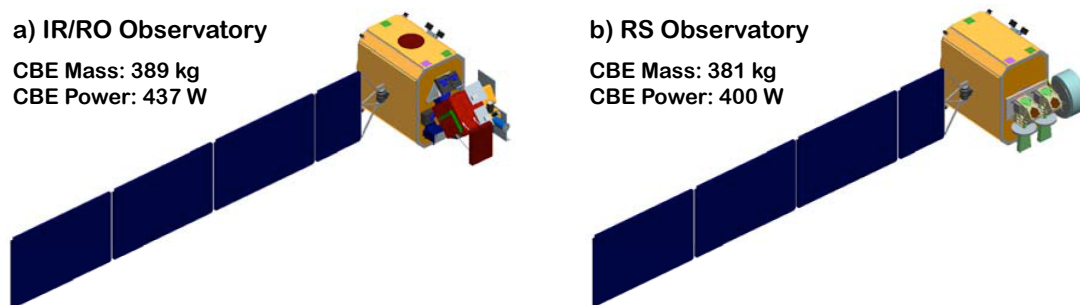
Figure 5.1: CLARREO IR/RO AND RS OBSERVATORIES.

5.3.2 CLARREO MCR Baseline Mission

The CLARREO team studies showed that the CLARREO science objectives could be achieved with a much simpler mission design than originally outlined in the DS - the proposed design includes 6 instruments: two infrared (IR) spectrometers, two reflected solar (RS) reflected spectrometers, and two GNSS radio occultation (RO) instruments, with all measurements from one polar orbit plane. The Science Value Matrix for this mission option is shown in Table 5.1. The measurement requirements and instruments concepts at the CLARREO MCR 2010 are summarized in Section 4.

A fundamental strategy in the CLARREO MCR design was to use small observatories, each with one spectrometer (either IR or RS) and an RO instrument, to provide the flexibility of launching on smaller launch vehicles. The goal of this approach was to lower the cost of access to space and provide multiple options for instrument and observatory development pathways. Using this strategy, the CLARREO MCR full mission design called for a total of four simple observatories, two are combined infrared and radio occultation instrument observatories, and two are reflected solar instrument observatories. Illustrations of these observatories are shown in Figure 5.1.

The MCR concept planned to launch each observatory into a 609 km altitude, 90° inclination polar orbit with Right Ascension of the Ascending Node (RAAN) close to 0° or 180°. The orbit inclination was motivated by providing global coverage and to sample the full Earth's diurnal cycle. The choice of orbit altitude was motivated by optimizing for ground track repeat cycle, reference inter-calibration opportunities and pointing, and launch vehicle capabilities. The constrain for the orbit RAAN is for maximizing the number of reference inter-calibration opportunities. The mission plan was to inject four observatories into the chosen orbit with two dual-manifested Minotaur IV+ launches: (1) July 2018: two IR observatories (each with GNSS-RO), and (2) May 2020: two RS observatories. The full mission outline is shown in
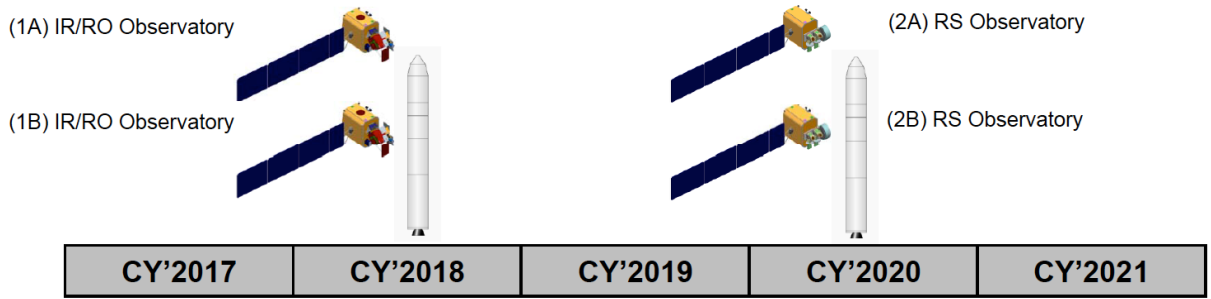
Figure 5.2: THE CLARREO BASELINE MISSION OUTLINE: SIX INSTRUMENTS, FOUR OBSERVATORIES, TWO DUAL-MANIFESTED LAUNCHES ON MINOTAUR IV+ VEHICLES IN 2018 AND 2020.

Figure 5.2. The observatories are injected into the same orbit plane and maneuvered for in-track spacing that optimizes the science and inter-calibration motivated sampling. At the end of 5 years, the observatories are de-commissioned and passivated for an uncontrolled re-entry within 25 years.

| Parameter | IR/RO Observatory | | RS Observatory | |
	IR Instrument	RO Instrument	RS Instrument	RS Gimbal
Instrument	FTS	Receiver/Antennas	2 Grating Spectrometers	Single Axis
Mass	76 kg	18 kg	69 kg	14 kg
Parameter	124 W	35 W	96 W	17 W
Data Rate	228 kbps	119 kbps	0.4 to 72 Mbps	< 5 kbps
Data Volume	20 Gb/day	10 Gb/day	69 Gb/day	300 Mb/day

Table 5.2: CLARREO IR/RO and RS observatory concepts. All numbers are CBE (2010).

The concepts and parameters of the IR/RO and RS observatories are summarized in Table 5.2 and illustrated in Figure 5.1. Both observatories use a common spacecraft bus with the same subsystems: three-axis stabilized with reaction wheels and torque rods, 1553B and RS-422 C&DH interfaces, hydrazine blow-down propulsion system, and S-band and X-band communications. Observatory operations are similar except for instrument calibration and reference inter-calibration operations. The IR/RO observatories carry on-board calibration and verification systems, and IR instruments are in an Earth-pointed LVLH attitude 100% of the time. Reflected solar observatories maneuver periodically for reference inter-calibration, solar calibration, and lunar verification. At the MCR, reference inter-calibration operations for CERES and VIIRS instruments were estimated at an average of 4/day ($\sim$ 30 min/day)[8], and Solar calibration and lunar verification operations at once per month. The RS calibration and reference inter-calibration are accomplished through a combination of spacecraft maneuvering (yaw) and RS instrument gimbal rotations (roll). The Current Best Estimate (CBE) mass/power were 389 kg / 437 W and of 381 kg / 400 W for IR/RO and RS observatories, respectively.

Two observatories could be launched together on a single Minotaur IV+ vehicle to further lower the access to space costs for the mission. Illustrations of observatories, stowed in a

---

[8]The current CLARREO mission concepts plan for more inter-calibration operations to provide an on-orbit reference standard for up to 40 sensors in LEO and GEO.

2018 Dual IR Launch   **2020 Dual RS Launch**
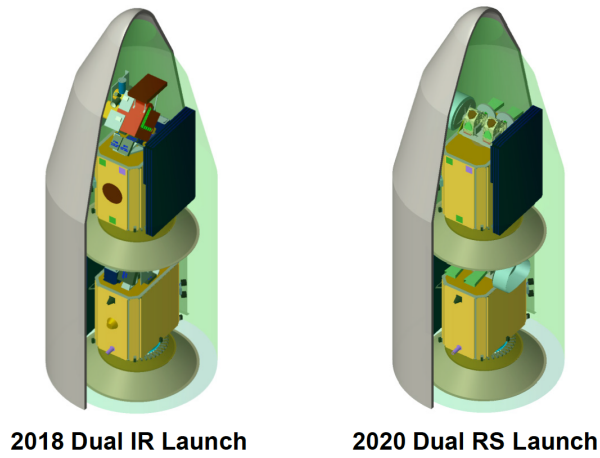
Figure 5.3: THE CLARREO IR/RO AND RS OBSERVATORIES STOWED IN MINOTAUR IV+ VEHICLES FOR TWO DUAL-MANIFESTED LAUNCHES.

Minotaur IV+ rocket for dual-manifested launches, are shown in Figure 5.3. Available mass growth above CBE to the Minotaur IV+ allocations were estimated at 43% for the IR/RO observatory, and 46% for the RS observatory. Minotaur IV+ interfaces are understood and have been accommodated by the CLARREO mission concept.

The MCR mission design is also compatible with launching the CLARREO observatories into required orbit on several small to mid-size launch vehicles: Falcon 1e, Taurus XL, and Athena II. The compatibility with other launch vehicles is illustrated in Figure 5.4. In each case, vehicle-specific observatory modifications would be required to account for interface changes. The Minotaur IV+ encompasses the Falcon 1e and the Taurus 3210 for: tip-off rates, orbit injection dispersions (propellant loading), and lateral c.g. requirements. Both IR/RO and RS observatories are configured to fit within the Falcon 1e fairing volume, with available mass growth above CBE at 39% to 42% for IR/RO and RS observatories, respectively.
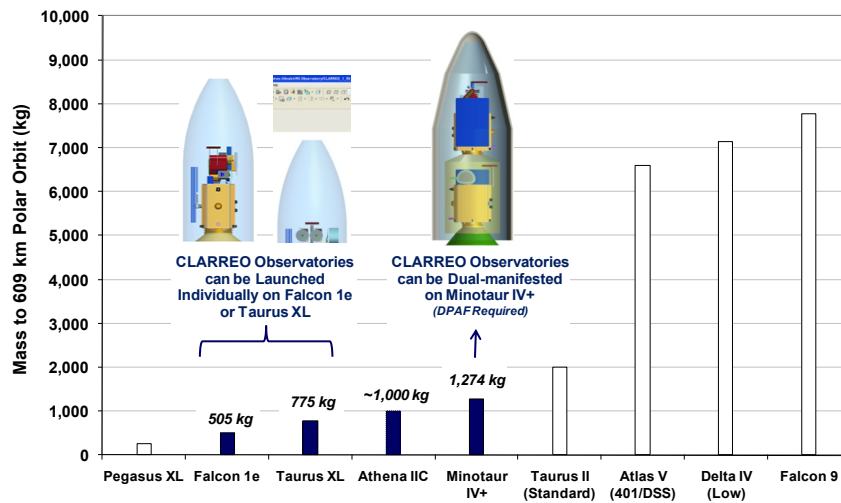
Figure 5.4: LAUNCH VEHICLE FLEXIBILITY FOR CLARREO'S IR/RO AND RS OBSERVATORIES.

The mission requirement on producing climate record length drives requirements for spacecraft and instrument reliability. Preliminary reliability assessments have been conducted from mul-

170

tiple independent sources (LaRC, GSFC, APL, S/C vendor) for CLARREO spacecraft and supplemented with instrument reliability assessments from the GSFC team. For the MCR mission concept, spacecraft reliability is 0.76, and reliability of infrared and reflected solar instruments is 0.80 at five years of operations.

In November 2010, the CLARREO Project demonstrated readiness to begin Phase A at a fully successful Mission Concept Review. The mission design described above was determined to be sufficiently mature, with built-in flexibilities to be robust to future programmatic and technology developments. At the time, it was expected that by 2020 the full mission would be operational and producing the climate record benchmarks needed for scientific and climate policy progress. Unfortunately, due to NASA budget considerations, CLARREO was placed into an extended pre-Phase A with a launch readiness date of no earlier than 2023.

5.3.3 CLARREO MCR Threshold (Minimum) Mission

As part of the standard NASA mission management procedures (NPR 7120.5E), Baseline and Threshold Investigations must be defined. The "Baseline Investigation," described in Section 5.3.2, is the "investigation that, if fully implemented, would fulfill the Baseline Science Requirements, which are the performance requirements necessary to achieve the full science objectives of the investigation." In comparison, the "Threshold (or Minimum) Investigation" is a "descoped Baseline Investigation that would fulfill the Threshold (or Minimum) Science Requirements, which are the performance requirements necessary to achieve the minimum science acceptable for the investment."
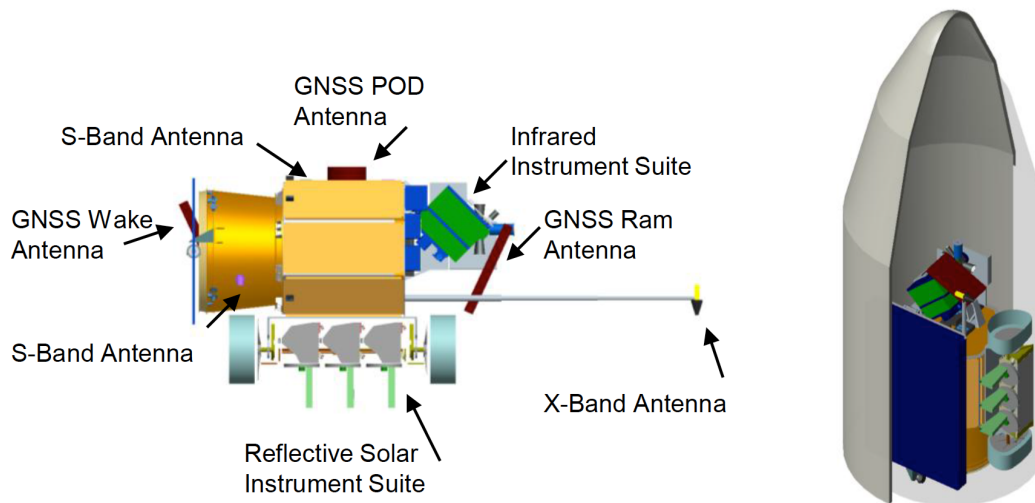
Figure 5.5: CLARREO MINIMUM MISSION CONFIGURATION ON SINGLE SPACECRAFT (RS INSTRUMENT FROM DAC4), AND SINGLE RS/IR/RO OBSERVATORY ACCOMMODATION WITHIN MINOTAUR IV+ FAIRING.

Ideally, the Minimum Investigation is defined by a set of requirements that: (1) save significant resources (e.g. 10% of mission cost), (2) lead to savings that are realizable during the mission if it were to go over cost/schedule reserve, (3) have sufficient science value that the mission is still worth doing (i.e., science value/cost not too far from original mission, and/or sufficient uniqueness of mission science value remaining). The idea of a minimum mission is that if the mission science requirements fall below this level, then the mission is not worth flying at all.

There tends to be a range of mission descope options that exist between the Baseline and Minimum Mission, with varying ranges of lost science value traded against savings in cost and schedule.

For CLARREO, the difference between the Baseline and Minimum mission is characterized primarily in terms of climate trend accuracy, which is a critical parameter for testing climate models. The Science Value Matrix described in Section 5.2, provides a methodology for relating the overall science value to science impact, decadal trend accuracy, climate record length, independent verification, and risk factors for each element of the mission architecture. Using the approach shown in Table 5.3, a CLARREO Minimum Mission with 3 instruments on a single spacecraft, launched into a 90° inclination polar orbit in 2021 on Minotaur IV+, was defined and found to achieve 64% of the Baseline Mission science at a significantly reduced cost of $\sim$ \$125M plus launch vehicle costs, when compared to the baseline. This does not represent a factor of 2 reduction in the costs because additional copies of instruments and spacecraft (built at the same time) are less expensive by factors of 2 to 5 than the first copy.

The Minimum Mission configuration and single RS/IR/RO observatory accommodation within Minotaur IV+ fairing is shown in Figure 5.5. The Reflected Solar instrument is relocated to the nadir deck for improved reference inter-calibration operations.[9] The observatory CBE mass/power budget was estimated at 814 kg / 691 W.

The CLARREO Minimum Mission reduced the number of satellites from 4 to 1. The obvious advantage of this mission architecture is that it represents a significant cost savings (e.g., 3 fewer instruments and only 1 satellite resulting in a 25% cost reduction). The disadvantage of this approach is that the sampling error increases, the time to detect climate trends increases, and the likelihood of mission success at all durations decreases due to the lack of redundant platforms. In addition, it eliminates the potential for independent verification amongst similar NASA-launched platforms and assumes verification via flights of high altitude aircraft, high altitude balloons, or via similar measurements by international partners (e.g., TRUTHS). Despite these shortcomings, the Minimum Mission allows ESD to initiate the climate record and maintain a significant percentage of the CLARREO science described in the Decadal Survey [NRC 2007].

In summary, we conclude that the single satellite Minimum Mission does lead to degradation of decadal trend accuracy, but at moderate levels. And, that this option does provide mission cost savings ($> 10\%$) that could be readily realized. Finally, the science value/cost of the minimum mission is sufficiently high to provide compelling science of value to the community.

5.4 CLARREO on the ISS – NASA LaRC & GSFC Concept

This section gives an overview of the mission concept for flying CLARREO RS and IR spectrometers on the International Space Station (ISS). In this mission option, the radio occultation data is acquired from the COSMIC constellations. The CLARREO team performed a feasibility study of using the Japanese Experiment Module Exposed Facility (JEM-EF) on ISS

---

[9]The RS instrument concept, shown in Figure 5.5, predated the MCR and is from DAC4, it included 3 spectrometers. The MCR version of the RS instrument consists of 2 grating spectrometers.

CLARREO MCR Minimum: 1 observatory with RS/IR/RO								
CLARREO Science Objective	**Related Climate Change Variable**	F_{si}	F_{cv}	$F_{crl}^{1/2}$ (75%)	F_{ta} IR	F_{ta} RS	F_{ta} RO	SV_{so}
Cloud Feedback SW	Reflected SW flux, albedo RS Cloud Properties	**2**	1.5	1.8	0	1.05	0	**5.7**
Cloud Feedback LW	Earth Emitted LW flux IR Cloud Properties	**1**	1.0	1.8	1.03	0	0	**1.9**
Cloud Feedback Net	Net Cloud Radiative Forcing	**5**	1.3	1.4	1.03	1.05	0	**9.6**
Temperature Response & Lapse Rate Feedback	Temperature Profile	**3**	1.5	1.8	1.03	0	1.0	**8.3**
Water Vapor Response & Water Vapor Feedback	Water Vapor Profile	**3**	1.5	1.8	1.03	0	0.2	**1.7**
Aerosol Direct Radiative Forcing	Aerosol Radiative Forcing Aerosol Properties	**1.5**	1.5	1.8	0	1.0	0	**4.0**
Snow & Ice Albedo Feedback	Reflected SW flux, albedo Snow/Ice & Cloud Cover	**1.5**	1.5	1.8	0	1.05	0	**4.3**
Land Albedo Change & Radiative Forcing	Reflected SW flux, albedo	**0.5**	2.0	1.8	0	1.05	0	**1.8**
Vegetation Index Change	Vegetation Index	**1**	2.0	1.8	0	1.05	0	**3.8**
Sum of Mission Science Value								41.1
Total Mission Science Value relative to MCR Baseline								64%

Table 5.3: Science Value Matrix for the MCR CLARREO Minimum Mission.

as a host platform for the CLARREO MCR instrument designs. The scope and self-imposed constraints used in this study are described below.

Scope of Accommodation Study: To streamline the trade space, several self-imposed constraints were utilized. Primarily, the study was aimed at illustrating feasibility and not to develop a concept at an MCR level of maturity. This study was performed to answer high-level questions about the ability of the ISS to support the mass, volume, power, data, and field-of-regard requirements for the IR and RS instruments. This study does not include the GNSS-RO because the ISS, as a host platform for it, was ruled out in an earlier design study.

(a) CLARREO preferred location (5) on JEM-EF. (b) CLARREO payload attached to JEM-EF.
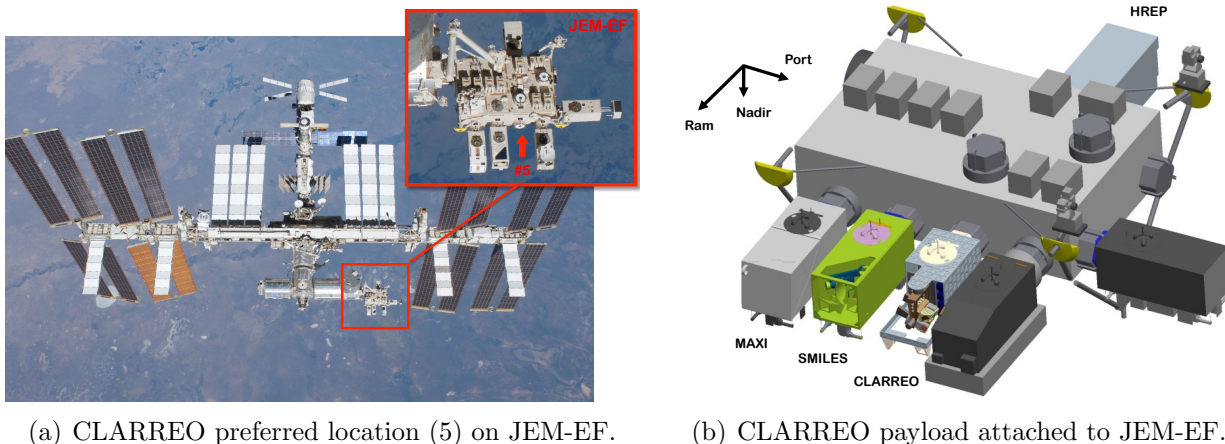
Figure 5.6: CONCEPT OF CLARREO MISSION IMPLEMENTATION ON THE ISS.

Conceptually, the instruments were "in storage" to leverage the high-fidelity MCR instrument design concepts. In this sense the instruments were not optimized for the ISS because this would have required a new design cycle. The instruments had gone through several design iterations and peer reviews with relatively well understood mass, volume, power, and data requirements. The modifications made to the instruments were minimal and predominantly in mechanical structure and mounting interfaces. Although the IR and RS could have been located at different ISS locations, e.g. the IR on JEM and the RS mounted like Stratospheric Aerosol and Gas Experiment (SAGE III) on an ExPRESS Logistics Carrier (ELC), the decision was made to design an integrated CLARREO payload.

There are several items which would need further work in order to fully develop this concept. For example, the JEM-EF's capability to handle instrument electronics thermal requirements is more than adequate, but a detailed study on how the RS thermal design could be migrated to the JEM-EF was not performed. There was also no attempt to optimize mass or power requirements, no vibration nor jitter analyses, no contamination analysis, and no conops for times when the ISS is out of its nominal attitude.

CLARREO Lessons Learned: Many trade studies were performed prior to CLARREO MCR. A portion of these trade studies were aimed at configurations of free-flyers, which could support the IR, RS, and GNSS-RO instruments simultaneously. Although the GNSS-RO was not included as part of the ISS study, there were still trades which gave insight into "favorable" or "less favorable" ways to configure the IR and RS instruments. For example: (a) The

174

RS instrument needed to be on the ram/wake end of the spacecraft to have the best field of regard for solar calibration and lunar verification. (b) The RS instrument required nadir views with large off-nadir view angles for reference inter-calibration. (c) The RS instrument needed a two-axis gimbal for pointing agility and to avoid IR data loss, which would be caused by large bus motions. (d) The IR instrument could be mounted close to the spacecraft and still have unobstructed nadir, zenith, and off-zenith views for benchmarking, a cold reference, and periodic polarization checks. (e) The overall instrument configuration worked best when radiators were placed on the spacecraft "cold" side for thermal maintenance.

Parameter	JEM EF	CLARREO ISS
Mass	550 kg (standard site)	$\sim$ 453 kg with GFE ($\sim$ 20% margin)
Power	3 kW (standard site)	$\sim$ 250 W ($\sim$ 92% margin)
Thermal	3 kW (fluid cooling loop)	$\sim$ 250 W
Data Rate	1 Mbps (MIL-STD-1553) 10 Mbps (10 Base-T Ethernet) 43 Mbps (Shared-Negotiated)	$\sim$ 640 kbps to $\sim$ 72Mbps Highest rate: RS solar calibration requires data buffering at the payload
Data Volume	Negotiable up 1.5 Tb	$\sim$ 90 Gb/day
Volume	$0.8 \times 1.0 \times 1.85$ m	Complies (stowed)

Table 5.4: CLARREO-ISS ACCOMMODATION COMPLIANCE MATRIX.

JEM-EF overview: The Japan Aerospace Exploration Agency (JAXA) provided JEM-EF was determined to be the most likely candidate for supporting both instruments. This was due to the mass, volume, power, and data capabilities and largely unobstructed nadir and zenith views. In addition, the Naval Research Laboratory (NRL) HICO-RAIDS Experiment Payload (HREP), deployed in October of 2009, consisted of two science payloads in a common payload supported by the JEM-EF. This fact lent credence to combining both CLARREO science instruments into a common JEM-EF payload. Considering the lessons learned from the MCR studies, as well as instrument requirements, site No. 5 was chosen as the best candidate as shown in Figure 5.6a. The No. 3 and No. 1 locations to the left of location No. 5 are considered as backups.

CLARREO ISS Payload Concept: The integrated JEM-EF concept for CLARREO is shown in Figure 5.7. The concept packages both the IR and RS instruments inside of an aluminum payload carrier with cutouts for instrument field-of-regard. The carrier is necessary to provide mechanical support structure for the instruments as well as JEM-EF and H-II Transfer Vehicle (HTV) interfaces. The MCR instruments are shown to scale with respect to the payload carrier envelope. The Payload Interface Unit (PIU), Flight Releasable Grapple Fixture (FRGF), and HTV Cargo Attachment Mechanism – Passive (HCAM-P) are Government Furnished Equipment (GFE) required for JEM-EF payloads. The PIU is the mechanical, electrical, data, and thermal interface to the JEM-EF. The HCAMs are the mechanical interface between the payload carrier and the HTV. The grapple fixture is used by the robot arm on the JEM-EF to hold and attach the payloads into their operational locations.

The CLARREO-on-ISS concept leverages off of MCR lessons learned in several areas. First, the IR instrument is located nearest to the JEM-EF/PIU interface. Second, the RS instrument is located away from the JEM-EF/PIU at the ram end of the payload carrier. This is to optimize the RS field of regard which includes angles close to the ISS velocity vector (ram
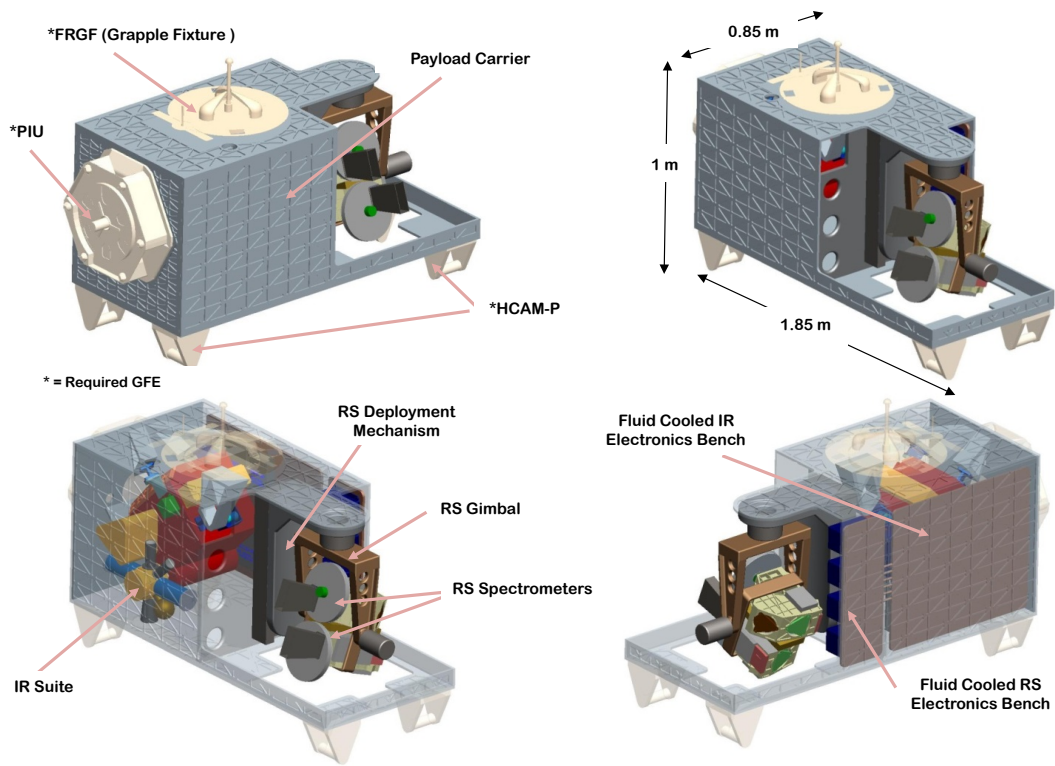
Figure 5.7: CLARREO ISS PAYLOAD CONCEPT.

direction). In place of radiators used on the CLARREO MCR free-flyer concepts, the huge thermal capacity of the ISS is used by incorporating a fluid cooled electronics bench for both instrument's electronics boxes. These benches are both located on one side of the payload carrier to minimize the amount of additional hardware to route cooling fluid through the system.

To support the variety of viewing angles required by the RS, a concept utilizing two mechanisms was developed. To facilitate the large off nadir pointing and tracking required for reference inter-calibration, as well as the pointing needed for solar calibration and lunar calibration verification, a two-axis gimbal concept was developed. However, there would still be structures from the payload carrier, as well as additional payloads to port and starboard, which would limit the operational field of regard. Requirements for JEM-EF payloads limit excursions from the ram end of the payloads because the ICS-EF payload in port No. 7 functions as an additional communications capability. The deployment mechanism extends toward nadir to increase the unobstructed field-of-regard of the RS, while at the same time avoids violation of the JEM-EF payload envelope.

InfraRed Suite Operations: The CLARREO/ISS IR instrument is a Fourier Transform Specter (FTS) for SI-traceable measurements of the mid and far-IR spectrum of the Earth and atmosphere. It utilizes one ambient blackbody, one phase-change blackbody, and deep space as on-orbit calibration sources. A scene select mechanism is used for ISS motion compensation and calibration source selection. The IR instrument concept is described in Section 4.3.

The IR suite was the easier instrument to accommodate as part of this concept. This was due largely to the comparatively small instrument field-of-view and well-defined viewing locations

176

(a) Nadir   **(b) Off-Zenith**   **(c) Zenith**
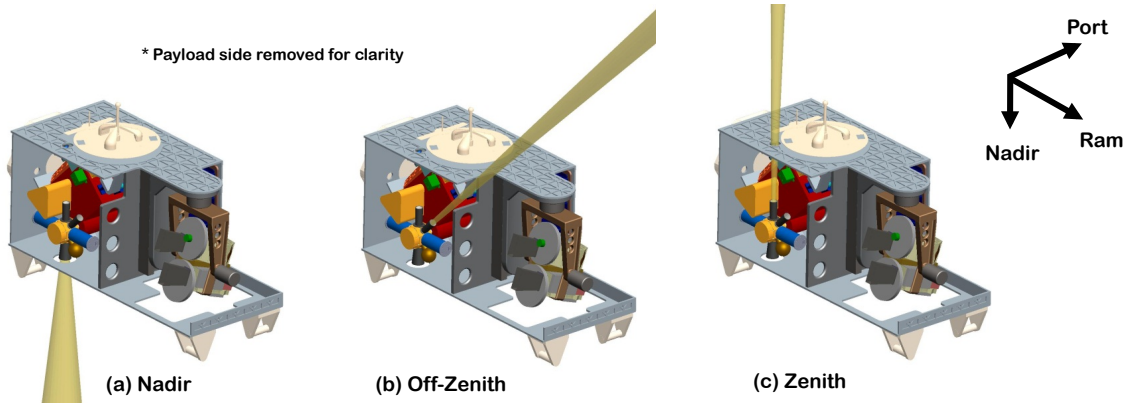
Figure 5.8: IR INSTRUMENT OPERATIONAL MODES: (A) NADIR VIEW TO POINT-AHEAD AND LOOK-BEHIND FOR MOTION COMPENSATION, (B) OFF-ZENITH VIEW FOR POLARIZATION CHECK, AND (C) ZENITH VIEW FOR "COLD" SOURCE CALIBRATION.
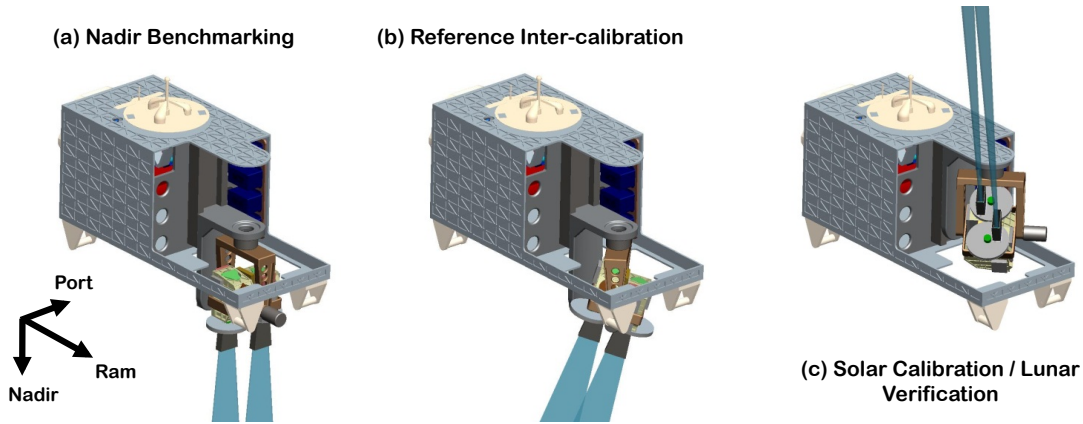
Figure 5.9: RS INSTRUMENT OPERATIONAL MODES: (A) NADIR VIEW FOR BENCHMARK OBSERVA-TIONS (DEPLOYED POSITION), (B) REFERENCE INTER-CALIBRATION VIEWS (DEPLOYED POSITION), AND (C) POINTING FOR SOLAR CALIBRATION OR LUNAR VERIFICATION (STOWED POSITION). NOTE: THE DEPLOYED RS INSTRUMENT POSITION ALSO OFFERS SOLAR/LUNAR CALIBRATION CAPABILITY.

of nadir, zenith, and off-zenith. The JEM-EF provides unobstructed views at all of these angles. The three viewing modes of the IR instrument are illustrated in Figure 5.8. These are very similar to free-flyer mission option.

Reflected Solar Instrument Operations: The CLARREO/ISS RS suite consists of a pair of pushbroom hyperspectral imagers with high spatial and spectral resolution. The RS instrument measures solar spectral reflectance of the Earth and its atmosphere relative to the solar irradiance spectrum. On-orbit calibration is performed using the Sun and Moon as sources obtained through precision apertures, neutral density filters, and perforated plates rotated via filter wheels. Field-of-regard for reference inter-calibration, solar calibration, and lunar calibration verification is achieved with a two-axis gimbal and deployment mechanism. The CLARREO RS instrument concept is summarized in Section 4.2.

As discussed earlier, the RS takes two additional mechanisms in order to facilitate required data collection modes. The addition of the two-axis gimbal and deployment mechanism increases the available field-of-regard from the JEM-EF. Figures 5.9a and 5.9b show the nadir-

deployed RS and gimbal to demonstrate nadir benchmarking and reference inter-calibration modes of operation, respectively. For nadir views, the RS could remain in the stowed configuration and only be deployed during inter-calibration periods. This would be determined during detailed con-ops development as it would be dependent on the number of planned reference inter-calibration events. In cases where several opportunities occur close together, it would probably be advantageous to leave the RS deployed and return to nadir pointing between events.

Also shown in Figure 5.9c is an example of use of the two-axis gimbal while the RS is stowed during a solar calibration or lunar calibration verification event. These events occur predominantly above the ram-port viewing plane. Therefore, having the RS instrument and gimbal stowed would occur most often during calibration-verification. There are opportunities, however, when the RS instrument could be deployed to facilitate solar calibration. In similar fashion to the IR instrument, details of the con-ops would need further development.

At a high-level, the concept of utilizing the JEM-EF as a host platform appears feasible. The JEM-EF provides accommodations which support needs for mass, power, data, and thermal management. At the same time, the CLARREO ISS mission concept meets requirements for mass and envelope and can be packaged in a JEM-EF compatible payload carrier. Additional design work could be performed to optimize the CLARREO IR and RS if additional mass margin or increased field-of-regard were needed.

CLARREO on the ISS mission option offers thee best overall science value of 72% for the lowest cost. The Science Value Matrix for this mission concept is shown in Table 5.5. Due to the ISS 52° inclination orbit, CLARREO will not have coverage of Earth's polar regions. This is accounted by introducing additional fingerprinting capability factor of 0.83 for all science objectives. However, flying in a precessing orbit will enhance temporal uniformity of sampling for inter-calibration of existing sensors [Roithmayr et al., 2014a]. For this mission option, the radio occultation data is acquired from the COSMIC constellations.

CLARREO on ISS: RS and IR instruments, RO data acquired								
CLARREO Science Objective	**Related Climate Change Variable**	F_{si}	F_{cv}	$F_{crl}^{1/2}$ (75%)	F_{ta} IR	F_{ta} RS	F_{ta} RO	SV_{so}
Cloud Feedback SW	Reflected SW flux, albedo RS Cloud Properties	**2**	1.5	2.5	0	1.05	0	**6.5**
Cloud Feedback LW	Earth Emitted LW flux IR Cloud Properties	**1**	1.0	2.5	1.03	0	0	**2.1**
Cloud Feedback Net	Net Cloud Radiative Forcing	**5**	1.3	1.8	1.03	1.05	0	**10.2**
Temperature Response & Lapse Rate Feedback	Temperature Profile	**3**	1.5	2.5	1.03	0	1.0	**9.6**
Water Vapor Response & Water Vapor Feedback	Water Vapor Profile	**3**	1.5	2.5	1.03	0	0.2	**1.9**
Aerosol Direct Radiative Forcing	Aerosol Radiative Forcing Aerosol Properties	**1.5**	1.5	2.5	0	1.0	0	**4.6**
Snow & Ice Albedo Feedback	Reflected SW flux, albedo Snow/Ice & Cloud Cover	**1.5**	1.5	2.5	0	1.05	0	**4.9**
Land Albedo Change & Radiative Forcing	Reflected SW flux, albedo	**0.5**	2.0	2.5	0	1.05	0	**2.2**
Vegetation Index Change	Vegetation Index	**1**	2.0	2.5	0	1.05	0	**4.4**
Sum of Mission Science Value								**46.4**
Total Mission Science Value relevant to MCR Baseline								**72**%

Table 5.5: Science Value Matrix for CLARREO mission on the ISS (Section 5.4). Additional factor for all science objectives: fingerprinting capability = 0.83 (fraction of Earth's coverage). This factor was set to 1.0 for other mission concepts. Note: for ISS mission option the radio occultation data is acquired from the COSMIC constellations.

5.5 CLARREO 2014 Concept: Sun-Synchronous & Polar Orbits

The CLARREO-light mission concept is developed by NASA LaRC and GSFC teams.

CLARREO 2014 mission concept assumptions:

⋄ Surrey SSTL-150, 7-year lifetime (92%).

⋄ IR interferometer, 3-year lifetime design (85%).

⋄ Assume same reliability for both IR and RS missions.

⋄ IRON orbit 765 km altitude 1:30 LECT sun-synchronous ascending orbit.

⋄ SOLARIS flies in 90° inclination polar orbit, 609 km altitude, on dedicated spacecraft.

⋄ IR and RS and RO are independent time series done in parallel. They are only combined for a key analyses (e.g. IR/RO/RS climate change fingerprinting from level 3 data sets).

5.5.1 InfraRed Instrument Concept – IRON

The InfraRed Orbiting NIST (IRON) concept IR instrument and spacecraft bus fee-flyer design goal was a lightweight, low-cost IR spectrometer alternative, integrated onto a Rapid Spacecraft Deployment Office (RSDO) catalog bus (the Surrey SSTL-150), orbited by a Pegasus XL launch vehicle. The concept developed from a careful reassessment of the CLARREO MCR design, evaluating the ability of a reduced-capability spacecraft IR instrument to meet most of the science requirements of the CLARREO mission. The end-result was an IR instrument with mass reduced relative to the CLARREO MCR design from 76 kg to approximately 45 kg CBE (with cover, radiators and cables, but not including the payload-launch vehicle adapter ring), and with power requirements reduced from 124 W average (233 W peak) to 75 W average (100 W peak).
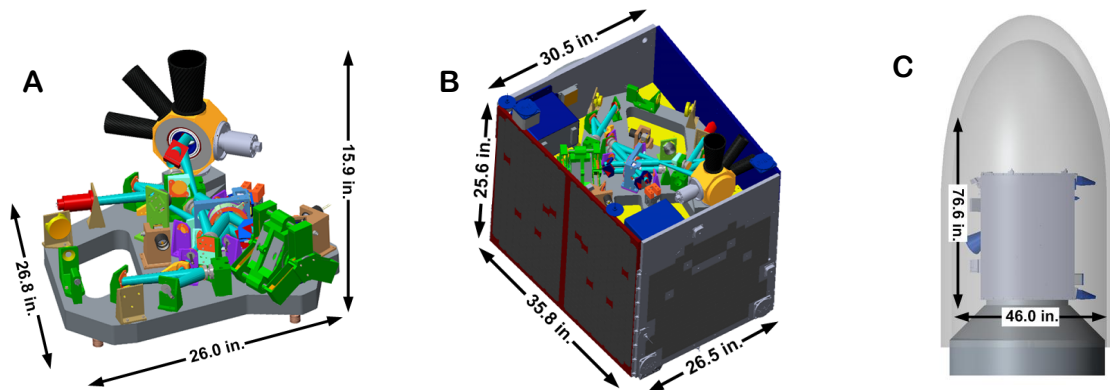

Figure 5.10: (a) IRON – a lightweight IR spectrometer concept (b) IRON instrument integrated into Surrey SSTL-150 spacecraft, and (c) IRON inside the Pegasus LV fairing.

Several changes to the CLARREO MCR concept design accomplished this mass and power reduction in IRON, including:

(a) A smaller spacecraft bus and launcher were possible by deciding to fly the IR and RS instruments on separate spacecraft buses. This also allowed a more flexible mission architecture, with observation and calibration sequences more in line with instrument specific requirements.

(b) Flying the IR instrument spacecraft in a sun-synchronous orbit, leading to a minimal number of spacecraft maneuvers. This orbit exposed one side of the spacecraft, covered with solar panels (no gimbals), continuously to the sun for maximum power, and one side of the spacecraft continuously to deep space, providing a surface for mounting a multi-stage passive radiative cooler for the MCT detectors, and a radiator housing for the Verification BlackBody (VBB).

(c) Experience assessing measurement uncertainty in the risk-reduction IR Calibration Demonstration System (CDS) indicated a VBB could be operated at a single cold temperature since the CDS uncertainty is a smoothly varying function of calibration blackbody temperatures below the instrument ambient temperature. This simplification allowed for passive cooling of the VBB radiating to space on the anti-sun side of the bus and reduced the maximum heater power required for temperature control.

(d) Rotating the input polarization plane relative to the optical bench by 45°, with a dihedral mirror system at the optical bench input, allowed for mounting the optical bench flat to a spacecraft deck facing nadir. This significantly reduced structural complexity and mass compared to the MCR design which had required mounting the optical bench at 45° on the spacecraft deck.

(e) Modifying the scene pointing control system to separate a cross-track stepper positioning to view the earth scene, space view, and the calibration black bodies, from the fine in-track spacecraft motion compensation mechanism. This simplified scene select mechanism and motor design and put the space calibration view in the cross direction rather than forcing it to be in the ram/ wake, or zenith directions.

(f) Passively cooling the VBB and the MCT detectors, as well as removing all active control of optical bench temperature, reduced the instrument power requirements and heater control system mass. The current generation of operational sounders, mounted on the nadir decks of spacecraft in sun-synch orbits have proven that optical bench temperatures can be highly stable even without active control.

(g) Removing the quantum cascade laser (QCL) and its input integrating sphere from the instrument verification system. The QCL was to provide an instrument line shape and single-wavelength reflectance measurement. Changing the 45° space view to a 45° off-nadir view on the anti-sun side of the bus and detect instrument polarization sensitivity with a spacecraft roll. Given the frequency of this measurement this compromise did not significantly reduce nadir viewing duty cycle and makes it possible to mount the instrument to the nadir deck without having to look up through the spacecraft body.

(h) Overall the design changes reduced mass, mounting complexity of the IR instrument, and simplified the spacecraft bus, while at the same time reducing power requirements through reduced thermal loads and an all-passive cooling system.

These engineering compromises affected the science capabilities when compared to the MCR design. The impacts were most noticeable in:

(a) Reduced inter-calibration opportunities for non-sun synch satellites. At the proposed 98° inclination, 765 km orbit, less frequent coincident opportunities exist for the Earth Observation System (EOS) A-train scientific instruments, Joint Polar Satellite System (JPSS),

hyperspectral weather systems and other polar orbiting satellite systems.

(b) Loss of diurnal coverage for benchmark and fingerprinting. The impact of this loss will require further analysis, although spectral fingerprinting not requiring diurnal observations should remain unaffected.

(c) The instrument polarization sensitivity measurement requires a periodic spacecraft roll maneuver. The expectation is that these roll maneuvers, accomplished by spacecraft bus reaction wheels, should occur once per month or less frequently.

(d) A heated halo positioned in front of the VBB is the only method of on-orbit verification of the calibration blackbody spectral reflectivity and emissivity. The signal using this method should be much larger than a QCL option and would also provide information for the entire IR instrument spectral bandpass.

(e) Using a single, low temperature for the VBB results in incomplete mapping of detector nonlinearity. The impacts of this proposal are currently being evaluated. Assessment of the measurement uncertainties of several IR interferometers in addition to the IR CDS, with blackbodies operated over a wide temperature range, will be required.

(f) ILS must be derived from atmospheric line shapes without the QCL. The ILS determined in this way, is verified with multiple, instead of a single, lines. The caveat is that one must choose relatively weak atmospheric absorption bands with minimal Doppler or pressure broadening effects.

5.5.2 Reflected Solar Instrument Concept – SOLARIS

SOLARIS: Compared to MCR design (two spectrometers): Instrument mass reduces from 77 kg to 35 kg CBE. Power reductions still being evaluated but not expected to change significantly due to data rates and pointing requirements, essentially identical as MCR design.
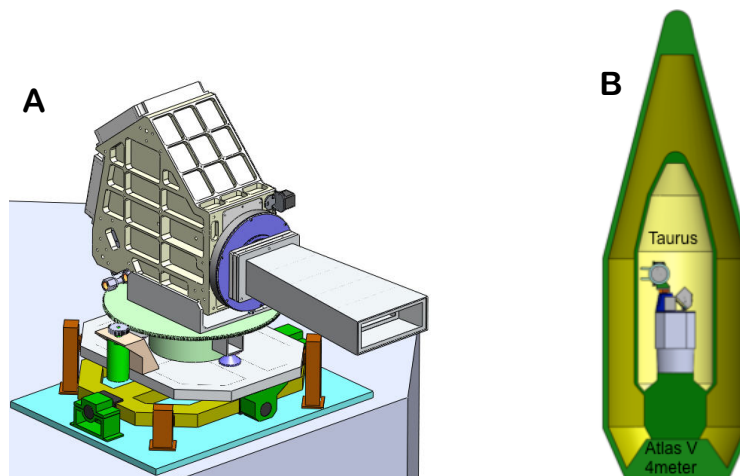
Figure 5.11: (A) SOLARIS, NEW ONE-SPECTROMETER APPROACH TO THE CLARREO RS INSTRUMENT, (B) SOLARIS INSTRUMENT INSIDE NOMINAL ATLAS AND TAURUS FAIRINGS FOR SIZE REFERENCE.

5.5.3   Science Value and Cost Estimates

Science Value Matrix for the CLARREO 2014 mission concept is shown in Table 5.6. In conclusion, Surrey spacecraft reliability is high despite low cost. Relative to the MCT Baseline: 86% of science versus 72% of science for ISS option, because ISS option does not cover polar regions for benchmarking. The IR and RS time series can be separated for net cloud feedback. For climate change don't need the instantaneous matching that would be required for normal retrievals.

CLARREO 2014 Concept: Small RS and IR observatories								
CLARREO Science Objective	**Related Climate Change Variable**	F_{si}	F_{cv}	$F_{crl}^{1/2}$ (70%)	F_{ta} IR	F_{ta} RS	F_{ta} RO	SV_{so}
Cloud Feedback SW	Reflected SW flux, albedo RS Cloud Properties	**2**	1.5	2.3	0	1.05	0	**7.2**
Cloud Feedback LW	Earth Emitted LW flux IR Cloud Properties	**1**	1.0	2.3	1.03	0	0	**2.4**
Cloud Feedback Net	Net Cloud Radiative Forcing	**5**	1.3	2.3	1.03	1.05	0	**15.4**
Temperature Response & Lapse Rate Feedback	Temperature Profile	**3**	1.5	2.3	1.03	0	1.0	**10.7**
Water Vapor Response & Water Vapor Feedback	Water Vapor Profile	**3**	1.5	2.3	1.03	0	0.2	**2.1**
Aerosol Direct Radiative Forcing	Aerosol Radiative Forcing Aerosol Properties	**1.5**	1.5	2.3	0	1.0	0	**5.2**
Snow & Ice Albedo Feedback	Reflected SW flux, albedo Snow/Ice & Cloud Cover	**1.5**	1.5	2.3	0	1.05	0	**5.4**
Land Albedo Change & Radiative Forcing	Reflected SW flux, albedo	**0.5**	2.0	2.3	0	1.05	0	**2.4**
Vegetation Index Change	Vegetation Index	**1**	2.0	2.3	0	1.05	0	**4.8**
Sum of Mission Science Value								**55.6**
Total Mission Science Value relative to MCR Baseline								**86%**

Table 5.6: Science Value Matrix for the CLARREO 2014 mission concept.

5.6   CLARREO Data Products

The CLARREO data products are designed for validation and testing of climate models on decadal scales (see Section 2.7). The GCM community has been engaged during pre-formulation mission studies. Climate simulation experiments have been developed to help define measurement and data product requirements (see Section 2.6). Ultimate users of CLARREO climate benchmarking data products will be policy makers (see Section 3). Another large user community of the CLARREO data is presented by the instrument calibration teams – reference inter-calibration to on-orbit standards (see Section 2.8) will enable higher accuracy climate data records derived from operational sensors. Other potential users include the weather data assimilation teams for improved weather forecasts and applied science researchers interested in agriculture, energy, and regional climate effects.

The CLARREO science data products will be grouped into four processing levels:

◇ *Level-1:* Geolocated and calibrated emitted spectral infrared radiance, reflected solar spectral radiance and nadir reflectance, reflected solar spectral radiance and reflectance for on-orbit inter-calibration, and GNSS-RO time delays.

◇ *Level-2:* Cloud mask, GNSS-RO refractivity, temperature, geopotential height profiles.

◇ *Level-3:* Climate benchmark products – space- and time-averaged spectral infrared radiance and reflectance (global, 10° latitudinal zones, 30° by 30° regions, seasonal and annual).

◇ *Level-4:* Reference inter-calibration infrared and solar reflected products (user specified).

A more detailed list specifying data product coverage, spatial and temporal resolutions, key parameters, and estimated data releases is provided below:

Level-1 CLARREO RS Benchmarking Product:
   Coverage: global, 1 granule per orbit (daytime only)
   Spatial: 10 km spatial average full spectral resolution, 0.5 km full spatial resolution
          15 band spectral average, both at full 100 km swath width
   Temporal: instantaneous
   Wavelengths: 320 – 2300 nm, 8 nm resolution
   Key Parameters: reflected spectral solar radiance and nadir reflectance
   Availability: launch + 6 months

Level-1 CLARREO IR Benchmarking Product:
   Coverage: global, 1 granule per orbit
   Spatial: 25 km IFOV, 200 km spacing
   Temporal: 8 sec. integration every 30 sec.
   Wavelengths: $200 - 2000$ cm^{-1}, 1 cm^{-1} resolution
   Key Parameters: emitted infrared spectral radiance
   Availability: launch + 6 months

Level-1 CLARREO IR & RS Benchmarking Merged Product:
   Coverage: global, 1 granule per orbit (daytime only)
   Spatial: 25 km FOV, 200km spacing. RS data spatially averaged to match IR IFOV
   Temporal: every 30 sec
   Wavelengths: $320 - 2300$ nm, 8 nm resolution; $200 - 2000$ cm^{-1}, 1 cm^{-1} resolution

Key Parameters: emitted infrared spectral radiance; reflected spectral solar radiance and nadir reflectance
Availability: launch + 6 months

Level-1 CLARREO RS Inter-Calibration Product:
    Coverage: global, 1 granule per orbit (daytime only)
    Spatial: full spectral and spatial (0.5 km) resolution
    Temporal: on-orbit matched, instantaneous
    Wavelengths: 320 − 2300 nm, 4 nm sampling
    Key Parameters: reflected spectral solar radiance and nadir reflectance
    Availability: launch + 6 months

Level-1 CLARREO GNSS-RO Product:
    Coverage: global, daily granules
    Spatial: 200 km horizontal tangent path, altitudes of 2 − 20 km
    Temporal: time scale for single occultation
    Key Parameters: time delay
    Availability: launch + 6 months

Level-2 CLARREO Cloud Mask Product:
    Coverage: global, 1 granule per orbit
    Spatial: 25 km every 200 km; 10 km & 0.5 km, 100 km swath width (daytime)
    Temporal: IR, every 30 sec along groundtrack. RS, continuous along ground track
    Key Parameters: cloud mask, surface geotype identification, elevation
    Availability: launch + 1 year

Level-2 CLARREO GNSS-RO Product:
    Coverage: global, orbit or daily granules
    Spatial: 200 km horizontal tangent path, altitudes of 2 − 20 km
    Temporal: time scale for single occultation
    Key Parameters: refractivity, dry temperature, geopotential height, dry pressure
    Availability: launch + 1 year

Level-3 CLARREO IR Benchmarking Product:
    Coverage: global, 1 granule per instrument, merged multi-satellite product
    Spatial: global, 10° latitudinal zones, 30° × 30° regions
    Temporal: seasonal, annual
    Wavelengths: $200 - 2000$ cm^{-1}
    Key Parameters: average emitted infrared spectral radiance
    Availability: launch + 1 year

Level-3 CLARREO RS Benchmarking Product:
    Coverage: global, 1 granule per instrument, merged multi-satellite product
    Spatial: global, 10° latitudinal zones, 30° × 30° regions
    Temporal: seasonal, annual
    Wavelengths: 320 − 2300 nm
    Key Parameters: average reflected spectral solar radiance and nadir reflectance
    Availability: launch + 1 year

Level-3 CLARREO GNSS-RO Product:

Coverage: global, 1 granule per instrument
Spatial: global, 10° latitudinal zones, 30° × 30° regions
Temporal: seasonal, annual
Key Parameters: refractivity, dry temperature, geopotential height, dry pressure
Availability: launch + 1 year

Level-4 CLARREO Inter-calibration Products:
The Level-4 CLARREO inter-calibration data products will be available via Multi-Instrument Inter-Calibration (MIIC) framework (see Section 2.8.4), hosted at NASA LaRC ASDC. The MIIC framework includes multi-sensor inter-calibration event prediction, data access, sampling and averaging algorithms, histograms, and data analysis tools. The framework is designed to be flexible to provide results for inter-calibration in the RS and IR, specified by the users.

CLARREO Estimated Data Volume:
Estimated CLARREO data archive volume (all products): 220 GBytes/day; 80 TBytes/year. We should note that this estimate was made at the CLARREO Mission Concept Review (2010) for a relatively small on-orbit inter-calibration effort for the CLARREO RS: 3 – 5% of full resolution data (up to 30 min/day). Taking into account CLARREO RS ability to inter-calibrate all imagers in the GEO and Landsat sensors, CLARREO data volume can increase a factor of 4 by taking full resolution data from the RS instrument up to 10% for off-nadir inter calibration of LEO and GEO sensors, and 10% of nadir inter-calibration of the Landsat sensors.

5.7 Mission Cost Estimates

The CLARREO mission options were costed using the Basis Of Estimates (BOE) tool, developed and used at NASA Langley Research Center since 1992. The BOE tool objectives are: (1) To maximize the use of available information by using descriptive, in-depth input parameter sets; defining input at common element level where elements are familiar, comparable to those in other projects; using systematic process and minimizing need for analyst judgment. (2) To model the process as faithfully as possible. Strive for algorithms that mimic the process and enhance understanding of results (constructive), and reflect observed trends for small parameter value changes (sensitivity analysis). (3) To provide useful output, feedback through many potential points of comparison for analysis of project planning and improvement of modeling process. The BOE's pre-defined structure is consistent with NPR-7120.5D. The input into the BOE's database and model includes: historical data, vendor quotes, grass roots engineering estimates, parametric estimates, constraints (schedule, funding, etc.), and pricing data. The BOE model provides comprehensive output for reviewers and project implementation personnel: hours, staffing levels and dollars, separated by function, by phase at the level of definition.

The CLARREO mission option's science value, relative to the MCR Baseline, and cost estimates in real-year dollars, are summarized in Table 5.7. A mission concept to fly two CLARREO instruments (RS and IR spectrometers) on the International Space Station (see Section 5.4), because of the higher reliability of the ISS as a spacecraft, offers the best overall science value of 72% (see Table 5.5) for the lowest cost.

NRC Outline	Science Value	Cost Estimate ($RY)
Decadal Survey (2007): 11 instruments, 3 SC in 3 P90 orbits	112%	$\sim$ \$1,6B Est. 3 Launches in 2018 − 2020
CLARREO Mission Options	**Science Value**	**Cost Estimate ($RY)**
MCR Baseline Mission (2010): 6 instruments, 4 smaller or 2 larger SC in 2 P90 orbits	100%	\$800M − \$1000M + Launch Vehicles Launches in 2018, 2020
MCR Minimum Mission (2010): 3 instruments on 1 SC in a single P90 orbit	64%	\$675M − \$750M + 1 Launch Vehicle Launch in 2021
ISS Mission Concept (2012): 2 instruments on ISS, RO data from COSMIC	72%	\$340M − \$390M Launch provided by ISS EV-2 ISS full cost guidelines
Sun-synch & P90 orbits (2014): 2 instruments on 2 small SC, RO data from COSMIC	86%	$\sim$ \$500M Including 2 Launches on Pegasus

Table 5.7: Mission science values relative to the CLARREO MCR Baseline and cost estimates for the NRC recommended outline [NRC, 2007] and CLARREO mission options in chronological order.

References

Aghedo, A. M., Bowman, K. W., Worden, H. M., Kulawik, S. S., Shindell, D. T., Lamarque, J. F., Faluvegi, G., Parrington, M., Jones, D.B.A, Rast, S., 2011a: "The vertical distribution of ozone instantaneous radiative forcing from satellite and chemistry climate models," *Journal of Geophysical Research: Atmospheres (1984 – 2012)*, 116 (D1).

Aghedo, A. M., Bowman, K. W., Shindell, D. T., Faluvegi, G., 2011b: "The impact of orbital sampling, monthly averaging and vertical resolution on climate chemistry model evaluation with satellite observations," *Atmospheric Chemistry & Physics Discussions*, 11(3).

Anderson, J. A. Dykema, R. M. Goody, H. Hu, and D. B. Kirk-Davidoff, 2004: "Absolute, spectrally-resolved, thermal radiance: a benchmark for climate monitoring from space," *J. Quant. Spec. Radiat. Trans.*, 85, pp. 367 – 383.

Arechi, A.V., G.A. McKee, and C.N. Durell, 2011: "RF-excited plasma lamps for use as sources in OGSE integrating spheres," *Proc. SPIE*, Vol. 8153, San Diego, California.

Barnes, W.L, and V. V. Salomonson, 1993: "MODIS: A global image spectroradiometer for the Earth Observing System," *Critical Rev. Opt. Sci.Technol.*, v. CR47, pp. 285 – 307.

Berk, A., L.S. Bernstein, G.P. Anderson, P.K. Acharya, D.C. Robertson, J.H. Chetwynd and S.M. Adler-Golden, 1998: "MODTRAN Cloud and Multiple Scattering Upgrades with Application to AVIRIS," *Remote Sens. Environ.*, 65, pp. 367 – 375.

Berk, A., P.K. Acharya, L.S. Bernstein, G.P. Anderson, J.H. Chetwynd, Jr., M.L. Hoke, 2000: "Reformulation of the MODTRAN band model for finer spectral resolution," *proceedings of SPIE*, Vol. 4049, Orlando, Florida.

Berk, A., G.P. Anderson, P.K. Acharya, L.S. Bernstein, L. Muratov, J. Lee, M. Fox, S.M. Adler-Golden, J.H. Chetwynd, M.L. Hoke, R.B Lockwood, J.A. Gardner, T.W. Cooley, C.C. Borel, P.E. Lewis and E.P. Shettle, 2006: "MODTRAN5: 2006 Update," *Proc. SPIE*, Vol. 6233, 62331F.

Bernstein, L.S., A. Berk, P.K. Acharya, D.C. Robertson, G.P. Anderson, J.H. Chetwynd and L.M. Kimball, 1996: "Very Narrow Band Model Calculations of Atmospheric Fluxes and Cooling Rates," *Journal of Atmospheric Sciences*. Vol. 53, No. 19, pp. 2887 – 2904.

Best, F.A., D. P. Adler, S. D. Ellington, D. J. Thielman, H. E. Revercomb, 2008: "On-orbit Absolute Calibration of Temperature with Application to the CLARREO Mission," *Earth Observing Systems XIII SPIE*, 7081, 10pp.

Best, F. A., Knuteson, R. O., Revercomb, H. E., Tobin, D. C., Gero, P. J., Taylor, J. K., Rice, J., Hanssen, L. and Mekhontsev, S., 2009: "Determination of the Atmospheric Emitted Radiance Interferometer (AERI) blackbody emissivity and radiance using multiple technique," *Proc. Characterization and Radiometric Calibration for Remote Sensing*, Logan, UT.

Best, F.A, Adler, D.P, Pettersen, C., Revercomb, H.E., Perepezko, J.H., 2010: "On-orbit absolute temperature calibration using multiple phase change materials: overview of recent technology advancements," *Proceedings of SPIE*, Vol. 7857, Bellingham, WA, 78570J.

Best, F.A., Douglas P. Adler, Claire Pettersen, et al., 2012: "On-orbit absolute radiance

standard for the next generation of IR remote sensing instruments," *Proceedings Volume 8527. Multispectral, Hyperspectral, and Ultraspectral Remote Sensing Technology*, Techniques and Applications IV, doi:10.1117/12.977559.

Bhatt, R.; Doelling, D. R.; Morstad, D.; Scarino, B.R.; Gopalan, A., 2014a: "Desert-Based Absolute Calibration of Successive Geostationary Visible Sensors Using a Daily Exoatmospheric Radiance Model," *IEEE Transactions on Geoscience and Remote Sensing*, vol. 52, no. 99, pp. 3670 – 3682, doi: 10.1109/TGRS.2013.2274594.

Bhatt, R., D. R. Doelling, A. Wu, X. Xiong, B. R. Scarino, C. O. Haney, and A. Gopalan, 2014b: "Initial Stability Assessment of S-NPP VIIRS Reflective Solar Band Calibration using Invariant Desert and Deep Convective Cloud Targets," *Remote Sens.*, 6, pp. 2809 – 2826; doi:10.3390/rs6042809.

BIPM (Bureau International des Poids et Mesures), 2008: "Evaluation of measurement data – Guide to the expression of uncertainty in measurement," *Joint Committe for Guides in Metrology (JCGM)*, 120 pp.

Bony, S., R. Colman, V. M. Kattsov, R. P. Allan, C. S. Bretherton, J. L. Dufresne, A. Hall, S. Hallegatte, M. M. Holland, W. Ingram, D. A. Randall, B. J. Soden, G. Tselioudis and M. J. Webb, 2006: "How well do we understand and evaluate climate change feedback processes?" *Journal of Climate*, 19, pp. 3445 – 3482.

Bovensmann, H., J.P. Burrows, M. Buchwitz, J. Frerick, S. Noel, V. Rozanov, K.V. Chance, and A.P.H. Goede, 1999: "SCIAMACHY: Mission objectives and measurement modes," *Journal of Atmos. Science*, 56, pp. 127 – 150.

Breiman, L., 2001: "Random forests," *Machine learning*, 45(1), pp. 5 – 32.

Brown, S.W., Eppeldauer, G.P., and Lykke, K.R., 2000: "NIST facility for Spectral Irradiance and Radiance Responsivity Calibrations with Uniform Sources," *Metrologia*, Vol. 37, 579 – 582, 2000

Brown, S. W., G. P. Eppeldauer, and K. R. Lykke, 2006: "Facility for spectral irradiance and radiance responsivity calibrations using uniform sources," *Applied Optics*, 45, pp. 8218 – 8237.

Buijs, H., et al., 2008: "Beamsplitters for various occasions," Workshop on Infrared Remote Sensing Applications.

Chahine, M. T., and co-authors , 2006: "AIRS: Improving Weather Forecasting and Providing New Data on Greenhouse Gases," *Bull. of the Am. Met. Soc.*, v. 87, n. 7, pp. 911 – 926.

Chen, T., W.B. Rossow, and Y. Zhang, 2000: "Radiative effects of cloud-type variations," *Journal of Climate*, 13 (1), pp. 264 – 286.

Chander, G., T. J. Hewison, N. Fox, X. Wu, X. Xiong, and W. Blackwell, 2013: "Overview of inter-calibration of satellite instruments," *IEEE Trans. Geosci. Remote Sens.*, v. 51, n. 3, pp. 1056 – 1080.

Chung, E.-S., B.J. Soden, and A.C. Clement, 2012: "Diagnosing climate feedbacks in coupled ocean-atmosphere models," *Surv. Geophys.*, doi: 10.1007/s10712-012-9187.

CLARREO official website, 2014: *http://clarreo.larc.nasa.gov*

Clerbaux, N, J.E. Russell, S. Dewitte, C. Bertrand, D. Caprion, B. De Paepe, L. Gonzalez, Sotelino, A. Ipe, R. Bantges, H.E. Brindley, 2009: "Comparison of GERB instantaneous radiance and flux products with CERES Edition-2 data," *Rem. Sens. of Environ.*, 113, pp. 102 – 114.

Clough, S.A., M.J. Iacono, and J.-L. Moncet, 1992: "Line-by-line calculations of atmospheric fluxes and cooling rates: Application to water vapor," *J. Geophys. Res.*, 9, 15, 761-15, 785.

Clough, S.A., M.W. Shephard, E.J. Mlawer, J.S. Delamere, M.J. Iacono, K. Cady-Pereira, S. Boukabara, and P.D. Brown, 2005: "Atmospheric radiative transfer modeling: a summary of the AER codes, short communication," *J. Quant. Spectrosc. Ra.*, 91, pp. 233 – 244.

Cooke, R., B.A. Wielicki, D.F. Young, M. G. Mlynczak, 2013: "Value of Information for Climate Observing Systems," *Environ. Syst. Decis.*, 12 pp.

Cooke, R., B.A. Wielicki, M. G. Mlynczak, 2015: "Real Option Value of Earth Observing Systems," *Climate Policy*, in press.

Cox, C.V., J. E. Harries, J. P. Taylor, P. D. Green, A. J. Baran, J. C. Pickering, A. E. Last, J.E. Murray, 2010: "Measurement and simulation of mid- and far-infrared spectra in the presence of cirrus," *Quarterly Journal of the Royal Meteorological Society*, 136, n. 648, pp. 718 – 739.

Cox, C., and W. Munk, 1956: "Slopes of the sea surface deduced from photographs of sun glitter," *Bull. Scripps Inst. Oceanogr.*, 6, pp. 401 – 488.

Crone, L., and D. Crosby, 1995: "Statistical applications of a metric on subspaces to satellite meteorology," *Technometrics*, pp. 324 – 328.

Datla, R. U., J. P. Rice, K. Lykke and B. C. Johnson, J.J. Butler and X. Xiong, 2009: "Best practice guidelines for pre-launch characterization and calibration of instruments for passive optical remote sensing," NISTIR 7637, 47 pp.

Dee, D., 2005: "Bias and data assimilation," *Quart. J. Roy. Met. Soc.*, 131, pp. 3323 – 3343.

Derber, John C., Wan-Shu Wu, 1998: "The Use of TOVS Cloud-Cleared Radiances in the NCEP SSI Analysis System," *Mon. Wea. Rev.*, 126, pp. 2287 – 2299.

Desbiens, R., Genest, J., Tremblay, P., 2002: "Radiometry in line-shape modeling of Fourier-transform spectrometers," *Applied optics*, 41(7), pp. 1424 – 1432.

DelSole, T., M. K. Tippett, and J. Shukla, 2011: "A significant component of unforced multi-decadal variability in the recent acceleration of global warming," *Journal of Climate*, 24, pp. 909 – 926.

Doelling, D.R., L. Nguyen, and P. Minnis, 2004: "On the use of deep convective clouds to calibrate AVHRR data," *Proc. SPIE 49th Ann. Mtg., Earth Observ. Syst. IX Conf.*, Denver, CO, Aug. 2 – 6, pp. 281 – 299.

Doelling, D.R., D. Morstad, R. Bhatt, and B. Scarino, 2011: "Algorithm Theoretical Basis Document (ATBD) for deep convective cloud (DCC) technique of calibrating GEO sensors

with Aqua-MODIS for GSICS," GSICS. Available at
http://gsics.nesdis.noaa.gov/pub/Development/AtbdCentral

Doelling, D., C. Lukashin, P. Minnis, B. Scarino, and D. Morstad, 2012: "Spectral reflectance corrections for satellite intercalibrations using SCIAMACHY data," *Geosci. Rem. Sens. Lett.*, 8, pp. 119 – 123, doi:10.1109/LGRS.2011.2161751.

Doelling, D. R., D. Morstad, B.R. Scarino, R. Bhatt, and A. Gopalan, 2013a: "The Characterization of Deep Convective Clouds as an Invariant Calibration Target and as a Visible Calibration Technique," *IEEE Trans. Geosci. Remote Sens.*, Vol 51, No. 3, pp. 1147 – 1159, 10.1109/TGRS.2012.2225066.

Doelling, D.R., B. R. Scarino, D. Morstad, A. Gopalan, R. Bhatt, C. Lukashin, P. Minnis, 2013b: "The calibration of geostationary visible imagers using operational hyper-spectral SCIAMACHY radiances," *IEEE Trans. Geosci. Remote Sens.*, Vol. 9, No1, pp. 119 – 123, 10.1109/TGRS.2012.2227760.

Doelling, D.R., N.G. Loeb, D.F. Keyes, M. Nordeen, B.A. Wielicki, D.F. Young, M. Sun, 2013c: "Geostationary Enhanced Temporal Interpolation for CERES flux products," *J. Atmos. Oceanic Tech.*, Vol. 30, 1072 – 1090.

Doelling, D. R., K.V. Khlopenkov, A. Okuyama, C. O. Haney, A. Gopalan, B. R. Scarino, M. Nordeen, R. Bhatt, L. Avey, 2014a, "MTSAT-1R visible imager point spread correction function, Part I: The need for, validation of, and calibration with." Accepted by *IEEE Trans. Geosci. Remote Sens.*

Doelling, D. R., A. Wu, X. Xiong, B.R. Scarino, R. Bhatt, C.O. Haney, D. Morstad, A. Gopalan, 2014b: "The radiometric stability and scaling of collection 6 Terra and Aqua-MODIS VIS, NIR, and SWIR spectral bands," submitted to *IEEE Trans. Geosci. Remote Sens.*

Dykema J.A., Anderson J.G., 2006: "A methodology for obtaining on-orbit SI-traceable spectral radiance measurements in the thermal infrared," *Metrologia*, 43, pp. 287 – 293.

Eplee, R.E. Jr., et al., 2012: "On-orbit calibration of SeaWiFS," *Applied Optics*, 51, 8702 – 8730.

Espejo, J., G. Drake, K. Heuerman, G. Kopp, A. Lieber, P. Smith, and B. Vermeer 2011: "A hyperspectral imager for high radiometric accuracy Earth climate studies," *Proc. SPIE*, 8158, doi:10.1117/12.893803.

Evans K.F., and G.L. Stephens, 1991, "A new polarized atmospheric radiative transfer model," *J. Quant. Spectrosc. Radiat. Trans.*, 46, pp. 413 – 423.

Feldman, D. R., C. A. Algieri, J. R. Ong, and W. D. Collins, 2011a: "CLARREO shortwave observing system simulation experiments of the twenty-first century: Simulator design and implementation," *J. Geophys. Res.*, 116, D10107, doi:10.1029/2010JD015350.

Feldman, D. R., C. A. Algieri, W. D. Collins, Y. L. Roberts, and P. A. Pilewskie, 2011b: "Simulation studies for the detection of changes in broadband albedo and shortwave nadir reflectance spectra under a climate change scenario," *J. Geophys. Res.*, 116, D24103, doi:10.1029/2011JD016407.

Feldman, D.R., W.D. Collins, 2014: "Pan-Spectral Observing System Simulation Experiments

of Shortwave Reflectance and Longwave Radiance for Climate Model Evaluation," *Geoscientific Model Development Discussions*, 7(3), 3647 – 3670, doi:10.5194/gmdd-7-3647-2014.

Feldman, D. R., et al., 2014b, "The role of far-infrared surface emissivity in climate," *P. Natl. Acad. Sci.*, USA, in press.

Flato, G, J. Marotzke and co-authors, 2013: "Evaluation of climate models," *IPCC report WG1 AR5*, Chapter 9.

Forest, C.E., P.H. Stone, A.P. Sokolov, M.R. Allen, and M.D. Webster, 2002: "Quantifying Uncertainties in Climate System Properties with the use of Recent Climate Observations" *Science*, 295, 113 – 117.

Foster, G. and S. Rahmstorf, 2011: "Global temperature evolution 1979-2010," *Env. Res. Letters*, 6, doi:10.1088/1748-9326/6/4/044022, 8 pp.

Fox, N, A. Kaisser-Weiss, W. Schmutz, K. Thome, D. Young, B. Wielicki, R. Winkler, E. Woolliams, 2011: "Accurate Radiometry from Space: an essential tool for climate studies," *Phil. Trans. R. Soc.*, A, 369, pp. 4028-4063, doi:10.1098/rsta.2011.0246

Franz, B.A., E.J. Kwiatkowska, G. Meister, and C.R. McClain, 2008: " Moderate Resolution Imaging Spectroradiometer on Terra: limitations for ocean color applications," *J. Appl. Remote Sens.*, 2(023525), doi:10.1117/1.2957964.

Genest, J., Tremblay, O., 1999: "Instrument line shape of Fourier transform spectrometers: analytic solutions for nonuniformly illuminated off-axis detectors," *Applied optics*, 38(25), 5438 – 5446.

Genest, J., Tremblay, P., 2002: "Impact of the optical aberrations on the line shape of Fourier-transform spectrometers," *Vibrational spectroscopy*, 29(1-2), pp. 3 – 13.

Genest, J., Tremblay, P., 2003: "Diffraction and line shape of Fourier-transform spectrometers," *Applied optics*, 42(22), pp. 4541 – 4548.

Genest, J., Tremblay, P., 2008: "Understanding Fourier-transform spectrometers," Quebec: University of Laval.

Gero, P. J., J. A. Dykema, J. G. Anderson, 2008: "A Blackbody design for SI-traceable radiometry for earth observation," *J. of Atmos. Oceanic Tech.*, 25, pp. 2046 – 2054.

Gero, P. Jonathan, Taylor, Joseph K., Best, Fred A., Garcia, Raymond K., Revercomb, Henry E., 2012: "On-orbit absolute blackbody emissivity determination using the heated halo method," *Metrologia*, Volume 49, Issue 2, S1-S8. Reprint No. 6631.

Goetz, A., 2009: "Three decades of hyperspectral remote sensing of the Earth: A personal view," *Remote Sens. Environ.*, 113, S5 – S16, doi:10.1016/j.rse.2007.12.014.

Goldberg, M., G. Ohring, J. Butler, C. Cao, R. Datla, D. Doelling, V. Gartner, T. Hewi son, B. Iacovazzi , D. Kim, T. Kurino, J. Lafeuille, P. Minnis, D. Renaut, J. Schmetz, D. Tobin, L. Wang, F. Weng, X. Wu, F. Yu, P. Zhang, and T. Zhu, 2011: "The Global Space-Based Inter-Calibration System (GSICS)," *Bull. Amer. Met Soc.*, 92, pp. 467 – 475.

Goody, R., J. Anderson, and G. R. North, 1998: "Testing climate models: An approach," *Bull. Amer. Meteor. Soc.*, 79, pp. 2541 – 2549.

Group on Earth Observations (GEO), 2005: "The Global Earth Observation System of Systems (GEOSS)," 10-Year Implementation Plan.

Group on Earth Observations (GEO), 2010: "A Quality Assurance Framework for Earth Observation: Principles," Version 4, January 2010.

GSICS, 2006: "Implementation Plan for a Global Space-Based Inter-Calibration System (GSICS)," WMO-CGMS, 22pp.

Hansen J.E., and Hovenier J.W., 1971, "The doubling method applied to multiple scattering of polarized light," *J. Quant. Spectrosc. Radiat. Trans.*, 11, pp. 809 – 812.

Haeffelin, M., B. Wielicki, J.-Ph. Duvel, K. Priestley, and M. Viollier, 2001: "Intercalibration of CERES and ScaRaB Earth radiation budget datasets using temporally and spatially collocated radiance measurements," *Geophys. Res. Lett.*, 28, pp. 167 – 170.

Hajj, G.A., E.R. Kursinski, L.J. Romans, W.I. Bertiger, and S.S. Leroy, 2002: "A technical description fo atmospheric sounding by GPS occultation," *J. Atmos. Solar Terr. Phys.*, 4, pp. 451 – 469.

Hanel, R. A., et al., 1971: "The Nimbus 4 Michelson interferometer," *Applied Optics*, 10, pp. 1376 – 1381.

Harries, J. E., 1996: "The greenhouse Earth: A view from space," *QJRMS*, 122, pp. 799 – 818.

Harries, J. E., 1997: "Atmospheric radiation and atmospheric humidity," *QJRMS*, 123, pp. 2173 – 2186.

Harries, J., et al., 2008: "The far-infrared Earth," *Rev. Geophys.*, 46, RG-4004, doi:10.1029/2007RG000233 .

Haskins, R.D., R.M. Goody, and L. Chen, 1997: "A statistical method for testing general a circulation model with spectrally resolved satellite data," *J. Geophys. Res.*, 102, 16, 563-16, 581.

Hewison et al., 2013: "GSICS Inter-Calibration of Infrared Channels of Geostationary imagers using Metop/IASI," *IEEE Transactions on Geoscience and Remote Sensing,* v. 51, n. 3.

Hilker, T., A. I. Lyapustin, C. J. Tucker, P. J. Sellers, F. G. Hall, Y. Wang, 2012: "Remote Sensing of Tropical Ecosystems: Atmospheric Correction and Cloud Masking Matter," *Rem. Sens. Environ.*, http://dx.doi.org/10.1016/j.rse.2012.08.035.

Hilker, T., A. I. Lyapustin, C. J. Tucker, F. G. Hall, R. B. Myneni, Y. Wang, J. Bi, P. J. Sellers, 2014: "Vegetation dynamics and rainfall sensitivity of the Amazon," *PNAS*, in review.

Hilton, F., and Coauthors], 2012: "Hyperspectral Earth observations from IASI: Five years of accomplishments," *Bull. Amer. Meteor. Soc.*, v. 93, pp. 347 – 370.

Hu B., B. A. Wielicki, P. Yang, P. W. Stackhouse, Jr., B. Lin, and D. F. Young, 2004: "Application of deep convective cloud albedo observation to satellite-based study of the terrestrial atmosphere: Monitoring the stability of spaceborne measurements and assessing absorption anomaly," *IEEE Trans. Geosci. Remote Sens.*, v. 42, n.11, pp. 2594 – 2599.

Huang, Y. and V. Ramaswamy, 2009: "Evolution and trend of the outgoing longwave radiation spectrum," *Journal of Climate*, 22, pp. 4637 – 4651.

Huang, Y., S. Leroy, P. J. Gero, J. Dykema, and J. Anderson, 2010a: "Separation of longwave climate feedbacks from spectral observations," *J. Geophys. Res.*, 115, D07104, doi:10.1029/2009JD012766, 9 pp.

Huang, Y., S. Leroy, J. Anderson, 2010b: "Determining Longwave Forcing and Feedback Using Infrared Spectra and GNSS Radio Occultation," *Journal of Climate*, 23, pp. 6027 – 6035.

Huang, Y., S. Leroy, and R. M. Goody, 2011: "Discriminating between climate observations in terms of their ability to improve an ensemble of climate predictions," *Proc. Natl. Acad. Sci.*, doi/10.1073/pnas.1107403108, 108, 10405 – 10409.

Huber, M. and R. Knutti, 2011: "Anthropogenic and natural warming inferred from changes in Earth's energy balance," *Nature Geoscience*, doi: 10.1038/NGEO1327, 6 pp.

Hunt, G., 1977: "Spectral signatures of particulate minerals in the visible and near infrared," *Geophysics*, 42(3), pp. 501 – 513.

Inness, A., Baier, F., Benedetti, A., Bouarar, I., Chabrillat, S., Clark, H., ... and Lefever, K., 2013: "The MACC reanalysis: an 8 year data set of atmospheric composition," *Atmospheric Chemistry & Physics*, 13(8).

IPCC, 2007a: "Climate Change 2007: The Physical Science Basis," Contribution of Working Group I to the Fourth Assessment Report of the Intergovernmental Panel on Climate Change [Solomon, S., D. Qin, M. Manning, Z. Chen, M. Marquis, K.B. Averyt, M. Tignor and H.L. Miller (eds.)]. *Cambridge University Press*, Cambridge, United Kingdom and New York, NY, USA, 996 pp.

IPCC, 2007b: "Synthesis report: Contribution of working groups I, II and III to the fourth assessment report of the Intergovernmental Panel on Climate Change Core Writing Team," *IPCC, Geneva, Switzerland*, p. 104.

Jin, Z., B. A. Wielicki, C. Loukachine, T. P. Charlock, D. Young, and S. Nol, 2011: "Spectral kernel approach to study radiative response of climate variables and interannual variability of reflected solar spectrum," *J. Geophys. Res.*, 116, D10113, doi:10.1029/2010JD015228.

Jin, Z., C. Lukachin, A. Gopalan, and W. Sun, 2012: "Correlation between SCIAMACHY, MODIS, and CERES reflectance measurements: Implications for CLARREO," *J. Geophys. Res.*, 117, D05114, doi:10.1029/2011JD017051.

Jin, Z., C. Lukashin, Y. Qiao, and A. Gopalan, 2013: "An efficient and effective method to simulate the Earth spectral reflectance over large temporal and spatial scales," *Geophys. Res. Lett.*, 40, pp. 374–379, doi:10.1002/grl.50116.

Jin, Z., C. Lukashin, Y. Roberts, B. Wielicki, D. Feldman, and W. Collins, 2014, "Interannual variability of the Earth's spectral solar reflectance from measurements and simulations," *J. Geophys. Res. Atmos.*, 119, doi:10.1002/2013JD021056.

Kalnay E. and co-authors, 1996: "The NCEP/NCAR 40-year reanalysis project," *Bull. Amer. Met. Soc.*, 77, pp. 437 – 471.

Kato, S., 2009: "Interannual variability of the global radiation budget," *Journal of Climate*, 22, pp. 4893 – 4907.

Kato, S., B. A. Wielicki, F. G. Rose, X. Liu, P. C. Taylor, D. P. Kratz, M. G. Mlynczak, D. F. Young; N. Phojanamongkolkij, S. Sun-Mack; W. F. Miller, Y. Chen, 2011: "Detection of atmospheric changes in spatially and temporally averaged infrared spectra observed from space," *Journal of Climate*, 24, pp. 6392 – 6407.

Kato, S., F. G. Rose, X. Liu, B. A. Wielicki, and M. G. Mlynczak, 2014: "Retrieval of atmospheric and cloud property anomalies and their trend from temporally and spatially averaged infrared spectra observed from space," *Journal of Climate*, in press.

Khlopenkov, K. V., D. R. Doelling, A. Okuyama, 2014: "MTSAT-1R visible imager point spread function correction, Part II: Theory," Accepted by *IEEE Trans. Geosci. Remote Sens.*

Kieffer, H. H., 1997: "Photometric stability of the lunar surface," *Icarus*, 139 , pp. 323 – 327.

Kieffer, H. H. and T. C. Stone, 2005: "The spectral irradiance of the Moon," *Astronomical Journal*, 129, pp. 2887 – 2901.

King, M.D., W. P. Menzel, Y. J. Kaufman, D. Tangre, B.-C. Gao, S. Platnick, S. A. Ackerman, L. A. Remer, R. Pincus, and P. A. Hubanks, 2003: "Cloud and aerosol properties, precipitable water, and profiles of temperature and water vapor from MODIS," *IEEE Tran. on Geo. and Rem. Sensing*, 41 (2), pp. 442 – 458.

King, M. D., S. Platnick, W. P. Menzel, S. A. Ackerman, and P. A. Hubanks, 2013: "Spatial and Temporal Distribution of Clouds Observed by MODIS onboard the Terra and Aqua Satellites," *IEEE Trans. Geo. Rem. Sens.*, 51, pp. 3826 – 3852, doi: 10.1109/TGRS.2012.2227333.

Kirk-Davidoff, D.B., R.M. Goody, and J.G. Anderson, 2005: "Analysis of sampling errors for climate monitoring satellites," *Journal of Climate*, 18, pp. 810 – 822.

Krzanowski, W., 1979: "Between-groups comparison of principal components," *Journal of the American Statistical Association*, pp. 703 – 707.

Kulawik, S. S., Bowman, K. W., Luo, M., Rodgers, C. D., and Jourdain, L., 2008: "Impact of nonlinearity on changing the a priori of trace gas profile estimates from the Tropospheric Emission Spectrometer (TES)," *Atmospheric Chemistry and Physics*, 8(12), pp. 3081 – 3092.

Kursinski, E.R., G.A. Hajj, S.S. Leroy, and B. Herman, 2000: "The GPS radio occultation technique," *Terr. Atmos. Ocean. Sci.*, 1, pp. 53 – 114.

Kursinski, E.R., G.A. Hajj, J.T. Schofield, R.P. Linfield, and K.R. Hardy, 1997: "Observing Earths atmosphere with radio occultation measurements using the Global Positioning System," *J. Geophys. Res.*, 102, pp. 23429 – 23465.

Kwiatkowska, E.J., B.A. Franz, G. Meister, C.R. McClain, and X. Xiong, 2008: "Cross calibration of ocean-color bands from Moderate Resolution Imaging Spectroradiometer on Terra platform," *Applied Optics*, 47(36), pp. 6796 – 6810.

Lacis A. A., J. Chowdhary, M.I. Mishchenko, and B. Cairns, 1998, "Modeling errors in diffuse-sky radiation: Vector vs. scalar treatment," *Geophys. Res. Lett.*, 25, pp. 135 – 138, doi:

10.1029/97GL03613.

Latvakoski, H., M. Watson, S. Topham, D. Scott, M. Wojcik, and G. Bingham, 2010: "A high-accuracy blackbody for CLARREO," *Infrared Remote Sensing and Instrumentation XVIII*, Marija Strojnik and Gonzalo Paez, Eds., Vol. 7808 of SPIE Proceedings Series International Society for Optics and Photonics.

H. Latvakoski, H., M.G. Mlynczak, D.G. Johnson, R.P. Cageao, D.P. Kratz, and K. Johnson, 2013: "Far-infrared spectroscopy of the troposphere: instrument description and calibration performance," *Applied Optics*, 52, pp. 264 – 273.

Latvakoski, H., M.G. Mlynczak, R.P. Cageao, D.G. Johnson, and D.P. Kratz, 2014: "Far infrared spectroscopy of the troposphere: Calibration with a cold background," *Applied Optics*, 53, pp. 5425 – 5433, http://dx.doi.org/10.1364/AO.53.005425

Lei, N., B. Guenther, Z. Wang, and X. Xiong, 2013: "Modeling SNPP VIIRS reflective solar bands optical throughput degradation and its impacts on the relative spectral response," *Proc. SPIE*, vol. 8866, Paper 55.

Leroy, S.S., 1997: "Measurement of geopotential heights by GPS radio occultation," *J. Geophys. Res.*, 102, 6971 – 6986.

Leroy, S. S., 1998: "Detecting climate signals: Some Bayesian aspects," *J. of Climate*, 11, pp. 640 – 651.

Leroy, S. S., 2001: "The effects of orbital precession on remote climate monitoring." *J. Climate*, 40, 4330 – 4337.

Leroy, S.S., J.G. Anderson, and J.A. Dykema, 2006a: "Testing climate models using GPS radio occultation: A sensitivity analysis," *J. Geophys. Res.*, 111, doi:10.1029/2005JD006145.

Leroy, S.S., J.A. Dykema, and J.G. Anderson, 2006b: "Climate benchmarking using GNSS occultation. In Atmosphere and Climate: Studies by Occultation Methods," U. Foelsche, G. Kirchengast, A. Steiner (Eds.), Springer, Berlin, 336pp.

Leroy, S. S., J. G. Anderson and G. Ohring, 2008a: "Climate signal detection times and constraints on climate benchmark accuracy requirements," *J. of Climate*, 21, pp. 841 – 846.

Leroy, S., J. G. Anderson, J. Dykema, and R. Goody, 2008b: "Testing climate models using thermal infrared spectra," *J. of Climate*, 21, 1863 – 1875.

Leroy, S.S., and J.G. Anderson, 2010: "Optimal detection of regional trends using global data," *J. of Climate*, 23, pp. 4438 – 4446.

Leroy, S.S., C.O. Ao, and O. Verkhoglyadova, 2012: "Mapping GPS radio occultation data by Bayesian interpolation," *J. Atmos. Ocean. Tech.*, 29, pp. 1062 – 1074.

Leroy, S.S., G. Redaelli, and B. Grassi, 2014: "Prioritizing data for improving the multi-decadal predictive capability of atmospheric models," *J. Climate*, Submitted.

Levy, R. C., Remer, L. A., Kleidman, R. G., Mattoo, S., Ichoku, C., Kahn, R., et al., 2010: "Global evaluation of the Collection 5 MODIS dark-target aerosol products over land," *Atmos. Chem. Phys.*, 10, pp. 10399 – 10420.

Liu, X., W. L. Smith, D. K. Zhou and Allen Larar, 2006, "Principal Component-based Radiative Transfer Forward Model (PCRTM) For Hyperspectral Sensors: Theoretical Concept," *Applied Optics*, 45, pp. 201 – 209.

Liu, X., D. K. Zhou, Allen Larar, W. L. Smith, and S. A. Mango, 2007, "Case Study a New Radiative Transfer Model and Retrieval Algorithm using EAQUATE Data," *Q. J. R. Meterol. Soc.*, 133, pp. 243 – 256.

Liu, X, D. K. Zhou, A. M. Larar, W. L. Smith, P. Schluessel, S. M. Newman, J. P. Taylor, and W. Wu, 2009,"Retrieval of atmospheric profiles and cloud properties from IASI spectra using super-channels," *Atmos. Chem. Phys.*, 9, pp. 9129 – 9142.

Loeb, N. G., B. A. Wielicki, W. Y. Su, K. Loukachine, W. B. Sun, T. Wong, K. J. Priestley, G. Matthews, W. F. Miller and R. Davies, 2007: "Multi-instrument comparison of top-of-atmosphere reflected solar radiation," *Journal of Climate*, 20, pp. 575 – 591.

Loeb, N.G., B. A. Wielicki, Takmeng Wong and Peter A. Parker, 2009: "Impact of Data Gaps on Satellite Broadband Radiation Records," *J. Geophys. Res.*, 114, D11109, doi:10.1029/2008JD011183.

Loeb, N.G, S. Kato, W. Su, T. Wong, F. Rose, D.R. Doelling, J. Norris, 2012: "Advances in Understanding Top-of-Atmosphere Radiation Variability from Satellite Observations," *Surv. Geophys.*, 33, 359 – 385, DOI 10.1007/s10712-012-9175-1.

Lukashin, C., B. A. Wielicki, D. F. Young, K. Thome, Z. Jin, and W. Sun, 2013: "Uncertainty estimates for imager reference inter-calibration with CLARREO reflected solar spectrometer," *IEEE Trans. on Geo. and Rem. Sensing, special issue on Intercalibration of satellite instruments*, 51, n. 3, pp. 1425 – 1436.

Lukashin, C., Z. Jin, G. Kopp, D.G. MacDonnell, and K. Thome, 2015: "CLARREO Reflected Solar Spectrometer: Restrictions for Instrument Sensitivity to Polarization," *IEEE Trans. Geo. Rem. Sens.*, v. 53, pp. 6703 – 6709, doi:10.1109/TGRS.2015.2446197

Lyapustin, A., Y. Wang, I. Laszlo, R. Kahn, S. Korkin, L. Remer, R. Levy, and J. S. Reid, 2011: "Multi-Angle Implementation of Atmospheric Correction (MAIAC): 2. Aerosol Algorithm," *J. Geophys. Res.*, 116, D03211, doi:10.1029/2010JD014986.

Lyapustin, A., Y. Wang, I. Laszlo, T. Hilker, F. Hall, P. Sellers, J. Tucker, S. Korkin, 2012: "Multi-Angle Implementation of Atmospheric Correction for MODIS (MAIAC). 3: Atmospheric Correction," *Rem. Sens. Environ.*, http://dx.doi.org/10.1016/j.rse.2012.09.002.

Maignan, F., F.-M. Breon, E. Fedele, M. Bouvier, 2009: "Polarized reflectances of natural sur- faces: Spaceborne measurements and analytical modeling," *Rem. Sens. Environment*, doi: 10.1010/j.rse.2009.07.022.

Masson, David, Reto Knutti, 2011: "Spatial-Scale Dependence of Climate Model Performance in the CMIP3 Ensemble," *Journal of Climate*, 24, pp. 2680 – 2692.

McNally, A. P., P D. Watts, J. A. Smith, R. Engelen, G. A. Kelly, J. N. Thepaut, and M. Matricardi, 2006: "The assimilation of AIRS radiance data at ECMWF," *Q. J. R. Meteorol. Soc.*, 132, pp. 935-957.

Meister, G., B. Franz, E. Kwiatkowska, and C. McClain, 2012: "Corrections to the Calibration

of MODIS Aqua Ocean Color Bands derived from SeaWiFS Data," *IEEE TGARS*, 50(1), 310 – 319, 10.1109/TGRS.2011.2160552.

Migliorini, S., Piccolo, C., and Rodgers, C. D., 2008: "Use of the Information Content in Satellite Measurements for an Efficient Interface to Data Assimilation," *Monthly Weather Review*, 136(7).

Minnis, P., S. Sun-Mack, D. F. Young, P. W. Heck, D. P. Garber, Y. Chen, D. A. Spangenberg, R. F. Arduini, Q. Z. Trepte, W. L. Smith, 2011a: "CERES Edition-2 cloud property retrievals using TRMM VIRS and Terra and Aqua MODIS datapart I: Algorithms," *IEEE Tran. on Geo. and Rem. Sensing*, 49 (11), pp. 4374 – 4400.

Minnis, P., S. Sun-Mack, Y. Chen, M. M. Khaiyer, Y. Yi, J. K. Ayers, R. R. Brown, X. Dong, S. C. Gibson, P. W. Heck, 2011b: "CERES Edition-2 cloud property retrievals using TRMM vVIRS and Terra and Aqua MODIS datapart II: Examples of average results and comparisons with other data," *IEEE Tran. on Geo. and Rem. Sensing*, 49 (11), pp. 4401 – 4430.

Mlynczak, M.G., J.E. Harries, R. Rizzi, P.W. Stackhouse, D.P. Kratz, D.G. Johnson, C.J. Mertens, R.R. Garcia, and B.J. Soden, 2002: "The Far-infrared: a frontier in remote sensing of Earth's climate and energy balance," *Proc. SPIE 4485*, 150, DOI:10.1117/12.454247.

Mlynczak, M. G., D.G. Johnson, H. Latvakoski, K. Jucks, M. Watson, D.P. Kratz, G. Bingham, W.A. Taub, S.J. Wallard, C.R. Hyde, and X. Liu, 2006: "First light from the far-infrared spectroscopy of the troposphere (FIRST) instrument," *Geophys. Res. Letters*, 33, L07704, doi: 10.1029/2005GL025114, 4 pp.

Montanaro, M., Z. Tesfaye, A. Lunsford, B. Wenny, D. Reuter, B. Markham, R. Smith, K. Thome, 2013: "Preliminary on-orbit performance of the Thermal Infrared Sensor (TIRS) on board Landsat 8," *Proc. SPIE*, Vol. 8866, San Diego, California.

Morstad, D. L., D. R. Doelling, R. Bhatt, and B. Scarino, 2011: "The CERES calibration strategy of the geostationary visible channels for CERES clouds and flux products," *SPIE Proceedings*, v. 8153, doi:10.1117/12.894650.

Myneni, R. B., J. Dong, C. J. Tucker, R. K. Kaufmann, P. E. Kauppi, J. Liski, L. Zhou, V. Alexeyev, and M. K. Hughes, 2001: "A large carbon sink in the woody biomass of Northern forests," *Proc. Natl. Acad. Sci. U. S. A.*, 98, 26, pp. 14784 – 14789.

Nadal, F., F.-M. Breon, 1999: "Parametrization of surface polarized reflectance derived from POLDER spaceborne measurements," *IEEE Trans. on Geo. Rem. Sensing*, 37, n. 3, pp. 1709 – 1718.

Nordhaus, W.D., 2008: "A question of balance: weighing the options on global warming policies," Yale University Press, New Haven.

NRC, 2007: "Earth Science and Applications from Space: National Imperatives for the Next Decade and Beyond," *The National Academy Press*, 428 pp.

NRC, 2012: "A National Strategy for Advancing Climate Modeling," *The National Academy Press*, 253 pp.

Ohring G. B., B. A. Wielicki, R. Spencer, B. Emery and R. Datla, 2005: "Satellite Instrument Calibration for Measuring Global Climate Change: Report on a workshop," *Bull. Amer.*

Meteor. Soc., 86, pp. 1303 – 1313.

Ohring, G. Ed., 2007: "Achieving Satellite Instrument Calibration for Climate Change (ASIC³),"
NOAA publication, 142 pp.

Pachauri, R. K., and A. Reisinger, 2007: "Climate Change 2007 Synthesis Report: Summary
for Policymakers," *IPCC Secretariat.*

Pan, Y., R. A. Birdsey, J. Fang, R. Houghton, P. E. Kauppi, W. A. Kurz, O. L. Phillips, A.
Shvidenko, S. L. Lewis, J. G. Canadell, P. Ciais, R. B. Jackson, S. W. Pacala, a D. McGuire,
S. Piao, A. Rautiainen, S. Sitch, and D. Hayes, 2011: "A large and persistent carbon sink in
the worlds forests," *Science*, 333, 6045, pp. 988 – 993.

Platnick, S., M. D. King, S. A. Ackerman, W. P. Menzel, B. A. Baum, J. C. Riedi, and R. A.
Frey, 2003: "The modis cloud products: Algorithms and examples from terra," *IEEE Tran.
on Geo. and Rem. Sensing*, 41 (2), 459 – 473.

Ramanathan, V., R. D. Cess, E. F. Harrison, P. Minnis, B. R. Barkstrom, E. Ahmad, and
D. Hartmann, 1989: "Cloud-radiative forcing and climate: results from the Earth radiation
budget experiment," *Science*, 243, pp. 57 – 63.

Rienecker, M.M., M.J. Suarez, R. Gelaro, R. Todling, J. Bacmeister, E. Liu, M.G. Bosilovich,
S.D. Schubert, L. Takacs, G.-K. Kim, S. Bloom, J. Chen, D. Collins, A. Conaty, A. da Silva,
et al., 2011: "MERRA - NASA's Modern-Era Retrospective Analysis for Research and Ap-
plications," *Journal of Climate*, 24, pp. 3624 – 3648, doi: 10.1175/JCLI-D-11-00015.1.

Richard, E., D. Harber, J. Rutkowski, K. OMalia, M. Triplett, G. Drake, J. Harder, P.
Pilewskie, S. Brown, A. Smith, and K. Lykke, 2011: "Future long-term measurements of solar
spectral irradiance by the TSIS spectral irradiance monitor: improvements in measurement
accuracy and stability," *11th International Conference on New Developments and Applications
in Optical Radiometry*, Maui, Hawaii.

Ringer, M.A., and S.B. Healy, 2008: "Monitoring twenty-first century climate using GPS radio
occultation bending angles," *Geophys. Res. Lett.*, 35, doi:10.1029/2007GL032462.

Revercomb, H. E., et al., 1988: "Radiometric calibration of IR Fourier transform spectrome-
ters: solution to a problem with the High-Resolution Interferometer Sounder," *Applied Optics*,
27.15: 3210-3218.

Revercomb, H. E., 1994: "Techniques for Avoiding Phase and Non-linearity Errors in Ra-
diometric Calibration: A Review of Experience with the Airborne HIS and Ground-based
AERI," *Proceedings of the 5th International Workshop on Atmospheric Science from Space
using FTS*, pp. 353 – 378.

Revercomb, H. E., et al., 2013a: "NASA Instrument Incubator Program: A New Class of
Advanced Accuracy Satellite Instrumentation (AASI) for the CLARREO Mission," Final
Report. University of Wisconsin, Space Science and Engineering Center.

Revercomb, H. E., et al., 2013b: "Vacuum Testing of the UW Absolute Radiance Interfer-
ometer (ARI) With End-to-End Verification Tests to Bring the Instrument to TRL 6," Final
Report. University of Wisconsin, Space Science and Engineering Center.

Roberts, Y. L., P. Pilewskie, and B. C. Kindel, 2011: "Evaluating the observed variability in

hyperspectral earth-reflected solar radiance," *J. Geophys. Res.*, 116, D24, doi:10.1029/2011JD016448, 23 pp.

Roberts, Y., P. Pilewskie, B. Kindel, D. Feldman, and W. Collins, 2013: "Quantitative comparison of the variability in observed and simulated shortwave reflectance," *Atmospheric Chemistry and Physics*, 13(6), pp. 3133 – 3147.

Roberts, Y., P. Pilewskie, and B. Kindel, 2014: "Evaluating the observed variability in hyperspectral earth-reflected solar radiance," *J. Geophys. Res.*, in review.

Roe, G. H. and M. B. Baker, 2007: "Why is climate change so unpredictable ?" *Science*, 318, pp. 629 – 632.

Roithmayr, C.M., and P.W. Speth, 2012: "Analysis of opportunities for intercalibration between two spacecraft," *Advances in Engineering Research Vol. 1*, Chapter 13, Edited: V.M. Petrova, Nova Science Publishers, Hauppauge, NY, pp. 409 – 436.

Roithmayr, C.M., C. Lukashin, P.W. Speth,D.F. Young, B.A. Wielicki, K.J. Thome, and G. Kopp, 2014a, "Opportunities to Intercalibrate Radiometric Sensors from International Space Station," *J. of Atm. and Oce. Tech.*, DOI: 10.1175/JTECH-D-13-00163.1

Roithmayr, C.M., C. Lukashin, P.W. Speth, G. Kopp, K. Thome, B.A. Wielicki, and D.F. Young, 2014b, "CLARREO Approach for Reference Inter-Calibration of Reflected Solar Sensors: On-Orbit Data Matching and Sampling," *IEEE TRGS*, v. 52, 10, pp. 6762 – 6774, 10.1109/TGRS.2014.2302397.

Rowlands, D.J. and Co-authors, 2012: "Broad range of 2050 warming from an observationally constrained large climate model ensemble," *Nature Geosci.*, 5, pp. 256 – 260.

Roy, D.. P. Lewis and C. Justice, 2002: "Burned are mapping using multitemporal moderate spatial resolution data – a bi-directional reflectance model-based expectation approach," *Rem. Sens. Environ.*, 83, pp. 263 – 286.

Saha S., S. Moorthi, H.-L. Pan and Co-authors, 2010: "The NCEP Climate Forecast System Reanalysis," *Bull. Amer. Meteor. Soc.*, 91, pp. 1015 – 1057

Schaaf C. B., Gao F., Strahler A.H., et al., 2002: "First operational BRDF, albedo nadir reflectance products from MODIS," *Rem. Sens. Environ.*, 83, pp. 135 – 148.

Schmidt, K. S., E. Bierwirth, P. Pilewskie, J. Redemann, R. E. Brandt, A. Lyapustin, C. Gatebe, C. Schaaf, and R. Kahn, 2009: "Airborne measurements of surface albedo in Alaska," *in Fall Meet. Suppl.*, Abstract A43A-0159, vol. 90.

Sexton, D.M.H., J.M. Murphy, M. Collins, and M.J. Webb, 2012: "Multivariate probabilistic projections using imperfect climate models part I: outline of methodology," *Climate Dyn.*, 38, pp. 2513 – 2542.

Sexton, D.M.H., and J.M. Murphy, 2012: "Multivariate probabilistic projections using imperfect climate models. Part II: robustness of methodological choices and consequences for climate sensitivity," Climate Dyn., 38, pp. 2543 – 2558.

Smith, N., W. P. Menzel, E. Weisz, A. Heidinger and Baum, B. A., 2013: "A uniform space-time gridding algorithm for comparison of satellite data products: Characterization and sensitivity studies," *J. Appl. Meteor. Clim.*, v. 52, pp. 255 – 268.

Smith,N., W. L. Smith, E. Weisz, and H. E. Revercomb, 2014: "Climate Monitoring with Satellite Data Records – An investigation into the continuity among AIRS, IASI, and CrIS soundings," To be submitted to the *J. Appl. Meteor. Clim.*

Smith, W. L. , H. M. Woolf, and W. J. Jacob, 1970: "A regression method for obtaining real time temperature and geopotential height profiles from satellite spectrometer measurements and its application to Nimbus-III 'SIRS' observations," *Mon. Wea. Rev.*, 98, 582 – 603.

Smith, W. L. , H. B. Howell, and H. M. Woolf, 1979: "The use of interferometric radiance measurements for sounding the atmosphere," *J. Atmos. Sci.*, 36, 566 – 575.

Smith, W.L. Sr., Revercomb, H., Bingham, G., Larar, A., Huang, H., Zhou, D., Li, J., Liu, X., and Kireev, S., 2009: "Technical Note: Evolution, current capabilities, and future advance in satellite nadir viewing ultra-spectral IR sounding of the lower atmosphere," *Atmos. Chem. Phys.*, 9, pp. 5563 – 5574.

Smith, W. L., E. Weisz, S. Kirev, D. K. Zhou, Z. Li, and Borbas, E.E., 2012: "Dual-Regression Retrieval Algorithm for Real-Time Processing of Satellite Ultraspectral Radiances," *J. Appl. Meteor. Clim.*, 51(8), pp. 1455 – 1476.

Soden, B. J. and I. M. Held, 2006: "An assessment of climate feedbacks in coupled oceanatmosphere model," *Journal of Climate*, 19, pp. 3354 – 3360.

Soden, B. J., I. M. Held, R. Colman, K. M. Shell, J. T. Kiehl and C. A. Shields, 2008: "Quantifying climate feedbacks using radiative kernels," *Journal of Climate*, 21, pp. 3504 – 3520.

Stamnes K., S.-C. Tsay, W. Wiscombe, and K. Jayaweera, 1988, "Numerically stable algorithm for discrete-ordinate-method radiative transfer in multiple scattering and emitting layered media," *Applied Optics*, 27, pp. 2502 – 2509.

Steiner, A.K., G. Kirchengast, B.C. Lackner, B. Pirscher, M. Borsche, and U. Foelsche, 2009: "Atmospheric temperature change detection with GPS radio occultation 1995 to 2008," *Geophys. Res. Lett.*, 36, L18702, doi:10.1029/2009GL039777.

Stephens, G. L., S.-C. Tsay, P. W. Stackhouse Jr, and P. J. Flatau, 1990: "The relevance of the microphysical and radiative properties of cirrus clouds to climate and climatic feedback," *J. of the Atmos. sciences*, 47 (14), pp. 1742 – 1754.

Stephens, G.L., and Coauthors, 2002: "The CLOUDSAT mission and the A-train," *Bull. Amer. Meteor. Soc.*, 83, pp. 1771 – 1790.

Stephens, G. L. 2005: "Cloud feedbacks in the climate system: A critical review", *Journal of climate*, 18 (2).

Stocker, T.F., D. Qin, G.-K. Plattner, M. Tignor, S. K. Allen, J. Boschung, A. Nauels, Y. Xia, V. Bex, and P. M. Midgley, 2013: "Climate change 2013: The physical science basis," *Intergovernmental Panel on Climate Change, Working Group I Contribution to the IPCC Fifth Assessment Report, AR5*, Cambridge Univ Press, New York.

Stott and Kettleborough, 2002: Nature, 416, pp. 723 – 726.

Stubenrauch, C.J., and Coauthors., 2013: "Assessment of global cloud datasets from satellites Project and Database initiated by the GEWEX Radiation Panel," *Bull. Amer. Meteor. Soc.*,

pp. 1031 – 1049, Doi:10.1175/BAMS-D-12-00117.1

Sun, J-Q., X. Xiong, W.L. Barnes, and B. Guenther, 2007a, "MODIS Reflective Solar Bands On-Orbit Lunar Calibration," *IEEE Tran. on Geo. and Rem. Sen.*, v. 45, n. 7, pp. 2383 – 2393.

Sun, J-Q., and X. Xiong, 2007b, "MODIS Polarization-Sensitivity Analysis," *IEEE Tran. on Geo. and Rem. Sen.*, v. 45, n. 9, pp. 2875 – 2885.

Sun, J-Q., X. Xiong, A. Angal, C. Hongda, A. Wu, and X. Geng, 2014, "Time-Dependent Response Versus Scan Angle for MODIS Reflective Solar Bands," *IEEE Tran. on Geo. and Rem. Sen.*, v. 52, n. 6, DOI: 10.1109/TGRS.2013.2271448

Sun, J-Q., X. Xiong, B. Guenther, and W. Barnes, 2003: "Radiometric stability monitoring of the MODIS reflective solar bands using the Moon," *Metrologia*, 40, S85 – S88.

Sun, J., A. Angal, X. Xiong, H. Chen, X. Geng, A. Wu, T. Choi, and M. Chu, 2012: "MODIS RSB calibration improvements in Collection 6," *Proc. SPIE 8528, Earth Observing Missions and Sensors: Development, Implementation and Characterization II*, 85280N.

Sun W., and C. Lukashin, 2013, "Modeling polarized solar radiation from ocean-atmosphere system for CLARREO inter-calibration applications," *Atmos. Chem. Phys.*, 13, pp. 10303 – 10324, doi: 10.5194/acp-13-10303-2103.

Sun W., G. Videen, and M.I. Mishchenko, 2014, "Detecting super-thin clouds with polarized sunlight," *Geo. Res. Lett.*, 41, pp. 688 – 693, doi: 10.1002/2013GL058840.

Sun W., C. Lukashin, and D. Goldin, 2014, "Modeling polarized solar radiation for CLARREO inter-calibration applications: Validation with PARASOL data," *J. Quant. Spectrosc. Radiat. Trans.*, submitted.

Sun, W., R.R. Baize, C. Lukashin, and Y. Hu, 2015: "Deriving polarization properties of desert-reflected solar spectra with PARASOL data," *Atmos. Chem. Phys.*, 15, 7725 – 7734, doi: 10.5194/acp-15-7725-2015.

Swanson, K. L., G. Sugihara, and A. A. Tsonis, 2009: "Long-term natural variability and 20th century climate change," *Proc. Nat. Acad. Sci.*, 106, pp. 16120 – 16123.

Schwarz, M., 2011: "CLARREO IIP Optical Design Report," Optical Engineering Report MOE201101, Midwest Optical Engineering LLC.

Tanre D., et al., 2011, "Remote sensing of aerosols by using polarized, directional and spectral measurements within the A-train: The PARASOL mission," *Atmos. Measur. Tech.*, 4, pp. 1383 – 1395, doi: 10.5194/amt-4-1383-2011.

Taylor, J. K., et al., 2009: "Analysis of the CrIS Flight Model 1 Radiometric Linearity," *Fourier Transform Spectroscopy*, Optical Society of America.

Taylor, J.K. Revercomb, H. E., Buijs, et al., 2010: "The University of Wisconsin Space Science and Engineering Center Absolute Radiance Interferometer (ARI)," *Multispectral, Hyperspectral, and Ultraspectral Remote Sensing Technology, Techniques, and Applications III*, Incheon, Korea, 13-14 October 2010 (proceedings). SPIE-International Society for Optical Engineering, Bellingham, WA, Paper 78570K. Reprint No. 6514.

Taylor, J.K., H.E. Revercomb, Henry Buijs, et al., 2012: "The University of Wisconsin Space Science and Engineering Center Absolute Radiance Interferometer (ARI), instrument overview and radiometric performance," *SPIE Asia-Pacific Remote Sensing*, Paper 8527-24, doi:10.1117/12.977533.

Taylor, J.K., 2014: "Achieving 0.1 K Absolute Calibration Accuracy for High Spectral Resolution Infrared and Far Infrared Climate Benchmark Measurements," PhD Thesis, University of Laval.

Taylor, K.E., R.J. Stouffer, G.A. Meehl, 2012: "An Overview of CMIP5 and the experiment design." *Bull. Amer. Meteor. Soc.*, 93, pp. 485 – 498.

Taylor, P.C., N.G. Loeb, 2013: "Impact of Sun Synchronous Diurnal Sampling on Tropical TOA Flux Interannual Variability and Trends," *Journal of Climate*, Vol. 26, 2184 – 2191.

Tett, S.F., D.J. Rowlands, M.J. Mineter, and C. Cartis, 2013: "Can top-of-atmosphere radiation measurements constrain climate predictions ? part ii: Climate sensitivity," *Journal of Climate*, 26(23), pp. 9367 – 9383.

Thies, B., and Bendix, J., 2011: "Satellite based remote sensing of weather and climate: recent achievements and future perspectives," *Meteorological Applications*, 18(3), pp. 262 – 295.

Thorne, P. W., and R. S. Vose, 2010: "Reanalyses suitable for characterizing long-term trends: Are they really achievable ?" *Bull. Amer. Meteor. Soc.*, 91, pp. 353 – 361.

Tobin, D. C., H. E. Revercomb, R. O. Knuteson, F. A. Best, W. L. Smith, N. N. Ciganovich, R. G. Dedecker, S. Dutcher, S. D. Ellington, R. K. Garcia, H. B. Howell, D. D. LaPorte, S. A. Mango, T. S. Pagano, J. K. Taylor, P. van Delst, K. H. Vinson, and M. W. Werner, 2006: "Radiometric and spectral validation of atmospheric infrared sounder observations with the aircraft-based scanning high-resolution interferometer sounder," *J. of Geophys. Res.*, 111, doi:10.1029/2005JD006094.

Toller, G., X. Xiong, J. Sun, B. N. Wenny, X. Geng, J. Kuyper, A. Angal, H. Chen, S. Madhavan, and A. Wu, 2013: "Terra and Aqua Moderate-resolution Imaging Spectroradiometer Collection 6 Level 1B Algorithm," *J. Applied Remote Sensing*, 7(1).

Trenberth, K. E. and J. T. Fasullo, 2010: "Tracking Earth's Energy," *Science*, 328 (5976), pp. 316 – 317.

Trenberth, K.E, A. Belward, O. Brown, E. Haberman, T. R. Karl, S. Running, B. Ryan, M. Tanner, and B. A. Wielicki, 2013: "Challenges of a sustained climate observing system," *Climate Science for Serving Society: Research, Modeling and Prediction Priorities, G.R. Asrar and J.W. Hurell, Eds., Springer,* 1350.

Turner, D.D., et al., 2012: "Ground-based high spectral resolution observations of the entire terrestrial spectrum under extremely dry conditions," *Geophys. Res. Lett.*, 39, L10801, doi:10.1029/2012GL051542.

US Interagency Social Cost of Carbon Memo, 2010.

Von Storch, H., F.W. Zwiers, 1999: "Statistical Analysis in Climate Research," *Cambridge University Press*, New York, 484 pp.

Wang, D.D., D. Morton, J. Masek, A.A. Wu, J. Nagol, X. Xiong, R. Levy, E. Vermote, R. Wolfe, 2012: "Impact of sensor degradation on the MODIS NDVI time series," *Rem. Sens. Environ.*, 119, pp. 55 – 61.

Weatherhead, E. C., G. C. Reinsel, G. C. Tiao, X.-L. Meng, D. Choi, W.-K. Cheang, T. Keller, J. DeLuisi, D. J. Wuebbles, J. B. Kerr, A. J. Miller, S. J. Oltmans, J. E. Frederick, 1998: "Factors affecting the detection of trends: Statistical considerations and applications to environmental data," *J. of Geophys. Research*, 103, pp. 17149 – 17161.

Wetherald, R.T., S. Manabe, 1988: "Cloud Feedback Processes in a General Circulation Model," *J. Atmos. Sci.*, 45(8), 1397 – 1416.

Welsch, C., H. Swenson, S. A. Cota, F. DeLuccia, J. M. Haas, C. Schueler, R. M. Durham, J. E. Clement, and P. E. Ardanuy, 2001: "VIIRS (visible infrared imager radiometer suite): a next-generation operational environmental sensor for NPOESS," *IEEE Geoscience and Remote Sensing Symposium*, IGARSS, vol. 3, pp. 1020 – 1022.

Weisz, E., W. L. Smith and Smith, N., 2013: "Advances in simultaneous atmospheric profile and cloud parameter regression based retrieval from high-spectral resolution radiance measurements," *J.G.R.-Atmospheres*, 118, pp. 6433 – 6443.

Wielicki, B. A., B. R. Barkstrom, E. F. Harrison, R. B. Lee III, G. L. Smith, and J. E. Cooper, 1996: "Clouds and the Earth's Radiant Energy System (CERES): An Earth Observing System Experiment," *Bull. Amer. Meteor. Soc.*, 77, pp. 853 – 868.

Wielicki, B. A., Doelling, D. R., Young, D. F., Loeb, N. G., Garber, D. P., and Mac-Donnell, D. G., 2008: "Climate Quality Broadband and Narrowband Solar Reflected Radiance Calibration Between Sensors in Orbit," *International Geoscience and Remote Sensing Symposium (IGARSS)*, v. 1, 2008, pp. I257 – I260.

Wielicki, B.A., D.F. Young, M.G. Mlynczak, K.J. Thome, S. Leroy, J. Corliss, J.G. Anderson, C.O. Ao, R. Bantges, F. Best, K. Bowman, H. Brindley, J. Butler, W. Collins, J.A. Dykema, D.R. Doelling, D.R. Feldman, N. Fox, X. Huang, R. Holz, Y. Huang, Z. Jin, D. Jennings, D.G. Johnson, K. Jucks, S. Kato, D.B. Kirk-Davido , R. Knuteson, G. Kopp, D.P. Kratz, X. Liu, C. Lukashin, A.J. Mannucci, N. Phojanamongkolkij, P. Pilewskie, V. Ramaswamy, H. Revercomb, J. Rice, Y. Roberts, C.M. Roithmayr, F. Rose, S. Sandford, E.L. Shirley, W.L. Smith, Sr., B. Soden, P.W. Speth, W. Sun, P.C. Taylor, D. Tobin, X. Xiong, 2013: "Achieving Climate Change Absolute Accuracy in Orbit," *Bull. Amer. Meteor. Soc.*, pp. 1519 – 1539.

Winker, D.M., J. Pelon, J. A. Coakley Jr., S. A. Ackerman, R. J. Charlson, P. R. Colarco, P. Flamant, Q. Fu, R. M. Hoff, C. Kittaka, T. L. Kubar, H. Le Treut, M. P. McCormick, G. Mgie, L. Poole, K. Powell, C. Trepte, M. A. Vaughan, and B. A. Wielicki, 2010: "The CALIPSO Mission, A global 3D view of aerosols and clouds," *Bull. Amer. Met. Soc.*, 91, pp. 1211 – 1229.

WMO/BIPM, 2010: "Report on the WMO-BIPM workshop on measurement challenges for global observation systems for climate change monitoring: traceability, stability and uncertainty," 30 March to 1 April 2010. WMO/TD-No. 1557, 96 pp.

WMO, Global Climate Observing System, 2011: "Systematic observation requirements for satellite-based data products for climate, 2011 Update," *GCOS-154*, 128 pp.

Wu, A., X. Xiong, Z. Jin, C. Lukashin, B.N. Wenny, J.J. Butler, 2015: "Sensitivity of Intercalibration Uncertainty of the CLARREO Reflected Solar Spectrometer Features," *IEEE TGRS*, v. 53, 4741 – 4751, 10.1109/TGRS.2015.2409030

Xiong, X., and W.L. Barnes, 2006, "An Overview of MODIS Radiometric Calibration and Characterization," *Advances in Atm. Sciences*, v. 23, n. 1, pp. 69 – 79.

Xiong, X., J. Butler, N. Lei, J-Q. Sun, J. Fulbright, Z. Wang, J. McIntire, A. Angal, 2013, "Improvements of VIIRS and MODIS solar diffuser and lunar calibration," *SPIE Proceedings 8866, Earth Observing Systems XVIII, 88661M (23 September 2013)*, doi: 10.1117/12.2024792

Zelinka, M.D., S. A. Klein, and D. L. Hartman, 2012: "Computing and partitioning cloud feedbacks using cloud property histograms, Part II: Attribution to changes in cloud amount, altitude, and optical depth," *Journal of Climate*, 25, 3736 – 3754.

Zhao, M. and Running, S. W., 2010: "Drought-induced reduction in global terrestrial net primary production from 2000 through 2009," *Science* (80), 329, pp. 940 – 433.

A   Appendix: Climate Trend Uncertainty

The accuracy of climate trends relative to a perfect climate observing system can be determined following a simple extension of the methodology of Leroy et al. [2008b]. In particular, we can define a climate trend uncertainty factor, U_a, as the ratio of the accuracy of an actual observing system like CLARREO to that of a perfect observing system. This uncertainty factor is given by $U_a = (\delta m / \delta m_p)$, where δm is the accuracy of a climate trend with the CLARREO observations, and δm_p is the accuracy of the same climate trend for a perfect observing system. From Leroy et al. [2008b] we can show that

$$(\delta m_p)^2 = 12(\Delta t)^{-3}(\sigma_{var}^2 \tau_{var}) , \qquad (A.1)$$

and

$$(\delta m)^2 = 12(\Delta t)^{-3}(\sigma_{var}^2 \tau_{var} + \sum \sigma_i^2 \tau_i) . \qquad (A.2)$$

Using Equations A.1 and A.2 the definition of the U_a, we can show that

$$U_a = (1 + \sum f_i^2)^{1/2} , \qquad (A.3)$$

where

$$f_i^2 = \frac{\sigma_i^2 \tau_i}{\sigma_{var}^2 \tau_{var}} . \qquad (A.4)$$

In Equations A.1 - A.4, σ_{var}^2 is the variance of the natural variability of the climate system for the variable of interest (SW CRF, spectral nadir reflectance, cloud cover, etc.); τ_{var} is the autocorrelation time for natural variability [Leroy et al. 2008b], $\sigma_i^2 \tau_i$ are the same two quantities for the variance and time-scale of observation error source, respectively; and Δt is the length of the climate time series. The units of the trend uncertainty provided by Equations A.1 and A.2 are defined by the units used in σ_{var}, τ_{var} and Δt. For example, use of the values from Table 2 will provide a trend uncertainty in temperature per year.

The autocorrelation time is a measure of the time between independent samples in a time series of measurements. The number of independent samples, in turn, governs the uncertainty due to noise in the measurement. Therefore, longer time-scale error sources have a larger impact on uncertainty than shorter time-scales. A key error source for decadal change is calibration accuracy, and its time-scale is taken as the instrument lifetime on orbit [Leroy et al. 2008b]. The reason for this choice is that accuracy of an instrument can vary over time, while systematic errors are also likely to be present that are intrinsic to the instrument design itself and its limitations. As a result, for climate change we must consider the worst possible case that provides a calibration time scale of the life of the instrument, taken here as 60 months for CLARREO. For natural variability, the value of τ can be derived as in Leroy et al. [2008b] or as in Weatherhead et al. [1998] (used in this study), where is τ is given by $\tau = (1 + \rho)/(1 - \rho)$, and where ρ is the lag-1 autocorrelation. For this study, we compared both methods and found similar results to within about 20%.

Finally, we can define an uncertainty factor, U_t, for climate trend detection. This uncertainty factor is the ratio of the time to detect climate trends at any confidence level for the CLARREO

observing system to that of a perfect observing system. The result also can be derived from Leroy et al. [2008b] using analogous definitions to Equations A.1 - A.4, and is given by

$$U_t = (1 + \sum_i f_i^2)^{1/3} . \tag{A.5}$$

Equations A.1 - A.5 provide a powerful method to understand the trade space of climate trend accuracy, detection, and observing system uncertainties.

B Appendix: Advanced Radiative Transfer Models

A radiative transfer model is a key component in an Observing System Simulation Experiments (OSSE) and climate fingerprinting. It relates the Top-of-Atmosphere (TOA) radiance measured by a satellite instrument to the properties of atmospheric temperature, water vapor, trace gases, clouds, and surface skin temperature. Due to the large number of spectral channels of a hyperspectral sensor and the complex nature of radiative transfer modeling through inhomogeneous atmosphere, simulating a TOA radiance (or reflectance) spectrum is a time consuming process. Well-known line-by-line radiative transfer models, such as LBLRTM [Clough et al., 2005], are accurate but too slow for OSSE applications. MODTRAN is a "narrow band model" fast atmospheric radiative transfer code that has been extensively validated and is much faster than LBL models [Berk et al., 1998; Berk et al., 2000; Berk et al., 2006; Bernstein et al., 1996]. However, it still takes a significant amount of time to calculate one TOA reflectance or radiance spectrum. We have developed a a Principal-based Radiative Transfer Model (PCRTM), which has orders of magnitude faster speeds relative to LBL and MODTRAN.
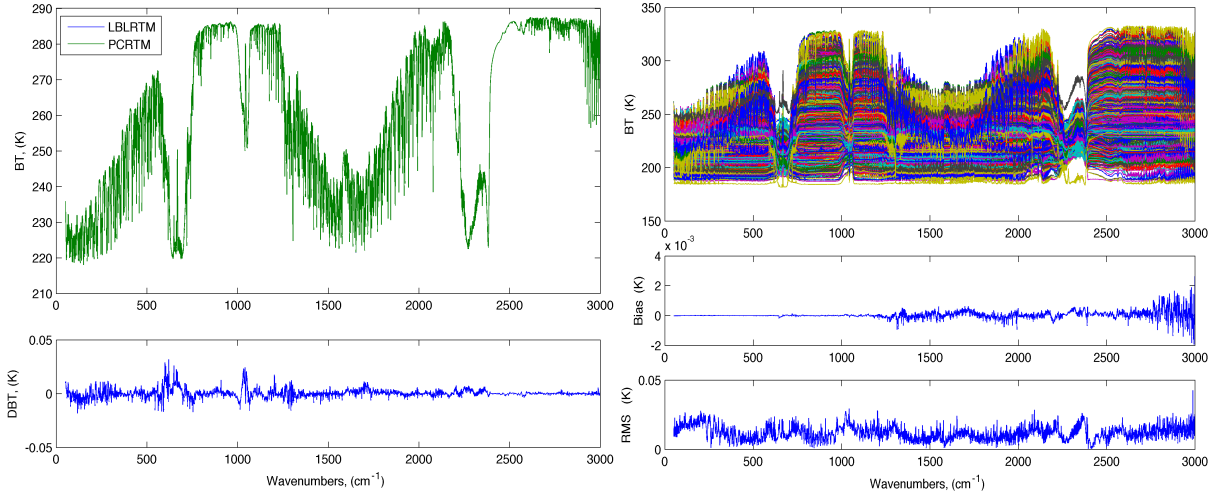

Figure B.1: Left: an example of calculated IR spectra from PCRTM and LBLRTM. Right: RMS and bias errors evaluated using 2000 spectra.

The main idea behind the PCRTM is to the treat the entire spectral region as a whole and to explore the spectral correlations among radiances at different frequencies [Liu et al., 2006; Liu et al., 2007; Liu et al., 2009]. Depending on the spectral resolution of the final spectrum, we can reduce the number of radiative transfer calculations by a factor of 30 to 970 relative to MODTRAN. The Principal Component (PC) scores are linearly related to the monochromatic TOA radiance or reflectance. Typically, only a few monochromatic radiative transfer calculations are needed after removing redundant information. The TOA reflectance or radiance spectrum is obtained by linearly combining the leading PCs with associated PC scores as weights.

A. PCRTM for Thermal InfraRed spectral region

The PCRTM calculation in the thermal IR spectral region mainly involves the atmospheric absorptions and emissions due to molecular species and clouds. It also includes thermal

emission from the earths surface and light scattering due to clouds. The accuracy of the PCRTM relative to the LBL model is very good. Figure B.1 is a comparison of calculated IR spectra from PCRTM and LBLRTM. The differences are less than 0.03 K in all spectral range from 50 cm^{-1} to 3000 cm^{-1}. We have performed the accuracy validation by calculating 2000 TOA radiance spectra under different atmosphere and surface conditions. The RMS errors are less than 0.03 K and bias errors are less than 0.002 K.
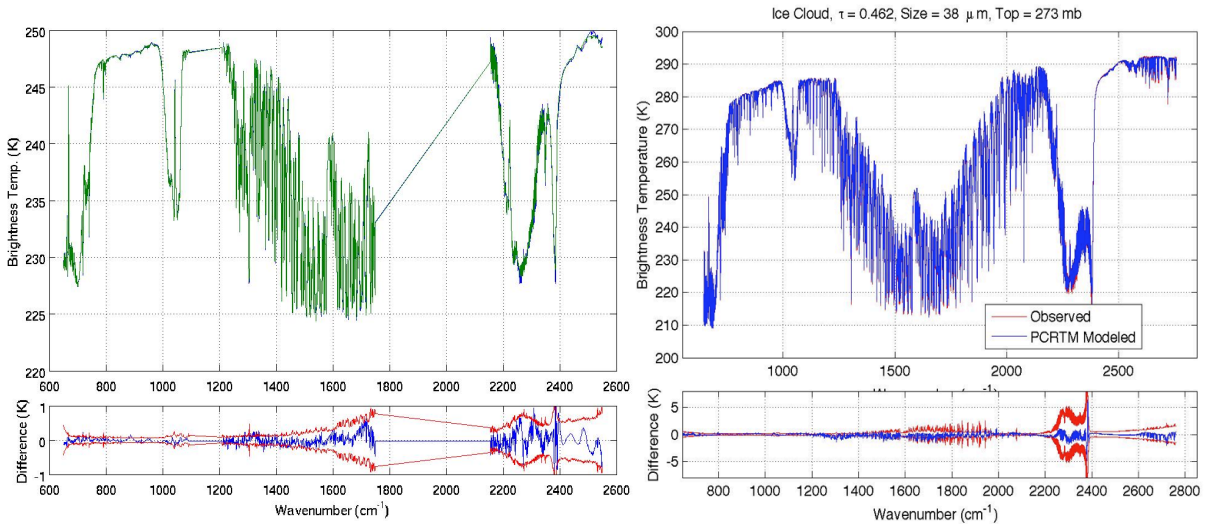

Figure B.2: LEFT: A CrIS OBSERVED FULL SPECTRAL RESOLUTION SPECTRUM (GREEN CURVE IN TOP PANEL) AND THE PCRTM CALCULATED SPECTRUM (BLUE CURVE IN TOP PANEL). THE BOTTOM PANEL IS THE DIFFERENCE BETWEEN THE TWO (BLUE CURVE). THE RED CURVE IS THE CrIS INSTRUMENT NOISE. RIGHT PANEL: IASI OBSERVED SPECTRUM (RED) AND PCRTM CALCULATED SPECTRUM (BLUE). THE DIFFERENCE BETWEEN THE TWO IS SHOWN IN THE BOTTOM PANEL (THE BLUE CURVE), THE RED CURVE IS THE IASI INSTRUMENT NOISE.

We have developed PCRTM models for CLARREO and various satellite and airborne hyperspectral sensors. The PCRTM model has been successfully used to analyze data from Atmospheric Infrared Sounder (AIRS), Infrared Atmospheric Sounding Interferometer (IASI), Cross-track Infrared Sounder (CrIS), NPOESS Airborne Sounder Testbed (NAST). Figure B.2 shows comparisons CrIS and IASI observed spectra with the PCRTM calculated spectra. The differences are typically less than the instrument noises (shown as the red curves on the lower panels). In addition to high accuracy, the PCRTM is orders of magnitude faster than the LBLRTM and MODTRAN calculations. Table B.1 lists the computational speed of the PCRTM for various sensors with spectral channel numbers ranging from 1317 to 19901. The PCRTM only takes a few miliseconds to calculate a spectrum.

B. PCRTM for Reflected Solar Spectral Region

In the solar spectral region from 300 nm to 2500 nm, the PCRTM only needs to perform radiative transfer calculations at about 300 monochromatic frequencies. The computational speed is about 800 faster relative to the medium speed correlated-k option in MODTRAN. Figure 3a shows selected TOA radiance spectra and 1b shows the RMS errors relative to MODTRAN using both dependent and independent data sets. Typically, the error is much smaller than 0.0006 mW/cm^2/sr/cm^{-1}, which is about 3 orders of magnitude smaller than the original radiance spectra. Typically, the relative error of TOA reflectance calculated

with PCRTM and that from MODTRAN is less than 0.05%. The input parameters to the PCRTM model includes satellite observation geometry, solar zenith and azimuthal angles, atmospheric temperature, water and trace gas profiles, cloud optical depth, cloud height, cloud thickness, cloud particle size, cloud phase, cloud fraction, aerosol type, aerosol optical depth, and aerosol height. The surface BRDF are calculated using Masuda's model for ocean and MODIS database for land. Figure B.3 shows an example of PCRTM calculated TOA reflectance spectrum and that observed by SCIAMACHY instrument. The atmospheric and surface properties used by the PCRTM are derived from the CERES Level-2 products.

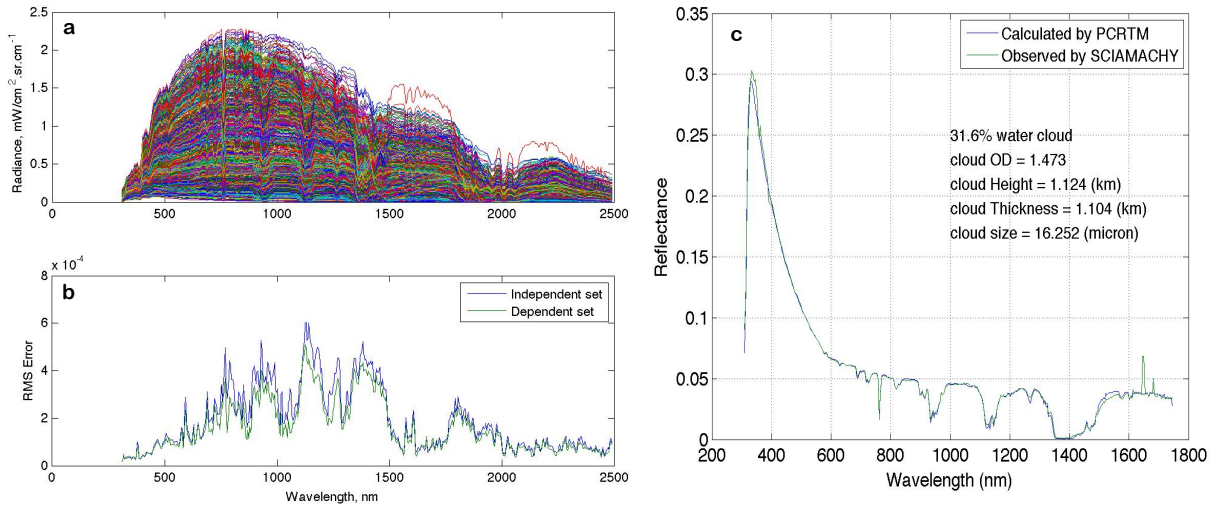| Sensor	Spectral Resolution	Channel Number	Computational Speed/Spectrum
CLARREO	0.1 cm^{-1}	19,901	0.022 sec
CLARREO	0.5 cm^{-1}	5,421	0.013 sec
CLARREO	1.0 cm^{-1}	2,711	0.012 sec
IASI	0.25 cm^{-1}	8,461	0.012 sec
AIRS	$0.5 - 2.5$ cm^{-1}	2,378	0.007 sec
CrIS	$0.625 - 2.5$ cm^{-1}	1,317	0.006 sec

Table B.1: PCRTM computational speed.

Figure B.3: a) selected TOA radiance spectra under different observation geometry and atmospheric and surface conditions. b) the RMS error of PCRTM calculated radiance spectral relative to those calculated using MODTRAN. c) Comparison of a PCRTM calculated TOA reflectance spectrum with that observed from the SCIAMACHY instrument. The atmospheric and surface properties used by the PCRTM are derived from the CERES Level-2 products.

C   Appendix: Polarization Distribution Models

Reflected solar radiation from the Earth's ocean-atmosphere system (320 nm to 2300 nm wavelength range) can be significantly polarized by the Earth's surface and by atmospheric components. Effects from polarization of reflected light bias radiometric performance of various operational spaceborne instruments, such as MODIS and VIIRS, and imagers in geostationary orbits. It is essential to evaluate and correct for this bias in order to perform accurate measurements of reflectance at the top-of-atmosphere [Lyapustin et al., 2014]. CLARREO goal is to perform on-orbit inter-calibration with the target instrument by providing observations coincident in time, and matched in space and viewing geometry. The inter-calibration process consists of iterative adjustments to the target sensor calibration to account for the polarization effects with respect to the observations made by CLARREO [Lukashin et al., 2013]. Knowing the inter-calibrated instrument's on-orbit sensitivity to polarization and polarization state of reflected light would determine the radiometric polarization correction.
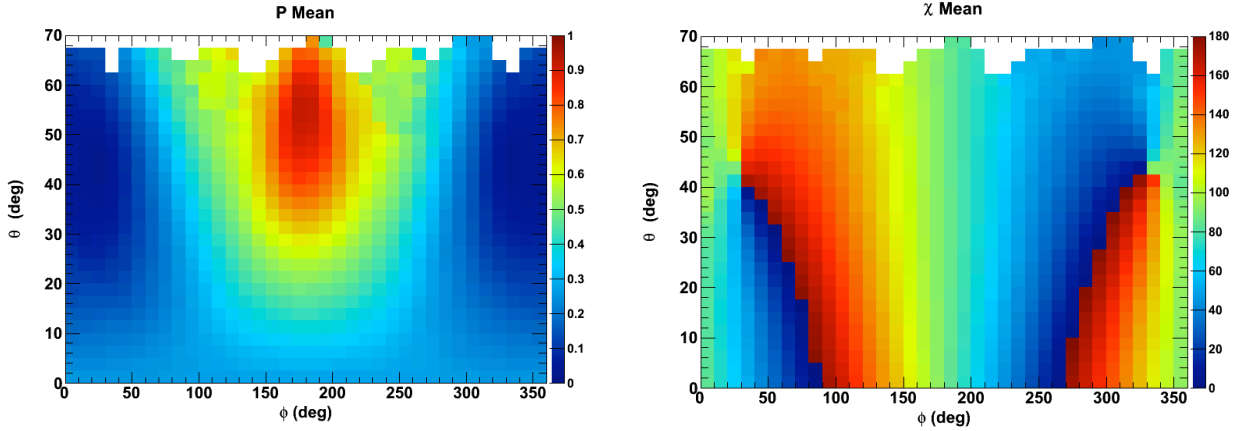

Figure C.1: PDM for the clear sky ocean scene based on PARASOL data. Left: degree of linear polarization, P. Right: angle of linear polarization, χ. Both parameters are averaged over the 2006 observations, for solar zenith angle between $40°$ and $50°$, and plotted versus the viewing zenith angle (θ) and relative solar azimuth (ϕ).

A. Empirical Polarization Distribution Models

Feasibility of the on-orbit inter-calibration have been demonstrated using existing data – by developing the Polarization Distribution Models (PDM) as functions of viewing scene type and geometry [Nadal and Breon, 1999; Lukashin et al., 2013]. A state of light at the top of the atmosphere is fully specified by three parameters: total radiance, I), degree of linear polarization, P, and angle of linear polarization, χ. Constructing a PDM is providing mean values and uncertainties for P and χ for every scene type globally, and as function of solar and viewed geometry.

The only available dataset containing the polarization parameters measured on orbit was collected by the POLarization and Directionality of the Earth's Reflectances (POLDER) instrument onboard the Polarization and Anisotropy of Reflectances for Atmospheric Sciences coupled with Observations from a Lidar (PARASOL) satellite. The satellite was operational between 2004 and 2013 and was flying as a part of the A-Train formation at 705 km altitude.

The instrument consisted of high-resolution a CCD detector capable of taking measurements from nine spectral channels from blue (443 nm) to infrared (1020 nm), three of which, 490, 670, and 865 nm, measured polarization. A unique feature of the instrument was the multi-angular sampling the same ground-pixel being imaged up to 15 times by the same pixel at different viewing angles.

From the Stokes parameters I, Q, and U measured by PARASOL, the relative degree of polarization P and the angle of linear polarization χ may be easily computed:

$$P = \frac{I_p}{I} = \frac{\sqrt{Q^2 + U^2}}{I}, \tag{C.1}$$

$$\chi = \begin{cases} \frac{1}{2}\arctan(U/Q) \text{ for } Q > 0, U > 0 \\ \frac{1}{2}\arctan(U/Q) + \pi \text{ for } Q > 0, U < 0 \\ \frac{1}{2}\arctan(U/Q) + \pi/2 \text{ for } Q < 0 \end{cases} \tag{C.2}$$

where χ is defined from 0° to 180° relative to instrument viewing plane. A PDM for a given scene type and solar zenith angle can be represented by two-dimensional histograms of viewing zenith angle θ versus relative azimuth ϕ, with the color axis representing P or χ. An example of a PDM using the 2006 PARASOL dataset for the clear-sky ocean scene is shown in Figure C.1. The plots show the values of P and χ averaged over the entire year. We note that for these plots the solar zenith angle was restricted to values between 40° and 50° and wind speed to below 2.5 m s^{-1}. To ensure the purity of the clear-sky selection, cloud fraction was required to be less than 1%. Due to the near absence of aerosols, both P and χ exhibit nearly perfect forward/backward ($\phi < 180°/\phi > 180°$) scattering symmetry as expected. The maximum degree of polarization, 0.9, is found at $\phi = 180°$, the direction opposite the Sun. That the degree of polarization is so high, close to its upper limit of 1, is not surprising given the highly polarizing nature of water surfaces. On the other hand, the degree of polarization is minimum when facing the Sun and in Figure C.1 (left plot) is seen to be less than 0.1. An example of PDM distribution for polarization angle χ is shown in Figure C.1 (right plot). As it is expected, χ values are close to 90° in scattering plane ($\phi = 0°; 180°$).

The uncertainty on the reflectance measured by an imager, such as MODIS or VIIRS, after its intercalibration with CLARREO may be found as:

$$\delta_{RI} = \sqrt{\delta_{\rho_0}^2 + \left(\frac{mP}{1 + mP}\right)^2 (\delta_m^2 + \delta_P^2)}, \tag{C.3}$$

where ρ_0 is the imager reflectance before the polarization inter-calibration is applied, m is the imager's sensitivity to polarization, and δ_{ρ_0}, δ_m and δ_P are the relative uncertainties on ρ_0, m and P, respectively. The δ_{ρ_0} in Equation C.3 is comprised of three components: CLARREO's own instrument accuracy (0.15%), inter-calibration sampling uncertainty after averaging (0.1%) and the target sensor stability uncertainty (0.1%). The combined value of the three uncertainties is 0.2%. The value of m is 0.03, which is roughly the sensitivity to polarization for both MODIS and VIIRS. Under these conditions and using the P PDMs discussed above we obtain the δ_{RI} dependencies as shown in Figure C.2. One finds that for realistic values of the uncertainty on the imager sensitivity, between 10% and 20%, the polarization bias can as high as nearly 1%. This dependency can be shown to be nearly invariant for bands between 670 nm and 865 nm.
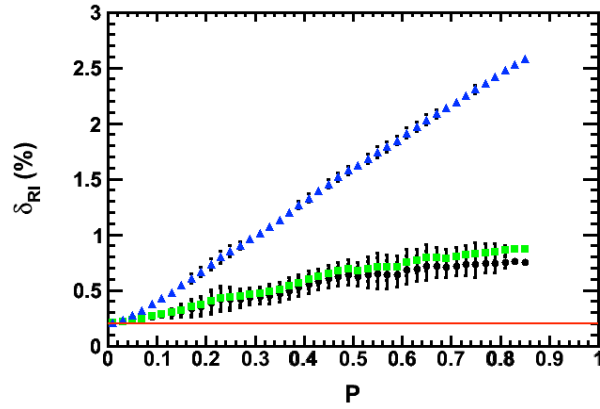
Figure C.2: Uncertainty in the inter-calibrated reflectance as a function of polarization for the 670 nm band derived from the dependence shown in the left plot. The imager sensitivity to polarization, was set to 0.03 (approximately MODIS and VIIRS sensitivity) and its relative uncertainty to 10% (third curve from the top, in black), 20% (second curve from the top, in green) and 100% (top curve, in blue). Also shown (bottom line, red) is the uncertainty in reflectance if the polarization is assumed to be zero.

In conclusion, CLARREO's inter-calibration approach in reflected solar may be tested using the empirical Polarization Distribution Models. Such models can be constructed using data from the three polarized channels at 490, 670, and 865 nm of the POLDER instrument aboard the PARASOL satellite. The PDMs may be broken down or combined by different scene types, such as clear-sky ocean, clear-sky vegetation, and deserts, as well as different types of cloudy scenes, such as ice or water clouds. Using radiative transfer modeling, the PDM's coverage can also be extended to the entire visible spectrum.

B. Theoretical Polarization Distribution Models

In Sun and Lukashin 2013, the authors employed the adding-doubling method [Hansen et al., 1971; Evans and Stephens, 1991], and coupled it with a rough-ocean-surface light reflection matrix [Cox and Munk, 1956], to model the reflected solar radiation from the ocean-atmosphere system. This adding-doubling radiative transfer model (ADRTM) outputs are far more accurate than the widely validated discrete-ordinate radiative transfer (DISORT) model [Stames et al., 1988] results [Sun and Lukashin, 2013; Lasis et al., 1998].

We also validated the ADRTM results with the PARASOL [Tanre, 2011] polarization measurements as displayed in Figure C.3 [Sun et al., 2014]. The PARASOL data used is from the 24-day measurements for a wind speed range of 6 to 9 m/s. In the modeling, the wind speed is 7 m/s, the sea-salt AOD is 0.06 at the wavelength of 670 nm, and the US standard atmosphere is used. We also incorporate a thin layer of undetected cirrus cloud with an optical depth of 0.18 in the ADRTM. We only show the data at the relative azimuth angle (RAZ) of 1.5° and 178.5°, respectively. We can see that the reflectance and degree of polarization (DOP) from the PARASOL data and the ADRTM model are in good agreement. We have demonstrated that the angle of linear polarization values from the PARASOL observations and the ADRTM are in very good agreement [Sun et al., 2014].

We also conducted the validation of the ADRTM for cloud scenes. Good agreement between model results and satellite data is shown for both liquid water clouds and ice clouds [Sun et
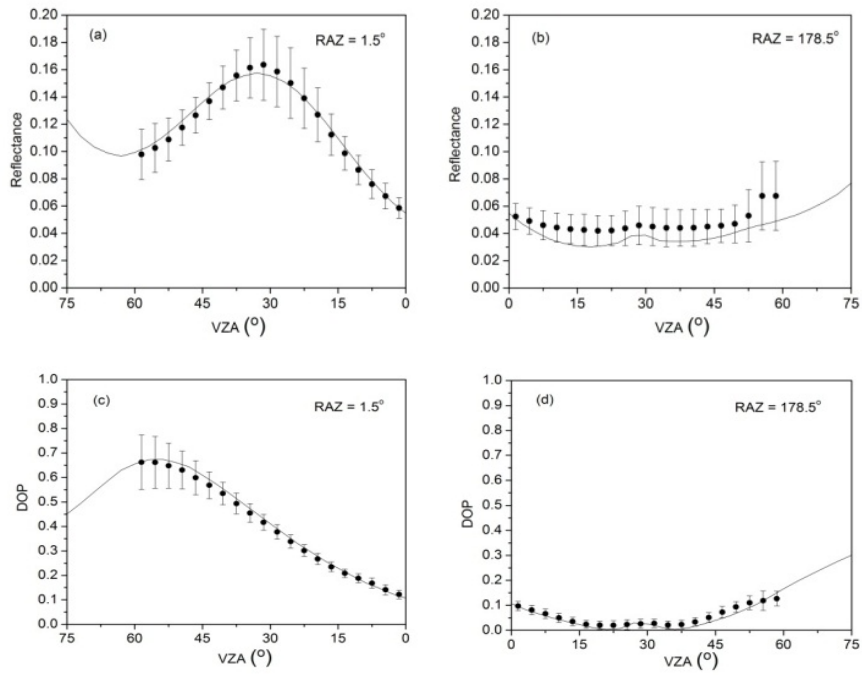
Figure C.3: DIRECTIONAL IRRADIANCE REFLECTANCE AND DEGREE OF POLARIZATION (DOP), AS FUNC-
TIONS OF VIEWING ZENITH ANGLE (VZA), AT A WAVELENGTH OF 670 NM FROM PARASOL DATA FOR
CLEAR-SKY OCEANS AVERAGED IN A SOLAR ZENITH ANGLE (SZA) BIN OF 27° – 30° (BLACK DOTS) AND
ADRTM RESULTS AT A SZA OF 28.5° (SOLID CURVE). ERROR BARS SHOW THE STANDARD DEVIATIONS
OF THE PARASOL DATA.

al., 2014]. Sensitivities of reflected solar radiation's polarization to various ocean-surface and
atmospheric conditions are addressed [Sun and Lukashin, 2013] and polarization features of
desert surfaces in [Sun et al., 2015] . These studies suggest that the modeling can provide a
reliable approach for making the spectral PDM's for CLARREO inter-calibration applications,
which cannot be achieved by empirical PDMs alone because of limited spectral coverage.

D Appendix: List of Acronyms

AASI – Advanced Accuracy Satellite Instrumentation
ABB – Ambient Blackbody
ABI – Advanced Baseline Imager
ADRTM – Adding Doubling Radiative Transfer Model
AERI – Atmospheric Emitted Radiance Interferometer
AIRS – Atmospheric InfraRed Sounder
AMSU – Advanced Microwave Sounding Unit
AOI – Angle of Incidence
API – Application Programming Interface
APL – Applied Physics Laboratory
AR4 – Forth Assessment Report (IPCC)
ARI – Absolute Radiance Interferometer
ARM – Atmospheric Radiation Measurement
ASDC – Atmospheric Science Data Center
ASIC3 – Achieving Satellite Instrument Calibration for Climate Change
BRDF – Bidirectional Reflectance Distribution Function
CBE – Current Best Estimate
CDS – Calibration Demonstration System
CERES – Clouds and Earth's Radiant Energy System
CEOS – Committee on Earth Observation Satellite
CFTS – Calibrated Fourier Transform Spectrometer
CHAMP – Challenging Mini-Satellite Payload
CLARREO – Climate Absolute Radiance and Refractivity Observatory
CMIP3 – Coupled Model Intercomparison Project
COMPASS – China's Global Navigation System
CORSAIR – Calibrated Observations of Radiance Spectra from the Atmosphere in the far-InfraRed
COSMIC – Constellation Observing System for Meteorology, Ionosphere, and Climate
COT – Cloud Optical Thickness
CPRS – Cloud Property Retrieval System
CRF – Cloud Radiative Forcing
CrIS – Cross-track Infrared Sounder
CSB – Cold Source Blackbody
DCC – Deep Convective Clouds
DERM – Diurnal Exothermic Radiance Model
DESDynI – Deformation, Ecosystem Structure, and Dynamics of Ice
DICE – Data Integration and Collection Environment
DISORT – Discrete Ordinate Radiative Transfer Model
DOP – Degree of Polarization
DR – Dual Regression
DS – Decadal Survey
DTGS- Deuterated Triglycine Sulfate (IR detector material)
ECMWF – European Centre for Medium-Range Weather Forecasts
ECV – Essential Climate Values

ELC – ExPRESS Logistics Carrier
EOS – Earth Observing System
ERA – ECMWF Re-Analysis
ERSST – Extended Reynolds Sea Surface Temperature
ESTO – Earth Science Technology Office
EV – Earth View
EVI – Earth Venture Instrument
FIREBIB – Far-Infrared Extended Blocked Impurity Band
FIRST – Far-Infrared Spectroscopy of the Troposphere
FM – Flight Model
FOR – Field of Regards
FORGE – Far-Infrared Observations of the Radiative Greenhouse Effect
FORUM – Far-infrared-Outgoing-Radiation. Understanding and Monitoring
FOV – Field-Of-View
FRGF – Flight Releasable Grapple Fixture
FTS – Fourier Transform Spectrometer
FWHM – Full-Width Half-Maximum
GCOS – Global Climate Observing System
GDAS – Global Data Assimilation System
GDP – Gross Domestic Product
GFE – Government Furnished Equipment
GFOV – Ground Field of View
GEO – Geostationary Earth Orbit
GFOV – Ground Field Of View
GISS – Goddard Institute of Space Studies
GLONASS – Global Navigation Satellite System
GNSS – Global Navigation Satellite System
GOES-R – Geostationary Operational Environmental Satellite R-series
GOS – Global Observing System
GPP – Gross Primary Productivity
GPS – Global Positioning System
GRACE – Gravity Recovery and Climate Experiment
GRAS – GNSS (Global Navigation Satellite System) Receiver for Atmospheric Sounding
GSICS – Global Spase-based Inter-Calibration System
ENSO – El Niño-Southern Oscillation EOS – Earth Observing System
HAM – Half Angle Mirror
H-CAM-P – HTV Cargo Attachment Mechanism-Passive
HIRS – High-resolution Infrared Radiation Sounder
HIS – High-resolution Interferometer Sounder
HREP – HICO and RAIDS Experiment Payload
HTV – H-II Transfer Vehicle
HySICS – Hyperspectral Imager for Climate Science
IASI – Infrared Atmospheric Sounding Interferometer
IB – In Band
ICESat-II – Ice, Cloud,and land Elevation Satellite
ICF – Information Content Framework
IGOR – Integrated GPS Occultation Receiver

IGS – International GNSS Service
IFOV – Instantaneous Field Of View
IIP – Instrument Incubator Program
ILRS – International Laser Ranging Services
ILS – Instrument Line Shape
IMG – Interferometric Monitor for Greenhouse Gases
INFLAME – IN-situ Net FLux within the AtMosphere of the Earth
ISCCP – International Satellite Cloud Climatology Project
IU – Intercalibration Uncertainty
IPCC – Intergovernmental Panel on Climate Change
IRIS – Infrared Interferometer Spectrometer
IR – InfraRed (wavelength range)
IRR – IASI Reduction Resolution
ISS – International Space Station
ITCZ – Intertropical Convergence Zone
JAXA – Japan Aerospace Exploration Agency
JEM-EF – Japanese Experiment Module Exposed Facility
LBLRTM – Line-By-Line Radiative Transfer Model
LC – Linear Combination
LECT – Local Equator Crossing Time
LEO – Low Earth Orbit
LRD – Launch Readiness Date
LRR – Laser Retro Reflector
LW – Longwave
MAIAC – Multi-Angle Implementation of Atmospheric Correction
MCR – Mission Concept Review
MCST – MODIS Calibration Science Team
MCT – Mercury Cadmium Telluride
MEI – Multivariate ENSO Index
MERRA – Modern-Era Retrospective Analysis for Research and Applications
MHS – Microwave Humidity Sounder
MIIC – Multi-Instrument Inter-Calibration (framework)
MODIS – Moderate Resolution Imaging Spectroradiometer
MODTRAN – Moderate Resolution Atmospheric Radiance and Transmittance Model
MTSAT – Multifunctional Transport Satellite
NAST – NPOESS Airborne Sounder Testbed
NDVI – Normalized Difference Vegetation Index
NIR – Near-InfraRed (wavelength range)
NPV – Net Present Value
NRC – National Research Council (USA)
NRL – Naval Research Laboratory
OARS – On-orbit Absolute Radiance Standard
OBPG – Ocean Biology Processing Group
OIT – Orbit Injection Time
OLR – Outgoing Longwave Radiation
OOB – Out Of Band
OSSE – Observing System Simulation Experiment

OVTS-Orbit Verification Test System
PAR – Photosynthetically Active Radar
PARASOL – Polarization & Anisotropy of Reflectances for Atmospheric Sciences coupled with Observations from a Lidar
PC – Polarization Correction
PCA – Principal Component Analysis
PCRTM – Principal Component Radiative Transfer Model
PDF – Probability Density Function
PDM – Polarization Distribution Model
PIU – Payload Interface Unit
POD – Precise Orbit Determination
POLDER – Polarization and Directionality of Earth's Reflectances
PRP-Partial Radiative Perturbation
PSF – Point Spread Function
PV – Photovoltaic
PW – Precipitable Water
QCL – Quantum Cascade Laser
RAAN – Right Ascension of Ascending Node
RAZ – Relative (solar) AZimuth
RBI – Radiation Budget Instrument
RESTful – REpresentational State Transfer
RF-Radio Frequency
RHUBC-II – Radiative Heating in Underexplored Bands Campaign
RMS – Root Mean Square
RO – Radio Occultation
ROLO – USGS Lunar Irradiance model
RS – Reflected Solar
RSB – Reflective Solar Bands
RSR – Relative Spectral Response
RT – Radiative Transfer
RTA-Radiative Transfer Algorithm
RUAG – Rüstungs Unternehmen Aktiengesellschaft
RU – Radiometric Uncertainty
RVS – Response Versus Scan
SAGE III – Stratospheric Aerosol and Gas Experiment
SBAF – Spectral Band Adjustment Factors
SC – SpaceCraft
SCC – Social Cost of Carbon
SCIAMACHY – SCanning Imaging Absorption SpectroMeter for Atmospheric CartograpHY
SD – Solar Diffuser
SDSM – Solar Diffuser Stability Model
SeaWIFS – Sea-Viewing Wide-Field-of-View Sensor
SER – Systems Engineering Report
SEU – Singular Event Upset
SI – International System of Units (Système International)
SOC – Surface Optics Corporation
SMAP – Soil Moisture Active-Passive

SLR – Satellite Laser Ranging
SNO – Simultaneous Nadir Overpass
S-NPP – Suomi National Polar-orbiting Partnership
SSA – Singular Spectrum Analysis
SSM – Scene Select Mirror
SSM/T2 – Special Sensor Microwave/Temperature & Humidity Profile
SST – Sea Surface Temperature
SV – Space View
SVM – Science Value Matrix
SW – Shortwave
SZA – Solar Zenith Angle
TEC – Total Electron Count
TLE – Two Line Element
TOA – Top of the Atmosphere
TPC – Transformed Principal Components
TRL – Technology Readiness Level
TRUTHS – Traceable Radiometry Underpinning Terrestrial and Helio Studies
TSIS – Total Solar Irradiance Spectrometer
USO – Ultra-Stable Oscillator
VCA – Vicarious Calibration Analysis
VIIRS – Visible Infrared Imaging Radiometer Suite
VOI – Value of Information
VIS – VISible (wavelength range)
VTBB – Variable Temperature Black Body
VZA – Viewing Zenith Angle
WASP – Wallops Arc Second Pointer
WMO – World Meteorological Organization
YSL – Years Since Launch